UNIVERSITY OF CALGARY

Stochastic Modeling of the Paskapoo Formation

by

Vance A. Matthews

A THESIS

SUBMITTED TO THE FACULTY OF GRADUATE STUDIES

IN PARTIAL FULFILMENT OF THE REQUIREMENTS FOR THE

DEGREE OF "MASTER OF SCIENCE"

GEOSCIENCE DEPARTMENT

CALGARY, ALBERTA

JANUARY 2011

UNIVERSITY OF
CALGARY

Abstract

Current groundwater resource practice for the evaluation of non-ideal groundwater systems is unable to address the heterogeneity inherent in these systems because it uses numerical models that simplify the underlying problem to a homogeneous isotropic problem. The workflow and methodology employed in this process systematically fails to adequately reproduce the system behaviour and provide for the proper analysis of pumping test data and characterization of the system of long-term safe yields. In Alberta, the Farvolden Q_{20} method is used for evaluating long-term water well yield from an aquifer. This concept was introduced in 1959 and is based on the theoretical estimate of water level drawdown in a pumping well after 20 years of pumping. The concept offers an estimation of maximum well yield but is based on a simplistic aquifer model which under many circumstances may result in faulty estimates in long-term yield (SRC 2006). Since 1959 there have been advances in pressure transient analysis that can be utilized to improve the evaluation of long-term yield.

In Alberta, the Paskapoo Formation covers 10,000 km^2 and is located adjacent to the deformed belt east of the Foothills. It is the largest single source of groundwater in the Canadian Prairies with approximately 85% of the wells being located between the cities of Calgary and Red Deer making this area one of the highest groundwater use areas in the country.

The continental sediments of the Paskapoo Formation represent the late-stage foreland infill (Hamblin 2004). The Paskapoo formation is located in the north central and south

central regions of Alberta and formed within a high energy sedimentation environment that attained a maximum thickness of 900 m within the core of the Alberta Syncline (Jerzykiewicz 1997, Hamblin, 2004).

The Paskapoo is geologically complex and is comprised of the Haynes member, Lacombe member, and the Dalehurst member. The Haynes member consists of thick, massive, and coarse-grained sandstones. The Lacombe member overlies the Haynes members and consists of channel sand and complexes encased in floodplain deposits which are characterized by siltstone, mudstone, shale, and minor coal. The Dalehurst member overlies the Lacombe member and is only present near the Hinton area immediately adjacent to the Foothills and is an erosional remnant.

The Paskapoo Formation is part of the Scollard-Paskapoo aquifer which lies at the top of the Cretaceous-Tertiary succession in the Alberta Basin. The hydrogeology of the system is very complex owing to variations in the depositional environments which were present throughout north central and south central Alberta during the Laramide Orogeny. The stratigraphy consists of randomly arranged sand channels and complexes embedded in low permeability overbank/flood plain deposits. Spatial distribution and connectivity of the permeable facies is variable and as such water yield is highly variable. Regionally, the system is topographically driven and pressures are slightly subhydrostatic (Bachu et al 2003).

The Scollard-Paskapoo system consists of a groundwater flow toward the north-northeast in a shallow gravity driven aquifer system characterized by meteoric recharge along local and regional topographic highs (Harrison et al 2006, Vogwill 1983). The elevation versus pressure head data indicate a moderately positive correlation suggesting that there is a regional topographic effect on flow (Harrison et al 2006).

High yielding areas of the Paskapoo Formation with fracturing have been classified as moderate to poor aquifers with yields range from less than 9 m^3/d to 35 m^3/d (Vogwill 1983). Yields in other areas have been recorded as high as 3200 m^3/d in the Wabamun Lake region (Harrison et al 2006). Transmissivity for Paskapoo aquifers ranges from less than 1.5 m^2/d to over 100 m^2/d, depending on the degree of fracturing, but has been recorded as high as 1,000 m^2/d. Storativity values range from 5×10^{-5} to 10^{-4} indicating that locally most aquifers are confined to varying degrees (Vogwill 1983). Regional permeability data for the Paskapoo indicate values ranging from 10 to 1000 millidarcies where the fracture network is present (Vogwill 1983).

The geology of the Paskapoo represents a heterogeneous anisotropic system consisting of a non-marine succession of irregular sandstone channels of variable thickness and sinuosity embedded in overbank deposits with a 3-dimensional fracture overprint. Current deterministic methods are not capable of representing the complexity required to reproduce the behaviour of non-ideal systems under steady-state or transient conditions. The level of geologic complexity and uncertainty present within the Paskapoo Formation

calls for the implementation of alternative workflows and methods for the evaluation of subsurface data.

A stochastic 3-dimensional geomodel approach to run a series of simulations that contain hydrofacies with geologically realistic shapes to produce realistic sharp physical and hydrologic boundaries between hydrofacies representative of the Paskapoo Formation for subsequent upscaling and simulation of steady-state and transient conditions is proposed in this project. A geomodel is developed using statistically relevant data based on an analogue model developed by Burns et al. (2010b). Property modeling is completed during the geomodeling process whereby the grid cells are populated with statistically appropriate geologic and hydraulic values. A series of simulated transient pumping tests are performed to evaluate system response and the utility of both long-term (approximately 8 to 15 hours) and short-term tests (4 hours) and subsequently the application of the Farvolden Q_{20}.

Pressure transient analysis is used to evaluate the transient pressure data to identify the presence of boundaries, prevailing flow regimes, and for parameter estimation. It is proposed that the workflow and the methodology described in this paper provides for a more rigorous methodology that is capable of representing the geology and hydraulic response of the system and that it is this workflow and methodology that should be employed instead of current groundwater evaluation practices that result in the use of simplified and at times inappropriate reservoir models such as Theis, Cooper-Jacob, and use of the Farvolden Q_{20} for quantification of long-term aquifer yield.

Acknowledgements

I would like to express my gratitude to my supervisor, Dr. Laurence R. Bentley, whose expertise, understanding, candidness, attitude, and enjoyable conversations made my graduate experience very rewarding. I appreciate his knowledge and skill in the many areas that this research has taken us (e.g., object modeling, geostatistics, numerical flow modeling, pressure transient analysis), and his assistance in reviewing and writing reports (i.e., thesis proposal and this thesis). I greatly appreciate his patience and belief that I would someday complete my research and the writing of this thesis, especially considering the life matters that I have experienced and at times the lack of much hard evidence during my graduate studies.

I would like to thank Dr. René Therrien of the Université Laval for his support and advice on trouble shooting modeling problems and HydroGeoSphere.

Finally, I would like to thank Dr. Erick Burns of the United States Geological Survey in Portland, Oregon for his advice and support with geomodeling and running upscaling algorithms. I appreciate all of his effort and his time spent during the many conversations we had over the telephone.

Table of Contents

List of Tables

List of Figures and Illustrations

List of Symbols, Abbreviations and Nomenclature

Symbol	Definition
bgs	below ground surface
EPM	equivalent porous media
gpm	gallons per minute
IARF	infinite acting radial flow
IRF	initial radial flow
Ma	million years
K	hydraulic conductivity
km^2	square kilometres
K_V	vertical permeability
K_H	horizontal permeability
L^2/T	length squared over time
m^3/d	cubic meters per day
m^2/d	square meters per day
m^3/yr	cubic meters per year
m/yr	meters per year
m	meters
mg/L	milligrams per litre
Δp	pressure change
PTA	pressure transient analysis
Q_{20}	Farvolden long-term well yield
U of C	University of Calgary
US	United States
USGS	United States Geological Survey

CHAPTER 1: INTRODUCTION

There has been an increase in the interest and demand for fresh water as a direct result of an increase in population, groundwater utilization, agricultural and industrial activities, and adverse effects to the environment from pollution, drought and global warming, and municipal economic and planning problems (c.f., Sen 1995; and Meyboom 1961). Groundwater is seen as a resource that requires best management practices for sustainability.

Without adequate guidelines and oversight of this natural resource, over-utilization could result in negative impacts leading to ecological, political, social and economic consequences yielding long term sustainability of the resource unattainable or at least financially taxing and challenging (International Symposium on Groundwater Sustainability 2006). For protection, management, and sustainable use of this precious resource we require improvements in regulatory frameworks, a better understanding of complex non-ideal systems and better tools and methodologies for evaluating groundwater resources.

Current Practice

The current practice for evaluating groundwater resources permits the use of limited geologic information, a single pumping test result, and invoking the assumptions that validate the simple numerical models of Theis (1935) and Cooper-Jacob (1946). Under Alberta Environment's Groundwater Evaluation Guideline (Alberta Environment 2003), both the Theis and Cooper-Jacob models are considered appropriate for use in pressure

transient analysis regardless of the geologic complexity. In other words, it is assumed that the aquifer is of infinite areal extent, that water is bounded by less permeable beds below for unconfined conditions and by less permeable beds above and below for confined cases, that the aquifer is homogeneous, isotropic, and of uniform thickness, the aquifer is elastically compressible and water is released instantaneously, and that flow is laminar and radially toward the production well (Alberta Environment 2003). Conventional deterministic mathematical models are incapable of addressing uncertainty in the inter-well spacing (i.e., variability in the geology and hydraulic parameters between wells) and are still used to describe the physical behaviour of the aquifer but lack the detailed reality of the physical geology and groundwater system. This can lead to inaccurate modeling results due to complex heterogeneities in hydraulic conductivity fields or the implementation of ill-conceived conceptual models (Burrows 2004).

Under local scale conditions application of these simplified models might be valid. However, since it is impossible to have deterministic knowledge of the geology, hydraulic parameters, and pressure measurements of these systems, we are uncertain as to the applicable temporal and physical scale of the problem. Depending on the connectivity of the hydraulically significant facies and the spatial distribution of these facies, the pressure response at an observation well may not provide any revealing insight into the system. Therefore in heterogeneous systems the Theis assumptions are always violated and use of this model may have limited diagnostic value.

The Farvolden Q_{20} method for estimation of the maximum theoretical long-term safe yield of a well was introduced in 1959. This method is presented in Alberta Environment's Groundwater Evaluation Guideline (2003) as part of the Best Management Practice for interpretation of pumping test data which is required when submitting an application for a water use allocation licence. The Farvolden Q_{20} is based on a theoretical model that was developed in the 1930's and 1940's for the flow of groundwater to a well. It is based on estimates of water level drawdown in the production well after 20 years of pumping (Maathuis and van der Kamp 2006). Here it is assumed that the drawdown per log cycle of time, there being 8 log cycles over a 20 year period, is one-eighth of the available head. This method offers an objective and quantitative estimate of the maximum well yield (Maathuis and van der Kamp 2006; Alberta Environment 2003). This practice fails to address the complexity and non-ideal response of groundwater systems that are innately heterogeneous and anisotropic. The Q_{20} concept only offers an estimation of maximum well yield based on the use of a simplistic model which may result in erroneous over or under estimates of aquifer productivity.

In Alberta, water diversion licences have been issued under the Water Act for non-ideal (geologically complex) systems (Paskapoo Formation) using these standard engineering practices. Both the municipalities of Irricana and Ponoka were issued licences using standard industry practices and the Q_{20}, yet a significant decline in available head at water supply wells rendered these wells unusable. We are systematically failing when applying these models under non-ideal conditions. The utility of these models should be restricted

to conditions that honour the model constraints. Over production of an aquifer leading to the depletion of available pressure head or the abandonment of a water supply well suggests the erroneous application of these models and indicates the need for improved evaluation methods.

Paskapoo Formation

The Paskapoo Formation is a geologically complex system which displays both lateral and vertical variability and was laid down during a late-stage foreland infill of the Alberta Basin throughout the north central and south central regions of Alberta during the Paleocene epoch (Figure 1.1). The geology of the Paskapoo Formation has been overprinted with a fracture network with negligible displacement as a result of tectonic activity (Hamblin 2004; Burns et al. 2010a). The uppermost bedrock unit covers approximately 10,000 square kilometres of south western Alberta.

Figure 1.1: Map showing the province of Alberta and the region underlain by the Paskapoo Formation after Burns et al. (2010b)

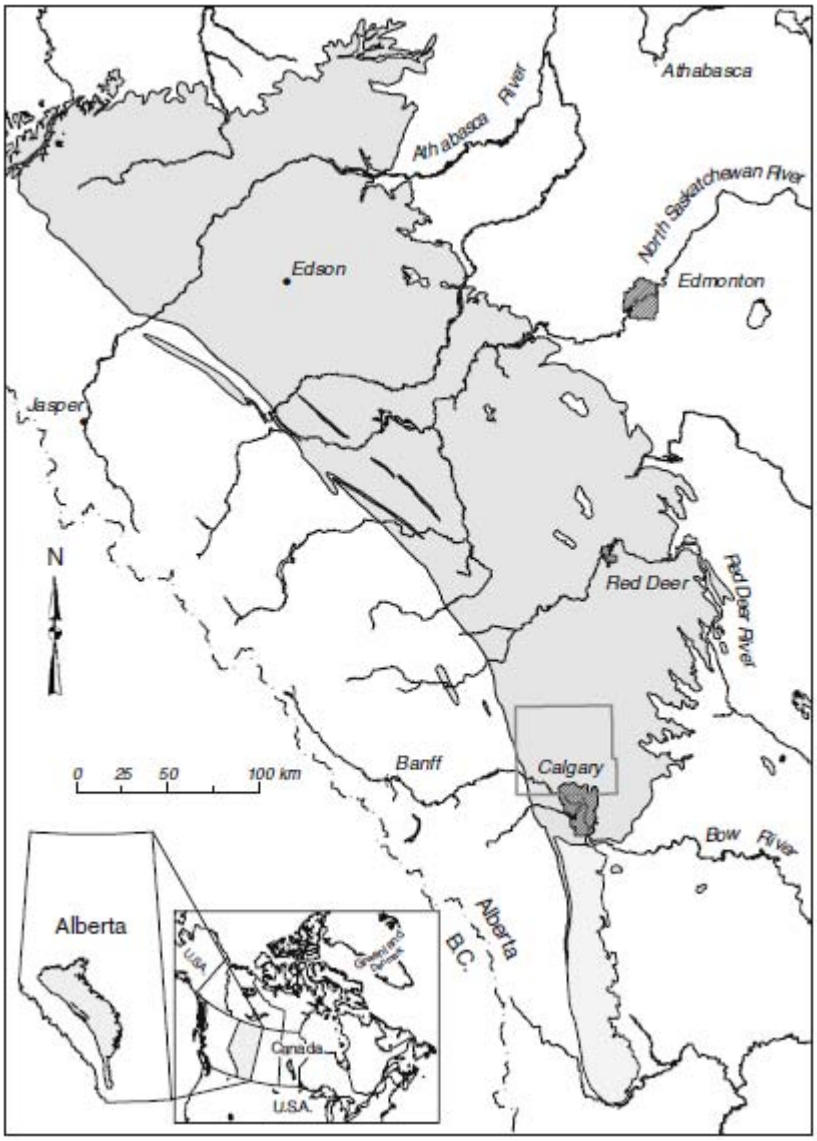

The uppermost Cretaceous and Paleocene strata form the bedrock of the Interior Plains of southern Alberta and the uppermost portion of a succession of five primary eastward thinning wedges that are undeformed in the north-eastern portion and in the central part

of the Alberta Basin. However, farther to the southeast these wedges were part of a series of thrust sheets (Jerzykiewicz 1997; Hamblin 2004). Increased subsidence rates affected crustal loading and sediment dispersal patterns during the Cretaceous Period (Hamblin 2004). The geology of the sedimentary succession is different between north central and south central Alberta as a result of variation in depositional and erosional processes (Bachu 1999). Distribution of fluvial deposited facies suggests deposition on large alluvial fans related to fault induced topography to the west. Subhumid to humid climatic conditions within the central part of the Alberta Basin resulted in development of swamps and marsh lands surrounding distal alluvial fans, ponds, and lakes (Jerzykiewicz 1997). Semiarid alluvial fan deposits developed in the southern part of the Alberta Basin.

The paleo-depositional environments varied spatially throughout geologic time as the foreland basin evolved. Prevailing drainage patterns proximal to the foreland basin were perpendicular to the mountain range where the basin was over filled by sediment and parallel to the mountain range in areas under filled by sediment. Reoccurring episodes of flash floods changed the drainage systems suggesting extensive fluvial depositional periods within the basin (Jerzykiewicz 1997). Fluvial and glacial erosional processes of the bedrock formed the top of the Paskapoo Formation. During this period an elongated north-south bedrock high developed functioning as a major water divide prior to glacial processes (Toth 1966).

The Paskapoo is comprised of the Haynes member, Lacombe member, and the Dalehurst member. The Haynes member consists of thick, massive, and coarse-grained sandstones.

The Lacombe member overlies the Haynes members and consists of channel sands and complexes encased in floodplain deposits which are characterized by siltstone, mudstone, shale, and minor coal. The Dalehurst member overlies the Lacombe member and is only present near the Hinton area immediately adjacent to the Foothills.

In the Calgary area the sediments of the Paskapoo Formation were deposited on an extensive floodplain east of the present Foothills and extending far to the east as a thinning cover of continental beds (Meyboom 1961). The surface bedrock within the Calgary area consists of Paleocene fluvial sandstones and floodplain mudrocks (Lerbeckmo and Sweet 2000). These sandstone beds vary in thickness which presents difficulty in tracing the sandstone laterally over large distances. The lower Paskapoo has a thick channel deposit of medium to coarse grained sandstone with minor conglomerate lenses and thin mudstone interbeds. These channels are typically multi-storied, 5 to 10 m thick and pinch out laterally over 100 to 150 m (Hamblin 2004).

The variability and distribution of the hydraulically conductive facies of the Paskapoo Formation owing to the temporal variability in the depositional environments within the southern portion of the Alberta Basin surrounding Calgary during basin development poses a significant challenge to sufficiently characterize the system both geologically and hydrogeologically. Connectivity studies of the channel sandstones in the West Nose Creek Watershed suggest that the system consists of relatively isolated channel sandstones and that a complex aquifer-aquitard relationship exists. Connectivity of paleo-fluvial remnants associated with channel deposits needs to be accounted for in

hydrogeologic evaluations (Burns et al. 2010b). Because of the complexity of these non-ideal systems and continued efforts to understand the Paskapoo within the Calgary region, we focus our research on the Paskapoo in the south central portion of the Alberta Basin.

Pressure Transient Analysis and the Derivative Plot

There is inherent difficulty in analyzing pumping test data collected from non-ideal systems using current practices. Application of the standard Theis and Cooper-Jacob models in pressure transient analysis of complex non-ideal systems fail where the influence of internal boundaries are felt, different flow regimes can exist simultaneously at varied stratigraphic levels, and standard log-log or semi-log plots cannot be interpreted easily. Analysis of drawdown test data using standard practices involves selection of a reservoir model and then estimating individual reservoir parameters from the log-log and semi-log plots. Subsequently, a type curve match is made of the data on the log-log plot and an estimate is again made of the reservoir parameters checking for consistency with the prior estimates (Horne 2005).

Another approach to evaluating pumping test data collected from non-ideal systems is the use of the derivative approach where the time rate of change of pressure during a test period is considered for analysis. Here models are diagnosed through pattern recognition of the different flow regimes present in a response. The Bourdet derivative, which was developed in the mid 1980's, delineates these flow regimes (Bourdet, D. 2002; Houzé et al. 2008; Chow, R. 2009). Derivative analysis of pumping test data allows for the

identification of boundaries and flow regimes present as the pressure wave propagates throughout the system in response to the abstraction or injection of fluid. Well responses consist of several flow regimes. The chronology of these regimes defines early time through late time responses of near wellbore conditions to the limits of the reservoir. The derivative response exhibits a characteristic shape during all flow geometries which allows for the determination of reservoir type. These flow geometries can be used to establish the type of flow occurring in the reservoir at a given time (Bourdet 2002).

Derivative analysis consists of grouping the conventional dimensionless pressure form and the dimensionless pressure derivative into a single-stage plot for interpretation. Horne (2005) reports that the use of the pressure derivative with pressure type curves reduces the uniqueness problem and provides increased confidence since the derivative plot lies within the region of the log scale with the greatest precision.

Features that are difficult to identify using a standard pressure plot are easier to recognize on the pressure derivative plot (Chaudhry 2004; Horne 2005). Use of the derivative plot to analyze well response lends itself to the identification of several flow regimes and identification of reservoir boundaries, closed systems, or reduction in permeability. In complex systems, flow may be distorted owing to the irregularity in the geometric shapes of the geologic objects, or may coincide but at different stratigraphic levels in complex geologic settings where there is considerable lateral and vertical variability in connectivity (Bourdet 2002). Flow regimes can help identify reservoir characteristics and the appropriate model to use for analysis.

Research

The geologic and hydrogeologic evaluation of complex subsurface environments poses a significant problem to characterizing system behaviour, selection of supply and observation well locations, parameter estimation, interference from other production or injection wells, and licensing. Because of the complexity of these non-ideal systems we cannot use a deterministic approach to model the geology and hydrogeology.

We want to investigate an alternative method of replicating system behaviour and evaluating data from these geologically complex aquifer systems. We look into the implications of these geological settings by introducing the use of geostatistics to describe the geologic characteristics of the system and implementation of stochastics due to the inability of developing a deterministic knowledge of the problem domain (Burrows 2004). Burrows (2004) used an equivalent porous medium (EPM) approach to modeling the spatial distribution of hydraulic parameters and resulting flow system of the heterogeneous fractured media of the Paskapoo. This lead to unsuccessful results due to limitations in assessing local complexities of the geometry and physical properties of the channel sand bodies and crevasses splays.

The geological heterogeneity results in an inherent uncertainty that is difficult to quantify yet necessary to model in complex systems (Burns et al. 2010a). An applicable approach to modeling these systems is to develop a geomodel (cf., Burns et al. 2010a; and Mallet 2002) to quantify uncertainty in the model geometry and hydraulic parameters. The

object-based modeling approach of geomodeling can stochastically simulate channel complexes, heterogeneity and uncertainty inherent in these systems. Here we are able to infer the behaviour of a statistically well defined aquifer (Deutsch 2002; Burns et al. 2010a). Statistical data of an analogue model developed by Burns et al. (2010b) is used as input to the stochastic model to describe the Paskapoo system. This model has been simplified by ignoring the presence of a three dimensional fracture overprint and its influence on groundwater flow.

We upscale the hydraulic parameters of our model to represent regional flow (as constrained by a straight-reach of the subterranean river valley) that can be considered on a scale on the order of approximately 10 km^2 by applying an upscaling algorithm (Burns et al. 2010b) to the 3-dimensional modeled geology. Once our geomodel is complete we stochastically generate equi-probable realizations and select a set of realizations which capture the range of hydraulic communication between maximum connectivity and minimum connectivity of the hydraulically conductive facies. The realizations are then used in groundwater flow simulations to explore the range of hydraulic responses that we can anticipate from the geologic setting of channel remnants embedded in overbank deposits.

We also want to look at these systems under transient pumping conditions to evaluate the different flow regimes present and use this information in selection of an appropriate pressure transient model to estimate reservoir properties. We will evaluate long-term tests (approximately 8 to 15 hours) and infer the utility of short-term pumping tests (4

hours) in non-ideal systems and determine the usefulness of evaluating long-term yield based on the identification of flow regimes and models other than the Theis equation. We do this by analyzing the pressure transient behaviour of these systems by using AQTESOLV, a standard hydrogeologic analysis tool and Kappa Engineering's Saphir, a pressure transient analysis tool used by Reservoir Engineers which permits the use of custom fit type curves.

CHAPTER 2: GEOLOGY AND HYDROGEOLOGY OF THE PASKAPOO FORMATION

The Alberta Basin is bounded by the Rocky Mountain trench to the west and southwest, the Tathlina High to the north and the Canadian Shield to the northeast and was formed during the Late Proterozoic by rifting of the North American Craton. During the Late Cretaceous the Cannonball Seaway occupied the area between the Canadian Shield and active Cordilleran belt (Hamblin 2004). The resulting Basin is a foredeep in front of the southern Canadian Cordillera foreland thrust and fold belt that extends from Alaska to New Mexico (Bachu 1999; Hamblin 2004; Jerzykiewicz 1997). Overthrusting of supercrustal rocks during the Columbian and Laramide orogenies intensified crustal loading causing a downward flexure of the lithosphere resulting in the basement tilting westward at shallow angles and increasing from <4m/km in the east near the Canadian Shield to up to less than 12 m/km near the western deformation front (Tokarsky 1971; Bachu 1999; Hamblin, 2004).

The crustal loading and downward flexure during basin development led to an eastward dispersal and a rapid deposition of a series of interfingering non-marine and marine fluvial sediments in asymmetric wedges during the Campian to Paleocene (Hamblin 2004). This led to alluvial fan and fluvial floodplain deposition. An increase in subsidence rates affected crustal loading and sediment dispersal patterns during the Campanian and Maastrichtian ages of the Cretaceous Period (Hamblin 2004). These sediments represent a series of transgressive-regressive cycles that over time are dominated by deposition of non-marine sediments as the seaway retreated southward.

Depositional environments were typically non-marine to the west and marine to the east (Hamblin 2004).

The sediments derived from erosion of Palaeozoic and Mesozoic sediments from the Rocky Mountains were laid down in a coarsening upward succession over a period of 25 million years and ranged in thickness up to 2.5 kilometres (Hamblin 2004). Vertical accretion sediments predominated over vertically stacked, channel-fill successions tens of metres thick indicating periods of fluvial deposition (Jerzykiewicz 1997; Hamblin 2004). Deposition of the Paskapoo during the reactivation of thrusting in the eastern Front Ranges represents the late-stage foreland infill (Hamblin 2004) and was unconformably deposited on top of the Upper Cretaceous/Paleocene Scollard Formation and the Upper Cretaceous rocks of the Edmonton Group, the Bearpaw Formation, and the Belly River Group (Lerbeckmo et al. 1995). The Paskapoo/Porcupine Hills correlates to the uppermost cyclothem and may represent one of three periods of thrusting separated by periods of tectonic inactivity (Hamblin 2004). Deposition of the Paskapoo was followed by glaciation and is capped by a veneer of glacial tills, clays, sands and gravels (Demchuk et al. 1991).

Depositional environments ranged from proximal conglomeritic alluvial fans to medial fluvial plain channel sandstones and overbank fines through the majority of the area to distal plain lacustrine and swamp (Hamblin 2004). The basin reached a maximum thickness during the Paleocene-aged Laramide Orogeny. The maximum reported thickness of the Paskapoo in the core of the Alberta Syncline is approximately 900 m

(Jerzykiewicz 1997). The Paskapoo consists of a succession of interbedded sandstones, siltstones, mudstones with thin coal beds (Lerbeckmo et al. 1995; Bachu and Michael 2003, Harrison et al. 2006).

The Paskapoo fluvially deposited sedimentary facies included a network of anastomosed channels that drained mid fan to distal alluvial fans into shallow lakes and ponds (Jerzykiewicz 1997). Facies also include braided and meandering, non-channelized sediments, a blanket sandstone of flood origin, a variety of fluvio-lacustrine facies including distributary channels and mouth bars of lacustrine deltas, and offshore lacustrine sediments. Mid to distal fan fluvial predominate but proximal conglomerates and distal coal and lacustrine sediments are also present (Jerzykiewicz 1997).

Shallow lakes and associated distributary mouth-bars and interdistributary swamps are particularly well developed in the upper, coal-bearing part of the Coalspur-Scollard-Willow Creek sequence. In the central part of the Alberta Basin, where the soil moisture regime was subhumid to humid, the distal alluvial fans, ponds, and lakes were surrounded by swamps and marshes (Jerzykiewicz 1997). During deposition of the Paskapoo, drainage was partly internal and blocked to the east. The Paskapoo is located in the north central and south central regions of Alberta (Figure 2.1).

Figure 2.1: Illustration of stratigraphic and hydrostratigraphic divisions of the Cretaceous-Tertiary succession in the Alberta basin (Bachu and Michael 2003)

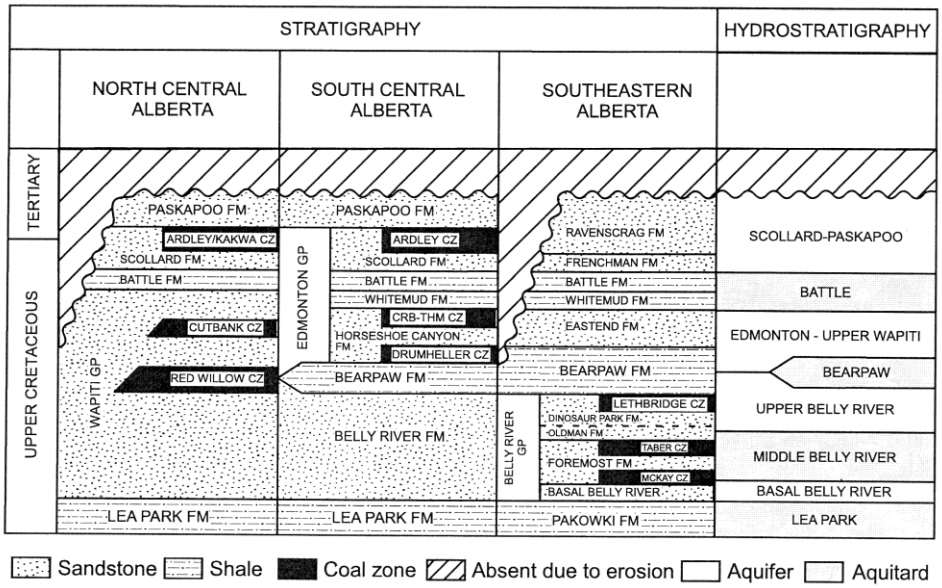

Volcanic material was transported from as far away as the interior British Columbia and as far south as Montana. The dominant transgressive regime was characterized by compressive forces in the south, thrusting and strong subsidence in the foreland basin, ended at about 58 Ma as convergence between the accreted terranes and the craton waned (Hamblin, 2004). This marked the final stage of foreland evolution in the Alberta Basin (Hamblin 2004). Supply of sediment was reduced and the regime was replaced by isostatic uplift and erosion in the basin during mid-Eocene time upon cessation of the Alberta Syncline subsidence (Hamblin 2004; Bachu 1999). Tertiary to Recent erosional processes have removed up to approximately 3000 m of sediments in the southwest and up to 1000 m of sediment in the northern portion of the basin (Bachu 1999). Erosional forces created the post Zuni erosional unconformity and peneplain, at or near the present-day land surface (Hamblin 2004). The Alberta Basin changed into a continental trough

limited in the northeast by forebulge topography which developed approximately along a line from Swan Hills to Cypress Hills (Jerzykiewicz 1997). An elongated north-south bedrock high that developed functioned as a major water divide prior to glacial processes.

The uppermost Cretaceous and Paleocene strata form the bedrock of the Interior Plains of southern Alberta and are the uppermost portion of a succession of five primary eastward thinning clastic wedges that infill the Alberta foreland basin (Jerzykiewicz 1997; Hamblin 2004). The final sequence of the sedimentary wedge represents fluvial strata which extended into Manitoba along the western margin of a marine seaway and later eroded after cessation of tectonic activity during Eocene time (Hamblin 2004).

The total thickness of the clastic wedges in the middle part of the Basin is approximately 4,200 m and the uppermost Cretaceous to Paleocene portion is approximately 3000 m thick (Figure 2.2). The region within west central Alberta is underlain by over 3,000 m of Phanerozoic sedimentary rock overlying the Precambrian basement (Parks and Toth 1995). These clastic wedges are undeformed in the north-eastern portion and in the central part of the Alberta Basin. Farther to the southeast the wedges were part of a series of thrust sheets in the foreland belt and have attained greater thickness (Jerzykiewicz 1997). The 68 Ma boundary separates two sets of clastic wedges. These differ in external geometry and facies; 1) Belly River – Edmonton, and 2) the Entrance-Paskapoo (Jerzykiewicz 1997). The lower part of the sedimentary eastward thinning wedge is dominated by coarser clastic material with a fining upward sequence (Hamblin 2004).

Figure 2.2: Foreland basin strata in west central Alberta (Bachu and Michael 2001).

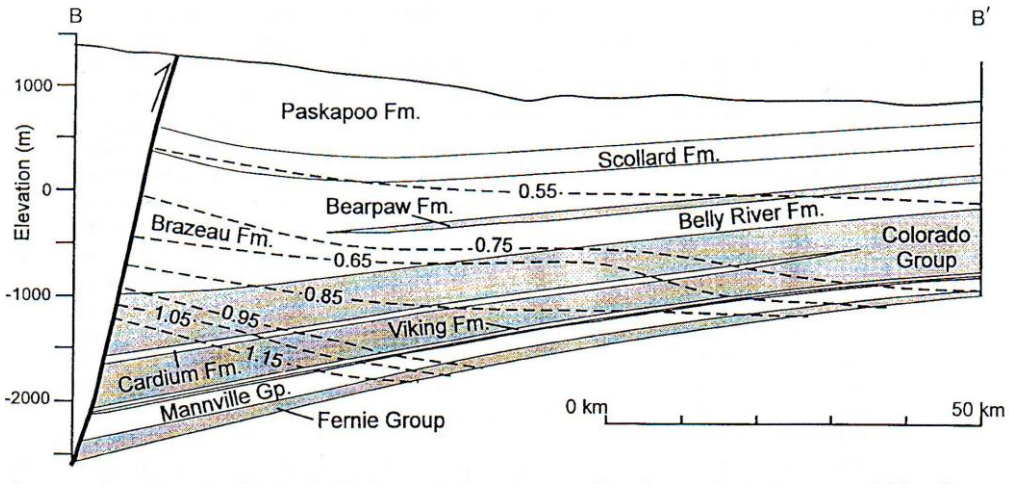

The paleo-depositional environments varied throughout geologic time as the foreland basin evolved. The prevailing drainage in the proximal portion of the foreland basin was perpendicular to the mountain range where the basin was overfilled with sediment and parallel to the mountain range in areas that were under filled by sediment, however, drainage was longitudinal south-eastward in distal areas of the basin (Jerzykiewicz 1997; Hamblin 2004). Paleocurrent measurements from the Paskapoo-Porcupine Hills strata indicate fluvial channels of three main directions, south-eastward (longitudinal to the uplift boundary), north-eastward (transversal), and south-westward (transversal but reversed in relation to the mountain front) (Carrigy 1971; Jerzykeiwicz 1997). Reoccurring episodes of widespread sandy flash floods changed the drainage systems within the basin resulting in two dispersal systems during the early to mid Paleocene, a north-easterly flow in south-western Alberta and a south-easterly flow in west-central Alberta (Hamblin 2004) and within the central and southern foothills a nearly uniform north-eastward dispersal (Jerzykiewicz 1997; Jerzykiewicz and LaBonte 1991).

The Haynes member, Lacombe member, and the Dalehurst member make up the Paskapoo. The Haynes member consists of a sequence of stacked amalgamated thick, massive, and coarse-grained sandstones. These sandstones are thick, massive and conglomeritic cliff forming sediment (Demchuk and Hills 1991). The sandstone beds are medium to coarse-grained and overlie the fine-grained Scollard Formation. They are marked by conglomeritic lags, trough and planar cross bedding and minor ripples, and roots and plant fragments, and siderite (Demchuk and Hills 1991). Minor interbeds of grey or greenish siltstone and mudstone are common and overlie a regional unconformity which represents a hiatus of approximately 1 to 2 million years (Hamblin 2004). Within the western plains of Alberta the Haynes member is characterized by quartz/chert sandstone, with interbedded sandy siltstones. This lithological sequence represents subaerial fluvial floodplain deposits where shallow ponds were once present. The lower 100 m is particularly coarse grained and well sorted with conglomeratic lenses (Hamblin 2004). The transition between the Haynes and Lacombe members is demarcated by a change from sandstone to argillaceous and carbonaceous strata (Demchuk and Hills 1991).

The Lacombe member overlies the Haynes and consists of channel sand and complexes encased in floodplain deposits which are characterized by siltstone, mudstone, shale, and minor coal. The Lacombe member has a lower sandstone fraction than that of the Haynes member. These sandstones are fine to medium-grained with minor conglomerate as lag deposits overlying erosional contacts, planar and wavy bedding. The Lacombe is

characterized by interbedded grey and green siltstone, mudstone, argillaceous coals, and minor fine grained sandstone. Sedimentary structures are preserved in the sediments such as rare planar and ripple cross-laminations, plant fragments, and pedogenic structures including rooting, slickensides, mottling, and cutans. Rare burrows and shells are found and siderite staining is abundant throughout the member. The Lacombe nominally includes the majority of the strata of the Paskapoo (Demchuk and Hills 1991; Hamblin 2004).

Burns et al. (2010b) reports that connectivity studies of the channel sandstones suggest a volume fraction 24% in the Lacombe member in the West Nose Creek Watershed in the south central area will result in an aquifer-aquitard system consisting of relatively isolated channel sandstones. Where the percentage of channel sandstones increase they tend to become well connected inferring that a single aquifer system may be a reasonable assumption for the basal Haynes member of the Paskapoo Formation. The results of previous studies (Burrows 2004) on the upper Paskapoo Formation, using an idealized homogeneous anisotropic conceptual model, suggest that the system should be viewed as a complex aquifer-aquitard system (Burns et al. 2010a).

The Dalehurst member overlies the Lacombe member and is only present near the Hinton area adjacent to the Foothills. It is an erosional remnant and maybe a lateral facies equivalent with portions of the Lacombe member. Economic coal deposits of the Obed-Marsh coal zone characterize the Dalehurst member (Demchuk and Hills 1991). The Dalehurst consists of interbedded fine-grained predominantly massive or planar bedded

with minor cross bedding sandstones and grey mudstones. Siltstones of the Dalehurst are greenish to black and contain plant fragments and pedogenic structures. Siltstones, mudstones, and shales have minor planar or wavy-disturbed laminations (Demchuk and Hills 1991).

The Paskapoo's uppermost bedrock unit covers approximately 10,000 square kilometres of south western Alberta. The system provides the primary source of water for the major populated areas of the province. The geology of the Paskapoo is complex and displays both lateral and vertical variability which has been overprinted with a fracture network with negligible displacement (Hamblin 2004; Burns et al. 2010a).

The Paskapoo Formation is the main fresh water bedrock aquifer where most local water wells are completed within the western plains of Alberta (Harrison et al. 2006; Vogwill 1983; Ozoray and Barnes 1978). The Upper Cretaceous-Tertiary succession is divided into five hydrostratigraphic grouping of aquifers and aquitards. The aquifer is referred to as the Scollard-Paskapoo aquifer which lies at the top of the Cretaceous-Tertiary succession in the Alberta Basin as presented in Figure 2.2 (Ozoray and Barnes 1978; Bachu and Michael 2003). Currently it is thought that the sands form channels and complexes that are in some areas vertically stacked. A 50 m thick basal sandstone lies at the base of the Paskapoo along the Scollard-Paskapoo contact in central Alberta. This contact which outlines a major unconformity of up to 4 million years (Eberth et al. 1995; Lerbekmo and Sweet 2000). The sub-Paskapoo disconformity at Scollard Canyon represents a hiatus of approximately 1.25 million years (Lerbekmo et al. 1995).

The hydrogeology and hydrostratigraphy of the Paskapoo Formation is very complex, consisting of randomly arranged sand channels and complexes embedded in low permeability overbank/flood plain deposits. As such, water yield is highly variable. Some of the sand units are permeable while other units are indurated with calcium carbonate or contain interstitial clays which effectively reduce porosity (Burns et al. 2010a).

Regionally, the groundwater flow within the Scollard-Paskapoo system is topographically driven (Bachu et al. 2003). The regional hydrogeology of the Scollard-Paskapoo is complex and characterized by both under-pressurized (i.e., sub-hydrostatic) and near normally pressurized areas or zones (Harrison et al. 2006).

These pressure data suggest higher hydraulic heads than the underlying Brazeau-Belly River aquifer. The hydraulic heads and inferred flow directions in the Brazeau-Belly River and Scollard-Paskapoo aquifers are shown along dip and along strike in Figure 2.3 (Bachu and Michael 2001). Within the Alberta basin, thick shaley aquitards retard the recharge from the ground surface, leading to sub-hydrostatic pressures in various aquifers (Bachu and Michael 2001).

Bachu (1999) studied flow systems within the Alberta Basin and determined that flow within the basin was driven by either sediment unloading and rebound or topography driven. Basin and small-scale topographically driven flow systems are present in the

north and south of the basin. Local topographically driven systems are common throughout the basin (Harrison et al. 2006). These shallow systems are characterized by meteoric recharge along the regional and local topographic highs (Figure 2.4) (Harrison et al. 2006). Hydraulic heads are highest in the west and lowest in the east. Figure 2.3 illustrates a cross section based on actual hydrostratigraphy and actual data for the Scollard-Paskapoo aquifer (Bachu and Michael 2001).

Figure 2.3: Hydraulic head distributions and inferred flow paths in the post-Colorado aquifers along dip and along strike sections, indicating topography driven flow in the water-saturated zone

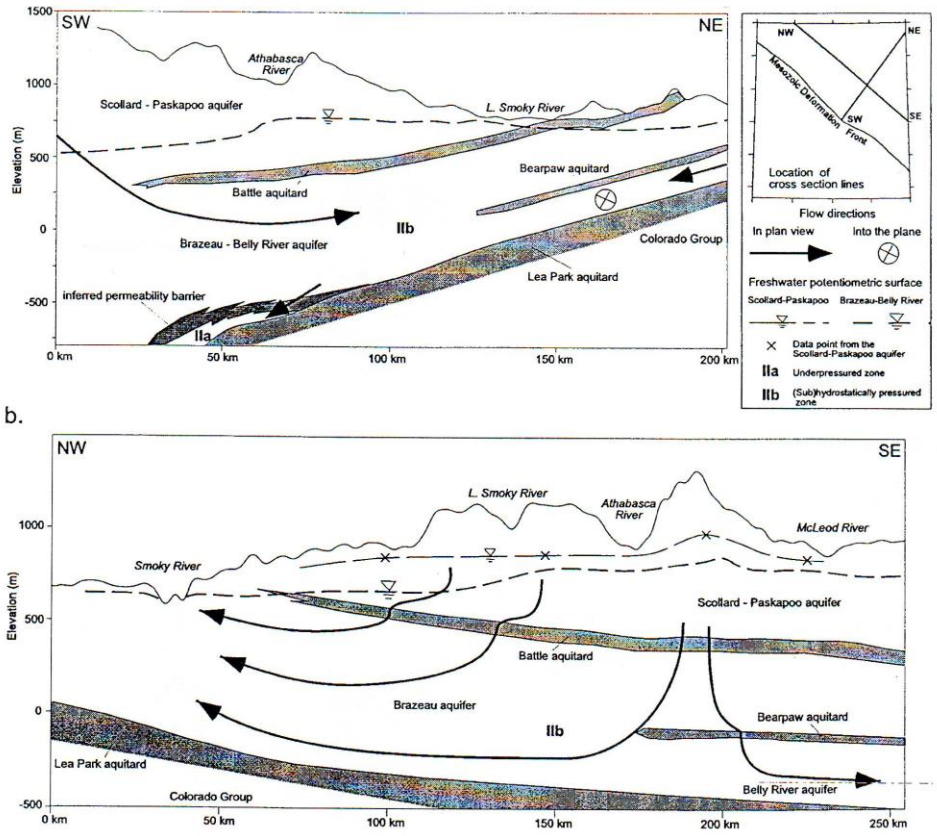

Two systems of groundwater flow have been thought to consist of a series of local and intermediate systems. Vogwill (1983) suggested that the Paskapoo consists of rapidly moving local and intermediate flow systems. These are characterized by rapid movement and are superimposed on a larger groundwater flow system, which is in a regional recharge configuration to the northeast and east from Edson area. Local flow systems in sub-horizontal sandstones and shales probably occur with the well-fractured sandstones units acting as "collectors" for the downward moving groundwaters of overlying units. Groundwater flow through the permeable sandstones is rapid and emerges on hillsides and slopes as contact springs and in lower areas as soapholes, hummocky terrain, or muskeg. Groundwater that escapes these sandstone collectors continue downward into the regional system eventually discharging to the Athabasca River or Edson Lowlands.

Figure 2.4: Cross sectional representation of flow systems in upper Cretaceous Tertiary strata of Alberta basin (Bachu et al. 2003)

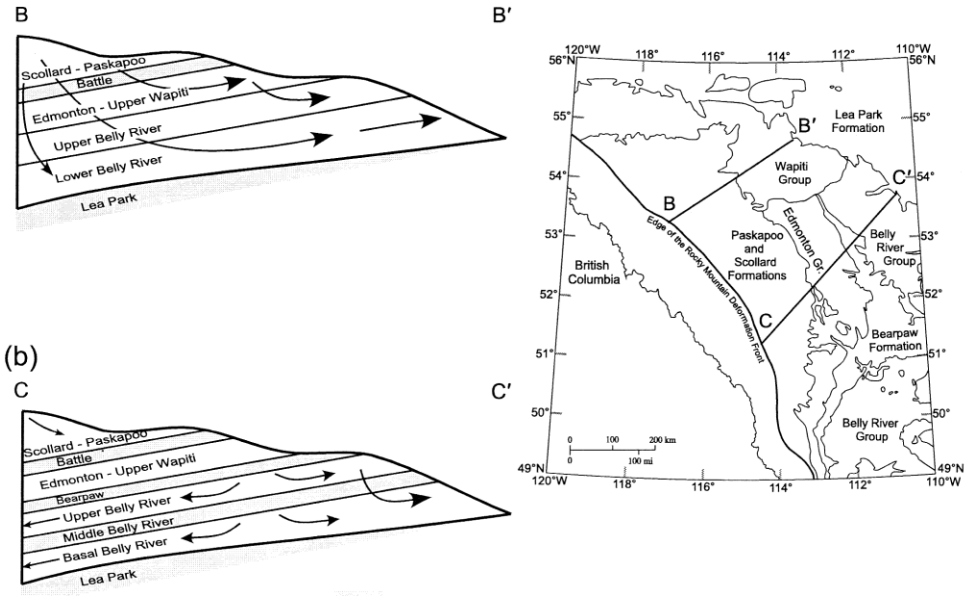

The Scollard-Paskapoo consists of groundwater flow toward the north-northeast in a shallow system characterized by meteoric recharge along local and regional topographic highs including parts of the deformed belt. Regional pressure data suggest that there is hydraulic communication between the Paskapoo and the Ardley Coal Zone (Harrison et al. 2006; Vogwill 1983). The elevation versus pressure head data indicate a moderately positive correlation suggesting that there is a regional topographic effect on flow (Harrison et al. 2006). Flow of meteoric water in the Scollard-Paskapoo aquifer at the top of the bedrock surface is in equilibrium with and driven by topography from recharge areas at high elevation near the fold and thrust belt to discharge areas to the east-northeast (Bach and Michael 2003).

The distribution of groundwater occurrence does not seem to be associated with or correlated with a particular stratigraphic horizon as saturated porous media is encountered at variable stratigraphic levels. Permeability tends to be random yet there seems to be some higher permeability zones associated with some sandstone bodies (Burns et al. 2010a). The uppermost water-bearing unit occurs at the unconsolidated/bedrock contact and a second zone occurs at variable depths within the bedrock and is associated with permeable sandstone bodies.

Within the north central Alberta area, geological information indicates the presence of coal beds within the upper Paskapoo which suggests a humid climate (Hamblin 2004). Fossil specimens have been recovered and catalogued from the Lacombe member and

represent channel abandonment and flood plain depositional environments (Hamblin 2004).

Within the region of the confluence of Blindman and Red Deer Rivers the Lacombe member also includes shales and coals, with subordinate sandstones and conglomerates (Grande et al. 2000). Grande et al. (2000) reports that the strata of the member represent primarily low-energy fluvial deposition with associated overbank environments including ponds and oxbow lakes. The upper contact of the Lacombe is an erosional surface and represents the present-day land surface west of the Red Deer Valley (Demchuk and Hills 1991).

The approximate thickness of the formation ranges from 600 m to over 1,100 m near the Edson area in the north (Vogwill 1983). The bedrock is overlain by a 6 m veneer of glaciolacustrine deposits consisting of lake or deltaic sediments of cross bedded or laminated sand, clay, and silt (Vogwill 1983).

Within the north central area near Edson, depth to the top of the first producing aquifer in the Paskapoo Formation ranges between 20 to 30 m. In the north central area, Ozoray (1972) reports that yields in this depth range are generally greater than approximately 86 m^3/d. Friable Paskapoo sandstones yield 3200 m^3/d, thick porous Paskapoo sandstones yield 650 to 3200 m^3/d, regionally characteristic sandstone interbedded siltstone of the Paskapoo yield 144 to 576 m^3/d, Paskapoo unfractured thick shales yield 7 to 36 m^3/d (Ozaray 1972). However, Harrison et al. (2006) reports that yield from the Paskapoo

within north central Alberta ranges from less that 6.5 m^3/d to over 325 m^3/d. Transmissivity for Paskapoo aquifers generally ranges from less than 1.5 m^2/d to over 100 m^2/d but can be as high as 1,000 m^2/d. Storativity values range from 5×10^{-5} to 10^{-4} indicating that locally most aquifers are confined to varying degrees (Vogwill 1983). Yield values range from 9 to 3300 m^3/d. In the Foothills, the Paskapoo Formation is also the main bedrock aquifer with transmissivity values ranging from 1.5 m^2/d to 15 m^2/d and yields 35 m^3/d to 170 m^3/d (Vogwill 1983).

Based on drill stem data and cross-sectional information (Vogwill 1983); the Paskapoo sandstone at a depth of 280 m has a hydraulic conductivity of 7×10^{-3} m/d. High yielding areas of the Paskapoo Formation have not been horizontally extended much beyond local scale (Vogwill 1983).

The Paskapoo Formation has been described using a series of discontinuous outcrops along the Red Deer and Blindman River Valleys in the central Alberta area as there does not appear to be a type section for the formation (Demchuk and Hills 1991).

Within the central Alberta area near Olds, the sediments of the Paskapoo were deposited by large river systems with strong flows which deployed upon a plain. Temporal lakes of insignificant depth would have formed. These temporal lakes likely only lasted a single season as a result of a warm dry climate (Toth 1966). The siltstones and sandstones of the Paskapoo are considered poor aquifers due to their montmorillonite content (Toth 1966). The thickness of the Paskapoo formation ranges from 240 to 360 m (Toth 1966).

Deeply incised channels exist in the bedrock surface and soft argillaceous bentonitic rock which represent the possibility of badland-type topography which preceded deposition of the drift (Toth 1966).

In central Alberta Toth (1966) has described the Paskapoo as being comprised of soft grey argillaceous sandstones, consolidated sandstones, conglomerates, siltstones, soft shales, clays, and claystone. Laminated lake sediments of siltstone alternating with layers of claystone and argillaceous and silty sandstone are common. Thin bands of well cemented sandstone are common and thin lenses of woody coal can occur in places. The sandstones are irregular and the grain size, lime content and porosity varies throughout the area. Cross bedding in the sands is common (Toth 1966). Mineralogically the Paskapoo consists of quartz, feldspar, shale, limestone, chert, and quartzite with clay content in the sandstones of less than 6% (Toth 1966).

Gabert (1975) reports that sandstone bodies in the Red Deer area tend to be laterally continuous over areas of 150 square kilometres. In some areas the sandstone bodies are replaced by siltstone/shale facies. Gabert also found that smaller sandstones of limited extent encased in mudstone sections of the upper Paskapoo in combination with Quaternary gravel sheets form important shallow aquifers. The unconformable contact between the underlying Scollard Formation and the Paskapoo Formation is found at the base of a 50 m yellowish-brown weathered fluvial sandstone which overlies mudrock and coal of the Scollard in central Alberta (Lerbekmo and Sweet 2000). Where the basal Paskapoo sandstone thins the formational boundary is more arbitrary. The basal

sandstone is overlain by light grey to olive green mudrocks, grey and brown sandstones, and more infrequently by organic-rich shales and thin argillaceous coals (Lerbekmo and Sweet 2000). The basal Paskapoo, as identified by Allen and Sanderson (1945) consists of medium to coarse grained cliff forming to conglomeratic, brown weathered, non-bentonitic sandstone resting on Scollard Formation argillaceous beds containing thin, light grey weathering, bentonitic sandstone (Lerbekmo et al. 1995) and has attained a thickness of approximately 50 m within the Ardley area (Lerbekmo et al. 1995).

The basal sandstone represents a composite channel sandstone that is typically medium grained, but occasionally is coarse grained and even conglomeratic lag deposits at the base of scours in the channel. The basal sandstone unit is 1.1 m thick and has a lag deposit of occasional shale clasts up to 2 cm in diameter (Lerbeckmo et al. 1995).

Within central Alberta near the Three Hills area, water was produced from the Paskapoo at depths less than 100 m and was typically drawn from channel sandstones, thin sandstone lenses, coal seams and drift-bedrock contact (Toth 1968). Near Red Deer, the Paskapoo sandstones range in thickness up to 30 m and have produced good quality water. The basal Paskapoo is approximately 100 m thick and composed of several vertical and laterally overlapping and coalescing sands each ranging 15-30 m thick by 10 to 15 m wide and separated by low permeability mudstone. Permeability of the Paskapoo was greatest in medium grained well sorted sandstones but varied vertically and laterally. These individual sandstones can be laterally continuous over 150 square kilometres and in some areas are replaced laterally by siltstone/shale facies.

Yield for the Paskapoo in south central Alberta near Rocky Mountain House ranges from 720 m^3/d to 2880 m^3/d (Tokarsky 1977). In Rocky Mountain House, the Paskapoo sandstones reportedly yield high flow rates in excess of 950 m^3/d with high transmissivity values (Tokarsky 1971).

However, within the Rocky Mountain House area, Vogwill (1983) states the inter-granular hydraulic conductivity is insignificant and that aquifer yield is highly variable due to the presence of a discrete fracture network and as a result hydraulic conductivity values are anisotropic. Water wells in this area that have been completed in synclinal structures have higher yield than those completed in anticlinal structures. Well yield of wells completed (Ozoray and Barnes 1978) in the sandstone and shales of the Paskapoo typically ranged from 38 to 190 m^3/d and others completed in the sandstone and shales ranged from approximately 9 to 38 m^3/d. It was suggested that where low well yields are observed water would have been sourced from unfractured shale and montmorillonitic sandstone underlying thin or clayey-silty drift (Ozoray and Barnes 1978). Yields from the Paskapoo tend to vary over short distances (Ozoray and Barnes 1978).

In south central Alberta proximal facies include semiarid alluvial fan deposits. Jerzykiewicz (1997) reports that only the mid fan and distal fan facies passing into playa, lake and swamp depositional units are preserved within the basin. The surface bedrock within the Calgary area consists of Paleocene fluvial sandstones and floodplain mudrocks (Lerbekmo and Sweet 2000). In the Calgary area grey and greenish sandstones and dark

shales constitute the Paskapoo and can consist of cherty, calcareous sandstones, siltstones, and mudstones with minor amounts of conglomerate, limestone, coal, and tuff beds (Meyboom 1961; Ozoray and Barnes 1978). The sediments were deposited on an extensive floodplain east of the present Foothills extending far to the east (Meyboom 1961). The sandstone beds vary in thickness which presents difficulty in tracing the sandstone laterally over large distances.

The lower Paskapoo has a thick channel deposit of medium to coarse grained sandstone with minor conglomerate lenses and thin mudstone interbeds. Channels are typically multi-storied, 5 to 10 m thick and pinch out laterally over 100 to 150 m (Hamblin 2004). Overlying and interbedded nonmarine fine grained deposits of greenish siltstone with paleosols, interbedded with minor silty, very fine grained sandstone acts as a vertical seal for pools of fluvial channel stratigraphic traps (Hamblin 2004).

The lithology of the sandstone typically consists of fine grained sands ranging up to a maximum size of 1 mm. The sandstones are composed of 30% quartz, 30% weathered feldspar, and 40% chert and calcareous matrix (Meyboom 1961) with thin bentonitic layers present. The average porosity of the Paskapoo sandstones within the Calgary region is 7 % (Parks and Toth 1995, Hamblin 2004). Carrey (1971) suggested that the sandstone porosity of the Paskapoo ranges from 1 to 35 % in outcrop but is generally between 8 to 15% due to the presence of unevenly distributed montmorillonite.

The Paskapoo Formation is overlain by surficial sediments of approximately 15 m in thickness within the region spanning Calgary, to the Front Ranges. In the north-eastern portion of the Calgary-Golden area studied by Ozoray (1972), up to 60 m covers surficial sediments.

Fine grained units range up to 50 m in thickness. Calcareous concretions, woody coal, and thin gastropod-rich limestone are present throughout. Hamblin (2004) reports that sandstone beds range up to 1 m thick pinching out laterally over several tens of meters having sharp gradational bases and horizontal ripple marks. Within the Paskapoo, the sandstone to siltstone ratio is about 1:2-5 (Hamblin 2004)

Meyboom (1961) reports that the rate of natural recharge to bedrock aquifers within the Calgary region amounts to 4.0×10^{-3} m/yr or 1 per cent of the mean annual rainfall. As the rate of recharge to bedrock aquifers is about 8.4 cubic meters per square kilometre per day, groundwater depletion may be expected in areas where more than 150 people per square mile depend on groundwater supplies (Meyboom 1961). Water that has penetrated into the bedrock will move downward through a succession of flat-lying sandstones and shale layers. (Meyboom 1961).

In south central Alberta near Calgary, the transmissivity has been reported to range from 1.2 to 2.7 m^2/d (Parks and Toth 1995). The Paskapoo aquifer of the Calgary region varies in thickness having porosities averaging 7%, good transmissivity and is under pressure (Hamblin 2004). Flow rates are low and are not recommended for water supply

in heavily populated areas due to low yield. There is considerable variability to the distribution of the sandstone deposits within the Paskapoo undergoing lateral changes over short distances. Inter-granular porosity of the thick porous sandstone aquifers is important to transmissivity characteristics of the Paskapoo (Hamblin 2004).

Water wells completed in the Paskapoo within the Calgary region seldom reach yields more than approximately 1 m^3/d due to the low transmissivity ranging from 1.2 to 2.4 m^2/d (Meyboom 1961). Regional yield values for the Paskapoo range from 144 to 720 m^3/d as a result of lower permeable sands or destruction of primary porosity by cementation (Tokarsky 1971).

The water table tends to be a subdued reflection of the topography and top of the bedrock elevation, ranging from 0 to 40 m bgs and suggests flow in the unconfined Scollard-Paskapoo aquifer system from regions of high elevation along the thrust and fold belt to the west to lower elevations in the northeast (Bachu and Michael 2003).

The groundwater of the Paskapoo Formation within the Spy Hill region consists of sodium-bicarbonate or sodium-sulphate type waters. The TDS of groundwater increases with depth ranging from less than 500 mg/L up to greater than 3,000 mg/L (EBA Engineering Consultants 2003). The salinity of the Scollard-Paskapoo system ranges from 100 to 3,000 mg/L (Bachu and Michael 2003). In the Paskapoo-Porcupine Hills of Western Alberta, the wells yield groundwater with 500 to 1,000 mg/L total dissolved solids (Hamblin 2004).

CHAPTER 3: MODELING

Deterministic models are based on the physical laws governing groundwater flow and rely on our knowledge of the characteristics of the system and of the available data. This allows for reasonable extrapolation beyond the available sampling but is only possible if the context of the data values is understood (Kresic 1997; Isaaks and Srivastava 1989). Goovaerts (1997) reports that using a deterministic modeling approach typically will associate a single estimated value at an unsampled location without documenting the potential error in the estimated value. It is assumed that this error is negligible. An inherent error exists in the estimated value considering that we do not have an exhaustive data set and our knowledge of the physical processes that control spatial variability over the study area is imperfect (Goovaerts 1997).

Subsurface fluid flow occurs in complex geological environments where the structural, lithologic, and petrophysical characteristics vary in ways that cannot be predicted deterministically in all of their relevant details (Zhang 2002). The characteristics of the aquifer exhibit discrete and continuous spatial variations on many scales which cause flow parameters to do likewise. Estimating the parameters at points where measurements are unknown or not possible entails a random error (Zhang 2002).

Deterministic approaches for the characterization of complex non-ideal systems can be inappropriate since such an approach requires an understanding of the spatial variability, and the estimation of a large number of parameters, which cannot be supported by a small number of measurements. Furthermore, the solution becomes fixed based on the values

that are assigned to the parameters (c.f. Anderson and Woessner 1992; Kresic 1997; Rubin 2003; Burns et al. 2010a). Due to sparse and imprecise data, these models cannot be considered fully reliable. A deterministic distribution of a parameter can only be obtained by having a measurement of that parameter at every location with the aquifer. Classical variogram and sequential gaussian simulations result in too smooth of a representation and are incapable of capturing the distribution and connectivity that characterizes these complex channel systems. At areas far away from the data points (i.e., geology and hydraulic parameters), interpolation schema honouring the data will produce a single smooth solution that does not reproduce possible high-frequency variations. This implies that regions away from any data points, the corresponding most probable solution can have only a smooth behaviour. This is typically different from the actual behaviour (Mallet 2002).

Therefore, a description of the subsurface geology detailing the complex distribution and association of channel sands and overbank deposits is not possible using a deterministic approach. Since this is not possible, a stochastic framework can be used to model parameters using random functions and for evaluating uncertainties (Anderson and Woessner 1992; Kupfersberger and Deutsch 1999; Mallet 2002; Zhang 2002).

One family of methods for simulating the sedimentological framework is commonly referred to as object-based simulation. These modeling approaches embed three dimensional objects representing different hydrofacies into a background matrix hydrofacies. Among the advantages of object-based models are the ability to

stochastically build a simulation that contains hydrofacies with geologically realistic shapes, and to produce realistically sharp boundaries between hydrofacies that may have strongly contrasting hydraulic properties. Object-based modeling of fluvial systems is conceptually a simple way to define the spatial arrangement of different facies within an aquifer (Mckenna and Smith 2004, Hatloy 1995).

Stochastic Models

Stochastic simulation is the process of drawing alternative, equally probable, joint realizations of the random variables from a random function model (Mallet 2002). The evaluation of the inherent variability of spatial and temporal data and irregular nature of data and the incorporation of these key concepts into a stochastic model is the basis of geostatistical modeling (Mallet 2002). The use of random functions is intended to introduce uncertainty through the generation of realizations of the system that are neither unique nor smooth (Mallet 2002, Rubin 2003). Stochastic approaches are motivated by having access to only incomplete information as a result of insufficient sampling, inadequacy of instrumentation, and insufficient sources of information (Mallet 2002, Rubin 2003). The reliability of models developed based on sparse or imprecise data should be carefully considered when evaluating the impact of uncertainty on modeling outputs (Mallet 2002; Zhang 2002; Penguin Books 2003; Parzen, 1962). Scarcity of data and uncertainty in the petroleum industry lead to the development of object-based modeling (Chiles and Delfiner 1999).

Aquifers or reservoirs show heterogeneous characteristics since a variety of geological processes were involved in their provenance (Kupfersberger and Deutsch 1999, Zhang 2002). The geological processes may be generally understood but fluid flow, pressures, initial and boundary conditions of the system can never be known in sufficient detail to provide a unique deterministic view of the aquifer (Kupfersberger and Deutsch 1999, Zhang 2002).

The complexity of non-ideal geological systems has resulted in the development of stochastic models. Two types of models, object-based and indicator map produce discrete realizations which make it possible to explicitly simulate three dimensional objects that represent facies distributions (i.e., sedimentological framework) of an aquifer (Le Ravalec-Dupin 2005). The distribution of these facies and associated hydraulic properties provide the basis for groundwater flow simulation (Hatloy 1995; McKenna and Smith 2004). This methodology can be used to provide a general outline towards a more efficient characterization of fluvial depositional settings for groundwater studies.

Selected Modeling Approach

The areas of the aquifer that consist of sandstone channels and complexes encased in floodplain deposits represent a challenge to hydrogeologic flow or transport analysis. Since it is difficult to develop a detailed 3-dimensional model of the non-ideal system, representation of the physical properties of the system and aquifer response must be pursued by some other means (Burns et al. 2010a). Modeling non-ideal geological and hydrogeological systems using standard industry practices presents challenges in

attempting to capture the inherent heterogeneity of the system. Previous studies, (cf., Burrows 2004; Fogg 1986; Bridge and MacKay 1993) indicate that conventional deterministic modeling methodology ignores the geological complexity of non-ideal systems subsequently results in models that cannot capture the characteristics of the hydraulic response system (Burns et al. 2010a). Due to the difficulty of generating a 3-dimensional geometry of the aquifer system we have chosen to adopt a stochastic modeling approach. Overviews of methods of generating physically relevant stochastic models of heterogeneity are presented by Koltermann and Gorelick (1996), Deutsch (2002), and de Marsily et al. (2005).

An appropriate approach is the development of an object-based stochastic model to describe the geologic complexity of the Paskapoo Formation. Using this approach we can statistically model facies geometries and relationships for the system which represent three dimensional geometrical objects (Burns et al. 2010a). The statistical model is defined in terms of the distribution of facies properties through the generation of equiprobable realizations of the aquifer facies and hydraulic properties (Burns et al. 2010a).

CHAPTER 4: STOCHASTIC GEOMODELING

The Irap Reservoir Modeling Software (RMS) platform for 3-dimensional reservoir property modeling was used for simulating pilot-scale geomodels of fluvial depositional environments similar to that of the Paskapoo Formation in the region of Calgary. A geomodel, as defined by Mallet (2002), is a set of mathematical methods that allow modeling in a unified way the topology, the geometry and the physical properties of geological objects while taking into account any type of data, both hard and soft of varying scale, related to these objects.

In building the geomodel, a series of integrated modules were used for interpolation and object-based modeling techniques to capture facies geometries constrained by the user input. Modeling stochastic distributions is a multi-step process which consists of development of a geomodel, upscaling, and flow simulation. Output of the distributed parameters and grid was accomplished using a custom script written using the RMS Internal Programming Language (IPL). The workflow used in building the geomodel included:

A) Developing a stratigraphic framework,

B) Grid design,

C) Facies modeling and sand fraction model based on hypothetical geomorphic model,

D) Property modeling,

E) Parameter transform, and

F) File export (facies, nodal coordinates, nodal connectivity, hydraulic conductivity, porosity, storativity) using Roxar's Internal Programming Language (IPL).

Pivotal to this process is the object-based facies modeling module used to distribute the facies and associated geometries throughout the model domain. Use of object-based facies models results in realizations which mimic the idealized geometries based on the statistics used to describe the permeable facies of the fluvial depositional environment. The approach results in geological shapes with realistic non-rectilinear continuity, which cannot be modeled with cell-based approaches (Deutsch 2002). Two key issues are addressed when setting up object-based models. The first issue addresses geological shapes and their parameter distributions, and the second is the algorithm used by Irap RMS for object placement.

The geological shapes are specified by equations internal to RMS. Sinuous channel shapes can be modeled by a 1-dimensional centerline surrounded by floodplain deposits. Crevasse splay objects can be attached to the channels. Channels can be clustered into channel complexes or belts and can be handled by the object placement algorithm. The relationships between the geological objects (facies) are described through facies modeling and the positioning is handled by the algorithm for stochastic placement. The Boolean algorithm is used in object-based facies modeling. Typically the objects are built up from the stratigraphic base of the model or can be embedded within a matrix of facies according to a stochastic process. Unconditional simulation is straightforward, objects are placed randomly until the global proportions of the different facies are

reproduced (Deutsch 2002). The spatial relationship between the hydraulically conductive facies (i.e., sand channels and crevasse splays) is specified in the facies modeling module to ensure correct connectivity. Through property modeling, hydraulic parameters are associated with a particular facies and these properties are used to populate the grid cells associated with each facies.

Hypothetical Geomorphic Analogue Model

The geomodel developed for this research was based on a hypothetical geomorphic model proposed by Burns et al. (2010b). This section presents a summary of the work performed by Burns et al. (2010b) related to the development of the hypothetical geomorphic model. Burns et al. (2010b) studied modern river reaches and geomorphic descriptions of active channel systems to determine if a universal classification system either existed or could be developed to define the configuration of active or preserved channel systems. Gibling (2006) proposed an observationally-based classification of sandstone bodies deposited in fluvial depositional environments. The categories used to describe the fluvial systems included a) low-sinuosity mobile channel belts, b) high-sinuosity mobile channel belts, and c) fixed channel belts. Based on an extensive literature review and review of Paskapoo data, Burns et al. (2010b) was able to statistically describe the characteristics of the Paskapoo as it applies to the West Nose Creek watershed area in Calgary. This statistical information of the Paskapoo within the West Nose Creek watershed area was used as input into the geomodel for this research.

The upper portion of the modern-day Paskapoo bedrock aquifer system was likely deposited by a fixed channel belt system which is characterized by multiple interconnected, low gradient, laterally stable channels with low width to depth ratios (Burns et al. 2010b). These systems are typically subject to rapid sedimentation rates which tend to preserve mud-encased buried channel-fill and crevasse splay sand bodies. Width to depth ratios of channel-fills for these systems are variable and have thicknesses that rarely exceed 15 m but can be up to 30 m in thickness. Crevasse splays are variable in shape and tend to consist of channel sand and overbank deposits rarely exceeding a few meters in thickness. Within anastomosed systems, overbank mud makes up approximately 70 to 90 % of the basin-fill while the sandy channel-fills and crevasse-splays make up approximately 10 to 30% (Burns et al. 2010b). Channel thickness in larger fixed belt systems can range between 3 to 15 m in the paleo-record with the thickest estimated at approximately 33 m. Channel structures can measure between 15 to 300 m in width and have been measured as wide as 2.4 km. The width to thickness ratio typically has ranged between 5 and 50; however it has been documented as high as 150 by Gibling (2006).

Burns et al. (2010b) surmised that the sand channels will be well preserved with higher permeability and porosity than the surrounding overbank deposits. Crevasse splays should have intermediate hydraulic characteristics but studies have suggested that if 10% by weight of the splay is overbank fines, permeability will be much closer to overbank values than sand channel values (Burns et al. 2010a).

Core and outcrop data of the Paskapoo was used to determine facies type in the Calgary area. Data indicates that the aquifer systems contain sand-dominated paleo-channels, crevasse splays, mudstone-dominated over bank deposits and other minor components such as coal and paleosols (Burns et al. 2010b). It was assumed that sandstone and floodplain deposits could be distinguished and that the channel sands are thick enough to allow for distinct contacts to be recorded. Furthermore, it was assumed that crevasse splays may or may not be explicitly recorded in core descriptions or otherwise would be less than one meter in thickness (Burns et al. 2010b). Primary permeability of cores indicated floodplain deposits were at least three orders of magnitude less than the channel sandstones. The high permeability contrast and low channel fraction and thick sequences of overbank deposits support the hypothetical geomorphic model of a system consisting of well-preserved mud-encased channel sands (Burns et al. 2010b). Burns et al. (2010b) studied the relationship between facies distribution and hydraulic response. As part of the work performed by Burns et al. (2010b), a sensitivity analysis was performed to determine the relationship between flow response and facies modeling parameters. To evaluate the effect of fluvial parameters on the net flow through the Paskapoo formation, synthetic flow simulations were performed by imposing a fixed head difference across a box populated with fluvial facies. One set of model parameters was selected as a reasonable estimate based on literature values and results of hydrogeologic work performed in the West Nose Creek Watershed (Burns et al. 2010b). The set of model parameters as selected by Burns et al. (2010b) to be representative of the Paskapoo in the Calgary area is summarized in Table 4.1.

Table 4.1: Summary of Hypothetical Geomorphic Analogue Model Parameters

Geomodel Parameter (for West Nose Creek Watershed)	Value
Facies Fraction (of model domain)	
Channels	21% (± 3%)
Crevasse Splays	10%
Floodplain Overbank Deposit	69%
Channel Thickness (meters)	
Mean	7.5
Standard Deviation	3.5
Minimum	0.5
Maximum	20
Channel Width (meters)	
Mean	75
Standard Deviation	35
Minimum	10
Maximum	200
Channel Width-Thickness Correlation	0.5
Channel Meander Amplitude (meters)	
Mean	200
Standard Deviation	50
Channel Sinuosity	1.35
Channel Direction (Azimuth degree)	
Mean	90
Standard Deviation	10

Splay Thickness Relative to Channel	
Mean	0.15
Standard Deviation	0.03
Relative Splay Lobe Width (normal to channel)	3
Absolute Lobe Length (meters parallel to channel)	500
Number of Crevasse-Belts per Channel	
Minimum	1
Maximum	8
Crevasse Splay Vertical Position	Random
Crevasse Splay Horizontal Geometry	Isolated
Hydraulic Conductivity (meters/second)	
Sand Channels	1E-03
Crevasse Splays	1E-04
Floodplain Overbank Deposit	1E-06

Geomodel Grid Size Evaluation and Flow Performance

In order to select an appropriate model domain size for this research and to evaluate the applicability of the hypothetical geomorphic model parameters as they relate to the size of the domain, two separate geomodels were developed, 100 realizations of each model were generated, and flow simulations of each model for each of the three principal directions of flow were conducted to evaluate and compare flow performance. Since the focus of this research is to evaluate the hydraulic response of a non-ideal system and the propagation of the pressure wave due to the abstraction of water from a pumping well, vertical infiltration of water into the system and the effects of topography were ignored.

Spatial variations in recharge to the aquifer would affect flow velocities and the distribution of the pressure regime thereby potentially masking the net effect of the facies geometry on groundwater flow. Therefore each geomodel developed took the form of a 3-dimensional block model.

Limitations with the number of elements that can be handled by the groundwater flow simulator (HydroGeoSphere) constrained the discretization of each geomodel and subsequently the domain size. For this research consideration was given to model size since the domain must be of sufficient size to allow transient conditions to be simulated without the interference from the model boundaries being imposed on the pressure wave induced by the abstraction of water from a pumping well placed in the center of the model.

Two geomodels were generated for the purpose of flow simulation and performance evaluation as a function of grid discretization and model domain size. From the results of this study we will be able to determine the largest domain size and the coarsest grid discretization while still capturing the behaviour of a geologically complex aquifer system. A large domain size will allow for a longer transient simulation, so ideally the largest domain size possible is sought. Each geomodel was designed based on the hypothetical geomorphic analogue model and the discretization of each model was constrained by the limitations of HydroGeoSphere so that both the coarse-grid model and the fine-grid model, after upscaling, would have approximately 500,000 grid cells.

A coarse-grid geomodel of 500,000 uniform elements was developed. Each coarse-grid element is 50 meters by 50 meters by 0.5 meters, with the x-y grid being a symmetrical 60 by 60 elements and 200 elements in the z direction, giving a resulting model block size of 3,000 meters by 3,000 meters by 100 meters. It was noted that the size of the discretization for the coarse-grid model does not necessarily honor the statistics of the hypothetical geomorphic model. For example, the x-y element size is 50 meters by 50 meters, however the mean channel width is 75 meters, the minimum channel width is 10 m, and the maximum channel width is 200 m. By using this discretization, only the maximum channel width can be honoured. The coarse-grid geomodel is presented in Figure 4.1.

Figure 4.1: Coarse-grid geomodel

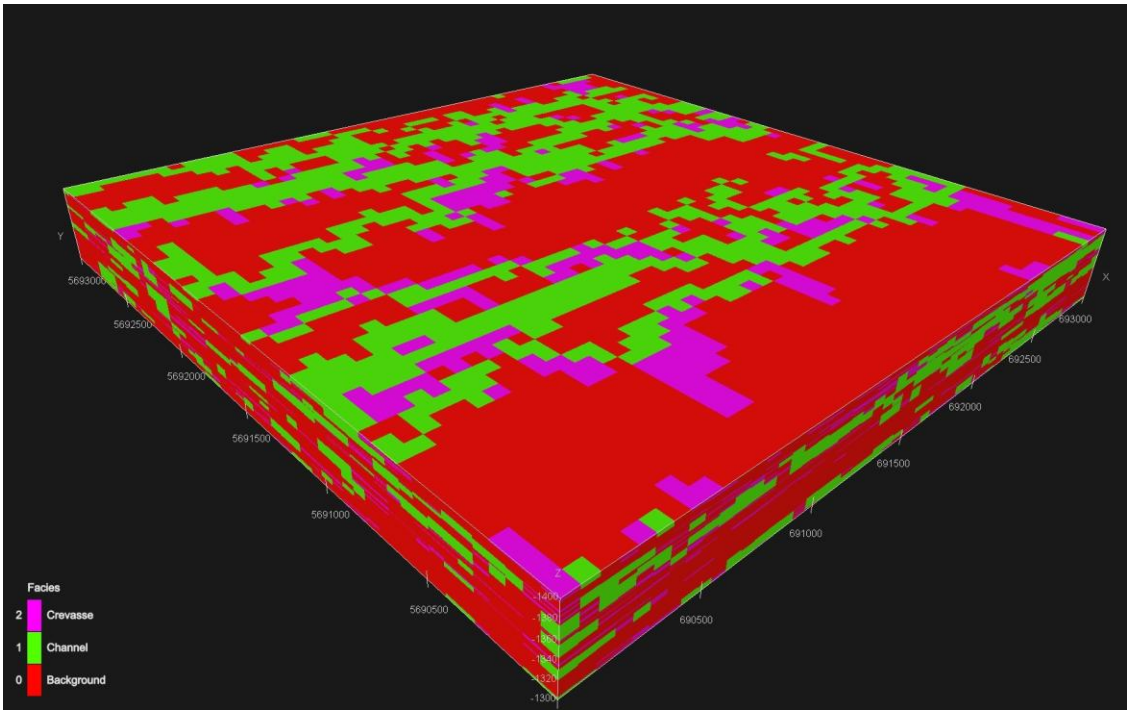

The fine-grid geomodel was developed using the same size domain, prior to upscaling, had 2,000,000 uniform elements. Each fine-grid element is 30 meters by 30 meters by 0.5 meters, with x-y grid being 100 by 100 elements and 200 elements in the z-direction, giving a resulting model block size of 3,000 meters by 3,000 meters, by 100 meters. The fine-grid geomodel was subsequently subjected to an upscaling algorithm (i.e., the reduction in number of elements) developed by Burns et al. (2010b), the performance of which is dependent upon the complexity of objects defined by the gridding facies (i.e., channel geometries). The reduction in grid nodes is approximately 4 to 5 times for the upscaling parameters considered (Burns et al. 2010b). Discussion of the general upscaling algorithm is deferred to the following section. The fine-grid geomodel is illustrated Figure 4.2. Both Figures 4.1 and 4.2 illustrate the spatial distribution of facies within the model domain. From Figure 4.2 it can be seen that the finer discretization of the model domain allows for an improvement of facies representation over the coarser discretization illustrated in Figure 4.1.

Figure 4.2: Fine-grid geomodel

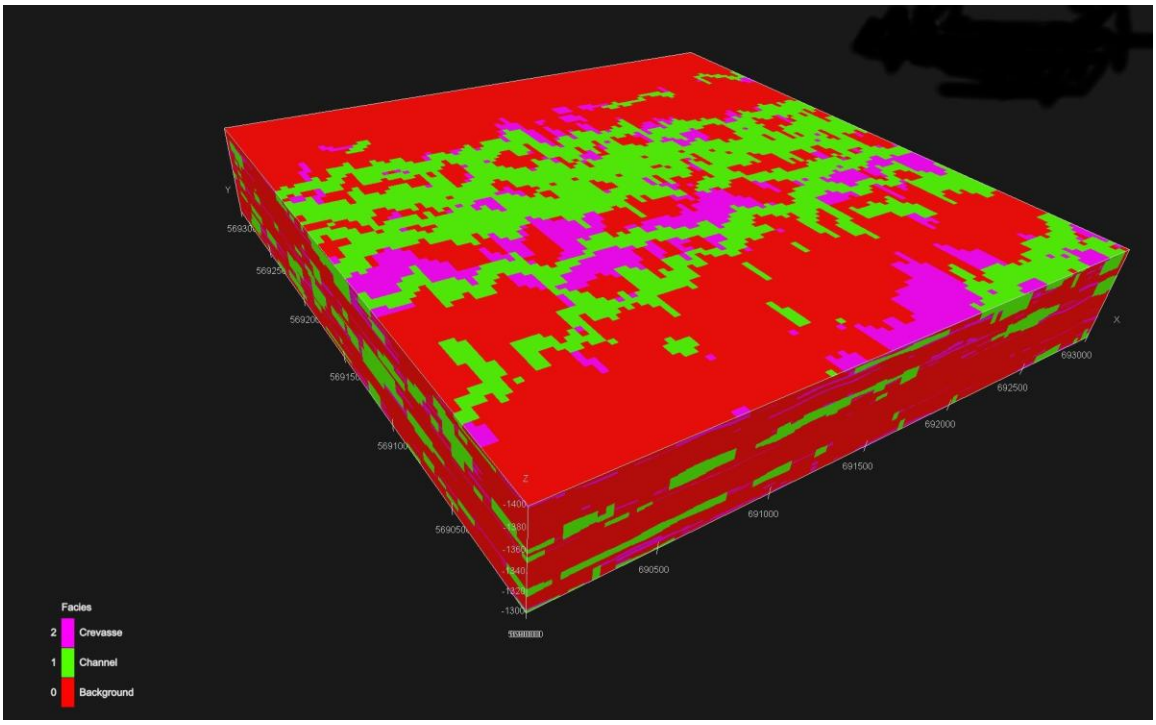

In the Paskapoo Formation near Calgary, primary hydraulic conductivity of paleo-sand channel complexes is several orders of magnitude higher than the overbank deposits. The higher connectivity of the channel deposits longitudinally is postulated to be important for controlling regional flow (Burns et al. 2010a). The sand channels were assigned a constant hydraulic conductivity, and it is believed that the splays are important for controlling flow laterally between sand channel complexes where channels do not intersect and subsequently were assumed to have a higher conductivity than the overbank deposits. The hydraulic conductivity parameters used in the upscaled fine-grid and coarse-grid models are summarized in Table 4.1.

Flow simulations were used to compare the general upscaled fine-grid model results with those of the coarse-grid results. Effective hydraulic conductivity was computed for each of the principal directions for both the coarse-grid and upscaled fine-grid models, and these values are compared. The principal directions are defined relative to the geomodel directions which are statistically defined (Burns et al. 2010a). The principal directions are a) longitudinal or parallel to the channels (Kx), b) transverse or perpendicular to the channels (Ky), and c) normal or vertical to channels (Kz). To simplify the interpretation and focus the analysis on upscaling and facies distributions, the hydraulic conductivity for each facies is held constant. This allows analysis of only effects of facies geometries as a function of grid discretization (Burns et al. 2010a).

Effective hydraulic conductivity (eff_{Kx}) is the net bulk hydraulic response of the modeled system as simulated along the simulated principal direction of flow. The effective hydraulic conductivity in each of the three principal directions (Kx, Ky, and Kz) was computed by summing the volumetric discharge for all elements on the influx side of the model domain normal to flow and obtaining the quotient of the flux and the product of the gradient and area perpendicular to fluid flow:

$$eff_{Kx} = \frac{q_x}{i * A} \qquad [4.1]$$

where q_x is the total volumetric discharge across the inflow faces, i is the imposed gradient and A is the cross sectional area. Mass balance error for each model run was calculated from the HydroGeoSphere list file. Using the solution from the model the mass balance error was defined by:

$$\%\ Mass\ Balance\ Error\ = \frac{\Delta(IN - OUT)}{\frac{(IN + OUT)}{2}} \qquad [4.2]$$

where $\Delta(IN - OUT)$ is the difference between the volumetric discharge at the inflow and outflow boundaries and $(IN - OUT)/2$ is the average volumetric discharge across the domain. Each simulation mass balance error was below 1%. Effective conductivity and mass balance error for each model simulation is listed in Appendix A.

Flow is computed using a fixed head difference across the model domain in each of the principle directions subject to no flow boundaries on all other boundaries. Groundwater flow was studied separately for each of the principal directions. The length, width, and height of the model domain provide the area and length over which the head difference is imposed, allowing the use of Darcy's Law to compute effective K for each direction (Burns et al. 2010a). The summary statistics (Tables 4.2 through 4.4) for the coarse-grid

and upcscaled fine-grid models for all three principal directions of flow were compared and plotted (Figures 4.3 through 4.5).

Table 4.2: Summary Statistics of Coarse-Grid and Upscaled Fine-Grid Effective Kx Hydraulic Conductivities

Parameter	Effective Coarse-Grid Kx (m/s)	Effective Upscaled Fine-Grid Kx (m/s)
Number of realizations	100	100
Mean	1.58×10^{-04}	1.49×10^{-04}
Standard Error	9.79×10^{-07}	9.03×10^{-07}
Median	1.55×10^{-04}	1.48×10^{-04}
Mode	1.50×10^{-04}	1.51×10^{-04}
Standard Deviation	9.79×10^{-06}	8.76×10^{-06}
Sample Variance	9.59×10^{-11}	7.67×10^{-11}
Kurtosis	4.29×10^{-01}	-5.08×10^{-01}
Skewness	2.92×10^{-01}	3.91×10^{-01}
Range	5.60×10^{-05}	3.91×10^{-05}
Minimum	1.27×10^{-04}	1.33×10^{-04}
Maximum	1.83×10^{-04}	1.72×10^{-04}
Sum	1.58×10^{-02}	1.40×10^{-02}
Confidence Level (95.0%)	1.94×10^{-06}	1.79×10^{-06}
P05	1.46×10^{-04}	1.36×10^{-04}
Q1	1.51×10^{-04}	1.42×10^{-04}
Q2	1.55×10^{-04}	1.48×10^{-04}
Q3	1.63×10^{-04}	1.55×10^{-04}
P95	1.77×10^{-04}	1.64×10^{-04}
Q4	1.83×10^{-04}	1.72×10^{-04}
Interquartile Range Q1-Q2	4.00×10^{-06}	1.29×10^{-04}
Interquartile Range Q2-Q3	8.25×10^{-06}	9.66×10^{-06}
Interquartile Range Q3-Q4	1.98×10^{-05}	2.05×10^{-05}

Figure 4.3: Cross Plot of Coarse-Grid vs. Upscaled Fine-Grid Effective Hydraulic Conductivities illustrating P05, P25, P50, P75, and P95

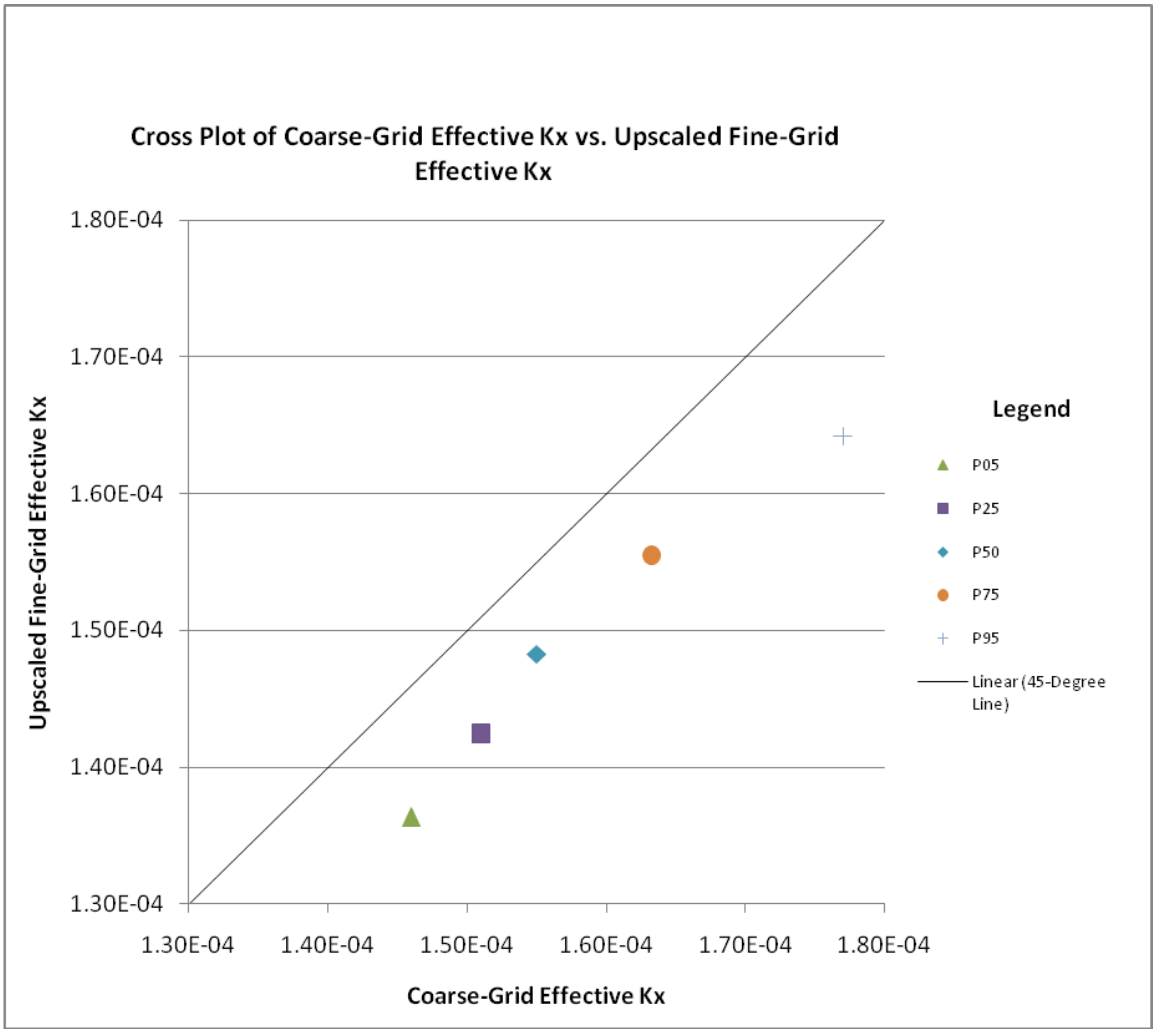

Table 4.3: Summary Statistics of Coarse-Grid and Upscaled Fine-Grid Effective Ky Hydraulic Conductivities

Parameter	Effective Coarse-Grid Ky (m/s)	Effective Upscaled Fine-Grid Ky (m/s)
Number of realizations	100	100
Mean	5.75×10^{-05}	4.61×10^{-05}
Standard Error	1.01×10^{-06}	1.75×10^{-06}
Median	5.89×10^{-05}	4.46×10^{-05}
Mode	6.03×10^{-05}	4.42×10^{-05}
Standard Deviation	1.01×10^{-05}	1.69×10^{-05}
Sample Variance	1.02×10^{-10}	2.87×10^{-10}
Kurtosis	$7.61 \times 10^{+00}$	$2.31 \times 10^{+01}$
Skewness	$-1.58 \times 10^{+00}$	$3.91 \times 10^{+00}$
Range	7.31×10^{-05}	1.50×10^{-04}
Minimum	2.91×10^{-06}	6.72×10^{-08}
Maximum	7.60×10^{-05}	1.50×10^{-04}
Sum	5.75×10^{-03}	4.34×10^{-03}
Confidence Level (95.0%)	2.00×10^{-06}	3.47×10^{-06}
P05	4.20×10^{-05}	3.30×10^{-05}
Q1	5.18×10^{-05}	3.91×10^{-05}
Q2	5.89×10^{-05}	4.46×10^{-05}
Q3	6.30×10^{-05}	5.06×10^{-05}
P95	7.30×10^{-05}	5.75×10^{-05}
Q4	7.60×10^{-05}	1.50×10^{-04}
Interquartile Range Q1-Q2	7.14×10^{-06}	5.50×10^{-06}
Interquartile Range Q2-Q3	4.06×10^{-06}	6.04×10^{-06}
Interquartile Range Q3-Q4	1.30×10^{-05}	9.97×10^{-05}

Figure 4.4: Cross Plot of Coarse-Grid vs. Upscaled Fine-Grid Effective Hydraulic Conductivities illustrating P05, P25, P50, P75, and P95

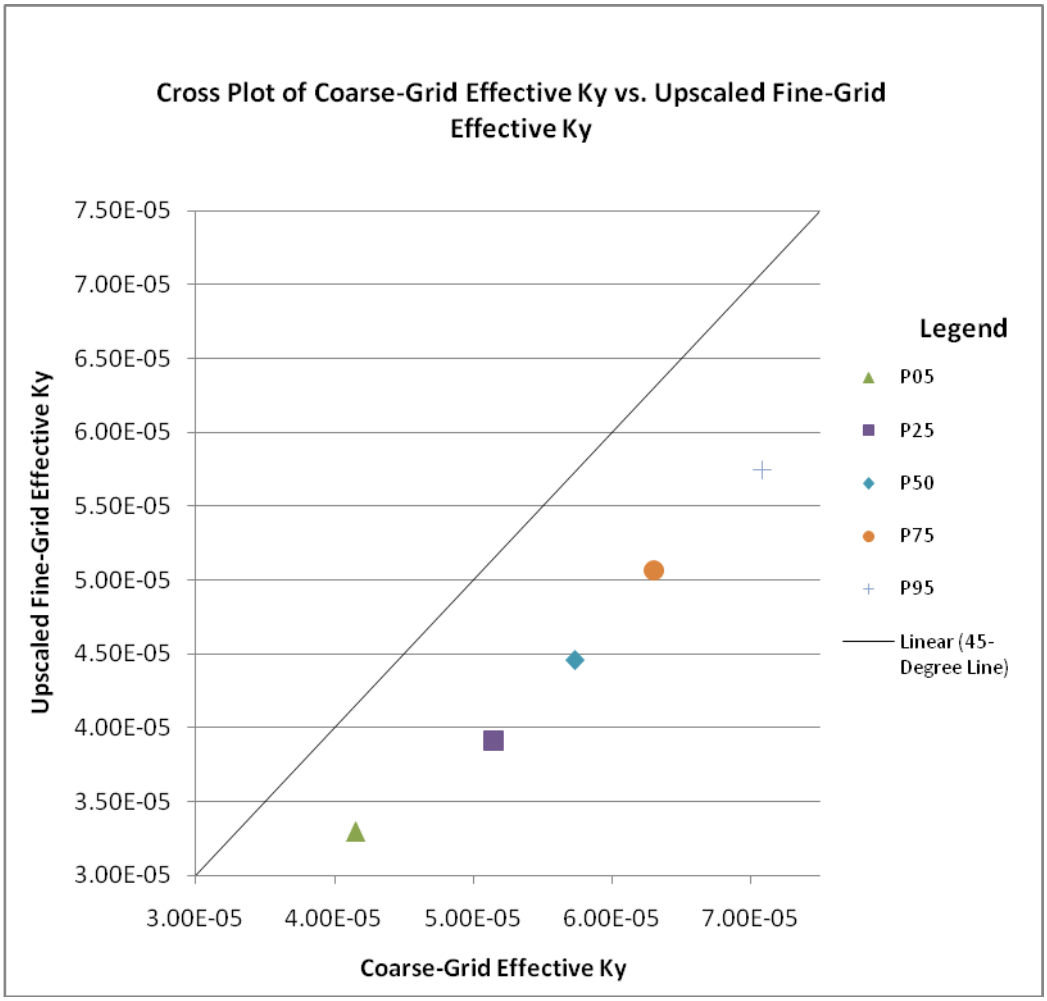

Table 4.4: Summary Statistics of Coarse-Grid and Upscaled Fine-Grid Effective Kz Hydraulic Conductivities

Parameter	Effective Coarse-Grid Kz (m\s)	Effective Upscaled Fine-Grid Kz (m/s)
Number of realizations	100	100
Mean	2.01×10^{-06}	1.80×10^{-06}
Standard Error	1.43×10^{-08}	2.16×10^{-08}
Median	2.08×10^{-06}	1.80×10^{-06}
Mode	2.14×10^{-06}	1.89×10^{-06}
Standard Deviation	1.43×10^{-07}	2.10×10^{-07}
Sample Variance	2.04×10^{-14}	4.40×10^{-14}
Kurtosis	$1.24 \times 10^{+00}$	$5.41 \times 10^{+01}$
Skewness	9.88×10^{-01}	$-6.37 \times 10^{+00}$
Range	7.49×10^{-07}	2.04×10^{-06}
Minimum	1.86×10^{-06}	3.83×10^{-08}
Maximum	2.61×10^{-06}	2.08×10^{-06}
Sum	$2.10 \times 10^{+04}$	1.69×10^{-04}
Confidence Level (95.0%)	2.83×10^{-08}	4.30×10^{-08}
P05	1.92×10^{-06}	1.67×10^{-06}
Q1	1.99×10^{-06}	1.75×10^{-06}
Q2	2.08×10^{-06}	1.80×10^{-06}
Q3	2.16×10^{-06}	1.88×10^{-06}
P95	2.35×10^{-06}	2.01×10^{-06}
Q4	2.61×10^{-06}	2.08×10^{-06}
Interquartile Range Q1-Q2	8.86×10^{-08}	5.35×10^{-08}
Interquartile Range Q2-Q3	7.99×10^{-08}	8.58×10^{-08}
Interquartile Range Q3-Q4	4.49×10^{-07}	1.96×10^{-07}

Figure 4.5: Cross Plot of Coarse-Grid vs. Upscaled Fine-Grid Effective Hydraulic Conductivities illustrating P05, P25, P50, P75, and P95

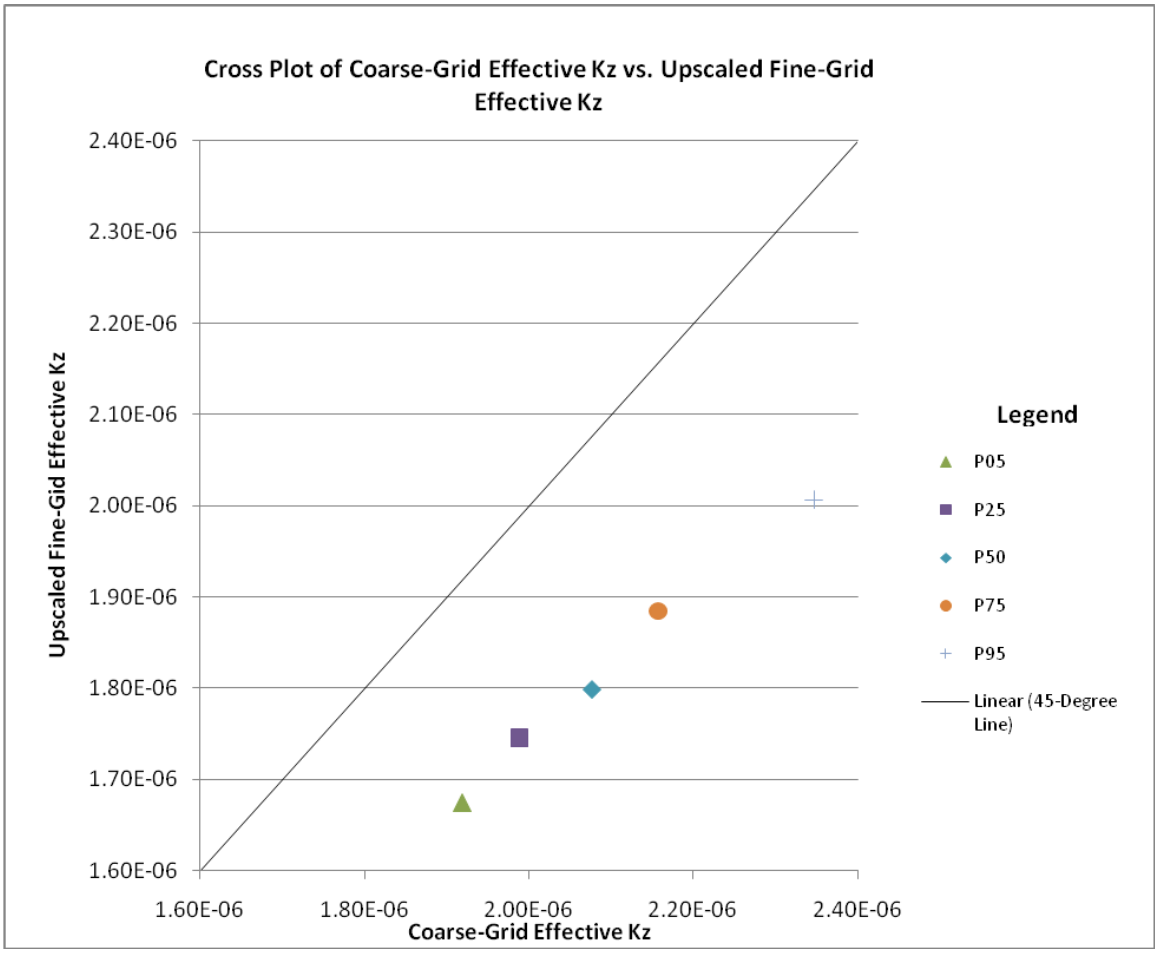

The effective hydraulic conductivities of the coarse-grid and upscaled fine-grid results for the 5th, 25th, 50th, 75th and 95th percentile were compared on cross plots (Figures 4.3-4.5). The flow response of the coarse-grid domain systematically resulted in higher effective hydraulic conductivities than that of the upscaled fine-grid domain in all three principle flow directions (Figures 4.3 through 4.5). It is likely that the discretization of the coarse-

grid model which did not honor the statistics of the hypothetical geomorphic analogue model as closely as the upscaled fine-grid model resulted in greater connectivity between permeable faces of the model and subsequently higher system conductivity. It is postulated that the crevasse splays are regionally important to the lateral flow of groundwater. Because the flow performance of the coarse-grid model over predicted the effective conductivity compared to that of the upscaled fine-grid model and that the grid discretization of the fine-grid model honored the statistics of the hypothetical geomorphic model more appropriately, the upscaled fine-grid geomodel and further grid refinement was selected for further investigation into the response of system behavior to the abstraction of water under transient conditions.

Results of the upscaled flow simulations indicate that the higher effective conductivity is parallel to the long axis of the channels and the least effective conductivity is along the vertical axis of the system. This would suggest that the primary valley directions should be known and grid cells should be populated with anisotropic conductivity values for regional scale modeling efforts.

Implementation of a General Upscaling Algorithm for Regional-Scale Flow Simulations

In order to investigate the effects of regional-scale flow in non-ideal groundwater systems, a mathematically viable grid with few enough cells to allow for numerical solution while still adequately representing the physical system through a distribution of physically relevant parameters is needed. Unfortunately, about 10 times more grid cells

may be simulated in the stochastic geomodel than can be used in the resulting flow model based on computational restrictions of a computer and the chosen flow simulator. If resultant shapes within the geomodel can be upscaled to a coarser grid, then upscaling may be accomplished prior to flow simulation alleviating the mismatch between geomodel and flow model (Burns et al. 2010b).

The upscaling algorithm (Burns et al. 2010b) uses local techniques which take averages of the distribution of fine-grid parameters (i.e., hydraulic conductivities, porosity, storativity, and facies). The grid and upscaled parameters are exported for use in flow simulation. A user-defined gridding facies was used to allow generation of an irregular coarse-grid that preserves facies geometry (Burns et al. 2010b). The upscaling algorithm defines new layers with tops and bottoms of user-defined smoothness that correspond to tops and bottoms of geologic objects which are considered contiguous facies that form substantial subsurface units. The upscaling algorithm utilizes the x-y rectangular grid generated by RMS and upscaling only occurs in the vertical direction. This ensures that the x-y geometry of any object described by the fine-grid model will be satisfied by the rectangular prisms constituting the HydroGeoSphere groundwater flow model.

The algorithm first searches to find each contiguous facies. Then every transition between the gridding facies and remaining facies is identified, resulting in an array of top and bottom transitions. Surfaces are assigned to model layers which are filled in so that every x-y cell location in every layer has an elevation. Hydraulic parameters are upscaled using local upscaling techniques. Burns et al. (2010b) reports that since

upscaling is only in the vertical direction and that the x-y discretization is not altered when upscaled to the coarse-grid; the upscaling algorithm only needs to average a stack of grid cells of uniform thickness. Thus, the effective horizontal hydraulic computation becomes the arithmetic average of the values of the fine-grid cells and the effective vertical hydraulic conductivity computation becomes the harmonic average of the fine-grid cells. The parameters of storativity and porosity are upscaled as volume averaged values. Once all parameters are calculated, grid and parameter files are exported to HydroGeoSphere input files (Burns et al. 2010b).

Stochastic Simulation of the Paskapoo Formation

Using Irap RMS, a fine-grid geomodel of the Paskapoo Formation aquifer system near Calgary, Alberta was created using the model parameters (Burns et al. 2010b) summarized in Table 4.1. Recall that the purpose of the model is to investigate the net effects of geologic heterogeneity on flow under steady state (as discussed in the previous section) and transient conditions imposed by the abstraction of water by a pumping well. The vertical migration of groundwater into and out of the system and the effects of topography were ignored resulting in the generation of a 3-dimensional geologic block model. Furthermore, to simplify the model, the 3-dimensional fracture overprint was not included in the geomodel. Recall that the fine-grid discretization honoured the hypothetical geomorphic analogue model statistics so that hydraulically conductive facies and geometries were more accurately represented. This model was selected for further grid refinement and investigation under transient conditions. Modeling of the non-ideal geologic system for transient conditions is a multistep process consisting of selection of a

reasonable set of hydraulic parameters which are constrained by the domain size, evaluating effective conductivity, evaluation of mass balance errors, and selection of ranked models, modeling steady state solutions, modification of boundary conditions to reduce interference by model boundaries, and modeling transient pumping conditions.

A total of 100 equiprobable realizations were generated of the fine-grid geomodel. A finer discretization was selected that more appropriately honoured the statistics of the analogue model. Prior to upscaling the model had 2,000,000 uniform cells. Each fine-grid element is 10 meters by 10 meters by 0.5 meters, with x-y grid being 100 by 100 elements and 200 elements in the z-direction, giving a resulting model block size of 1,000 meters by 1,000 meters, by 100 meters. The parameters summarized in Table 4.1 allowed the generation of important facies geometry of the channel sands, crevasse splays, and overbank deposits. These facies exhibit complex connectivity and as such control the preferential flow within the aquifer (Burns et al. 2010a).

Hydraulic Parameterization

A literature review of available hydraulic conductivity values for sandstones, siltstones, and shales was performed (Australian Government 2007; AQTESOLV 1998-2009). Available data on the Dakota Aquifer (a geologically complex system consisting of channel sands) was also reviewed for pertinent hydraulic values of the primary facies from the Kansas Geological Survey (1999). The data suggest conductivity values of sandstones, siltstones, and shales several orders of magnitude less for each facies than those used by Burns et al. (2010b). Conductivity values for shale ranged from 1.0×10^{-13}

m/s to 1.0 x 10^{-09} m/s, for sands ranged from 9.0 x 10^{-07} to 6.0 x 10^{-03} m/s, and for silts ranged from 1.0 x 10^{-09} m/s to 2.0 x 10^{-04} m/s. Based on the literature review and initial simulations, a set of constant hydraulic conductivity parameters were selected for each facies (Table 4.5). These parameter values were used in the subsequent fine-grid geomodels and upscaled prior to flow simulations.

Table 4.5: Hypothetical Hydraulic Parameters

Parameter	Hydraulic Conductivity (m/s)	Porosity (%)	Specific Storage (m^{-1})
Channel Sands	1E-05	30	1E-05
Crevasse Splays	1E-06	10	1E-05
Overbank Deposits	1E-012	1.0	1E-07

Groundwater Flow Model Methodology and Model Selection

HydroGeoSphere was selected for flow simulation. HydroGeoSphere is a fully coupled surface, vadose, groundwater fixed volume finite-element code. The HydroGeoSphere source code was altered to accept cell-by-cell coordinate and parameter files. In HydroGeoSphere, each element is defined by six nodes (for triangular prisms) or eight nodes (for rectangular prisms), and each node is defined by (x, y, z)-coordinates. Hydraulic properties are assigned to each element for flow simulation. The prisms are restricted in that they may have any irregular trapezoidal or triangular shape in the x-y plane, but the lines connecting the nodes in the z-direction must be vertical and must pass

through the entire model thickness. This means that the projection of the x-y grid is constant for all model layers, and it must be complex enough to describe all important geologic objects encountered at any depth (Burns et al. 2010b).

Flow simulations of all 100 equiprobable upscaled fine-grid realizations in the three principle flow directions (Kx, Ky, and Kz) were performed using HydroGeoSphere. In order to evaluate flow performance and effective hydraulic conductivity of each upscaled fine-grid model, a steady state solution for each model in each principle direction was generated by fixing a head difference across the model domain in each of the principle directions subject to no flow boundaries on all other boundaries. The model domain dimensions provide the area and length over which the head difference is imposed which will allow the use of Darcy's Law to compute effective K.

The summary statistics for the fine-grid simulations which used the parameter values presented in Table 4.5 were compared for each of the principle directions (Table 4.6). Due to the trend of the sand channels (parallel to the x-direction) the effective hydraulic conductivity in the x-direction had the highest mean value of 1.43E-06 m/s and the highest standard deviation. Figure 4.4 illustrates the histogram for the effective hydraulic conductivities in the x-direction and is negatively skewed. Figure 4.5 illustrates the histogram for the effective hydraulic conductivities in the y-direction and indicates a positive skewness. Due to the limited connectivity in the vertical direction the statistics of the effective conductivity in the z-direction suggest a very narrow distribution and low conductivity value indicating low connectivity in the vertical direction. Figure 4.6

illustrates the histogram for the effective conductivity in the z-direction and indicates a positive skewness.

Table 4.6: Summary Statistics of Effective Hydraulic Conductivities for Kx, Ky, Kz

Summary Statistics	*Effective Kx Statistics* *m/s*	*Effective Ky Statistics* *m/s*	*Effective Kz Statistics* *m/s*
Mean	1.42673E-06	2.63549E-07	4.40719E-11
Standard Error	3.61278E-08	1.80434E-08	9.48578E-12
Median	1.46532E-06	2.40565E-07	8.51719E-12
Mode	#N/A	#N/A	3.2356E-12
Standard Deviation	3.61278E-07	1.80434E-07	9.48578E-11
Sample Variance	1.30522E-13	3.25566E-14	8.99801E-21
Kurtosis	9.800162549	0.409600105	14.78438344
Skewness	-2.955394309	0.63736304	3.625816999
Range	1.87326E-06	8.01942E-07	6.01055E-10
Minimum	1.25662E-09	1.01874E-09	6.6398E-13
Maximum	1.87452E-06	8.02961E-07	6.01719E-10
Sum	0.000142673	2.63549E-05	4.40719E-09
Count	100	100	100
Largest(1)	1.87452E-06	8.02961E-07	6.01719E-10
Smallest(1)	1.25662E-09	1.01874E-09	6.6398E-13
Confidence Level(95.0%)	7.16854E-08	3.58021E-08	1.88219E-11

Aggregation of fine grid blocks of differing facies can result in an increase in the hydraulic conductivity of the upscaled coarse-grid. This could lead to perturbation in the

flow field that otherwise would not be present in the flow field observed if using just the fine-grid blocks. Le Ravalec Dupin (2005) reports that "flow rates at the boundaries of the aggregate of fine gridblocks must be the same as those of the coarse grid block". Upscaling can introduce spatial variability in the regional flow system through estimation to coarse-grid permeability equivalents and alter connectivity of hydraulically significant facies.

The upscaling process implicitly assumes optimal connectivity of permeable facies leading to an artificially improved connectivity amongst permeable facies in the x-y plane where the arithmetic mean is used to calculate conductivity (Burns et al. 2010b). The effective vertical hydraulic conductivity computation is performed using the harmonic average of the fine-grid cells. Burns et al. (2010a) reports that since splays are much thinner than channels and multiple splays may occur adjacent to a channel separated by overbank deposits in alternating layers, upscaling results in averaging a stack of cells of uniform thickness in the vertical direction. The effective hydraulic conductivity is systematically over-predicted as splay hydraulic conductivity increases, and the errors are greatest for estimates of vertical conductivity, followed by transverse conductivity (Burns et al. 2010b).

Figure 4.6: Histogram of the effective hydraulic conductivity Kx (m/s) for the upscaled fine-grid model solution

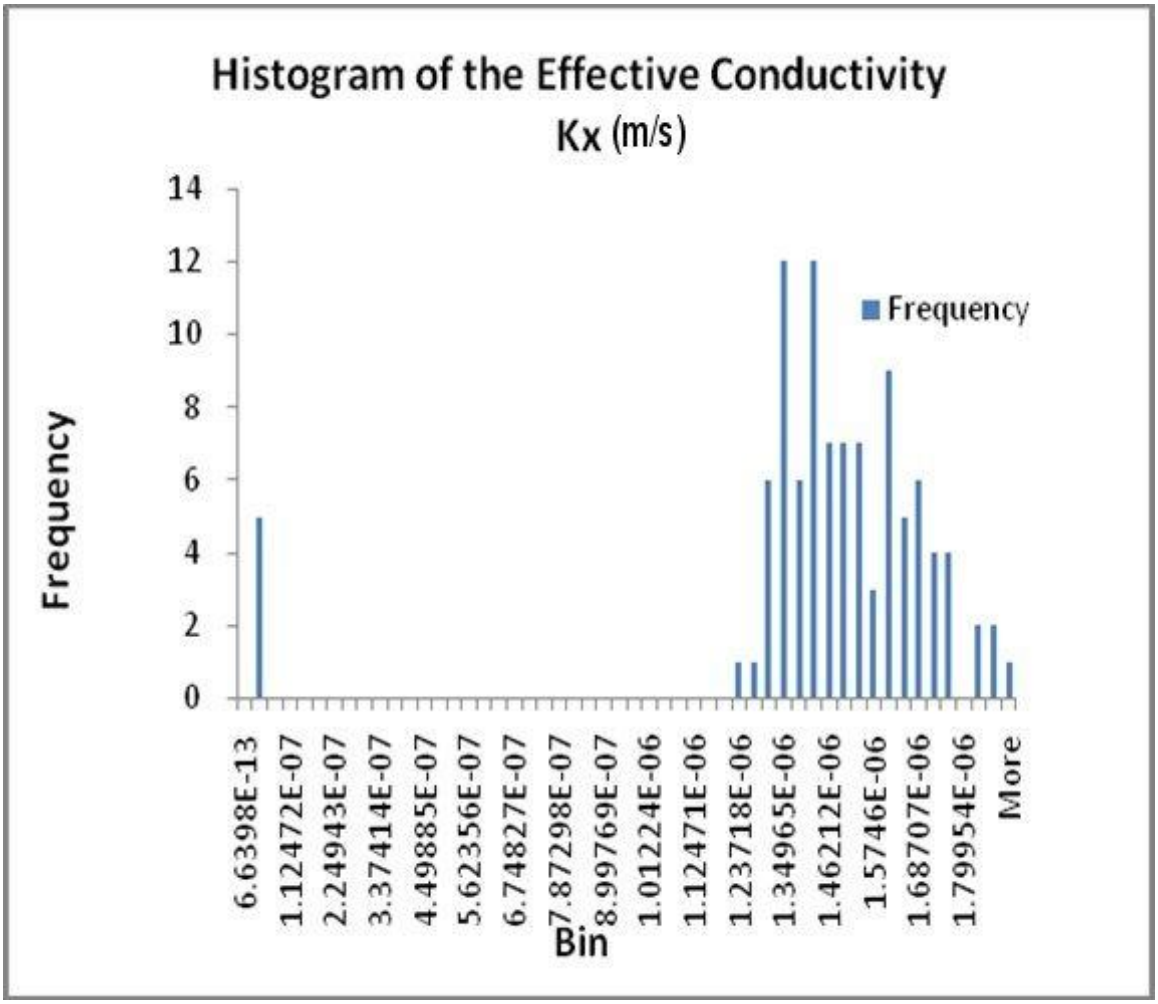

Figure 4.7: Histogram of the effective hydraulic conductivity Ky for the upscaled fine-grid model solution

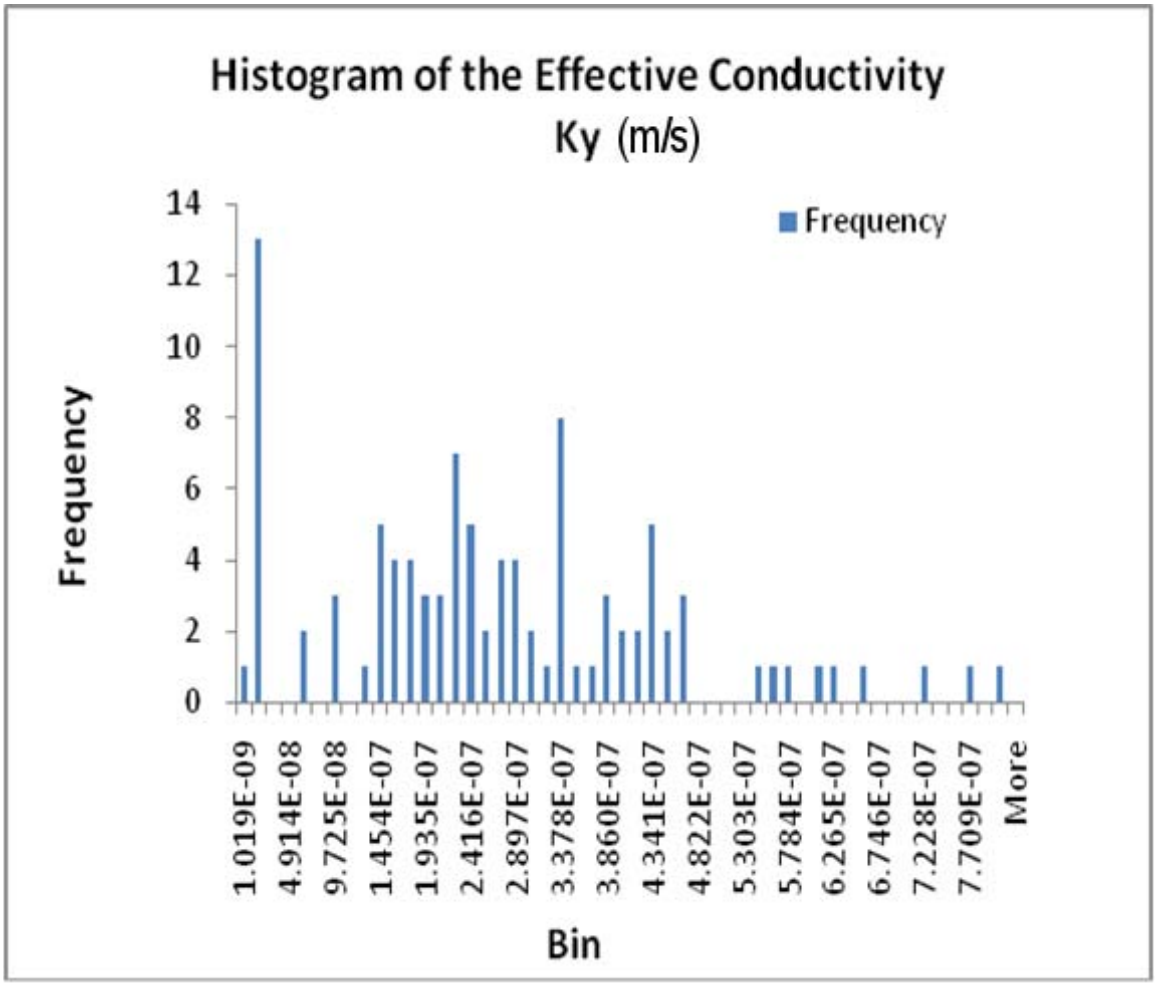

Figure 4.8: Histogram of the effective hydraulic conductivities Kz for the upscaled fine-grid model solution

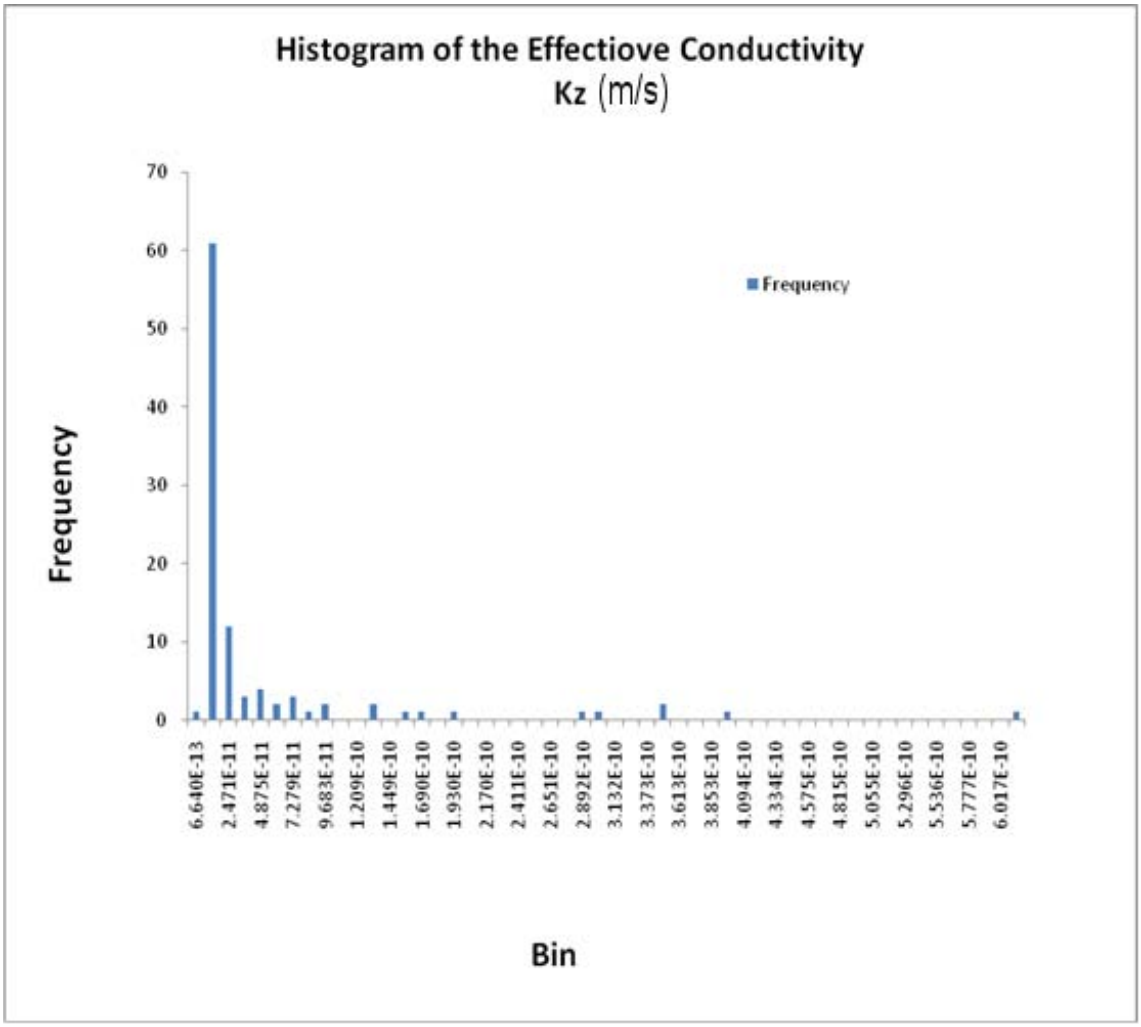

Five of the stochastic simulations were selected for transient flow simulation. These models were chosen to explore the role of connectivity in the determination of the effective hydraulic conductivity and to explore the character of pumping test response in Chapter 5. The simulations selected for transient flow were chosen to represent a range of effective hydraulic conductivities and were based on the model having a sand channel in the center part of the domain that could act as a pumping well location for the transient simulations. The effective conductivity of a model representing a ranking of P75 represents a value of a variable (hydraulic conductivity) below which 75 percent of observations fall. Higher ranked conductivities will have greater connectivity of channel sands and crevasse splays throughout the model domain. This connectivity may be due to vertically stacked channels, channel sand complexes laterally connected by crevasse splays, or substantially extensive crevasse splay facies throughout the model, possibly at a particular horizon representing a preferential pathway for flow. The selected models were based on the effective hydraulic conductivity parallel to the channel sands (Kx). The selected models for transient flow are Realization 6 (Rank:min), Realization 43 (Rank:max), Realization 46 (Rank:P68), Realization 48 (Rank:P90), and Realization 61 (Rank:P31).

Plan- and block-view images and cross sections were made of each of the selected realizations of the geomodel. Model images illustrate how the channel sand complexes are distributed both laterally and vertically within the model at varying stratigraphic levels and how they move vertically downward throughout the system. In many of the models it can be seen how the crevasse splays connect the channel sands together. In

some cases at certain stratigraphic depths channel sands do not exist and overbank deposits are the more common subsurface media. Figures 4.9 through 4.18 illustrate the variability in connectivity of permeable facies and hence the variability of the hydraulic response of the system. As the connectivity of the permeable facies increases the effective conductivity of the system will also increase. For example, as the connectivity of the crevasse splays increases thereby connecting channel sands within the y-plane, the effective conductivity Ky increases.

Figure 4.9 illustrates the distribution of channels in Realization 6 (Rank:min) at the top of the model and the lateral distribution of the channel sands (green) and connectivity by the crevasse splays (magenta) in a background matrix of overbank deposits (red). Figure 4.10 is a cross section of Realization 6 (Rank:min) and illustrates the connectivity between channel sands (green) by the crevasses splays (magenta) within the horizontal plane. The crevasse splays located in the upper half of the cross section laterally connect the sand channels together. There appears to be a lesser degree of connectivity between the channel sands in the lower half of the cross section.

Figure 4.11 is a geomodel of Realization 43 (Rank:max) illustrating the facies distribution. This geomodel illustrates the distribution of the channel sands (green) at depth and the vertical and lateral distribution of crevasse splays (magenta). Figure 4.12 is a 3-dimensional block geomodel of Realization 43. This geomodel illustrates channel sands and crevasse splays distribution on top and at the side. There appears to be a

greater concentration of channel sand facies in the lower portion of the model between the channel sands (green) and crevasse splays (magenta).

Figure 4.13 is a geomodel x-, y- and z-plane image of Realization 46 (Rank:P68). The geomodel illustrates how the crevasse splays (magenta) in the lower portion of the image surrounds the channel sand (green) and creates a lateral sheet of continuous hydraulic communication between facies. Figure 4.14 is a geomodel fence diagram of Realization 46 (Rank:P68). The diagram illustrates the distribution of channel sands (green) and crevasses splays (magenta) within the model. The upper portion of the model has very few crevasse splays compared to the lower portion. Where the crevasse splays (magenta) are present at a lower portion of the model would provide a preferential path for flow where the bulk of the permeability exists within the model.

Figure 4.15 is a geomodel illustration of the facies distribution in the x-, y-, and z-planes for Realization 48 (Rank: P90). This geomodel illustrates the permeable sand channels (green) in the upper portion of the model. Figure 4.16 is a geomodel cross section of Realization 48 (Rank: P90) in the x-, y-, and z-planes. This figure illustrates the prominent presence of overbank deposits (red) within the lower portion of the model where flow within the model would be restricted. At this stratigraphic level a pressure wave would not propagate very far in this portion of the model. Near the model boundary, in the upper portion of the model a large sand channel (green) can be seen which is laterally connected to a crevasse splay (magenta) which in turn is connected to a sand channel (green) on the right hand side of the image. Here, groundwater would be

able to move vertically downward through the vertically stacked channels (green) and then flow laterally through the crevasse splays (magenta) to other sand channels (green) within the system.

Figure 4.9: Realization 6 (Rank: min) – 3-dimensional Block Geomodel

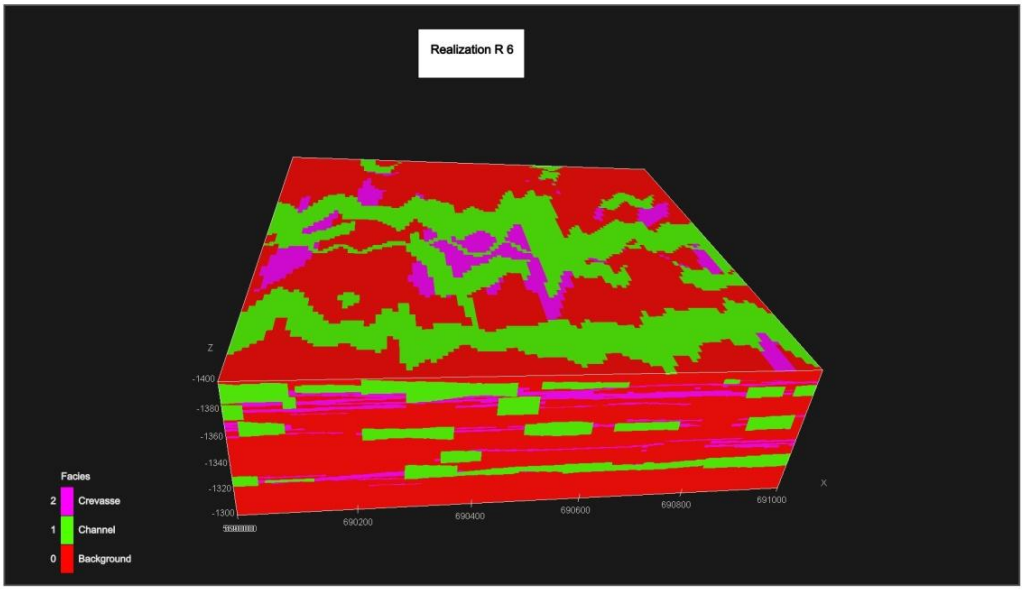

Figure 4.10: Realization 6 (Rank: min) – Geomodel Cross Section

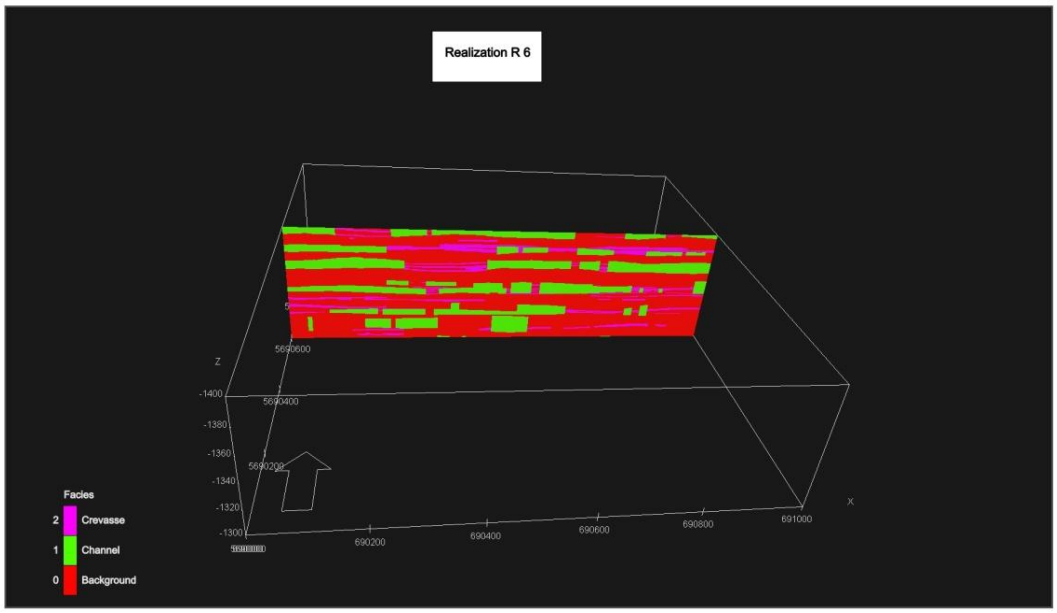

Figure 4.11: Realization 43 (Rank: max) – Geomodel of Facies Distribution

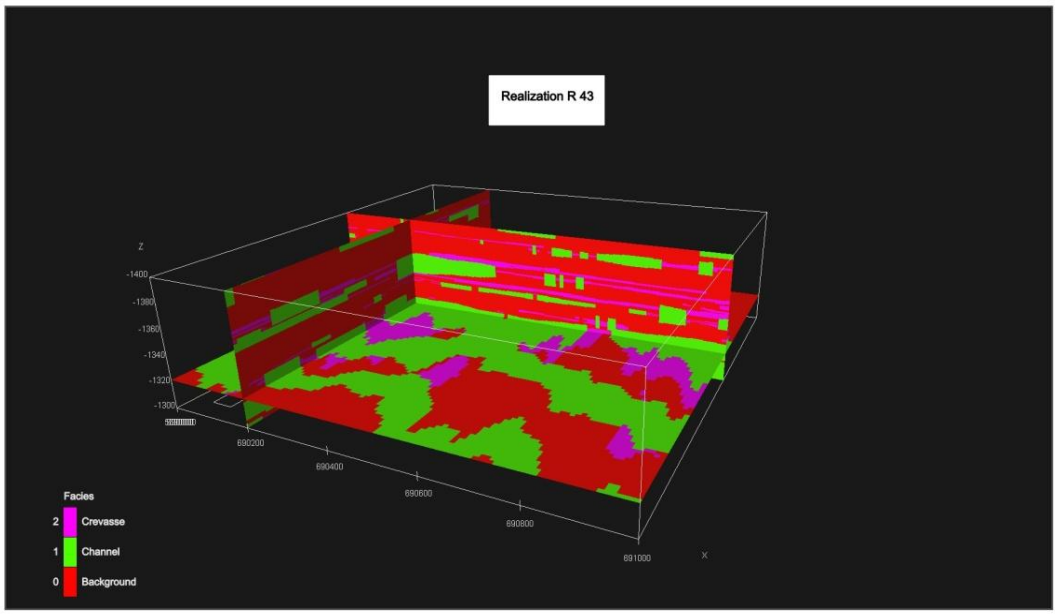

Figure 4.12: Realization 43 (Rank: max) – 3-dimensional Geomodel

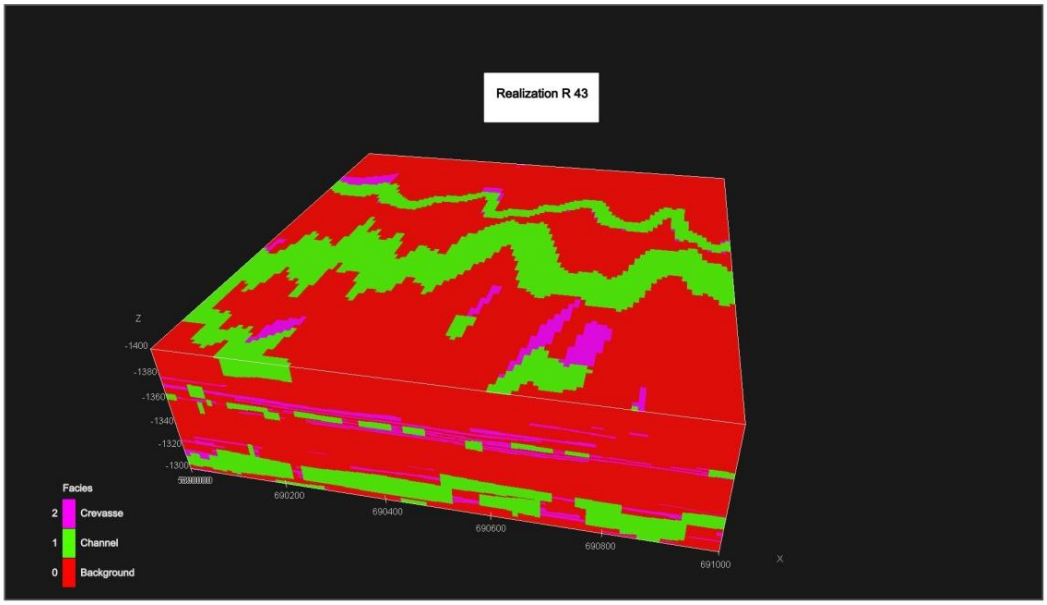

Figure 4.13: Realization 46 (Rank: P68) – Geomodel Illustrating the Facies Distribution

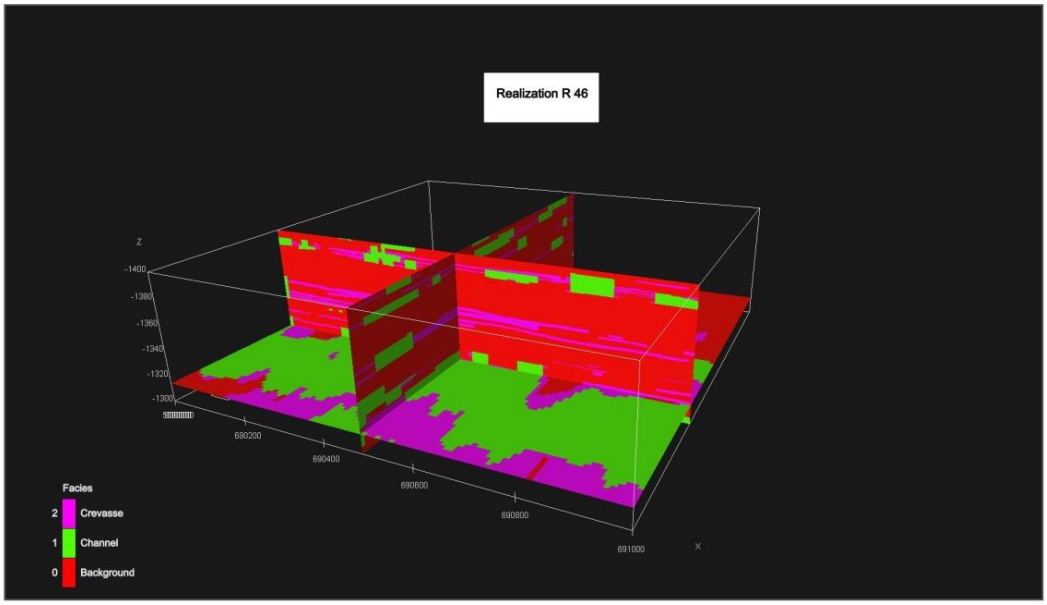

Figure 4.14: Realization 46 (Rank: P68) – Geomodel Illustrating the Facies Distribution in a Fence Diagram

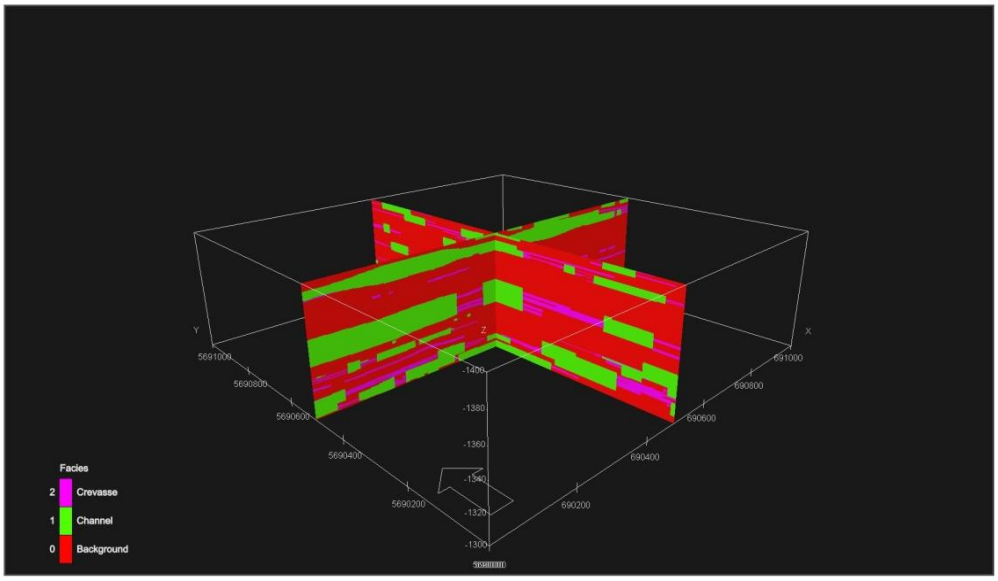

Figure 4.15: Realization 48 (Rank: P90) – Geomodel Illustrating the Facies Distribution in x-, y-, and z-planes

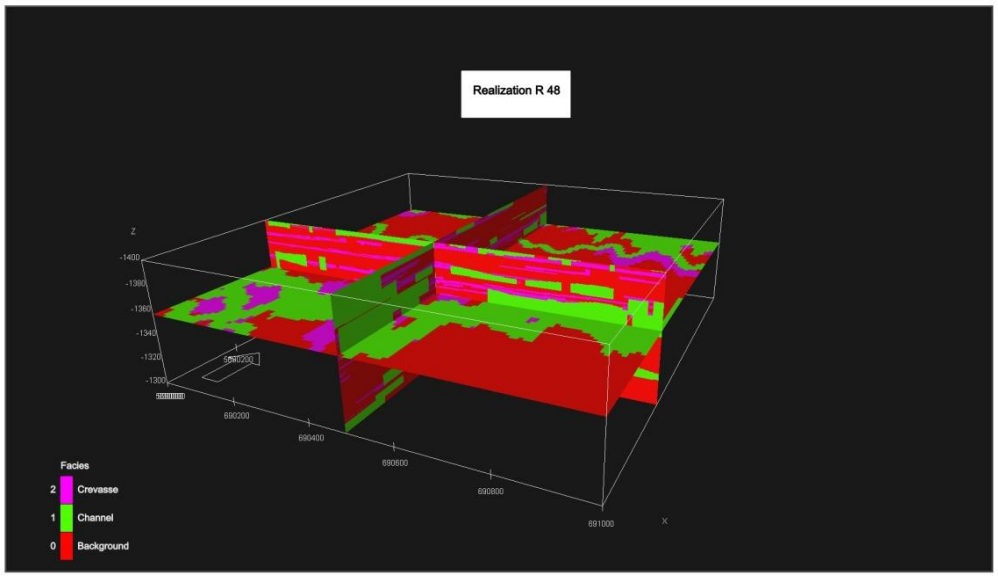

Figure 4.16: Realization 48 (Rank: P90) – Geomodel Illustrating the Facies Distribution in x-, y-, and z-planes

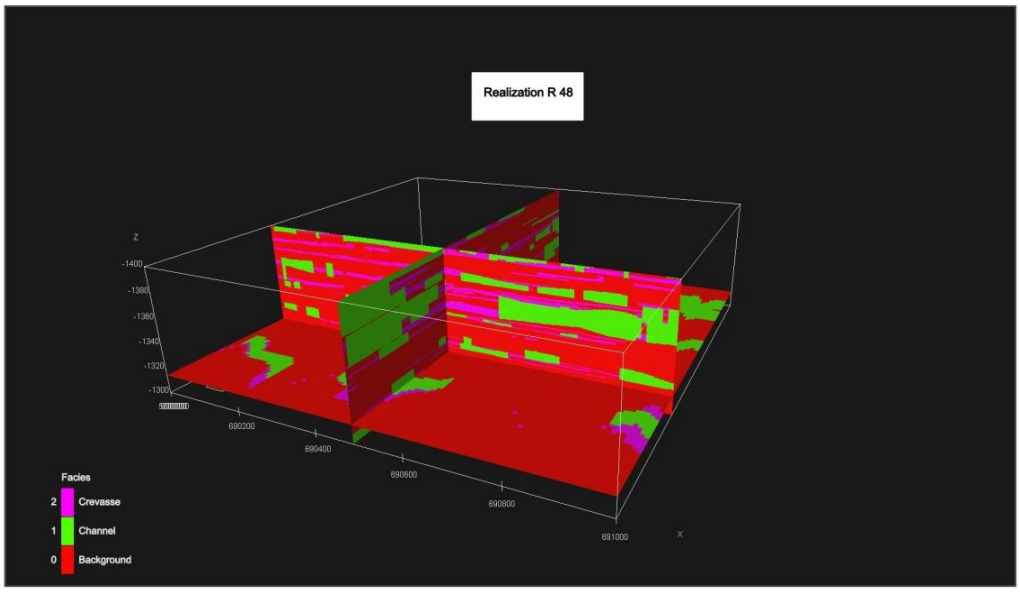

Figure 4.17 is a cross section of Realization 61 (Rank: P31) illustrating the facies distribution in the x-, y-, and z-planes. This image illustrates a large channel complex in the lower portion of the model resulting in a preferential pathway for greater flow parallel to Kx which would allow for lateral propagation of a pressure wave induced by pumping. Figure 4.18 is a fence diagram of Realization 61 (Rank: P31). The fence diagram illustrates a thick channel complex in the upper portion of the model where the pressure wave during a pumping test could propagate through the length of the model parallel to Kx. Recall that connectivity of the facies is variable and that the effective conductivity is variable. Therefore, the propagation and path of the pressure wave including the flow regimes that develop during transient conditions is a function of the distribution of permeability and connectivity of facies within the system.

Figure 4.17: Realization 61 (Rank: P31) – Geomodel Illustrating the Facies Distribution in x-, y-, and z-planes

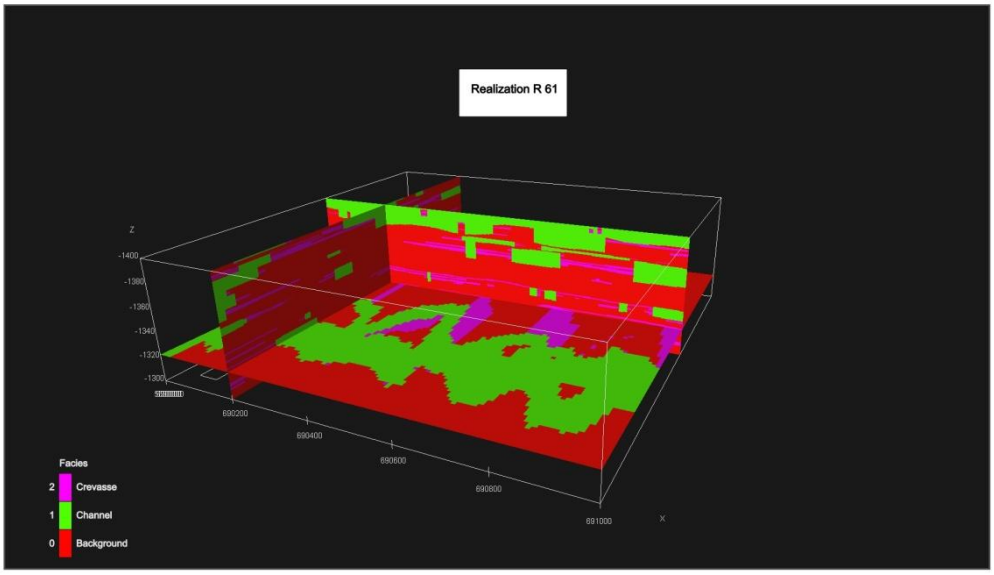

Figure 4.18: Realization 61(Rank: P31) – Geomodel Fence Diagram

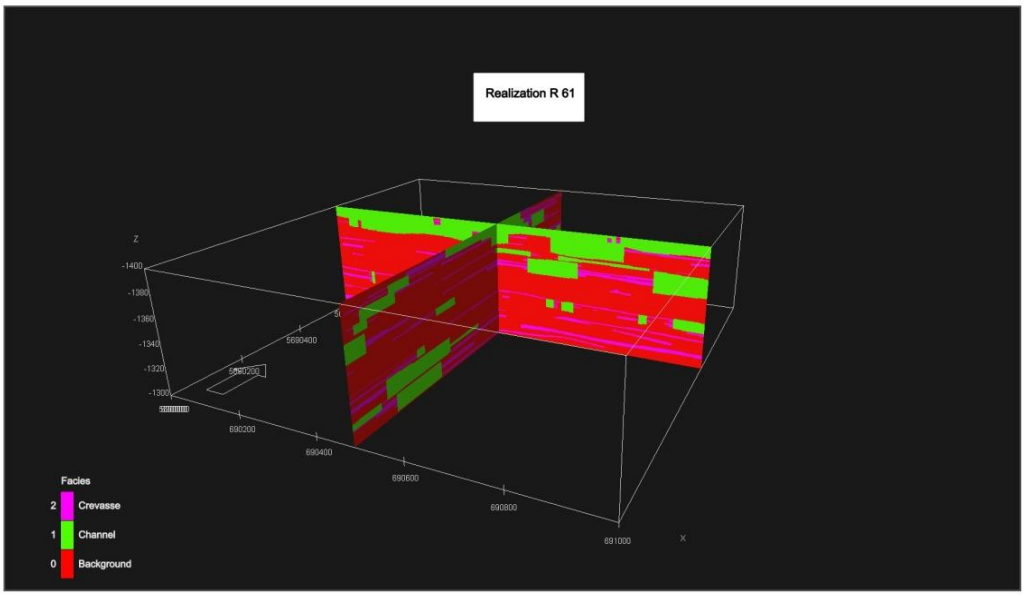

CHAPTER 5: TRANSIENT GROUNDWATER FLOW MODELING AND PRESSURE TRANSIENT ANALYSIS

The geometry of fluvial geological facies and the associated hydrostratigraphy and groundwater flow within these systems are very complex and difficult to characterize using standard industry practices and methodologies. Recall that current practices use traditional layer-cake geological models for flow and simplified hydrologic models for pressure transient analyses to estimate the aquifer parameters. The effect of heterogeneity and anisotropy on groundwater flow within these fluvial systems cannot be accounted for with these techniques. Field investigations involving interference testing where water is withdrawn from a production well at a known rate for a specified time and pressure response is monitored in an observation well may not provide any indication to connectivity, preferential flow paths, heterogeneity, and flow regimes leading to the introduction of errors in interpretation and subsequently tend to poorly predict long-term well yield.

We investigate the effects of heterogeneity by simulation of a pumping well, monitoring the system response using an observation well network and analyzing the pumping test data generated at the production well to estimate the aquifer parameters and to compare the response of the pressure and derivative curves to the flow response observed in the corresponding model. We also perform pressure transient analysis (PTA) using the hydrogeology industry standard software AQTESOLV and compare these results with those obtained by analyzing the same data using Kappa Engineering's PTA software Saphir. Saphir is an oil and gas industry standard program for performing PTA which

allows for custom curve fitting and is based on the Bourdet derivative as the main diagnostic tool which provides a means for identification of specific flow regimes which evolve during production.

In order to test the system performance under transient conditions a steady-state solution for each of the five realizations (R6 [Rank: min], R43 [Rank: max], R46 [Rank: P68], R48 [Rank: P90], and R61 [Rank: P31]) was first obtained for use as the transient models initial condition. The steady-state solution was modeled by assigning a first-type or Dirichlet boundary condition of equal head value along the x- and y- boundaries of the model. An equal value was assigned to each Dirichlet boundary condition in the model to create a solution with a constant head. By using a constant head across the model as our transient model's initial conditions, we only observe the effect of the pressure wave induced by the pumping on the system and the propagation of the wave as influenced by the distribution of the hydrofacies.

Flow simulations of a synthetic production well were conducted on the five realizations selected for transient simulation. The production well was placed near the center of the model domain (Figures 5.1 through 5.5) and the production zone in each of the wells was set in channel sands (green) with minor crevasse splay (magenta) or floodplain deposits (red). The figures illustrate the spatial variability of the permeable facies and their location in relation to the production well. Propagation of the pressure wave induced by abstraction of water from the production well will be primarily controlled by the

distribution of the most permeable hydrofacies. The wave will travel at a rate controlled by the formation diffusivity.

Figure 5.1: Realization 6 (Rank: min) – Production Well Placement within model domain. Magenta represents crevasse facies, green represents channel sand facies, and red represents background facies.

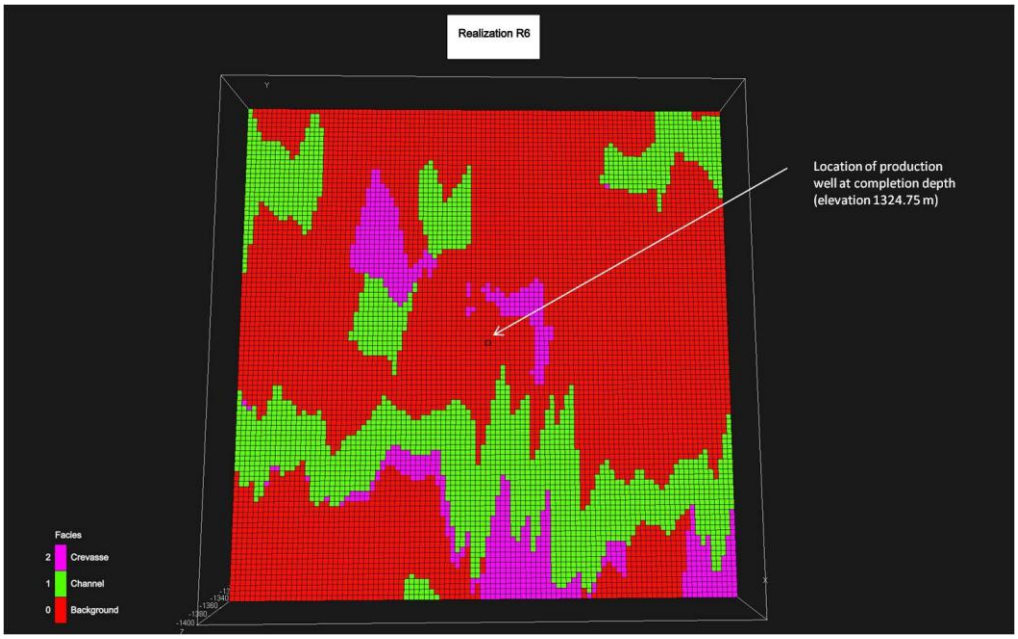

Figure 5.2: Realization 43 (Rank: max) – Production Well Placement within model domain. Magenta represents crevasse facies, green represents channel sand facies, and red represents background facies.

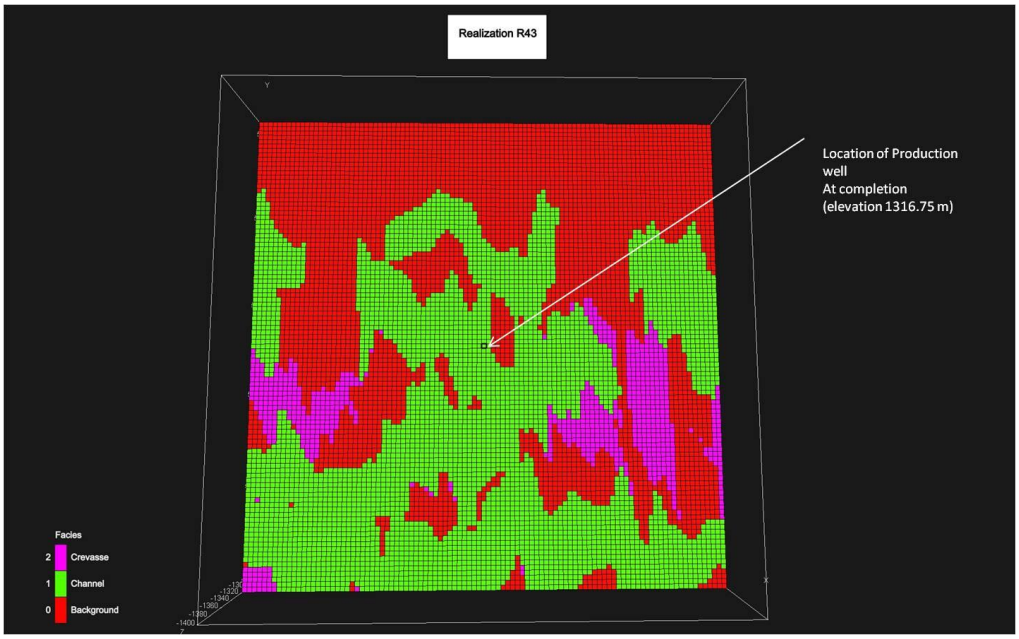

Figure 5.3: Realization 46 (Rank: P68) – Production Well Placement within model domain. Magenta represents crevasse facies, green represents channel sand facies, and red represents background facies.

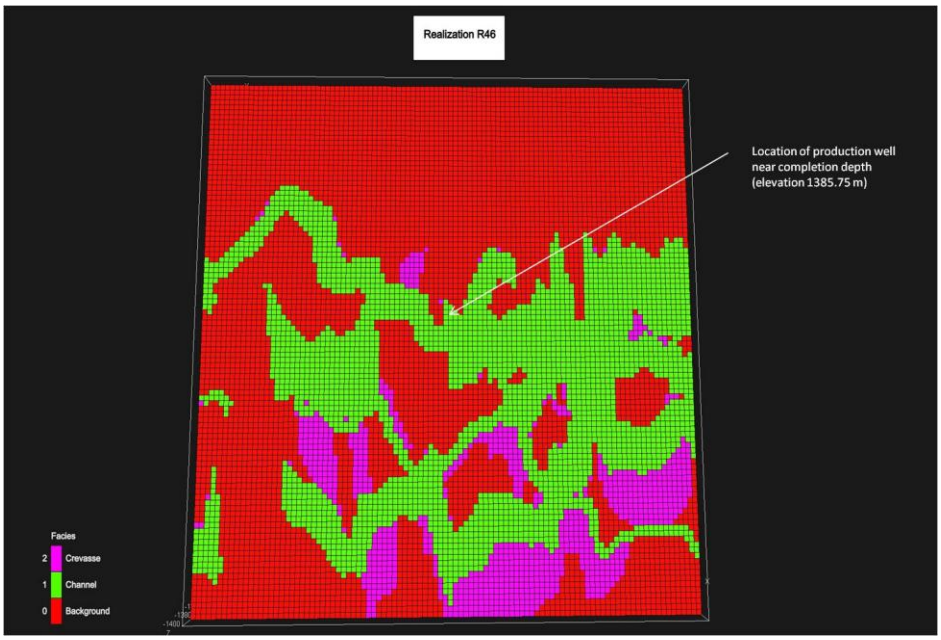

Figure 5.4: Realization 48 (Rank: P90) – Production Well Placement within model domain. Magenta represents crevasse facies, green represents channel sand facies, and red represents background facies.

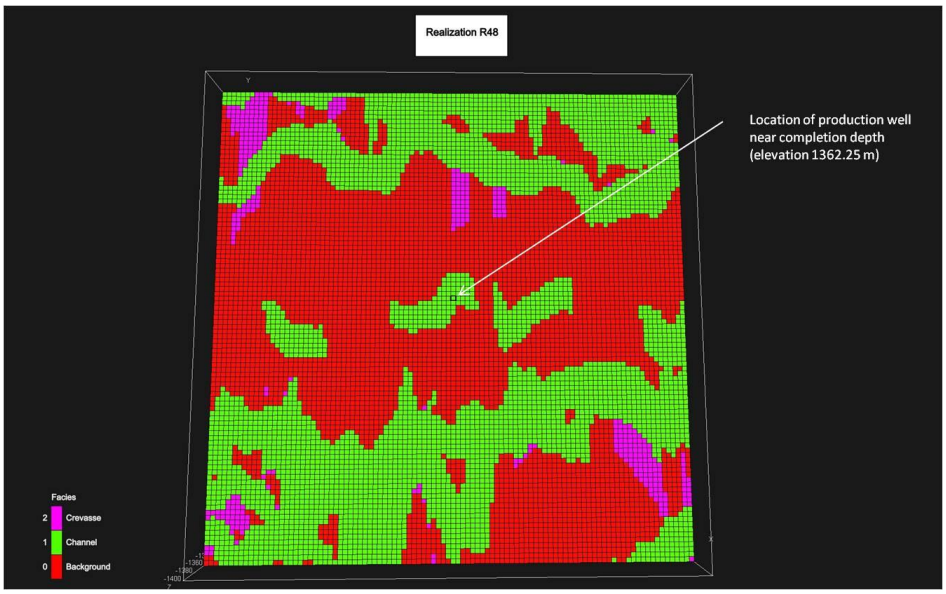

Figure 5.5: Realization 61 (Rank: P31) – Production Well Placement within model domain. Magenta represents crevasse facies, green represents channel sand facies, and red represents background facies.

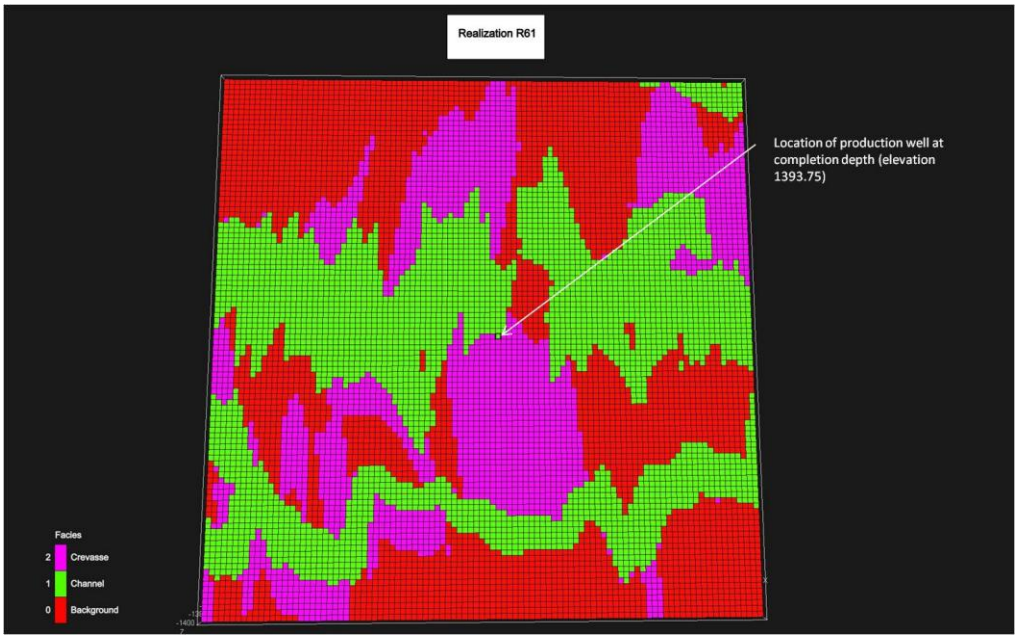

Modification of Boundaries

Due to the size of the model domain it is expected that the pressure wave induced from the production well will reach the model boundaries and subsequently these boundaries will influence the pressure response of the system observed in the production and observation wells. We want to minimize the effect of the model boundaries so that we only see the response of the system in the pressure and derivative curves during PTA. To accomplish this we assigned a leakance term (third type, Cauchy) along the x and y-boundaries.

This was accomplished by using an algorithm written in Matlab that searches through the hydraulic conductivity input file for each realization and identifies the elements located along the x-y boundaries of the model domain and reassigns a leakance value based on a user specified input value for ∂x, where ∂x is the distance from the x-boundary to a pressure point perpendicular to the boundary. First we select an initial value for ∂x. This is used as the initial input value for the algorithm. The algorithm then selects the hydraulic conductivity value K_x associated with each of the elements along the x-boundaries and assigns a value L_{Kx}, the leakance value along the x-boundaries, to each element based on the ratio between the hydraulic conductivity and the user specified distance ∂x as presented in equation 5.1.

$$\text{Leakance value for } L_{Kx} = \frac{K_x}{\partial_x} \qquad [5.1]$$

The equivalent distance ∂y, perpendicular to the y-boundary, can then be calculated from the 2-dimensional form of the flow equation of Darcy's Law for steady state flow through an anisotropic saturated porous medium presented in equation 5.2 (Freeze and Cherry 1979):

$$\frac{\partial}{\partial x}\left(K_x \frac{\partial h}{\partial x}\right) + \frac{\partial}{\partial y}\left(K_y \frac{\partial h}{\partial y}\right) = 0 \qquad [5.2]$$

$$K_x \frac{\partial^2}{\partial x^2} + K_y \frac{\partial^2}{\partial y^2} = 0 \qquad [5.3]$$

Equation 5.2 can be simplified to equation 5.3 and by assuming homogeneity to bring K out of the derivatives and rearranging this equation we can solve for ∂y which becomes the product of the user specified value for ∂x and the ratio between the square root of the horizontal hydraulic conductivity in the y-direction (K_y) and the horizontal hydraulic conductivity in the x-direction (K_x) as presented in the following equation 5.4.

$$\partial_y = \sqrt{\frac{K_y}{K_x}} \partial_x \qquad [5.4]$$

The leakance value L_{Ky}, for the each element along the y boundaries are then calculated by taking the ratio of the horizontal hydraulic conductivity in the y-direction K_y and the previously calculated distance ∂y as presented in the following equation 5.5.

$$\text{Leakance value } L_{Ky} = \frac{K_y}{\partial_y} \qquad [5.5]$$

Once the leakance values are calculated for the elements along the y-boundaries, these values are used to populate the associated boundary elements. Once all leakance values, L_{Kx} and L_{Ky}, have been assigned to the appropriate model boundaries, a 3-dimensional transient numerical simulation of the groundwater system is performed. From this

simulation, the travel time of the pressure wave is evaluated to determine the time it takes for the pressure wave to reach of the model boundaries. This process is continually repeated until there is no difference in travel times between simulations, thereby establishing a final value for ∂x and ∂y and associated leakance values. The effective conductivities, leakance values and distances are presented in Table 5.1.

Table 5.1: Summary of X-Y Leakance Boundary Values and Distances

Parameter	Realization 6	Realization 43	Realization 46	Realization 48	Realization 61
Effective Kx (m/s)	1.2×10^{-09}	1.9×10^{-06}	1.5×10^{-06}	1.7×10^{-06}	1.4×10^{-06}
Effective Ky (m/s)	4.3×10^{-07}	8.0×10^{-07}	2.2×10^{-07}	2.6×10^{-07}	3.3×10^{-07}
∂x (m)	100.00	100.00	100.00	100.00	100.00
∂y (m)	185.82	6.54	3.78	3.93	4.91
Leakance Kx (s^{-1})	1.2×10^{-11}	1.9×10^{-08}	1.5×10^{-08}	1.7×10^{-08}	1.4×10^{-08}
Leakance Ky (s^{-1})	2.3×10^{-09}	1.2×10^{07}	5.9×10^{-08}	6.7×10^{-08}	6.8×10^{-08}

Transient Model Development and Simulation

The purpose of the transient model is to evaluate production (pressure response to withdrawal of groundwater) and build-up (pressure response during recovery of the piezometric surface to static conditions) data from pumping tests conducted within a heterogeneous model domain, evaluate the aquifer system response, the presence of flow

regimes, the presence of boundary influence, and evaluate the applicability of current standard engineering practices and make recommendations for the improvement of characterizing heterogeneous systems. Furthermore, we want to compare drawdown and recovery curves to those obtained by Alberta Research Council (ARC) from pumping tests performed in the Paskapoo Formation in the early 1970's. During this time, the ARC conducted 122 pumping tests on wells completed within the Paskapoo Formation in the Edmonton area and obtained four general types of curves (Bibby 1977). The ARC noted that the curves did not conform to any theoretically predicted drawdown curve and was unable to explain the rationale for their shape.

Well logs obtained from the Alberta Environment Groundwater Information System (GIS) were reviewed to evaluate the average pumping rate used during pumping tests for wells completed within the Paskapoo Formation. Approximately 200 well logs were reviewed and based on the available data, it was determined that an average withdrawal rate of 46.5 m^3/d had been used during field pumping tests. Five of the one hundred realizations were selected for transient model simulations. Recall that these five realizations were selected based on effective conductivity and the presence of an appropriate permeable facies near the center of the model domain to allow for the pressure wave to propagate throughout the hydraulically conductive facies.

Each pumping test involved placement of a pumping or production well near the center of the model domain and monitoring the pressure response in the production well and an observation well network. Observation wells were placed throughout the model domain

and along all boundaries and within the channel sand and crevasse splay facies at locations and varying depths to monitor the transient response of the system. The coordinates for the pumping wells, withdrawal rates, and stratigraphic interval open to production for each of the five realizations are summarized in Table 5.2. Coordinates of the observation well network for each of the simulations and a plan view map of the distribution of the network is presented in Appendix B.

Each pumping test design consisted of a short-term test with a production period (i.e., groundwater withdrawal duration) of approximately 4 hours and a build-up (i.e., recovery) period of approximately 4 days. The long-term test was run with a production period of 15 days. The long-term modeling results were evaluated to determine when the pressure wave intersected the model boundaries. The period prior to intersection of the pressure wave with the model boundaries was used for PTA analysis and is assumed free of boundary interference which for this research is constrained by the model domain size. By analyzing the pressure data from the production well of each simulation prior to intersection of the pressure wave with the boundaries we avoid boundary influence and are then analyzing data representative of the aquifer system only. Both the short-term and long-term tests were run at a withdrawal rate of 46.5 m^3/d. Transient simulation details of the boundary conditions, pumping well location, rates, well radius, start times and output times are presented in Table 5.2.

Table 5.2: Transient Model Simulations

Parameter	Realization				
	6	**43**	**46**	**48**	**61**
Number of cells	420000	350000	430000	410000	350000
Initial (m)	43	43	43	43	43
Specified Head x-plane	43	43	43	43	43
Specified Head y-plane	43	43	43	43	43
Flow solver convergence criteria	1E-13	1E-13	1E-13	1E-13	1E-13
Pumping well (E) coordinates (UTM) (N)	690505 5690505	690495 5690505	690505 5690530	690505 5690545	690505 5690505
Pumping Well Interval (m)	1347.25 - 1342.75	1324.75 – 1316.75	1393.75 – 1385.25	1370.25 – 1362.25	1400.00 – 1393.75
Pumping Rate (m^3/d)	46.5	46.5	46.5	46.5	46.5
Pumping Well radius (m)	0.0762	0.0762	0.0762	0.0762	0.0762
Head Control (m)	0.5	0.5	0.5	0.5	0.5
Timestep Control					
Start Time (sec)	0.0	0.0	0.0	0.0	0.0
Initial Timestep (sec)	400	400	400	400	400
Timestep multiplier	1.2	1.2	1.2	1.2	1.2
Maximum Timestep (sec)	8000	8000	8000	8000	8000
End Time (day)	75	75	75	75	75
Output Times (day)	0.083	0.083	0.083	0.083	0.041
	0.17	0.17	0.17	0.17	0.08
	0.25	0.25	0.25	0.25	0.13
	0.37	0.50	0.37	0.35	0.17
	0.44	0.54	0.44	0.38	0.21

0.46	0.58	0.46	0.383	0.25
0.50	0.63	0.50	0.42	0.29
0.54	0.67	0.54	0.46	0.37
0.58	0.71	0.58	0.50	0.38
0.63	0.75	0.63	0.75	0.40
0.67	0.83	0.67	0.83	0.42
0.71	0.92	0.71	0.92	0.44
0.75	1.0	0.75	1.0	0.46
0.83	1.06	0.83	1.17	0.50
1	1.17	1	1.25	0.54
2	1.25	2	1.46	0.58
3	1.46	3	1.67	0.59
4	1.67	4	1.88	0.60
5	1.88	5	1.96	0.63
6	1.96	6	2	0.65
7	2	7	3	0.67
8	3	8	4	0.71
9	4	9	5	0.75
10	5	10	6	0.83
15	6	15	7	1
20	7	20	8	2
25	8	25	9	3
50	9	50	10	4
75	10	75	15	5
	15		20	6
	20		25	7
	25		50	8

		50 75		75	9 10
Number of observation wells	74	59	62	64	66

The pumping well coordinates listed in Table 5.2 are based on a UTM format where the first number listed (i.e., 690505) represents the Easting coordinate and the second number listed (i.e., 5690505) represents the Northing coordinate.

HydroGeoSphere can modify time step values as the solution proceeds, based on the transient behaviour of the system. The modeling parameter "Head Control" can be adjusted in the HydroGeoSphere input file. This parameter was used to designate the maximum allowed absolute change in nodal head during any time step.

Pressure Transient Analysis Background

To be able to make decisions related to reservoir production and management the deliverability, properties, and size of the reservoir need to be known (Horne 2005). Well test analysis provides a tool to accomplish this. Because the petroleum industry has advanced the science behind pressure transient analysis, the following discussion presents a summary of the theory behind pressure transient analysis from a petroleum reservoir perspective.

Pressure Transient Analysis (PTA), originally known as well test interpretation, uses the production or build rates from the tested wells and pressure response from nearby

observation wells and pressure responses from down hole measurements at the production well. PTA methods focus on evaluating specific flow regimes where both well productivity and the main reservoir properties can be determined.

Using well test analyses we can characterize the ability of the fluid to flow through the reservoir and to the well by estimating conductivity, transmissivity, initial pressures, production potential, and boundaries (distance, size, and shape). This way we develop a description of the reservoir. Since the reservoir is large the estimated parameters are average values (Bourdet 2002, Chaudhry 2004). A reservoir pressure indicates the reservoir's potential energy and its evolution allows us to forecast the production lifetime of the reservoir. Well test interpretation allows us to infer distant reservoir pressures from near wellbore measured pressures (Bourdet 2002, Horne 2005). By using interpretation models we can characterize the reservoir to help develop a production plan.

Production Test

During a production or drawdown well test, a transient pressure response is created by a temporary change in the production rate. The pressure transient is considered to be the response of the system to a specific flow rate history. Prior to the test the well is static, stable and opened to flow. The flow rate, which is supposed to be constant, is measured while the pressure of the reservoir is recorded. Both the flow rate and pressure are interdependent and are governed by the reservoir characteristics. Ideally, the well should be producing at constant rate but in practice, this is difficult to achieve and drawdown pressure can be erratic (Bourdet 2002, Chaudhry2004, Horne 2005). The analysis of

flowing periods (drawdown) is frequently difficult and inaccurate. For this reason it has become a standard practice to analyze pressure data from a build-up or recovery test (Bourdet 2002).

A drawdown test can be difficult to achieve since it is very difficult to make the flow rate of the well constant and the well condition may not initially be either static or stable especially if it was recently drilled (Horne 2005).

Build-Up Test

During a build-up or recovery test there is an increase in bottom hole pressure after shut-in of the well. Bourdet (2002) reports that before the test, the well must have been flowing long enough to reach a stabilized rate. During the shut-in period, the flow rate is accurately controlled (withdrawal rate is zero). The advantage of a build-up test is that the constant flow rate condition is more easily achieved. A disadvantage of a build-up test includes difficulty in achieving the constant rate production prior to the shut in. (Bourdet 2002, Horne 2005).

Interpretation Models

The models used in well test analysis control the behaviour (homogeneous, heterogeneous, bounded or infinite) of the simulated pressure response. Interpretation models are often different from the geological models due to the averaging of the reservoir properties. Layered reservoirs frequently show a homogeneous behaviour during tests. Analytical solutions or numerical models are used to generate pressure

responses to the specific production rate history of the well, and the model parameters are adjusted until the model behaviour output is similar to the measured behaviour of the system (Bourdet 2002). Where reservoir behaviour displays more than just the infinite acting radial flow regime several different models may be applicable to describe the test pressure response or behaviour of the system. For example, a system with channels which displays linear flow can be described by a reservoir model with a leaky fault or possibly parallel faults even though the system has no faults.

Flow Regimes

Different flow behaviours are usually classified in terms of rate of change of pressure with respect to time. Transient responses are observed before constant pressure or closed boundary effects are reached. The wellbore pressure transient reflects the pressure transmission in the reservoir. The pressure response reflects reservoir conditions further away from the wellbore as the test proceeds with time. In the late stages of the well testing the pressure response is affected by the influence of boundaries. Prior to this the pressure response does not see the reservoir boundaries and the response typically indicates a reservoir of infinite extent. The time between early wellbore response and late time boundary response is known as the infinite acting period. Modern well test interpretation models are capable of identifying several different flow types during the infinite acting period the most common is radial flow. Infinite acting radial flow is the basis of many well test interpretations techniques. The pressure variation with time is a function of the well geometry and the reservoir properties (Bourdet 2002, Horne 2005).

A limited number of flow geometries produce characteristic pressure behaviours (i.e., radial, linear, bi-linear, spherical). For each flow regime the pressure follows a well-defined time function. A complete well response is defined as a sequence of flow regimes. By identification of the pressure behaviours present in the response, the chronology and time limits of the different flow regimes are established (Bourdet 2002).

Derivative Analysis

In 1983, the Bourdet derivative, the slope of the semi-log plot displayed on the log-log plot added additional diagnostic capability to the methodology. Bourdet (2002) reports that the semi-log plot is a plot of the bottom hole pressure, plotted on the y-axis, versus the logarithm of time, plotted on the x-axis. This plot follows a straight line when all wellbore storage transitional effects are finished. The slope of the semi-log straight line is used to estimate the permeability thickness product and the skin coefficient (S) is estimated from the location of the straight line along the y-axis. The derivative plot represents the rate of change in the pressure response of the reservoir and can be used to identify flow regimes such as wellbore storage, transitional regimes and infinite acting radial flow when the reservoir is acting as though it is of infinite extent. Discussion of flow regimes is deferred to later in this section. To emphasize the radial flow regime the derivative is taken with respect to the logarithm of time. When infinite acting radial flow is established, the derivative becomes constant. Once the derivative stabilization is defined the wellbore storage coefficient and skin (i.e., a flow restriction at the interface between the reservoir and wellbore caused by drilling and mud infiltration into the sandface) can be evaluated (Bourdet 2002).

Mathematical models are used to match the measured pressure response and take into account the complete pressure and flow history thereby generating a corresponding model that matches the actual test history. The models are diagnosed through pattern recognition of the different flow regimes present in a response and by using the Bourdet derivative (Houzé et al 2008).

Pressure transient analysis was performed using Kappa Engineering's Saphir which includes the evaluation of the pressure and derivative curves. Saphir uses a methodology based on the Bourdet derivative as the main diagnostic tool which matches the measured data to the model taking into account the detailed production history and consideration of any flow regimes observed during the testing. Detailed information on pressure transient analysis theory is given by Bourdet (2002), Horne (2005), and Chaudhry (2004).

Pressure Transient Analysis Methodology

Two PTA methodologies were used in the analysis of the pumping test data. These methodologies are considered standard practice as described in Bourdet (2002) and Alberta Environment (2003) and are a) Hydrogeology, and b) Reservoir Engineering. These methodologies take into account slightly different approaches. The Hydrogeology methodology uses AQTESOLV for the pressure transient analysis and assumes a homogenous isotropic system, application of the Theis model and uses the drawdown (production) period of the pumping test data. Only the pressure curve is used when analyzing the data. Both wellbore storage and skin are ignored.

The Reservoir Engineering methodology uses Saphir for the analysis and considers the buildup (recovery) data only. This methodology includes use of a wellbore storage and skin model and relies on the derivative curve to indicate the appropriate flow regimes. Numerous reservoir models were used to analyze the pressure and derivative curves and the final reservoir and boundary models were selected based on a "best-fit" approach to these curves.

Pressure Transient Analysis and Evaluation of Long-Term Safe Yield

For the purpose of evaluating the pressure response of each realization, only the long-term modeling results were used in PTA. Because time is plotted on a logarithmic scale in PTA the difference between a 4 hour pumping test and an 8.8 or 15 hour pumping test is minimal and little value is achieved by analyzing both. Because the long-term (8.8 to 15 hours) 3-dimensional modeling results illustrated the pressure wave at its maximum extent within the model domain, the long-term test results were used in evaluating the pressure response in PTA. Furthermore, the long-term 3-dimensional modeling results also contained the well developed flow regimes in comparison to the short-term (4 hour) 3-dimensional modeling results.

Pressure transient analysis of the pumping test data and review of the pressure wave response at observation wells located along the boundaries indicated that the pressure wave was reaching the model boundaries between 8.8 hours to 15 hours and that pressure response of the system was influenced by boundary interference. This could be seen in the pressure transient analysis where the derivative curve drops or decreases as the

pressure wave intersects the boundary. This can be interpreted as a reduction in permeability or closed system. The effects of the model boundary were removed from the analysis by "clipping" or deleting the pressure response data after the boundary was intersected. This was done in Saphir by modifying the production rate history so that the production rate ceased at a time just before when the boundary would have been observed and in AQTESOLV by deleting the pressure response data at a time just before the specific realization's boundary intersection. The pressure transient analysis was then performed by applying the Theis model using AQTESOLV or by fitting the data with a "best-fit" custom curve using Saphir. The resulting conductivity values were then used to compare the safe long-term yield approximated by the Q_{20} procedure and a more complex model that considers interior boundaries. There is an inherent uncertainty associated with estimating a long-term 20 year yield based on reservoir parameters established from the evaluation of data obtained over short time period.

Pumping Tests and Pressure Transient Analysis Results

Realization 6 (Rank: min) Model Results

Realization 6 is the model domain with the least effective hydraulic conductivity parallel to the channel sands (Kx) of all 100 realizations. This implies the least lateral and vertical connectivity between the hydraulically conductive facies (sands and crevasse splays). The lateral and vertical distribution of the facies can be seen in Figures 4.9 and 4.10.

Multiple flow regimes are observed in both the short-term (4 hour) (Figure 5.6) and long-term (Realization 6 – 12 hours) (Figure 5.7) modeling results. The long-term tests allowed for the pressure wave to propagate further within the model domain through permeable facies which resulted in the improved development of flow regimes over that of the short-term (4 hour) modeling tests. We only use the long-term results for PTA.

Multiple flow regimes are observed at different stratigraphic levels within the model. Channelized flow occurs at depths ranging from 37 to 46 m which is coincident with the channel sands that occur at these depths (Figures 5.6 and 5.7). Figure 5.7 illustrates channel flow is occurring at a stratigraphic level of 1360.5 m (39.5 m depth) or 17.75 m above the pumping/discharge point of the production well. The sharp contrasting boundaries between the channels and overbank deposits are apparent. An irregularly shaped pressure wave extends laterally outward from the pumping well at depths ranging from 49 to 57 m (Figure 5.8). In Figure 5.8 it appears that there may be a component of radial flow near the center of the pressure wave, however, we also see the edges of the pressure wave intersecting the boundary between the channel sand and overbank deposits as seen in Figure 5.6. When calculating the radius of influence of a pumping well at a given flow rate, the mathematical model used to determine this value assumes homogeneity and isotropy and subsequently equal radial flow in all directions. This figure illustrates that the spread of the pressure wave is not equal in all directions since connectivity and permeability is not equal in all directions. Therefore, determining radial influence in non-ideal system can lead to erroneous values or assumptions. The extent and propagation of the wave is controlled by the formation diffusivity and the lateral

connectivity of the sands and crevasse splays. Figure 5.9 illustrates the distribution of the permeable facies at a depth of 51 m. By comparing the pressure wave distribution from Figure 5.8 to the distribution of the permeable facies in Figure 5.9, it can be seen that the wave forms the outline of the facies distribution around the production well.

The extent of the pressure wave can be seen in cross section to have been confined to the channel sands and any connecting crevasse splays. Figure 5.10 illustrates the distribution of the pressure wave in cross section. The edges of the pressure wave from the previous image can be matched up with the sharp contrasting boundaries between the sands and overbank deposits. Figures 5.11 and 5.12 illustrate the hydraulic conductivity distribution and the pressure wave distribution. It can be seen that the pressure wave flows within the channel sands. Figure 5.10 illustrates the pressure wave distribution throughout the channels sands at varying distances from the well at different stratigraphic levels where different flow regimes exist at the same time. Figure 5.11 illustrates the higher permeability zones of the channel sands (red and yellow) versus the lower permeability of the overbank deposits (blue). Here we would expect the pressure wave to propagate through the permeable zones of the sands as can be seen in the center of the cross section. Figure 5.12 illustrates the extent to which the pressure wave has propagated through the channel sands in cross section. It is evident that propagation is variable as connectivity and distribution of the hydrofacies is variable. It can be seen that the pressure wave (yellow) has extended through the channel sands that are present in the middle of the model as seen in the previous image.

Figure 5.6: Realization 6 early time (4 hours) results of pressure wave at 40 m. Pumping interval at 52.75 m to 57.25 m depth

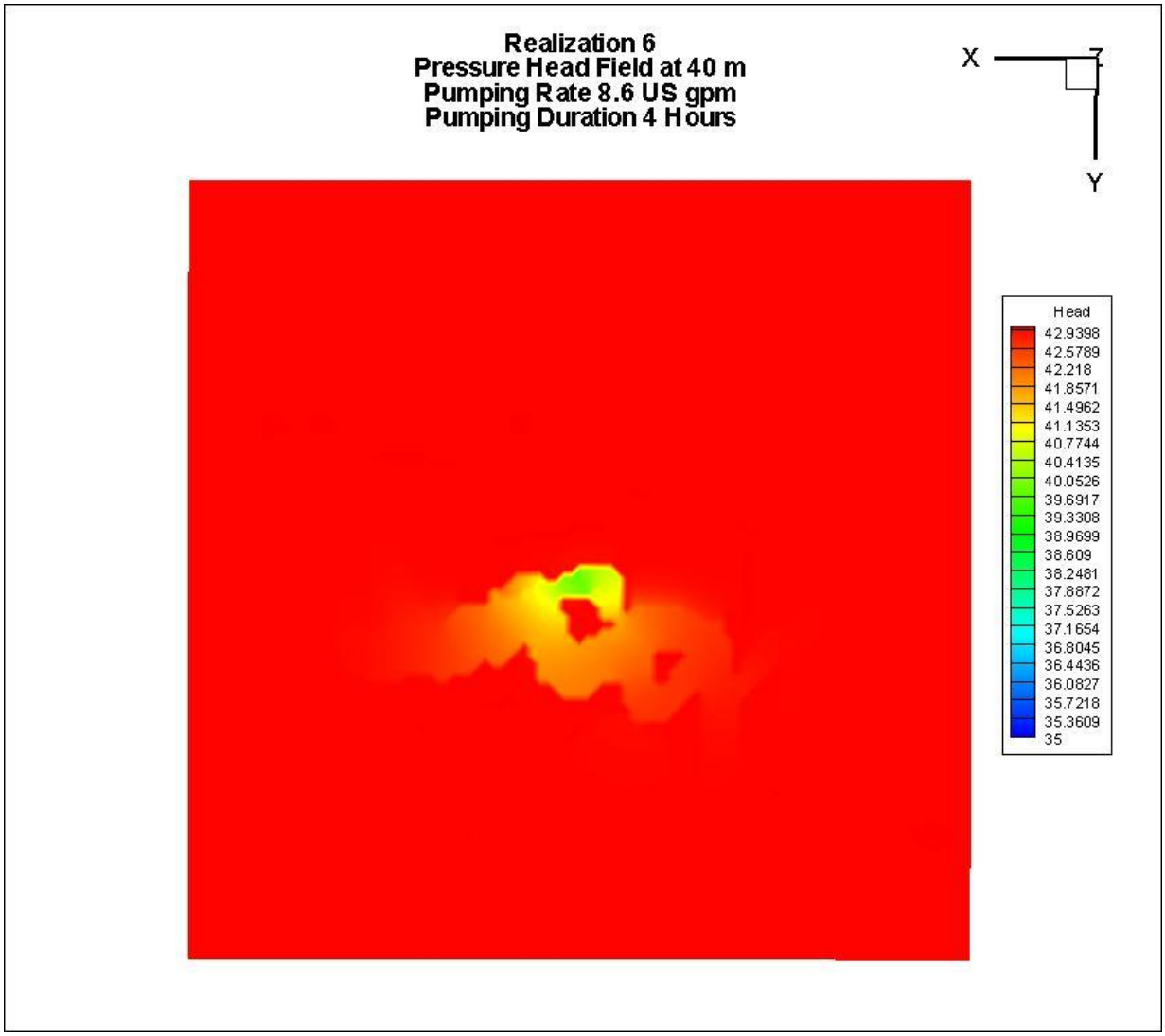

Figure 5.7: Realization 6 results after 12 hours of pumping at 39.5 m. Pumping interval at 52.75 m to 57.25 m depth

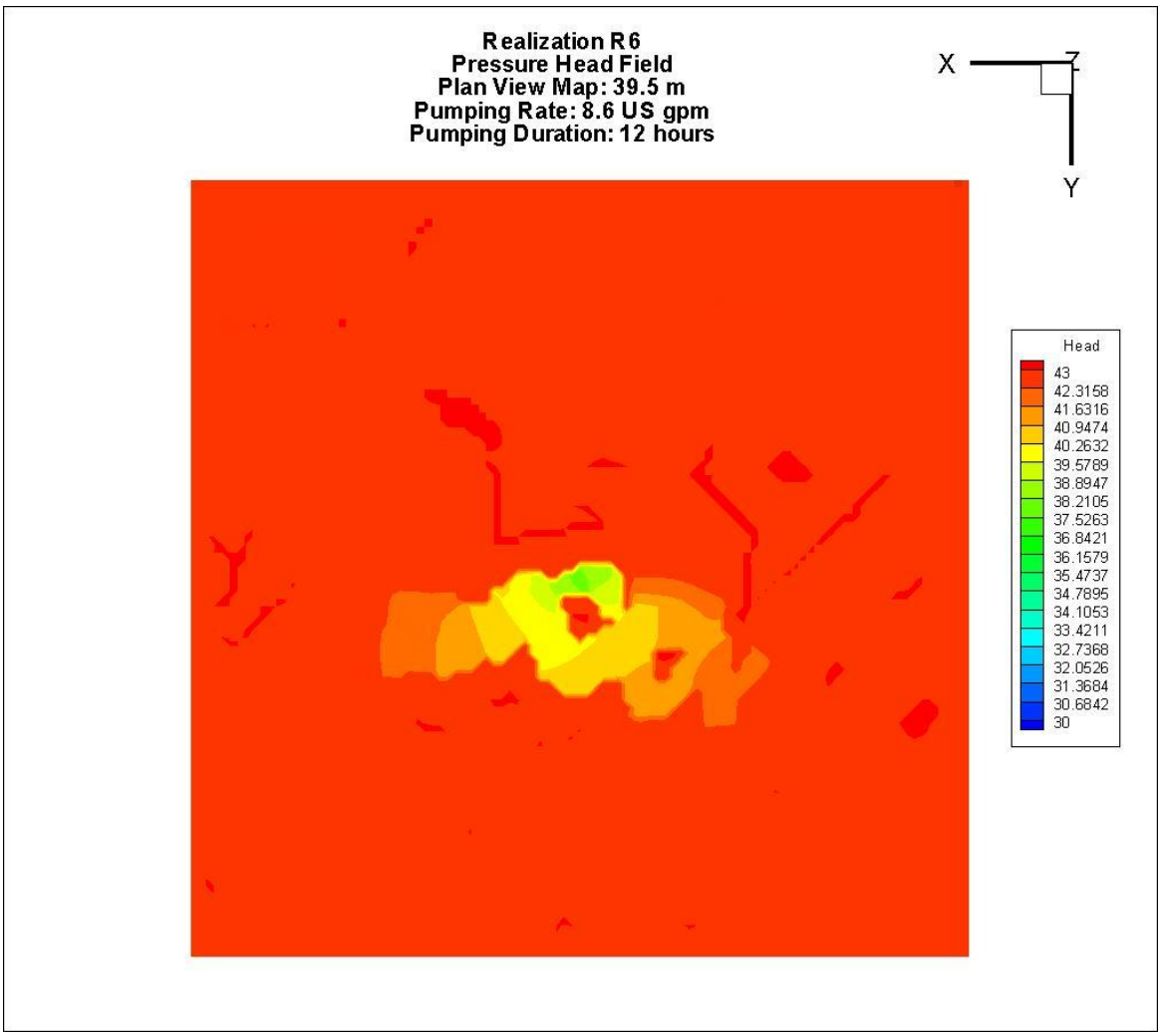

Figure 5.8: Realization 6 Pressure Head Field illustrating a very irregular pressure wave shape. Pumping interval at 52.75 m to 57.25 m depth

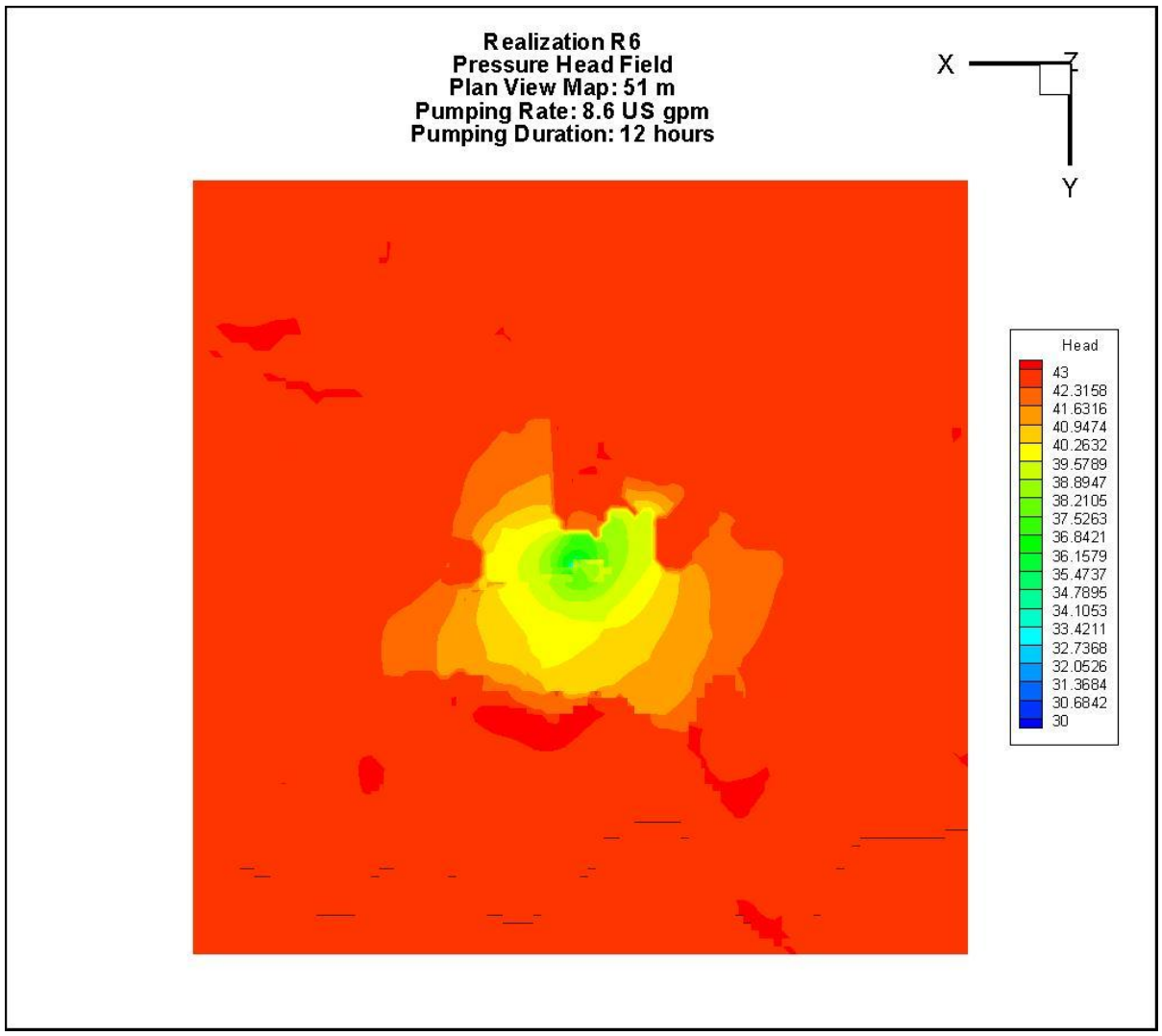

Figure 5.9: Realization 6 Hydraulic conductivity field illustrating facies distribution

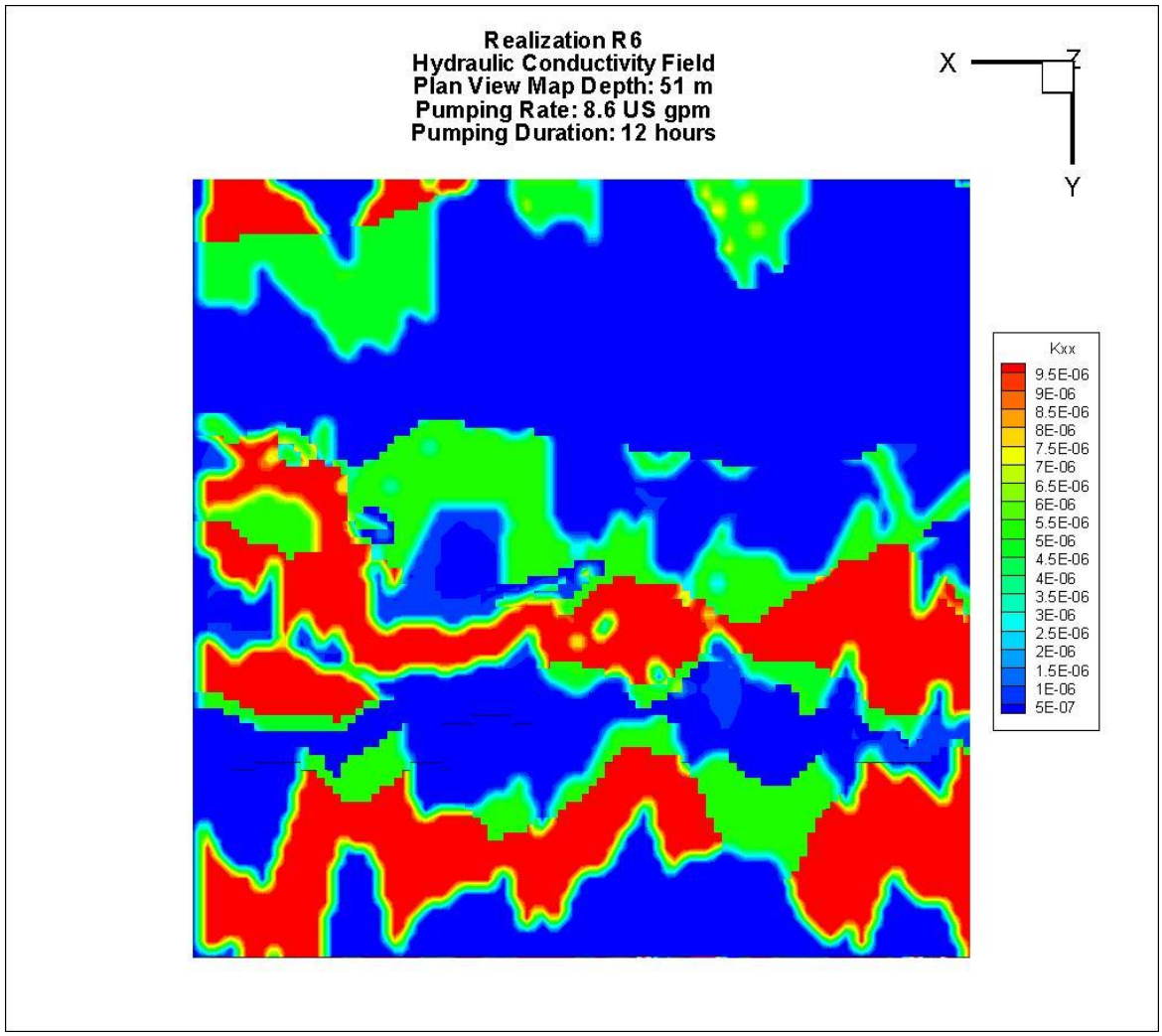

Figure 5.10: Realization 6 Pressure Head Field Cross Section

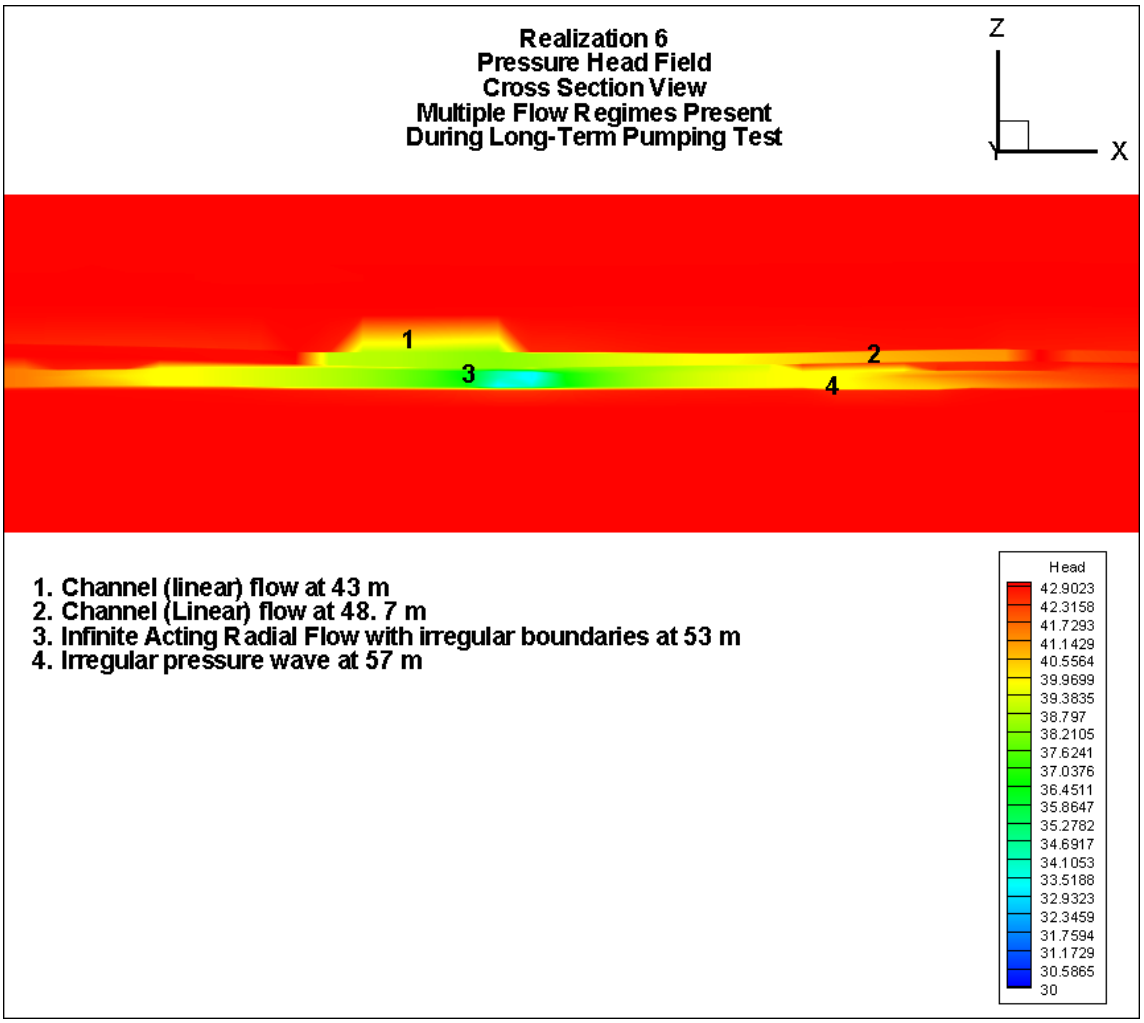

Figure 5.10 illustrates the different flow regimes along cross section at Y = 5690500 m after 12 hours of pumping. Because of the variability in the distribution of the hydrofacies along the x-y plane and along the z-plane several different flow regimes will exist.

Figure 5.11: Realization 6 hydraulic conductivity field cross section

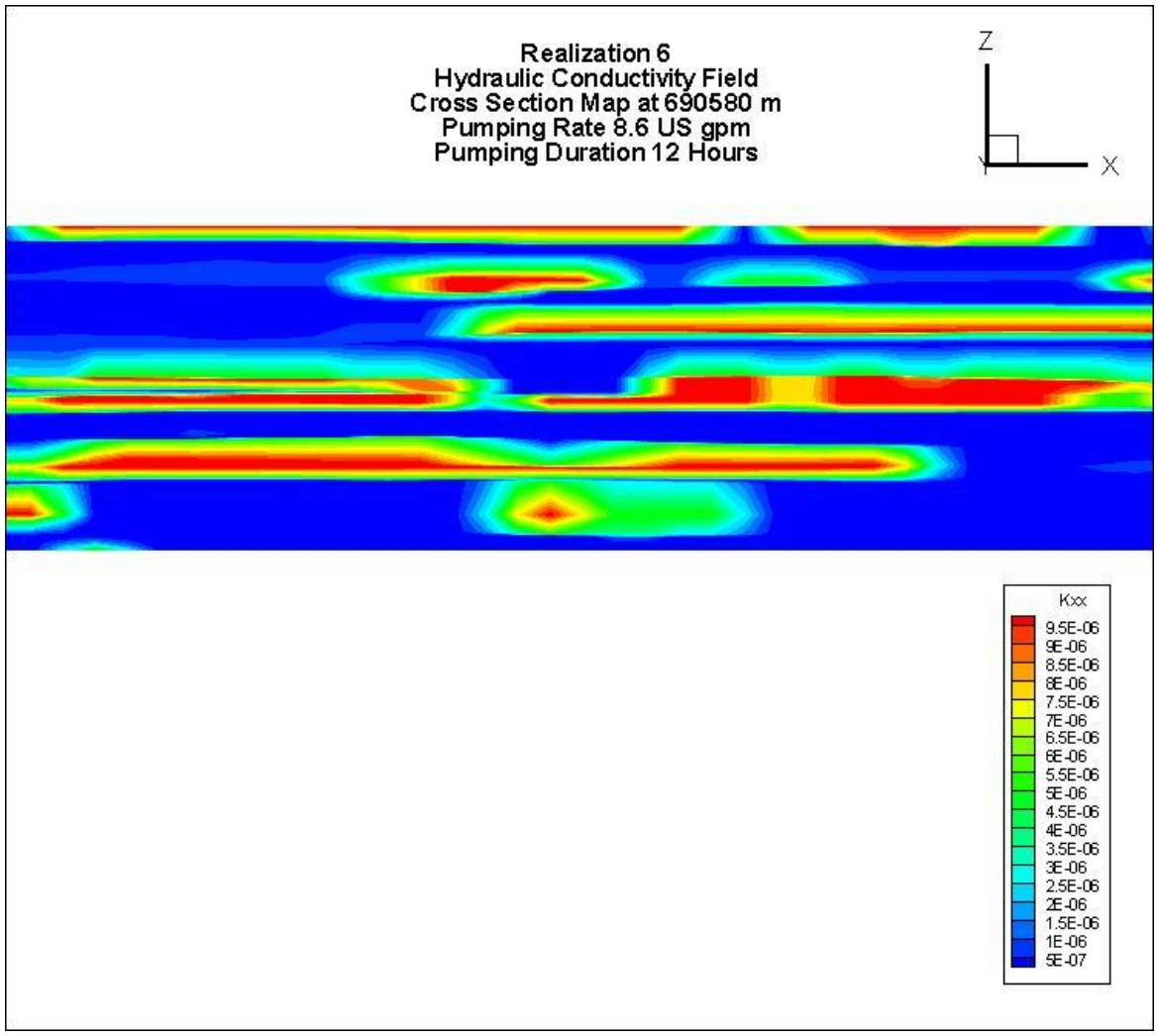

.

Figure 5.12: Realization 6 pressure head field cross section illustrating extent of pressure wave

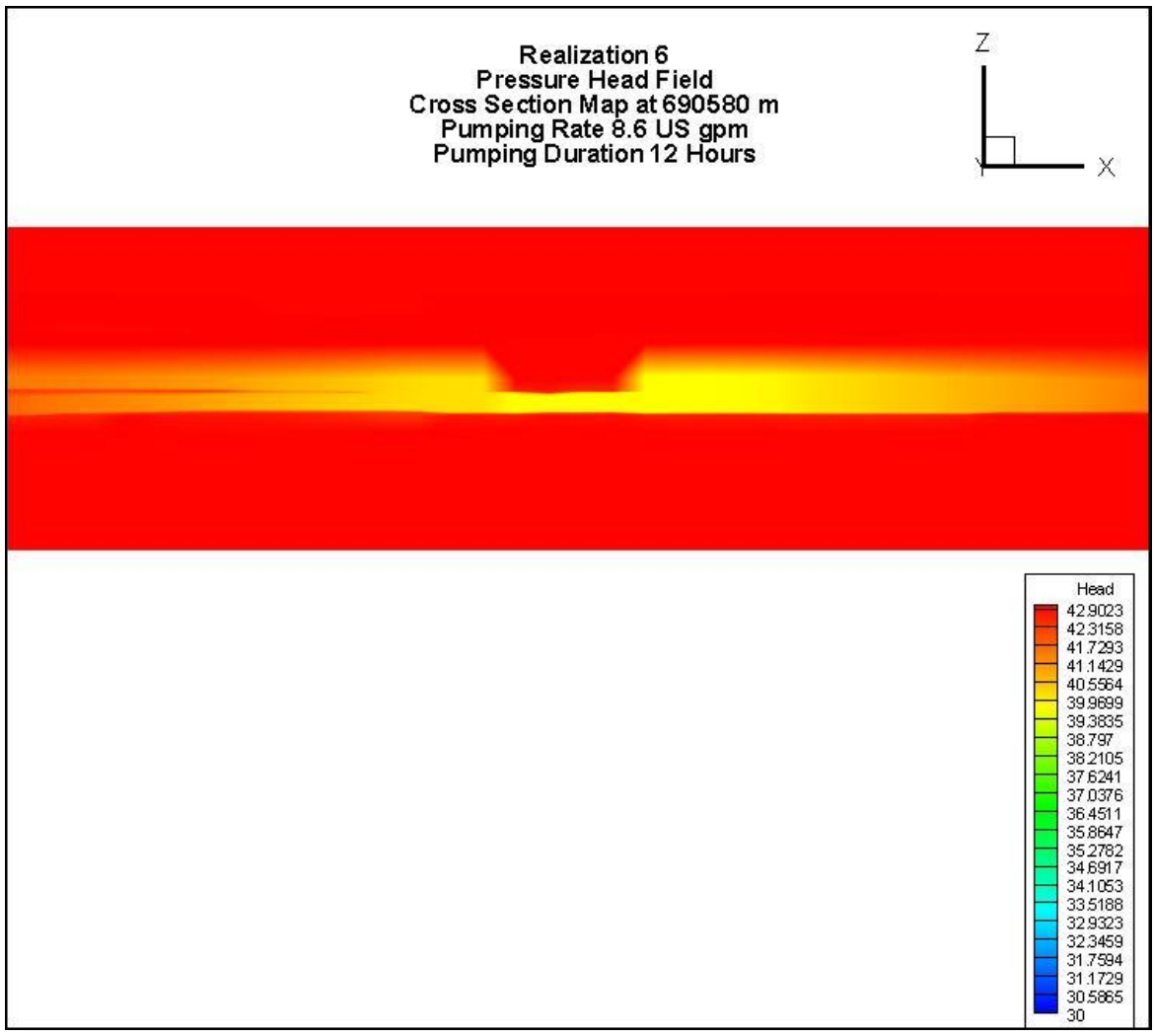

Realization 6 (Rank: min) Pressure Transient Analysis

The rate history and pressure measurements simulated during the model run for Realization 6 were used to perform Pressure Transient Analysis to evaluate the presence of flow regimes and reservoir characteristics. The aquifer thicknesses used in the analysis were taken from the model facies in all cases. Kappa Engineering's Saphir and

HydroSOLVE Inc.'s AQTESOLV were used to evaluate reservoir characteristics. To avoid any influence by the model boundaries, the rate history was edited so that the pumping period did not extend long enough to see the effects of the boundaries. The Δp was then re-extracted and the pressure data was analyzed. Using Saphir, a mathematical model was applied to the data and a solution was produced which included the use of the Bourdet derivative. An industry standard approach was applied when evaluating data using AQTESOLV. A standard industry approach was used when using AQTESOLV. The Theis model was applied to the pressure data and the solution was run until convergence.

Figure 5.13 illustrates the results of pressure transient analysis using Saphir. A standard model with constant wellbore storage, a vertical well, homogenous reservoir and leaky fault provided the best fit to the data of all the available PTA models provided in Saphir. Because input to the HydroGeoSphere model includes parameters for the screen radius and well radius, the model simulates wellbore storage. The skin effect evaluated by Saphir is a numerical artefact of how the pumping well is handled by the flow simulator. Because the pressure response at the well is averaged across the simulator grid block the resulting pressure drop as modeled by the flow simulator is less than what would actually be observed in the well resulting in a negative skin value.

Recall that in some cases more than one model can be used to provide an accurate PTA solution even though the PTA model used for interpretation may include reservoir elements (i.e., faults) that are not present in the 3-dimensional model but yet describe the

behavior of the system. Review of the Saphir output shows the pressure curve (upper curve) and the derivative curve (lower curve) illustrating an initial radial flow (IRF) after the effects of wellbore storage have ended and then an increase in the slope of the derivative curve which may be an indication of a linear flow regime beginning to develop. The linear flow regime is representative of the flow occurring in the channel sands of the model. However, any linear flow regime that evolved during the pumping period may not have significantly developed or occurred at a higher stratigraphic elevation (i.e., above the pump intake) and subsequently had less influence on the response. Figures 5.6 and 5.7 illustrate the presence of linear flow at 40 and 39.5 m at 4 hours and 12 hours respectively. Figure 5.8 illustrates the pressure head field at 51 m where the pressure wave had spread laterally outward due to connectivity of the permeable facies resulting in a PTA response that resembles a homogeneous reservoir. Figure 5.14 illustrates the results of the analysis by AQTESOLV using the Theis model.

Figure 5.13: Realization 6 Saphir pressure transient analysis of test data after 12 hours of pumping

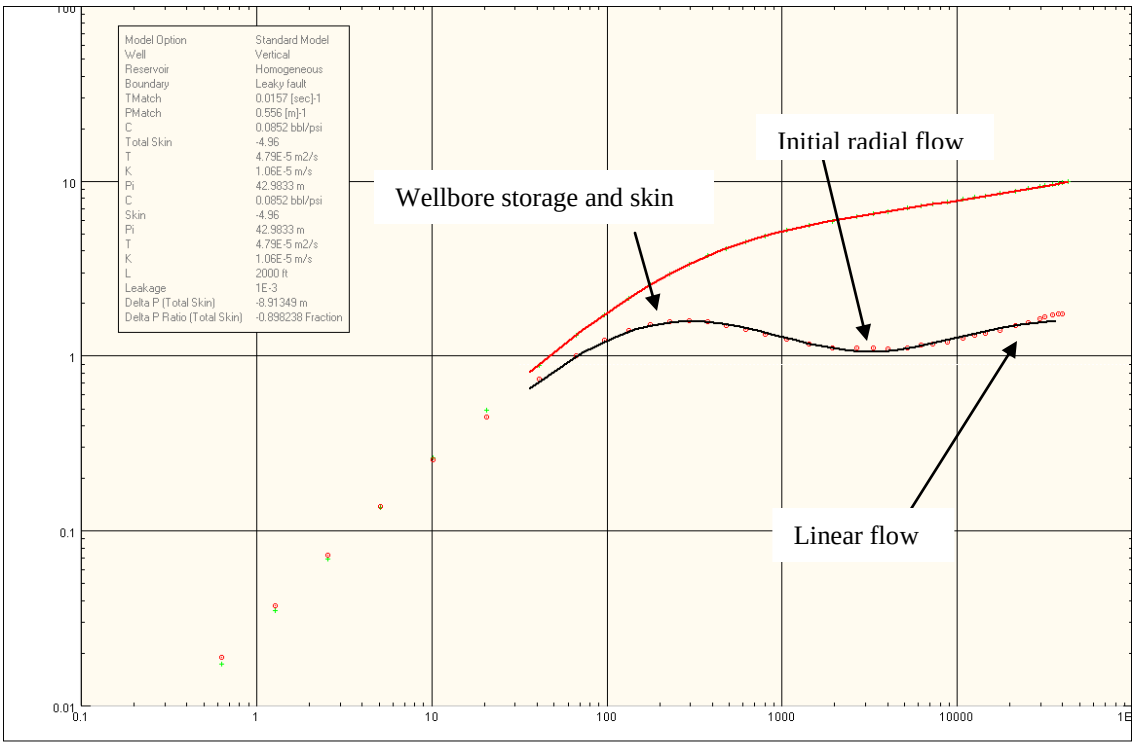

The Saphir model derived transmissivity for this solution is 4.79 x 10^{-05} m^2/s and hydraulic conductivity is 1.06 x 10^{-05} m/s. Figure 5.13 illustrates how it may be possible to use many different interpretation models to fit the data. The production well placed in the model is within a non-ideal system that does not consist of a fracture network. Several models were evaluated however; use of the leaky fault model best fit the pressure data recorded during the test.

Figure 5.14: Realization 6 AQTESOLV pressure transient analysis

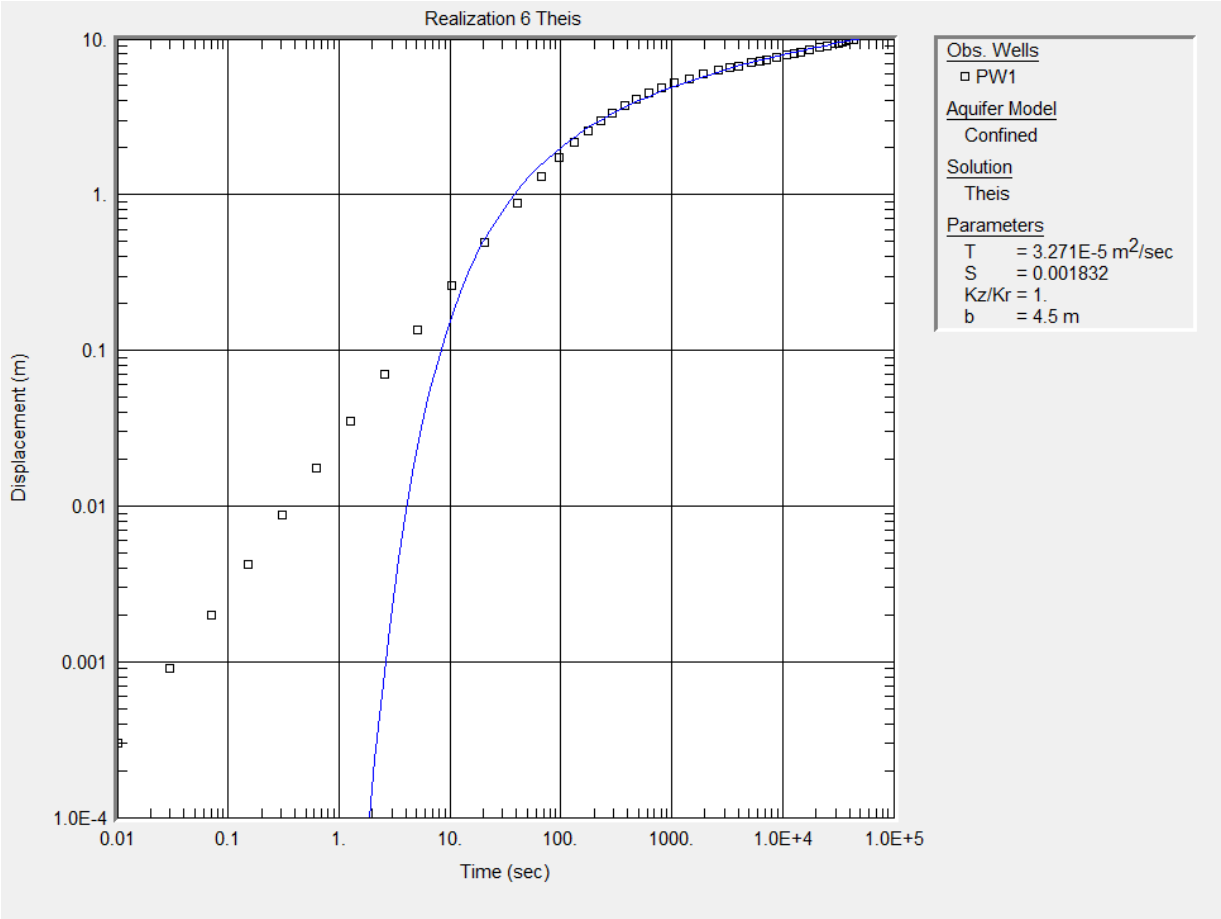

Figure 5.14 illustrates the results of the pumping test data using AQTESOLV and the Theis model for a confined aquifer. By comparison, the AQTESOLV solution (Figure 5.14) illustrates a poor fit to the data, mostly at less than 100 seconds. However, the pressure response within this time frame is a result of wellbore storage which was not modeled using AQTESOLV in this approach. This might suggest lower confidence in

the results and indicate that this system is not a homogeneous isotropic system. PTA analysis using Theis yielded a solution where the transmissivity is 3.27×10^{-05} m^2/s (hydraulic conductivity 7.27×10^{-06} m/s) and a storage value of 1.8×10^{-03}. The validity of the storage coefficient is questionable here because storage cannot be determined using only the pressure data from a pumping well. Pressure data from an observation well located close enough to observe a pressure drop due to the abstraction of water from the pumped well needs to be utilized to determine a storage coefficient. Furthermore, analysis of data will indicate variability in the storage coefficient as the distance and direction from the pumping to the observation well changes. Additionally, Saphir does not have the capability to calculate a storage coefficient. Due to this we will ignore the estimated storage coefficient.

The hydraulic conductivity determined by both Saphir (1.06×10^{-05} m/s) and AQTESOLV (7.27×10^{-06} m/s) less than the mean effective hydraulic conductivity Kx (1.49×10^{-04} m/s) and Ky (4.61×10^{-05} m/s) but are greater than the effective hydraulic conductivity eff_{Kx} evaluated for Realization 6 at 1.29×10^{-09} m/s. Both fall within the minimum and maximum effective hydraulic conductivity in the y-direction (6.72×10^{-08} m/s to 4.50×10^{-04} m/s). The Saphir derived value is closer to the hydraulic conductivity value (1.0×10^{-05} m/s) assigned to the channel sands in the model than that of the AQTESOLV derived value. This can likely be explained by the better fit and more sophisticated model applied by the Saphir analysis. Both the transmissivity and conductivity derived values are a function of the extent of the pressure wave.

Realization 6 (Rank: min) Theoretical Long Term Yield

The theoretical long term yield of a proposed production well determined by the Farvolden method is:

$$Q_{20} = (0.68)(T)(Ha)(0.7) \quad [5.3]$$

Where:

Q_{20} is the 20-year long term yield of the aquifer at the well point (volume/time)

T is the transmissivity (L^2/T)

Ha is the available head (m)

As previously stated, the Farvolden method requires the use of the Theis equation which assumes a laterally continuous homogeneous isotropic aquifer. Application of this method to an aquifer system which either does not behave as, or is not a homogenous isotropic system, is technically incorrect, scientifically flawed, and can lead to errors and omissions. These errors could have serious ramifications to the prediction of long-term well productivity.

The Theis solution yielded a transmissivity of 3.27×10^{-05} m^2/s and with an initial head of 43 m; the calculated Q_{20} is 2.50×10^{-04} m^3/s. This resulted in a long-term safe yield of 7,884 m^3/year. The Saphir derived transmissivity value of 4.79×10^{-05} m^2/s is only 1.52×10^{-05} m^2/s greater than the Thesis value. Using Saphir, a forward simulation was performed to predict the pressure head after a pumping duration of 20 years using the PTA solution reservoir model and parameters and the Q_{20} rate. The pressure head after

this period was -16.47 m which translates to approximately 60 m of drawdown indicating that the well could not sustain the proposed rate. Any stakeholder using the Q_{20} in this case would risk running the well dry, require well abandonment and would require expansion of their water supply drilling program.

Realization 43 (Rank: max) Model Results

Realization 43 is the model domain with the maximum effective hydraulic conductivity of all 100 realizations. This translates into the maximum lateral and vertical connectivity between the hydraulically conductive facies (sands and crevasse splays) where it would be expected that the pressure wave will propagate furthest in the model. The lateral and vertical distribution of the facies can be seen in Figures 4.9 and 4.10.

During the short-term and long-term pumping tests multiple flow regimes are observed at different stratigraphic levels within the model (Figures 5.15 through 5.17). Figure 5.15 illustrates the presence of channel sand at a depth of 66 m which is located approximately 17 m above the pumping well. However, although the boundaries of the channel sand are apparent against the overbank deposits, it does not appear that linear flow is occurring.

Because the sands of Realization 43 are laterally extensive and continuous we see radial flow (Figure 5.16) as depicted by the concentric rings around the pumping during the early time (4 hour) results. The pressure wave extends further into the channel sands as seen in the long-term test results just prior to interference from the boundaries (15 hours) as seen by the presence of the sharp contrasting boundaries of the channel sands and

overbank deposits which can be seen in the pressure wave distribution in Figure 5.17 and the facies distribution in Figure 5.18.

In cross section (Figures 5.19 and 5.20) it can be seen how the pressure wave has moved primarily through the sands close to the pumping well. However, as the pressure wave has propagated away from the well, it appears that the wave has moved into the overbank deposits and bridged areas between more permeable media at a depth of 1311 m. Furthermore, when we compare the pressure head field to the hydraulic conductivity field along the same cross section it appears that the pressure wave moves out into the overbank deposits as seen on the right and left hand sides of the diagram along the x-axis.

Figure 5.15: Realization 43 pressure head field at 66 m depth. Pumping interval at 75.25 m to 83.25 m depth

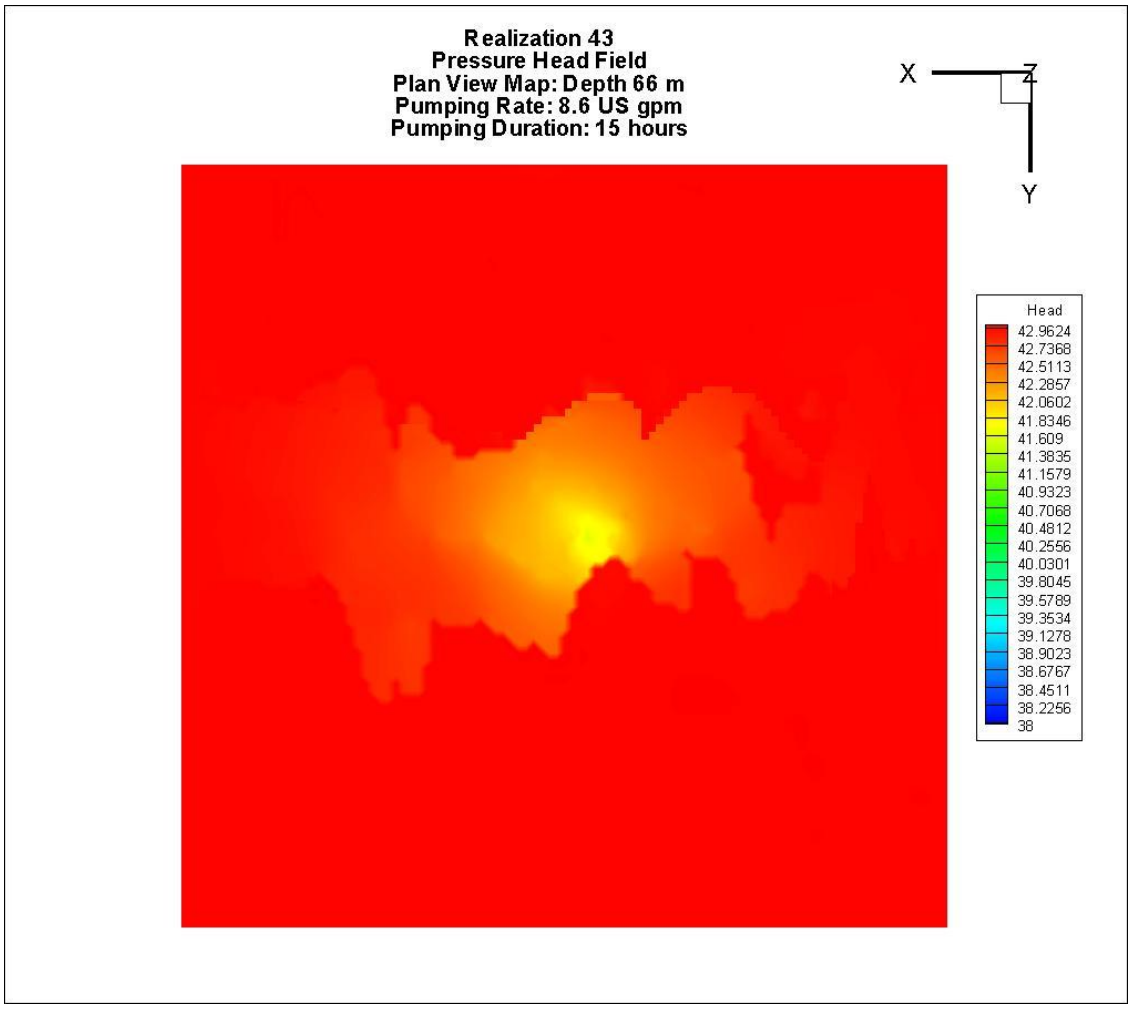

Figure 5.16: Realization 43 pressure head field at 82 m depth. Pumping interval at 75.25 m to 83.25 m depth

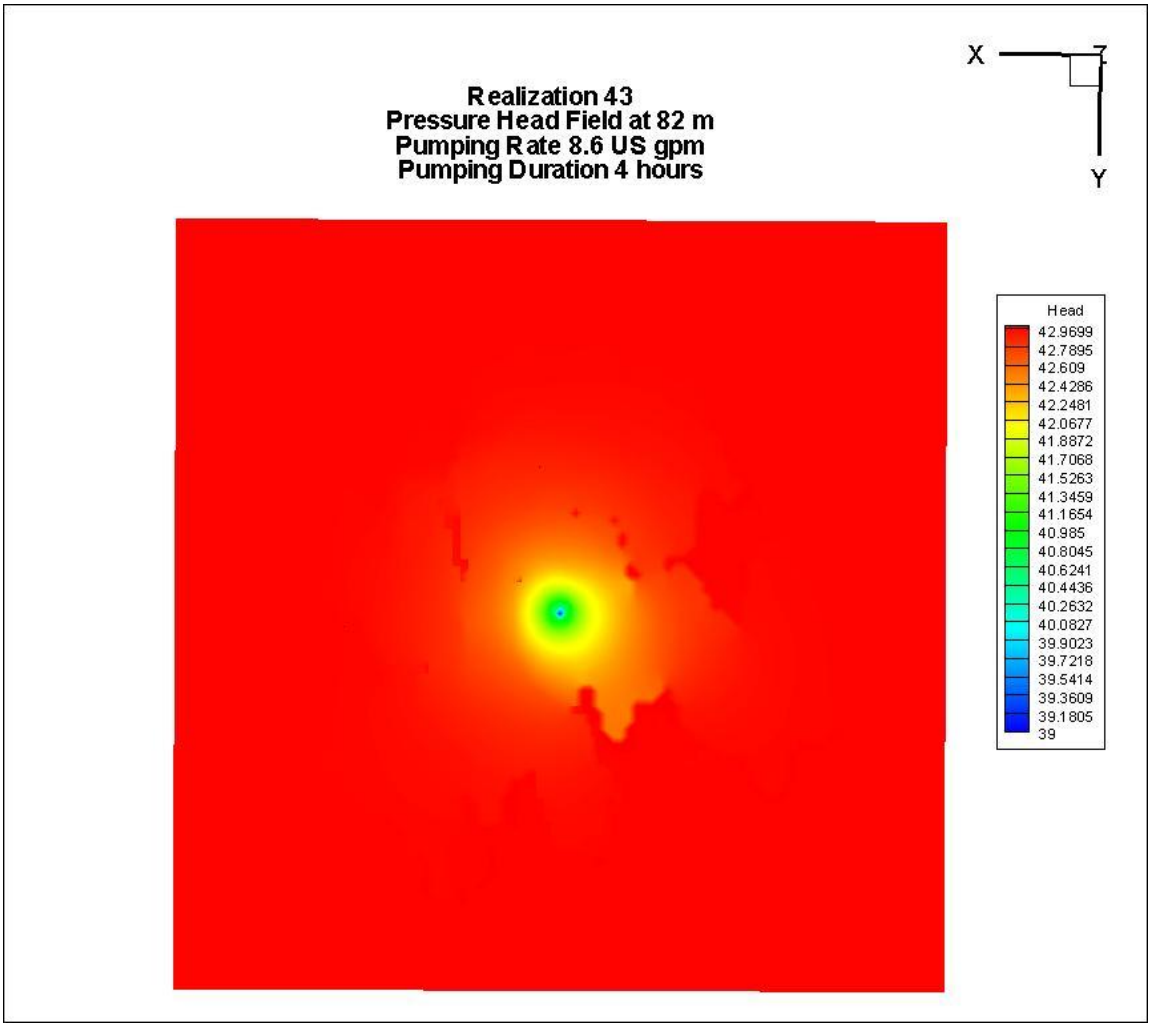

Realization 43 pressure head field early time (4 hours) at a depth of 82 m. There appears to be radial flow around the well until the pressure wave has propagated far enough to see the boundaries of the channel.

Figure 5.17: Realization 43 pressure head field after 15 hours of pumping at a depth of 82 m. Pumping interval 75.25 m to 83.25 m depth

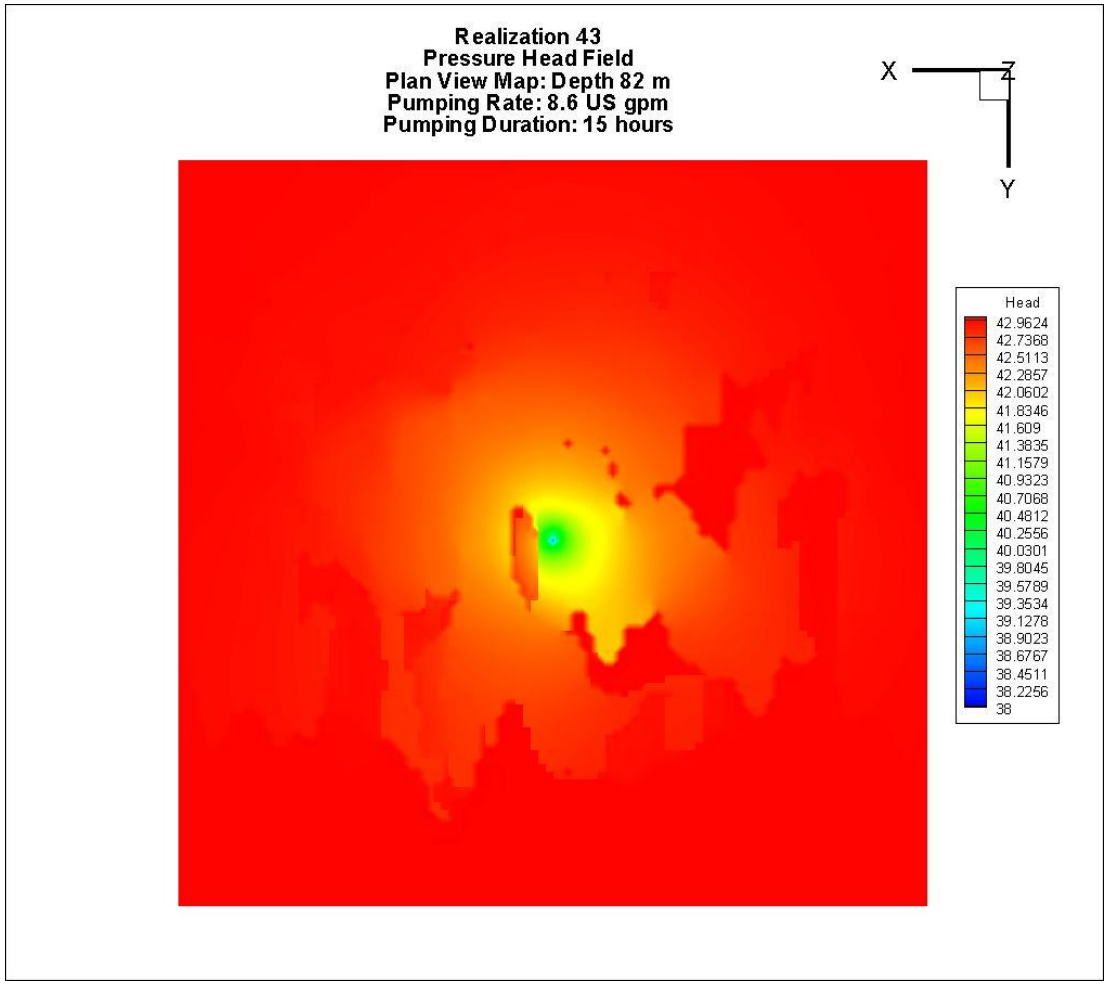

Figure 5.17 illustrates concentric rings of the pressure wave can be seen near the pumping well. The boundaries of the sands and overbank deposits can be clearly seen throughout the central region of the model.

Figure 5.18: Realization 43 Hydraulic conductivity field at a depth of 81 m

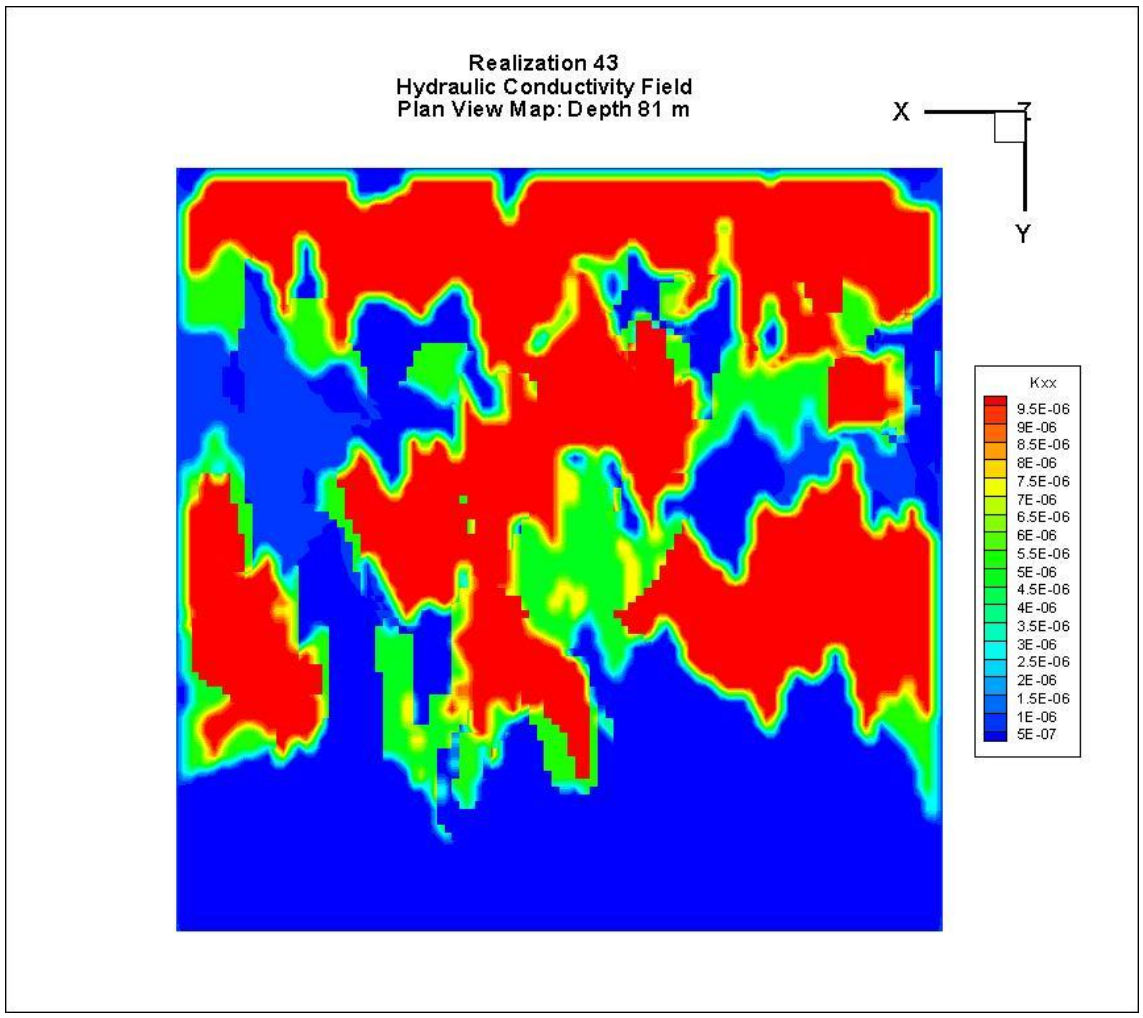

Figure 5.18 illustrates the lateral connectivity of the channel sands and crevasse splays against the overbank deposits.

Figure 5.19: Realization 43 pressure head field cross section at after 15 hours of pumping

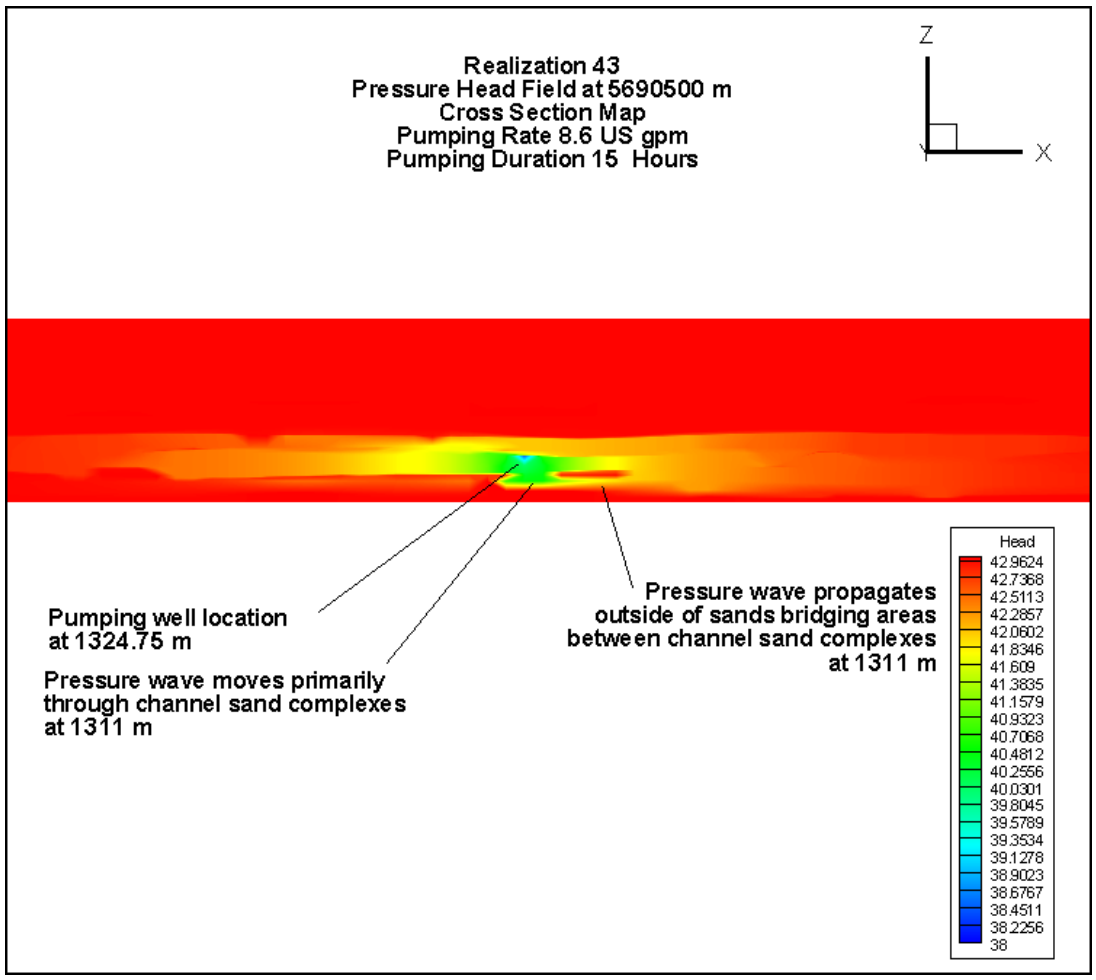

Figure 5.19 illustrates the pressure wave distribution within the hydraulically conductive facies. In the lower portion of the model the pressure wave appears to have bridged an area between sand bodies through overbank deposits.

Figure 5.20: Realization 43 pressure head field cross section at after 15 hours of pumping

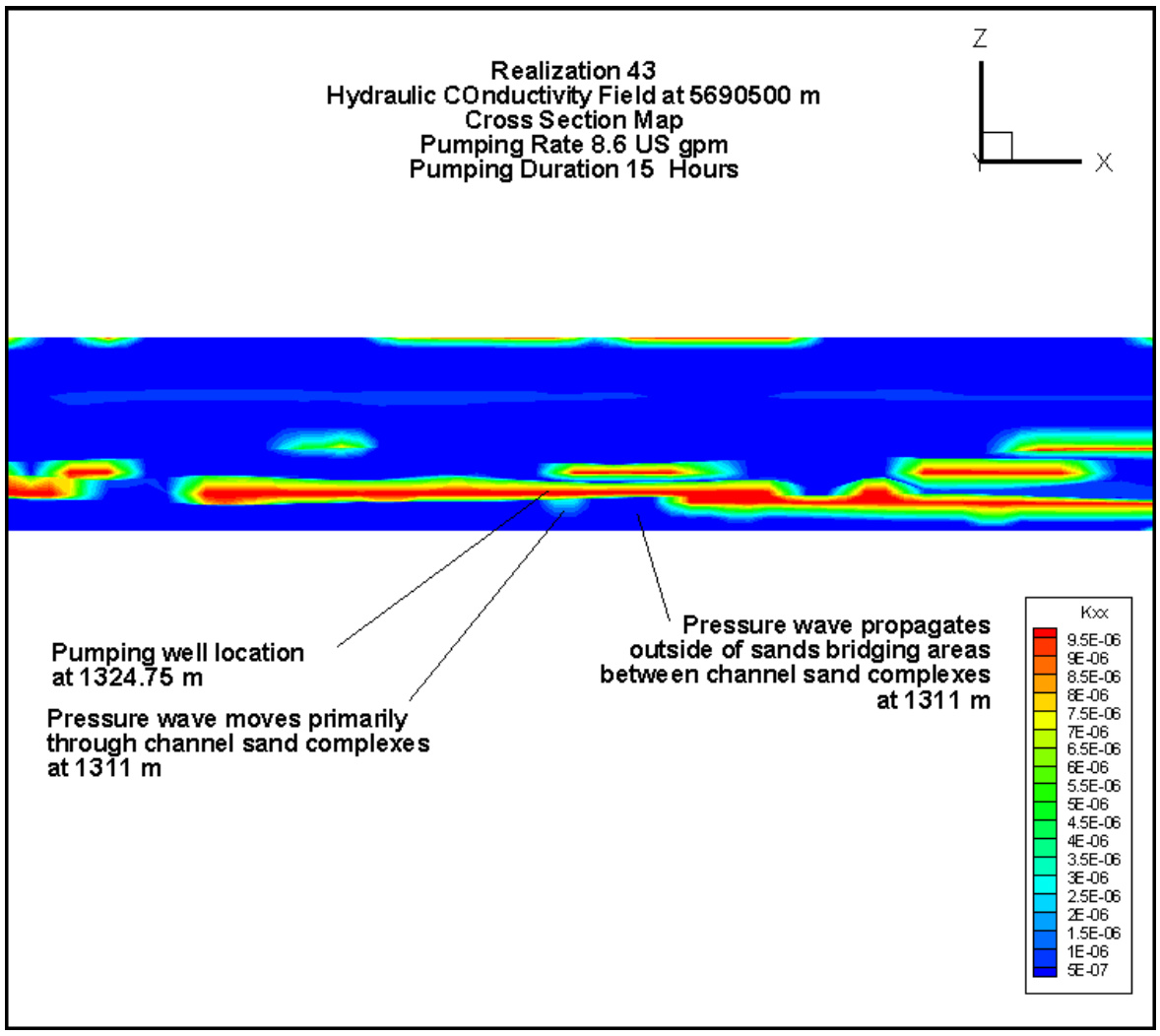

Figure 5.20 illustrates where sand channels exist and lateral and vertical connectivity. From figures 5.15 through 5.17 and 5.19 it can be seen that the pressure wave moves throughout the sands and moves into the overbank deposits bridging gaps between the more permeable sands.

Figures 5.21 and 5.22 represent typical drawdown versus time well responses for observations wells. Figure 5.21 illustrates the drawdown curve for observation well 59 which is located near the boundary of the model for Realization 43. Figure 5.22 illustrates the drawdown curve for a well, observation well 1, located near the center of the model close to the pumping well. All the drawdown curves for all the observation wells were reviewed to determine if there were any unique characteristics related to the well response. The heterogeneity in the system is not obvious in the drawdown curves of the observation wells.

Figure 5.21: Realization 43 drawdown versus time curve for observation well 59

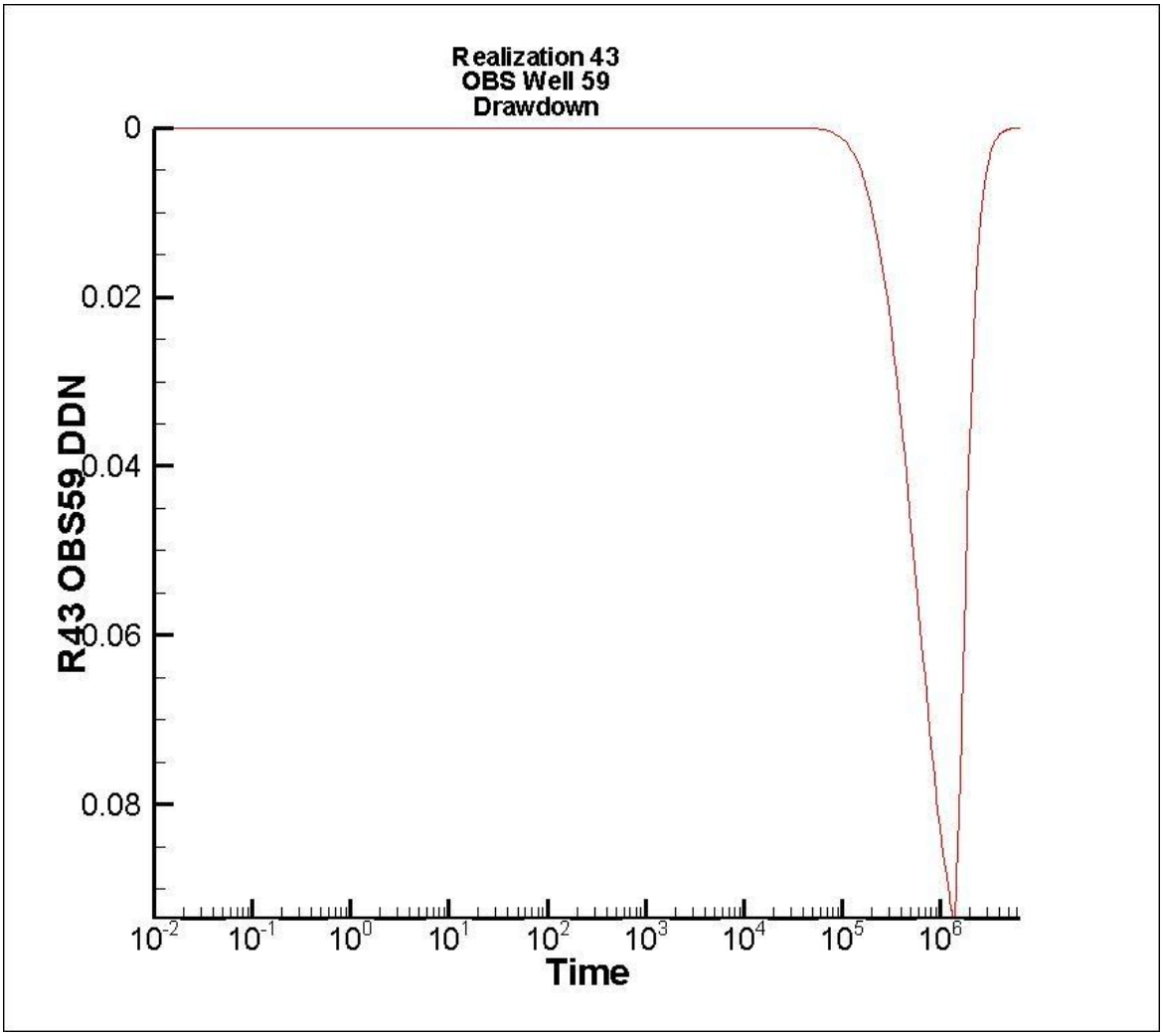

Figure 5.21 illustrates the drawdown curve, which has no unique features, represents a typical curve for many of the observation wells within the domain located at a distance from the pumping, closer to the boundaries.

Figure 5.22: Realization 43 drawdown versus time curve for observation well OBS1

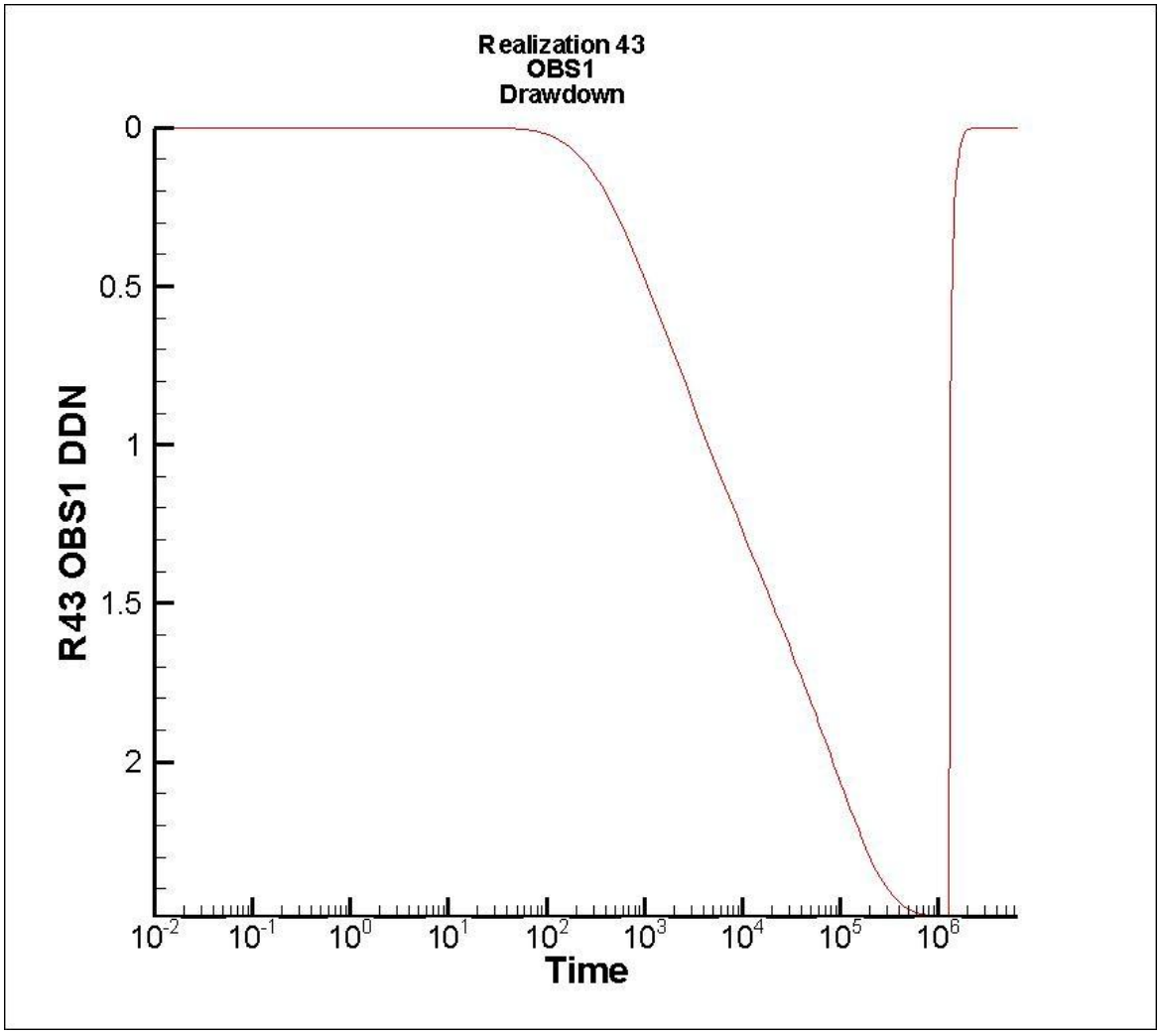

Figure 5.22 illustrates the drawdown curve which represents a typical response for a well in close proximity to the production well where drawdown is greatest.

Realization 43 (Rank: max) Pressure Transient Analysis

The methodology used for evaluating data from Realization 6 was also applied to Realization 43. Figure 5.23 illustrates the results of pressure transient analysis using Saphir. A standard model with a vertical well and homogenous reservoir of infinite extent was used to fit the data and provide a solution. Based on a review of the pressure data, a linear flow regime (channel flow) was not observed. Infinite Acting Radial Flow (IARF) was observed as represented by the flat straight line of the derivative curve. Therefore this system appears to behave as a homogenous infinite reservoir. Figure 5.24 illustrates the results of the analysis by AQTESOLV using the Theis model.

Figure 5.23: Realization 43 Saphir pressure transient analysis of test data

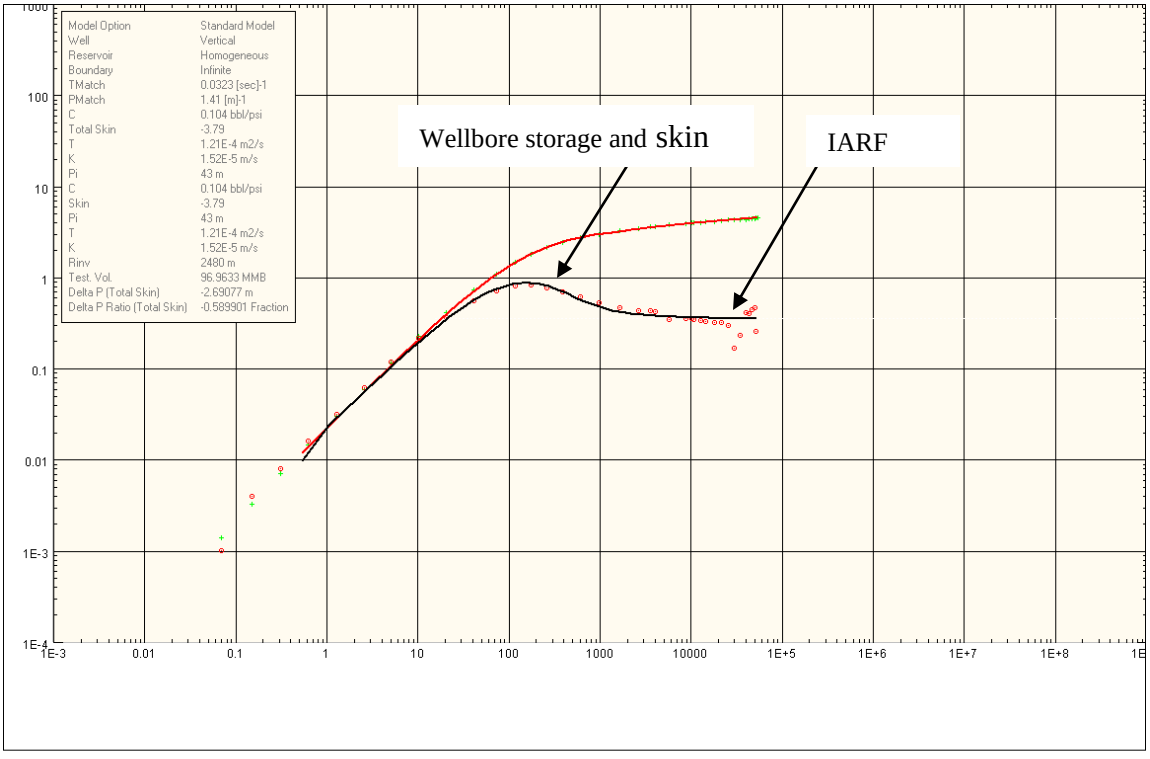

Log-Log plot: p-p@dt=0 and derivative [m] vs dt [sec]

The model used in the Saphir analysis for this solution yielded a transmissivity of 1.21 x 10^{-04} m^2/s and a hydraulic conductivity of 1.52 x 10^{-05} m/s.

Figure 5.24: Realization 43 AQTESOLV pressure transient analysis results of test data

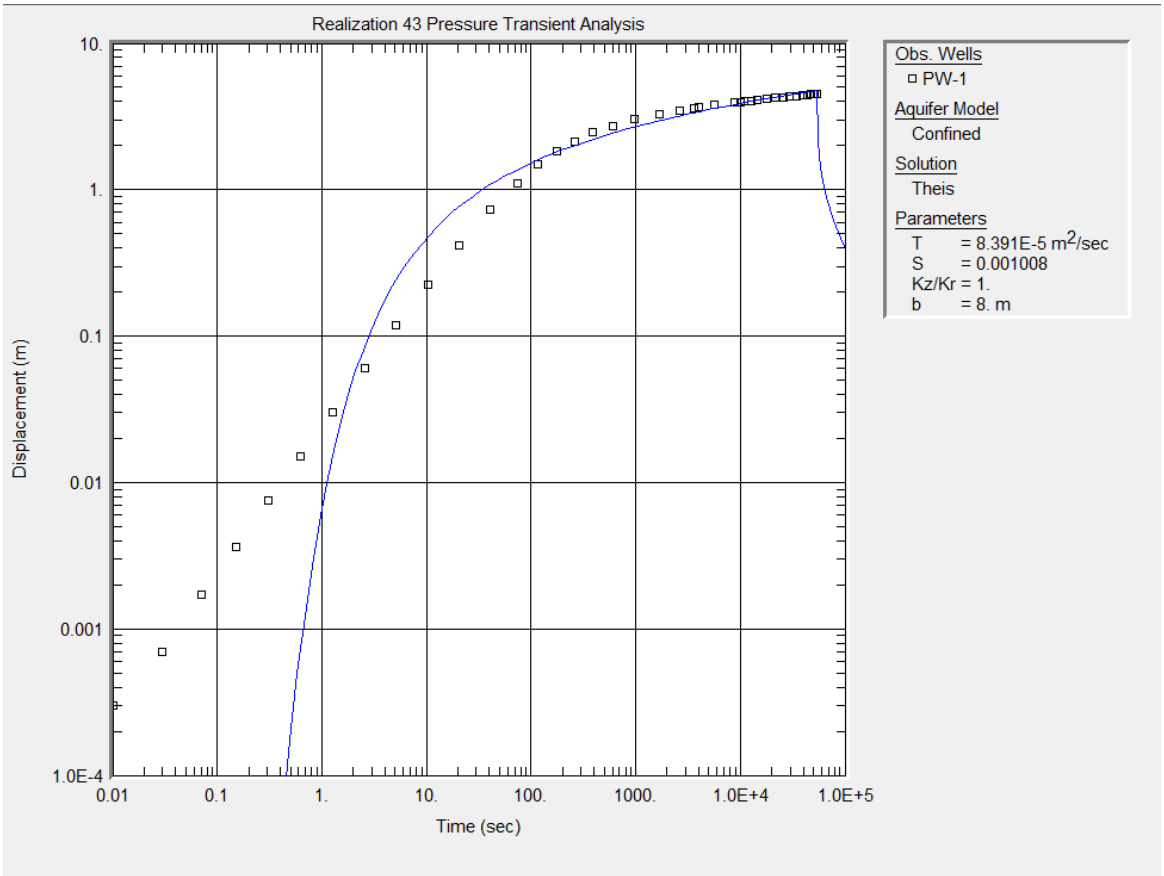

Analysis of pumping test data was performed using AQTESOLV and the Theis model for a confined aquifer. Only the first 54000 seconds of data was used to avoid boundary effects and yielded a solution where the transmissivity is 8.4 x 10^{-04} m^2/s. Figure 5.24 which illustrates the Theis solution to the data suggests a poor fit as can be seen by the solution not fitting the data points very well until we get to 1.0 x 10^{+04} seconds in the test.

This early time response is the result of the wellbore storage effect. This can typically be mitigated through the use of an interpretation that accounts for wellbore storage. Recall that the Saphir analysis allows the user to fit a custom curve and the analysis suggests a homogeneous infinite aquifer. Yet, using AQTESOLV and the Theis model solution, which assumes a homogeneous aquifer yields a poor fit, by comparison, for the first 1.0 x 10^{+04} seconds and a different value for transmissivity. This might suggest that the system is slightly more complicated than that which can be handled using a program such as AQTESOLV and requires the ability to manipulate the curve fits.

The hydraulic conductivity determined by both Saphir (1.52 x 10^{-05} m/s) and AQTESOLV (1.05 x 10^{-05} m/s) are similar and both are less than the mean effective hydraulic conductivity Kx (1.49 x 10^{-04} m/s) and Ky (4.61 x 10^{-05} m/s) but both are greater that the effective hydraulic conductivity eff_{Kx} evaluated for Realization 43 at 1.88 x 10^{-06} m/s. Both fall within the minimum and maximum effective hydraulic conductivity in the y-direction (6.72 x 10^{-08} m/s to 4.50 x 10^{-04} m/s). Both values are very close to the hydraulic conductivity value (1.0 x 10^{-05} m/s) assigned to the channel sands. This is due to the consistent lateral distribution of the sands adjacent to the production well.

Realization 43 (Rank: max) Theoretical Long Term Yield

For the first analysis using Saphir solution the transmissivity was 1.21 x 10^{-04} m^2/s. The Theis solution, using AQTESOLV, yielded a transmissivity of 8.4 x 10^{-05} m^2/s with an initial head of 43 m; the calculated Q_{20} is 0.0017 m^3/s. This resulted in a long-term safe

yield of 54,220 m^3/year. A forward 20 year prediction was performed using Saphir's reservoir model solution and derived model parameters. The forward prediction used the Q_{20} production rate of 54,200 m^3/year resulting in a drawdown of 21.8 m. It should be noted here that since we are evaluating a system that appears to behave as a homogeneous aquifer system, our estimation of the long-term yield is sustainable.

Realization 46 (Rank: P68) Model Results

Realization 46 represents a model domain with an effective hydraulic conductivity at the sixty eighth percentile of the 100 realizations. This translates into a lateral and vertical connectivity between the hydraulically conductive facies near the middle of maximum and minimum connectivity. The lateral and vertical distribution of the facies can be seen in Figures 4.13 and 4.14.

During the short-term (4 hour) pumping test, although some sharp contrasts can be seen between the overbank deposits and the channel sands, it appears that initial radial flow evolves first but the test does not run long enough for other flow regimes to develop. The concentric rings of the pressure wave that developed during the IRF period can be seen in Figure 5.25. The interface between the overbank and channel sand deposits can be seen in the image. Although the outline of the channel sands can be seen, it does not appear that linear flow has developed.

The results of the long-term (8.8 hours) test indicate the development of several different flow regimes at different stratigraphic levels within the model (Figures 5.26 through

5.29). Figure 5.26 illustrates radial flow at 13 m depth surrounding the pumping well in the center of the model, however, the pressure wave has propagated far enough through the permeable media that the interface between the sands and overbank deposits can be seen.

A distinct channel sand can be seen at surface in Figure 5.27. Given sufficient time, linear flow would develop in this media. Figure 5.28 illustrates the distribution of the pressure head field at a depth of 4 m. By the distribution of the pressure wave, it can be inferred that as the pressure wave propagated vertically upward toward the surface from the pumping well the wave has moved through connective sands and crevasse splays and spread out laterally and is separated by overbank deposits. At 12 m depth, the pressure wave has spread out radially from the well and the edge of the sand channel is observed yet linear flow does not appear to have developed (Figure 5.29).

Figure 5.30 illustrates the distribution of the pressure wave in cross section. The pumping well was placed approximately 15 m from the surface. It can be seen how the pressure wave has laterally spread through the upper part of the model through the sands and crevasse splays. The pressure wave has bridged an area between sands by propagating through the less permeable overbank deposits. It also shows where linear flow and radial flow occurs within the pumped region. Figure 5.31 illustrates the hydraulic conductivity in cross section where the permeable sands within the upper portion of the model match where the pressure wave is distributed. From comparison of

Figures 5.30 and 5.31 it can be seen that the pressure wave moves outside of the sands and into overbank deposits.

Figure 5.25: Realization 46 pressure head field early time (4 hours) results at a depth of 13 m. Pumping interval between 6.25 m and 14.75 m depth

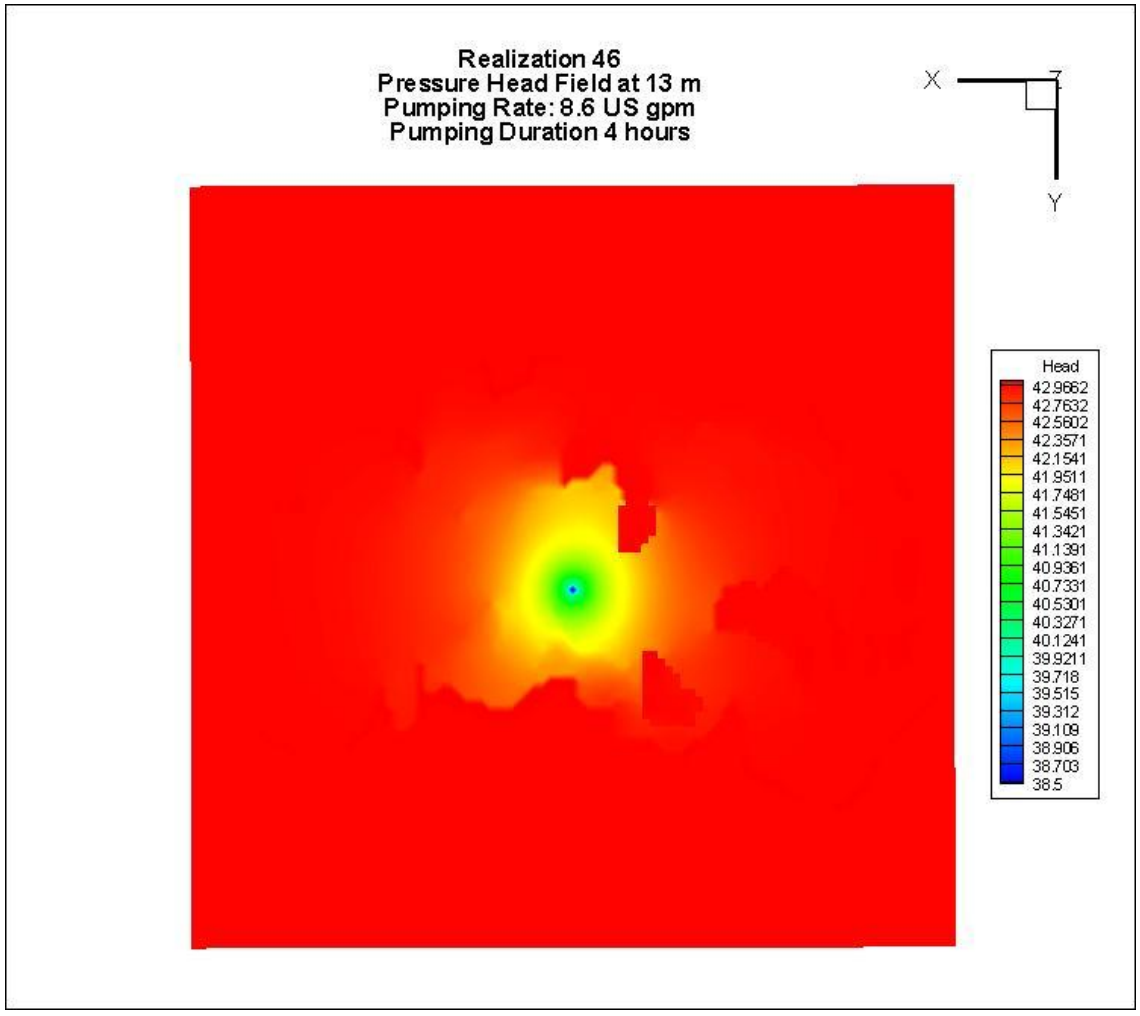

Figure 5.26: Realization 46 pressure head field at a depth of 13 m after 8.8 hours of pumping at a rate of 8.6 US gpm (46.5 m3/d). Pumping interval between 6.25 m and 14.75 m depth.

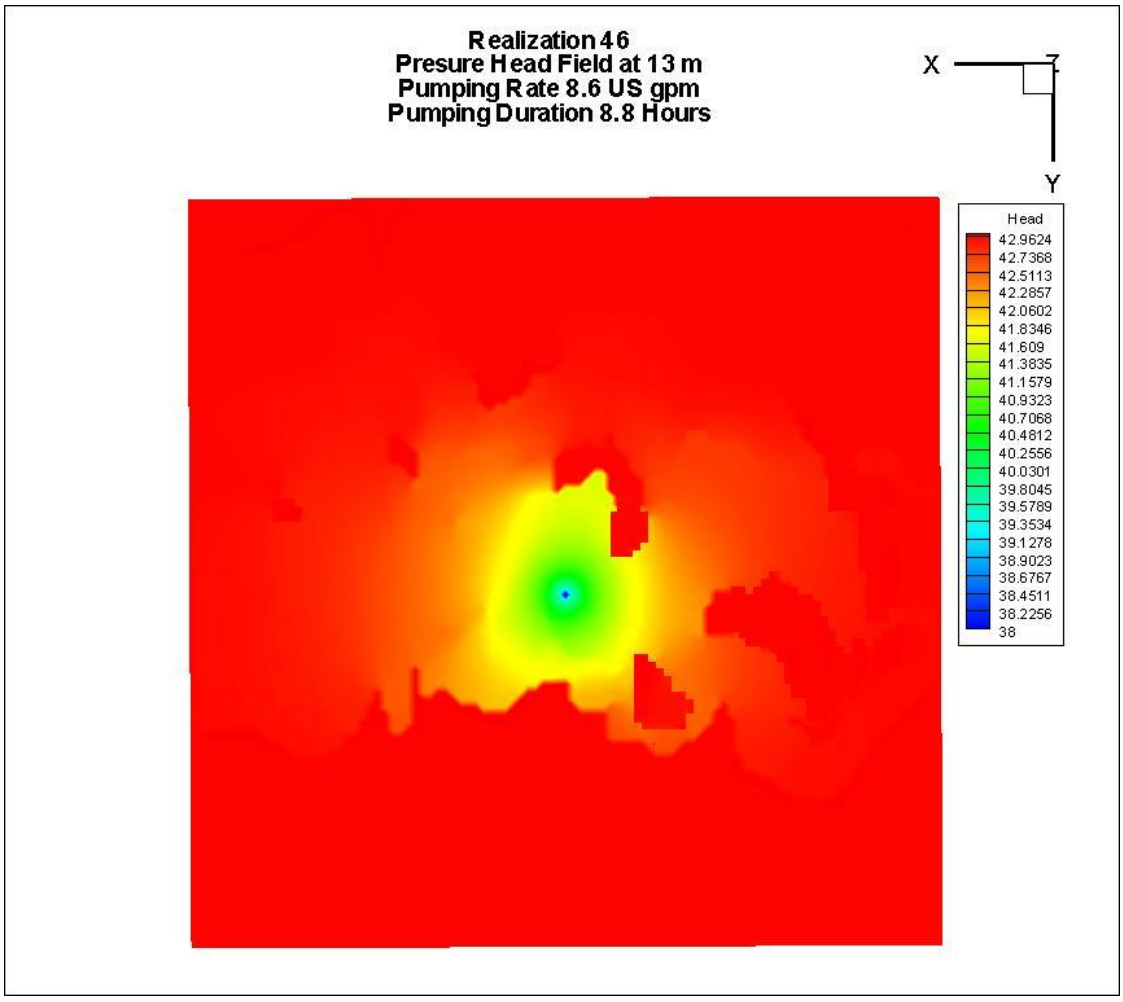

Figure 5.27: Realization 46 pressure head field illustrating channel (linear) flow at surface. Pumping interval between 6.25 m and 14.75 m depth.

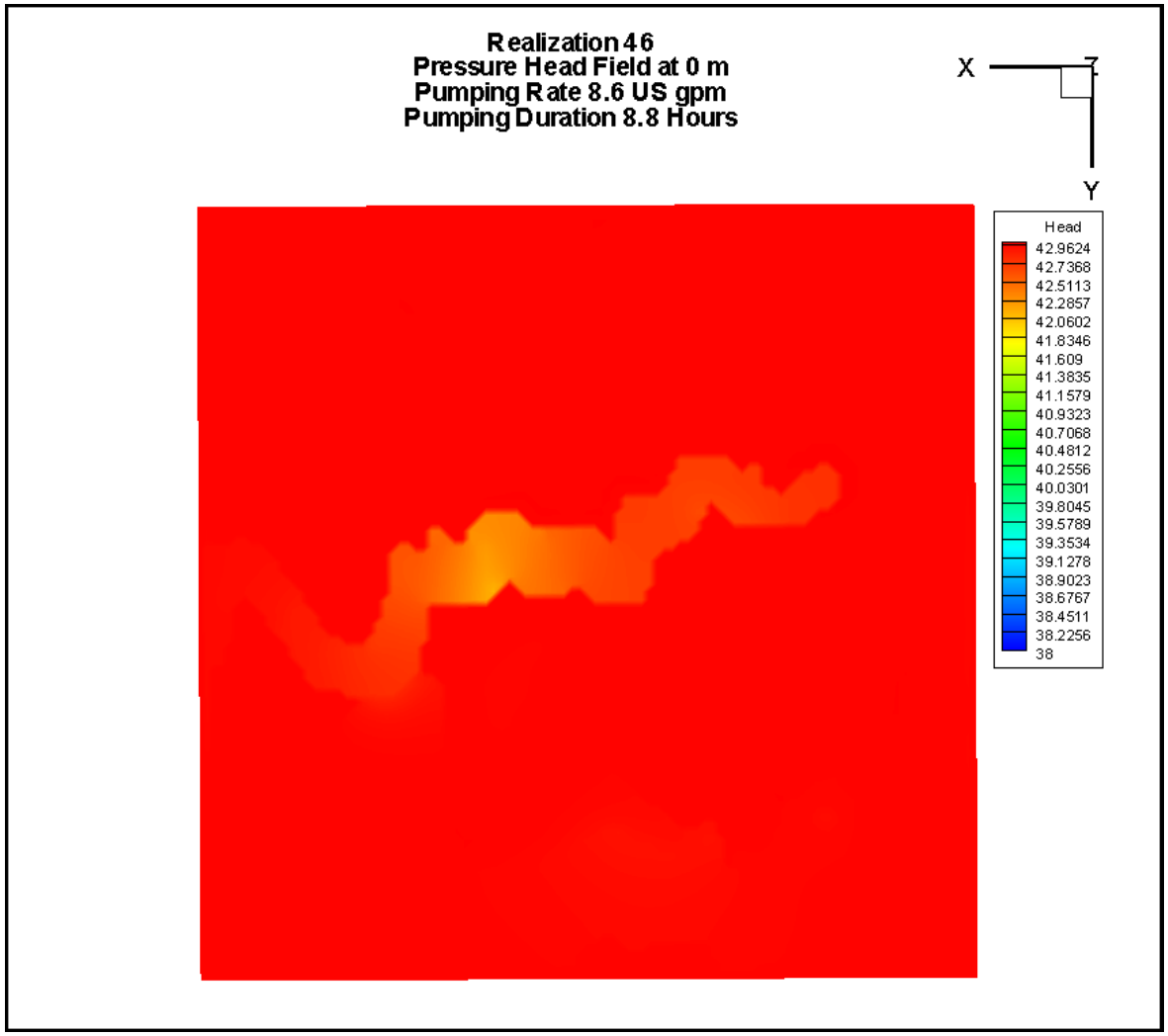

Figure 5.27 illustrates channel (linear) flow at surface. The sharp contrasting boundary between the sands and overbank deposits is apparent by the outline of the channel sands.

Figure 5.28: Realization 46 pressure head field at 4 m after 8.8 hours of pumping. Pumping interval between 6.25 m and 14.75 m depth.

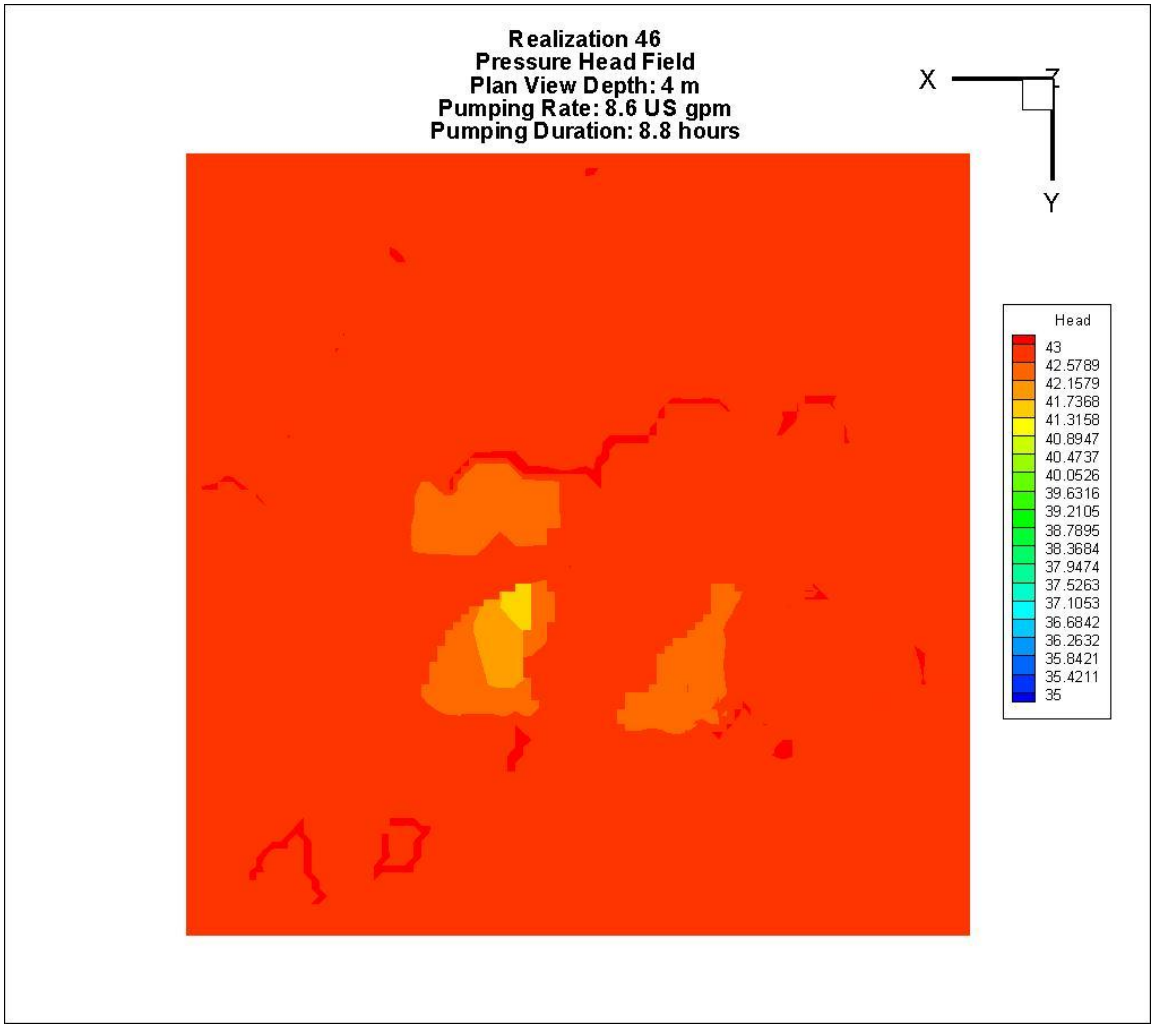

Figure 5.28 illustrates how the pressure wave has propagated vertically upward from the pumping point to the surface and as the wave has risen has moved into separate sands that are laterally separated by overbank deposits.

Figure 5.29: Realization 46 pressure head field at 12 m after 8.8 hours of pumping. Pumping interval between 6.25 m and 14.75 m depth.

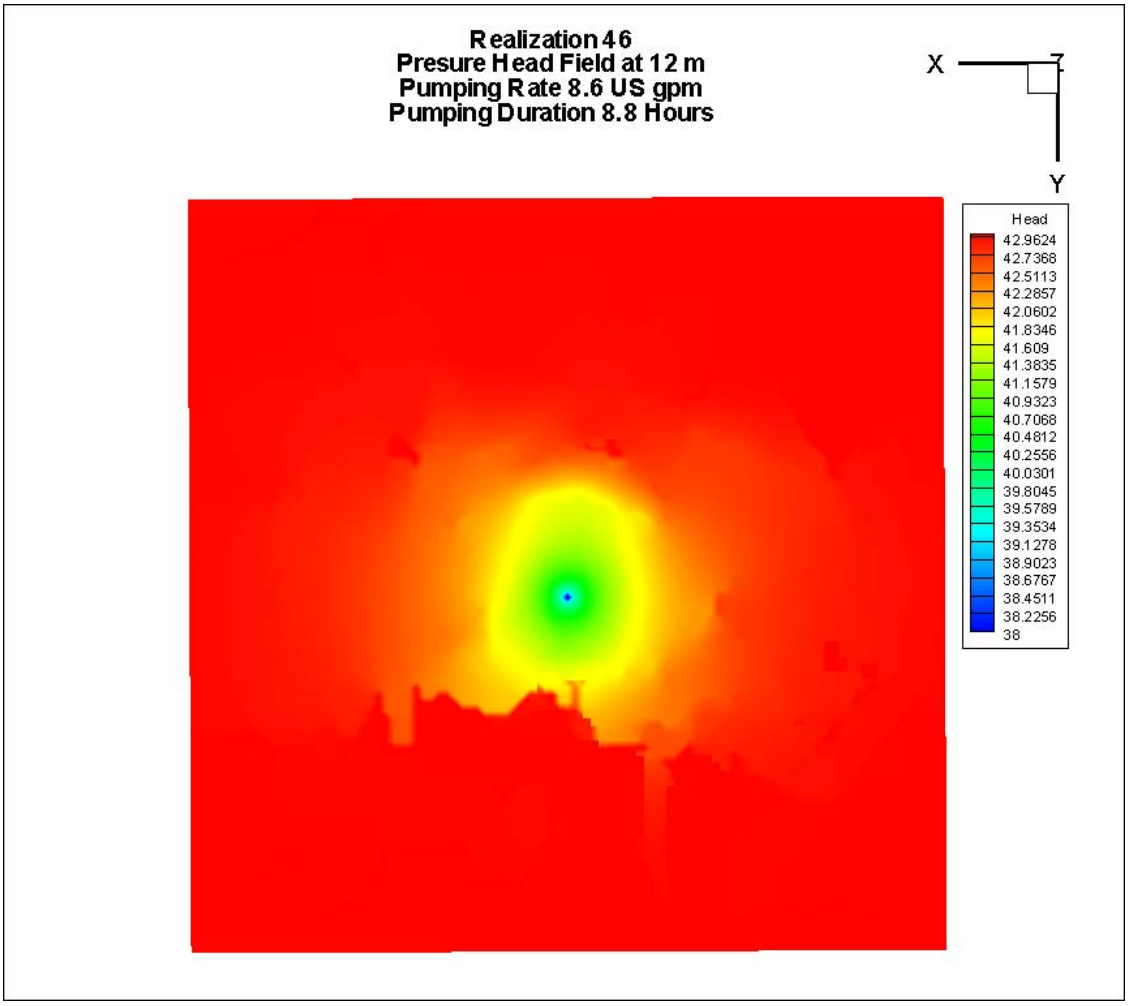

Figure 5.29 illustrates what appears to be a radial spreading of the pressure wave until it reaches the edge of a sand channel. This plan view image is at a depth of 12 m.

Figure 5.30: Realization 46 pressure head field cross section after 8.8 hours of pumping. Pumping interval between 6.25 m and 14.75 m depth.

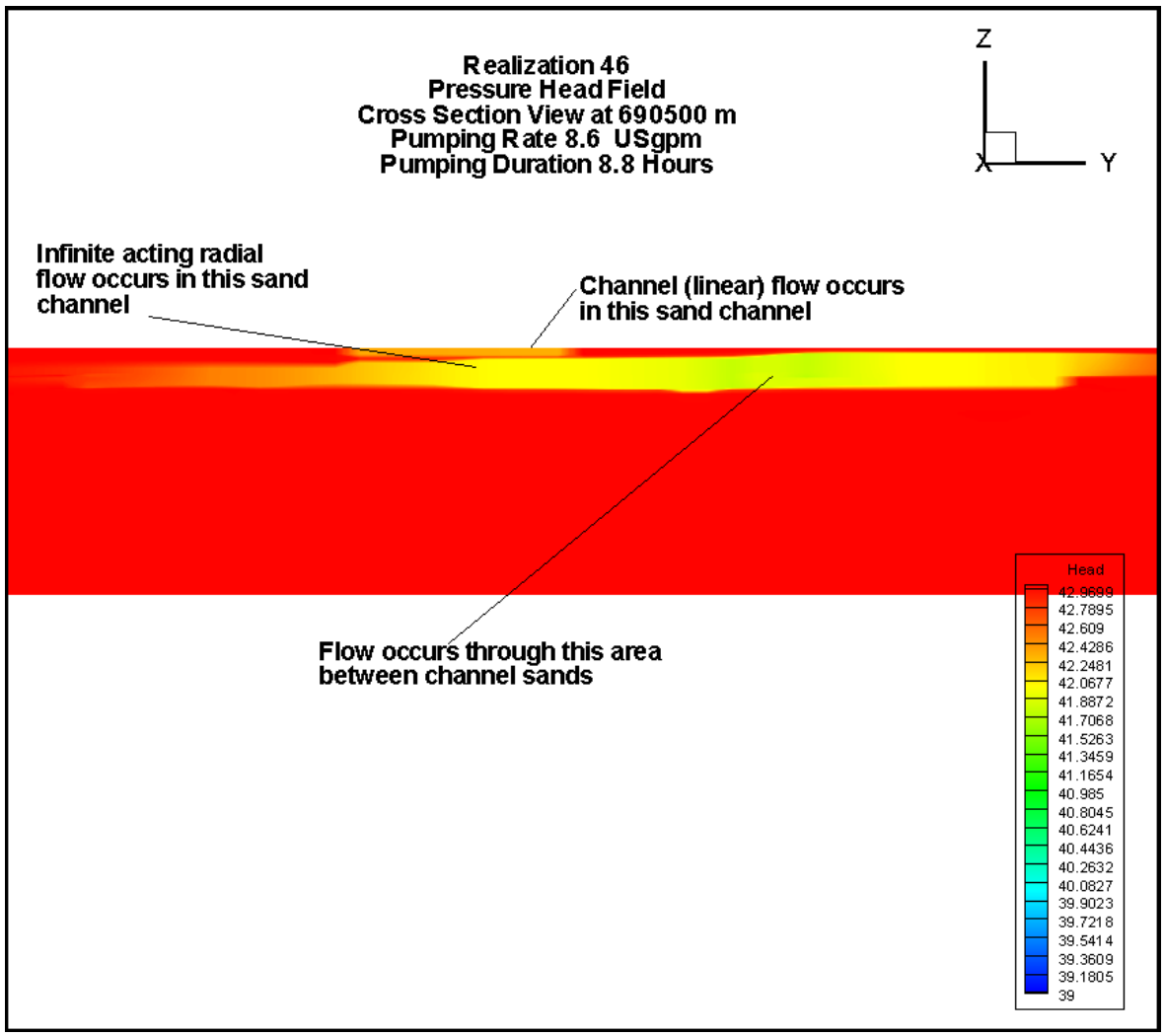

The figure illustrates the different flow regimes occurring at different stratigraphic levels during the same pumping test.

Figure 5.31: Realization 46 hydraulic conductivity field

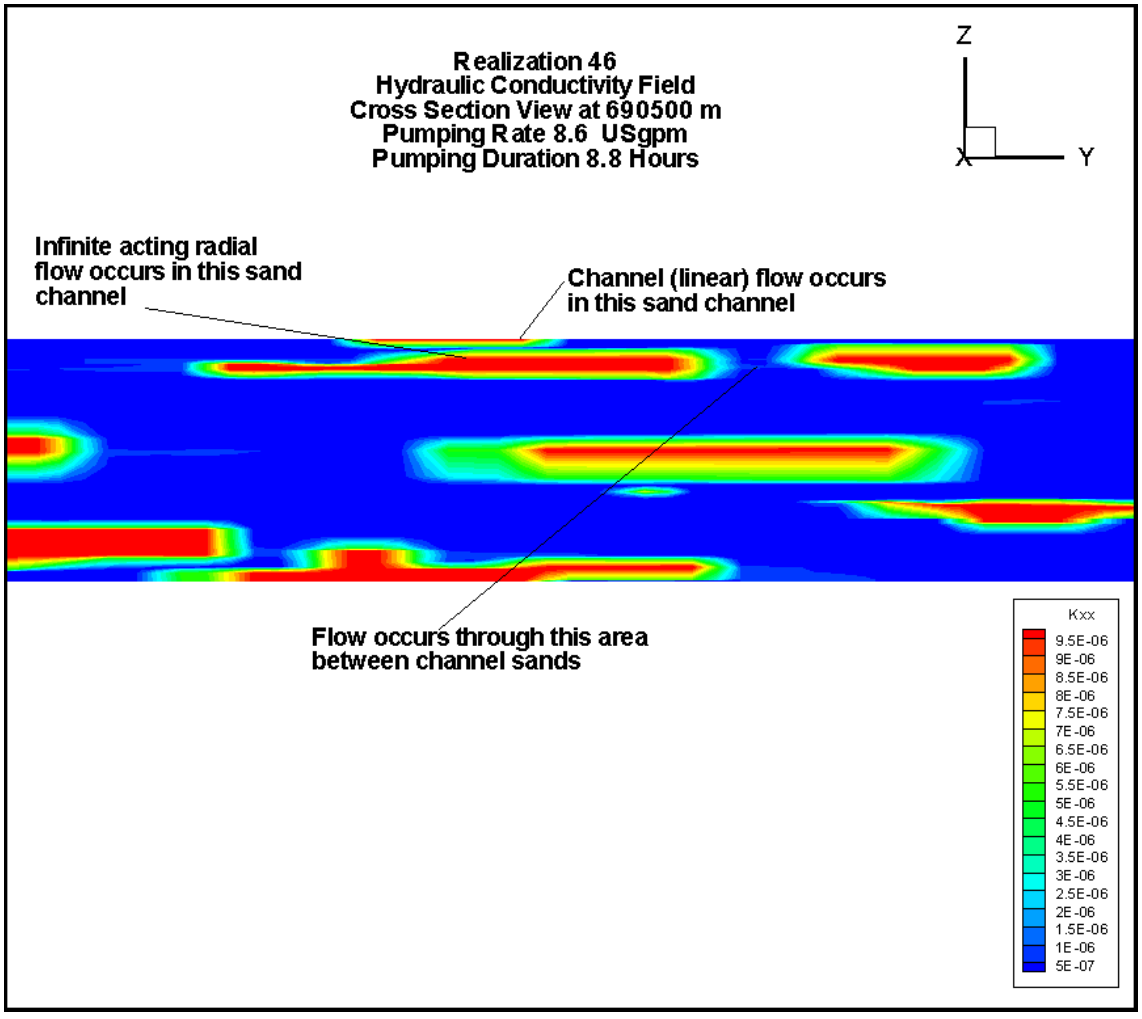

Figure 5.31 shows geologic objects where the pressure wave has propagated through including areas where the pressure wave has moved into the overbank deposits bridging gaps between the more permeable sands.

Realization 46 (Rank: P68) Pressure Transient Analysis

Figure 5.32 illustrates the results of pressure transient analysis using Saphir. A standard model with a vertical well and homogenous reservoir with a leaky fault was used to fit

the data and provide a solution for the long-term (8.8 hour) test. The figure illustrates that the solution provides a good fit to the data indicating that this system behavior is more complicated than a simple homogeneous reservoir. It can be seen in the figure where the derivative curve starts to become a half slope which is indicative of linear flow. The leaky fault within the model may account of a component of linear flow and leakage across some of the sharp contrasting zones. Figure 5.33 illustrates the results of the analysis by AQTESOLV using the Theis model.

Figure 5.32: Realization 46 pressure transient analysis using Saphir

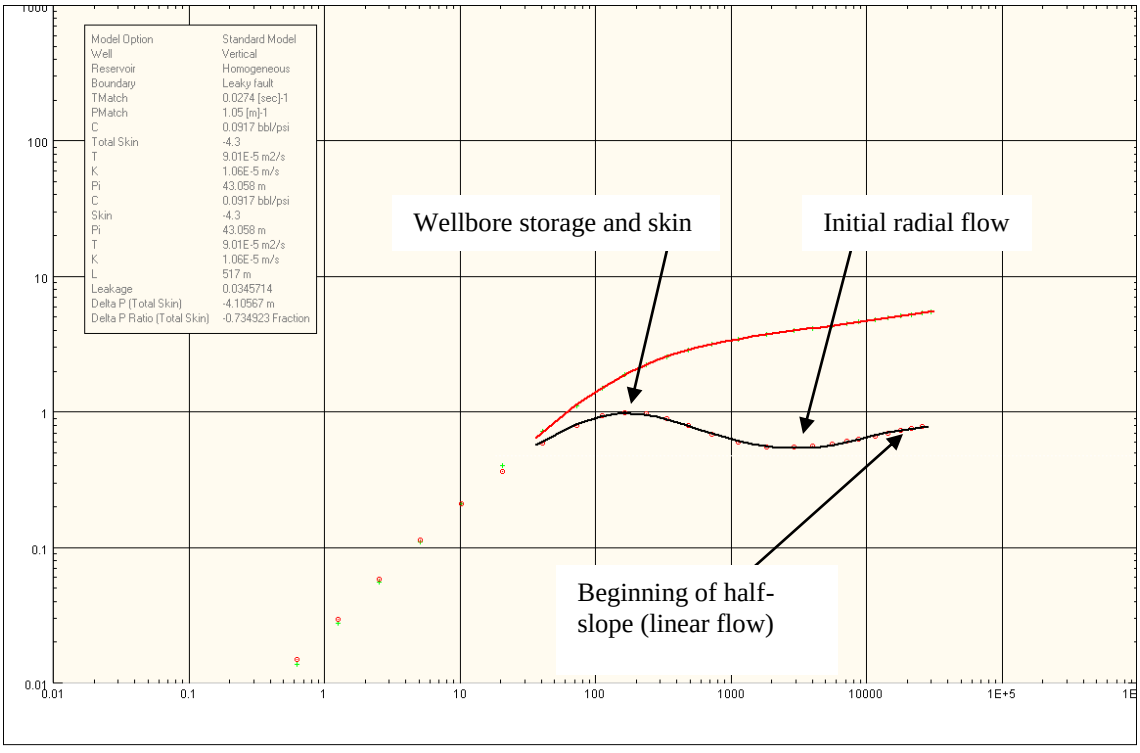

Log-Log plot: p-p@dt=0 and derivative [m] vs dt [sec]

The results of the Saphir analysis indicate a transmissivity value of the 9.01 x 10^{-05} m^2/s and a hydraulic conductivity of 1.06 x 10^{-5} m/s.

Figure 5.33: Realization 46 AQTESOLV pressure transient analysis of pumping test data after 8.8 hours of pumping

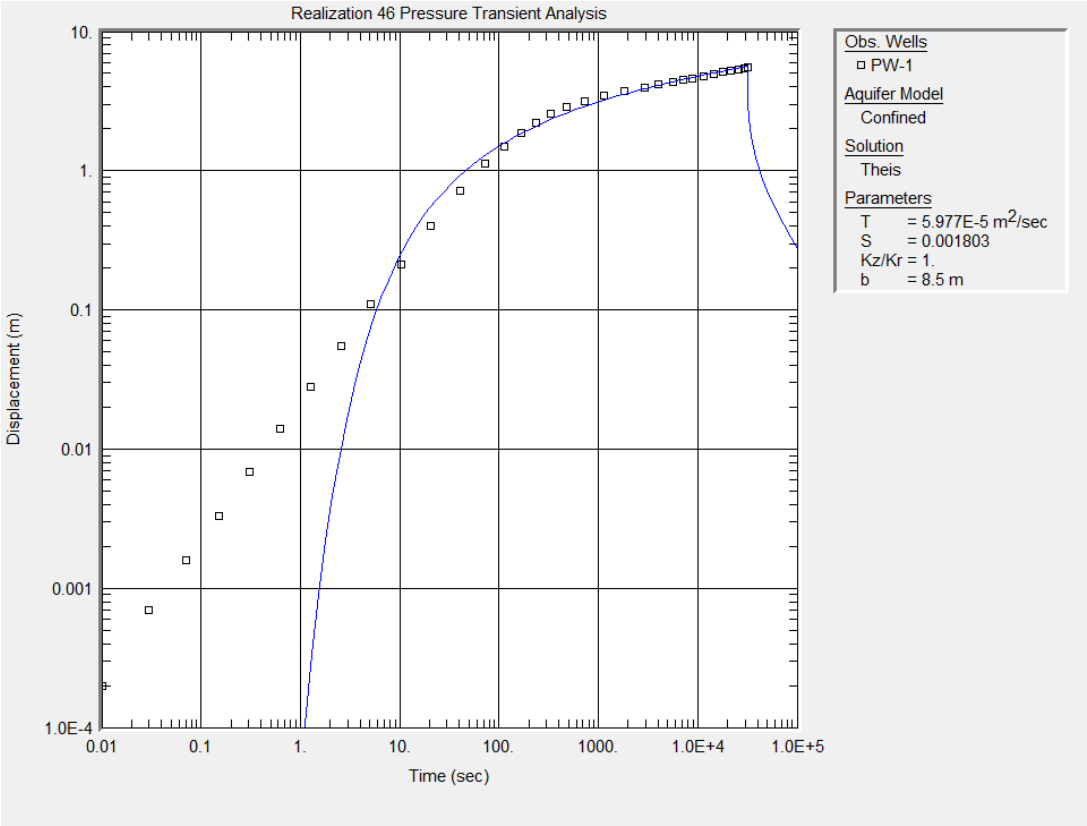

Figure 5.33 illustrates the pressure transient analysis of pumping test data after 8.8 hours of pumping. Pressure transient analysis of pumping test data was performed using AQTESOLV and application of the Theis confined aquifer solution. This solution yielded a transmissivity is 5.98 x 10^{-05} m^2/s (conductivity 7.03 x 10^{-06} m/s) and a storage value of 1.8 x 10^{-03}. By comparison, the AQTESOLV figure illustrates a poor fit to the data up to approximately 1.0 x 10^{+04} seconds (approximately 3 hours). As previously discussed, this early time response is due to wellbore storage and skin which was not modeled using this approach.

The hydraulic conductivity determined by both Saphir (1.06×10^{-05} m/s) and AQTESOLV (7.03×10^{-06} m/s) are both less than the mean effective hydraulic conductivity Kx (1.49×10^{-04} m/s) and Ky (4.61×10^{-05} m/s) but both are greater than the effective hydraulic conductivity eff_{Kx} evaluated for Realization 46 at 1.56×10^{-06} m/s. Both fall within the minimum and maximum effective hydraulic conductivity in the y-direction (6.72×10^{-08} m/s to 4.50×10^{-04} m/s). Only the Saphir derived conductivity is close to the hydraulic conductivity value (1.0×10^{-05} m/s) assigned to the channel sands.

Realization 46 (Rank: P68) Theoretical Long Term Yield

For the Theis solution (AQTESOLV) yielded a transmissivity of 5.98×10^{-05} m^2/s with an available drawdown of 43 m, the calculated Q_{20} is 0.00122 m^3/s. This resulted in a long-term safe yield of 38,580 m^3/year. The 20 year forward prediction using the Saphir model and associated parameters and the Q_{20} rate indicates a drawdown of 10.94 m which would indicate that the Q_{20} rate is sustainable for this scenario.

Realization 48 (Rank: P90) Model Results

Realization 48 represents a model domain with an effective hydraulic conductivity at the ninetieth percentile of the 100 realizations. The lateral and vertical distribution of the facies can be seen in Figures 4.15 and 4.16. Figure 5.34 shows the drawdown versus time for the pumping well. The drawdown portion of the curve has an irregular shape and changing slopes that are likely a function of how the pressure wave moves out into the sands, splays, and overbank deposits.

After 4 hours, a linear flow regime developed within well defined channel sand in the center of the model domain at a depth of 36 m (Figure 5.35). The channel sand does not appear to be wide and immediately laterally connected to other channel sands and seems to be isolated within the center of the model as seen in the hydraulic conductivity field at a depth of 35 m (Figure 5.36).

By 9.2 hours, the test has run long enough for multiple flow regimes to develop at different stratigraphic horizons. Linear flow regimes were observed at 23 and 36 m in depth (Figures 5.37 and 5.39). An irregular shaped pressure wave is observed at a depth of 32 m and does not seem to conform to any particular shape of any hydraulically conductive facies at that depth (Figure 5.38). The pressure wave may have likely propagated irregularly out from the pumping wells based on the presence of sands, splays and overbank deposits.

Figures 5.40 and 5.41 illustrate the distribution of the pressure wave in cross section illustrating the presence of linear flow distribution of facies. It can be seen where the majority of drawdown in the channels has moved through the crevasse splays and overbank deposits to other sands.

Figure 5.34: Realization 48 Drawdown versus time curve for pumping well PW1

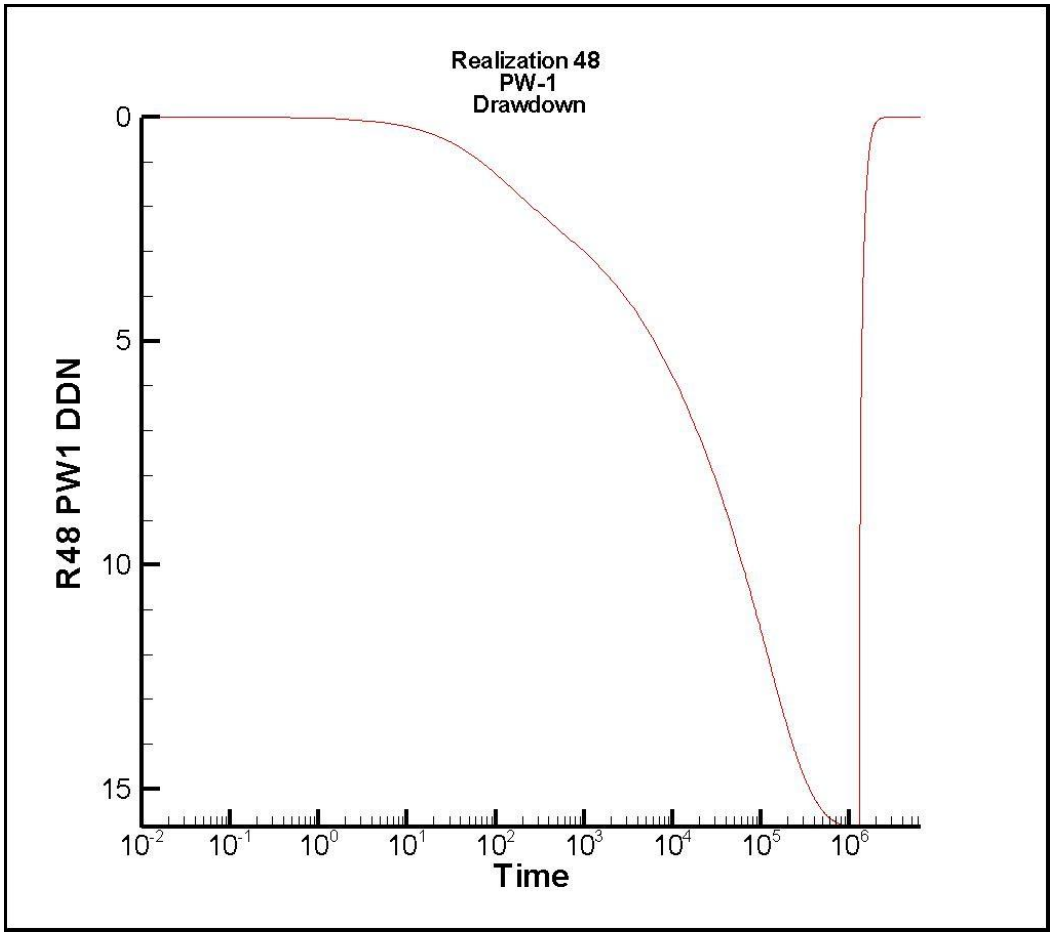

Figure 5.34 shows the drawdown curve for the pumping wells from the model run. The irregular shape of the curve is due to the presence of multiple flow regimes at different stratigraphic levels within region propagated by the pressure wave.

Figure 5.35: Realization 48 pressure head field early time (4 hours) data at 36 m depth. Pumping interval between 29.75 m to 37.75 m depth.

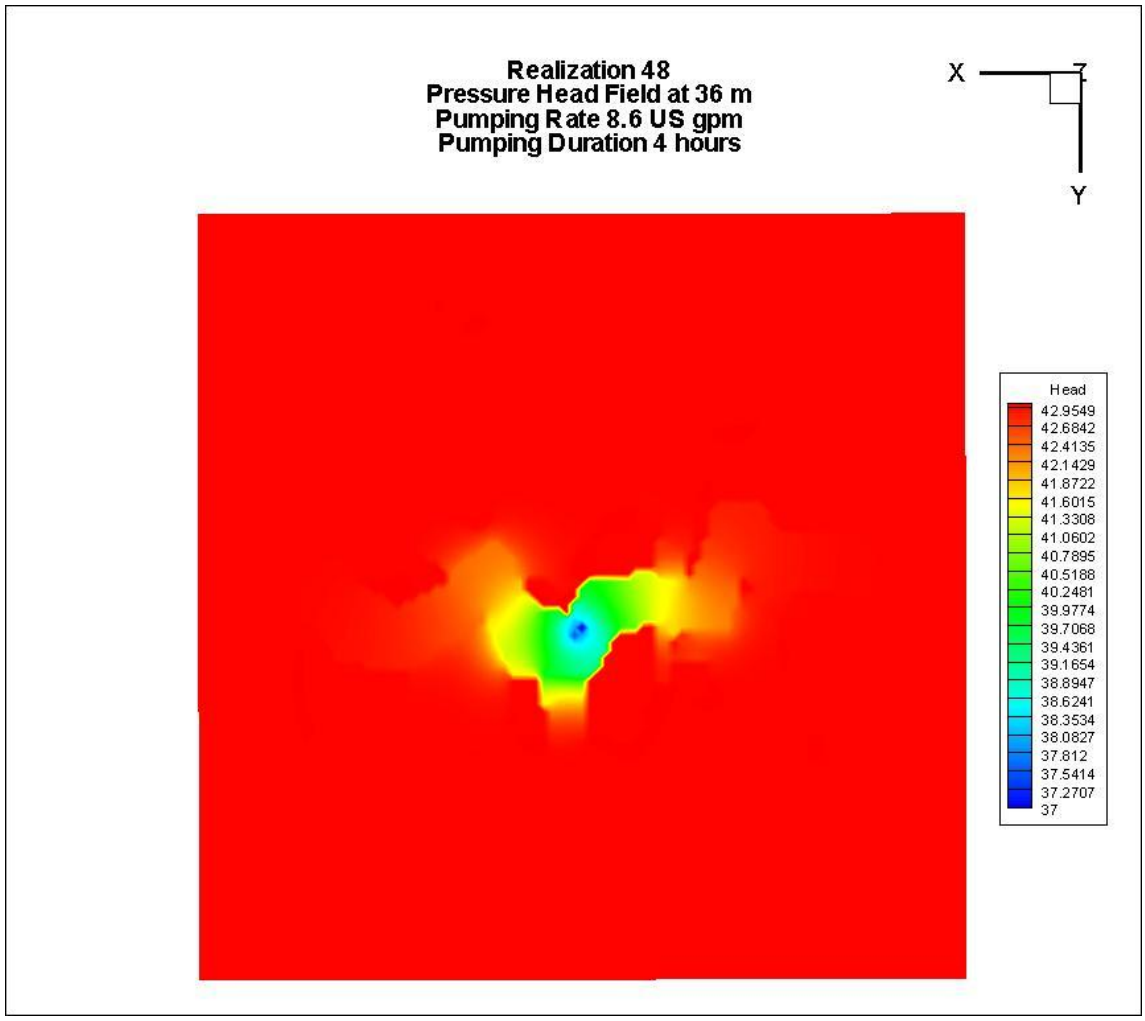

The figure illustrates the pressure wave distribution at a depth of 36 m and shows linear flow in a channel.

Figure 5.36: Realization 48 hydraulic conductivity field at 35 m depth

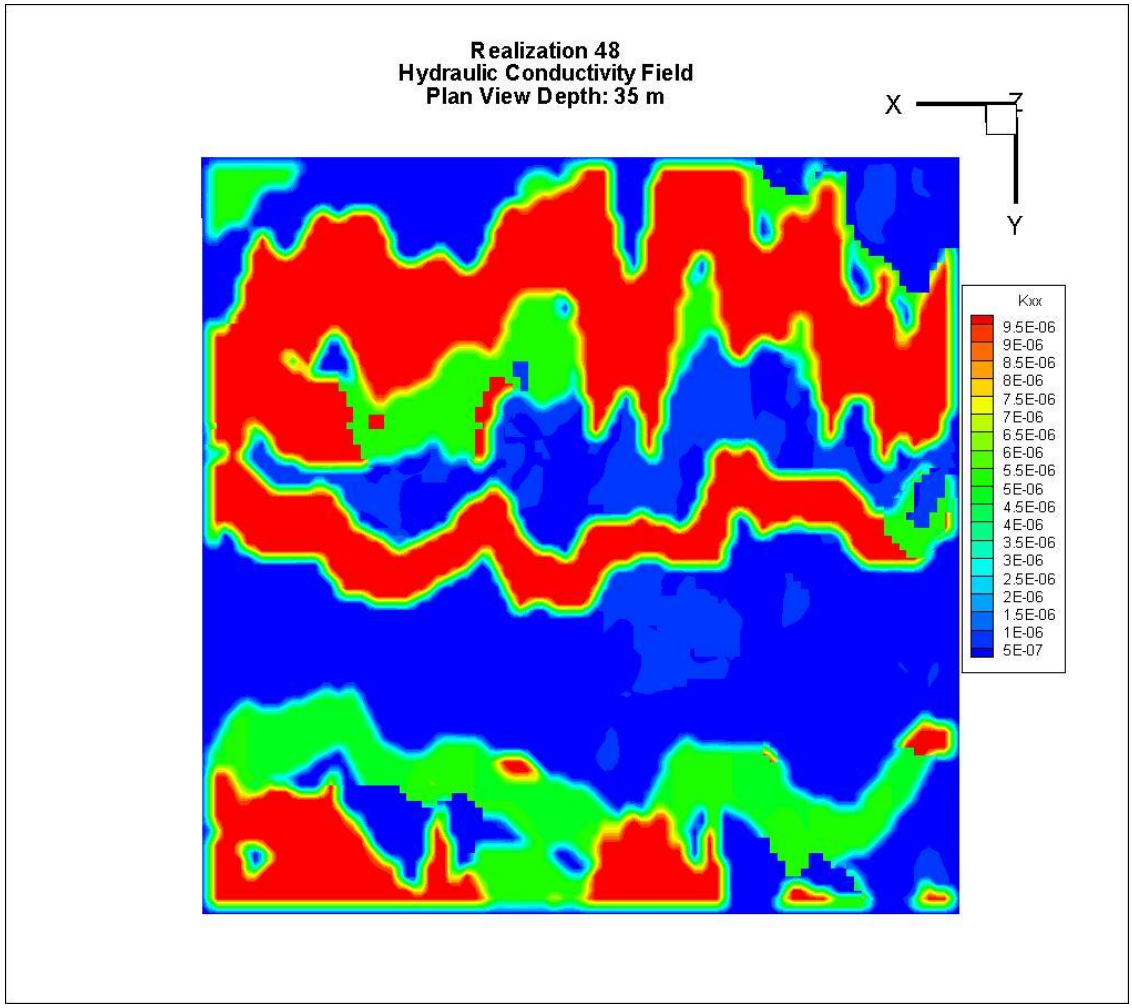

The figure illustrates the distribution of the hydraulically significant facies at a depth of 35 m. A single channel sand is present along the center of the model parallel to the x-axis.

Figure 5.37: Realization 48 pressure head field at 23 m depth after 9.2 hours of pumping. Pumping interval between 29.75 m to 37.75 m depth.

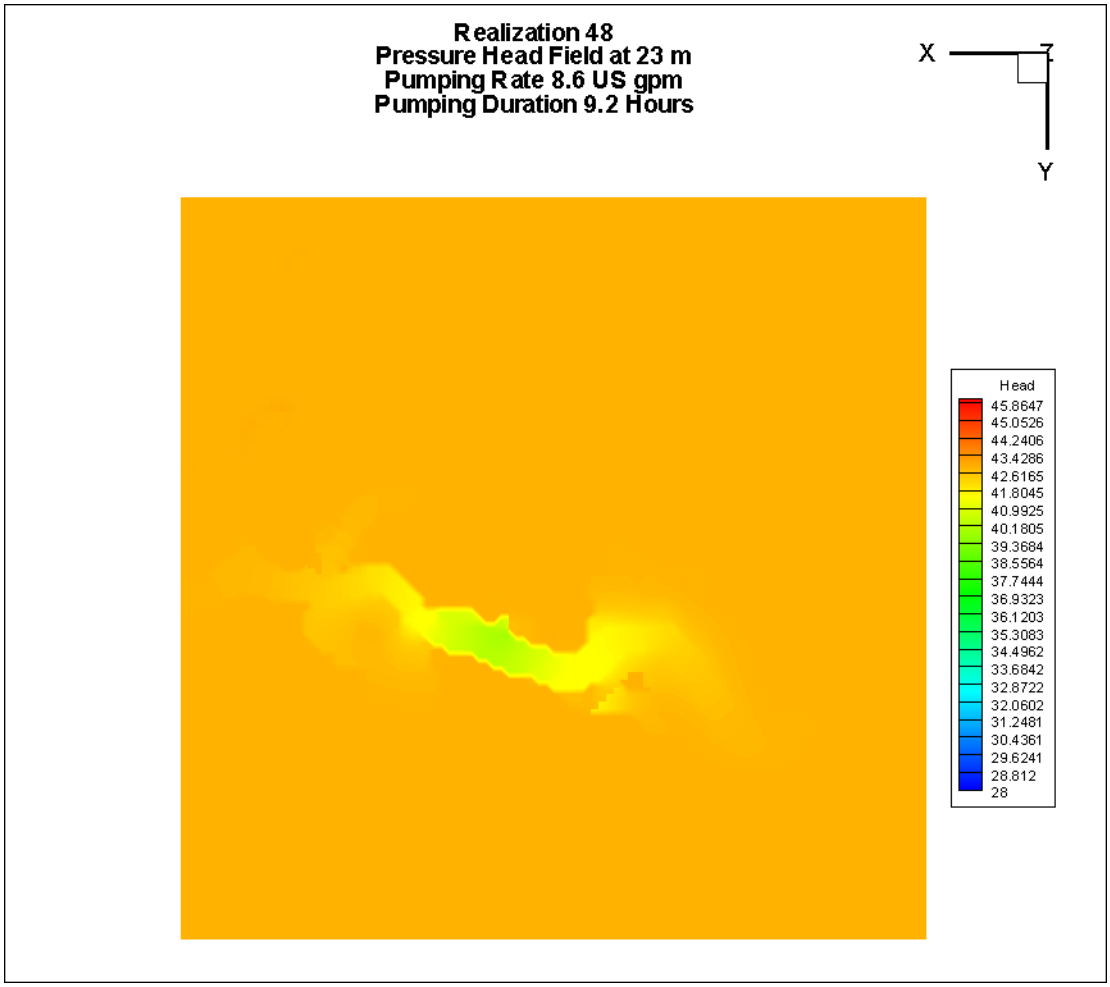

The figure illustrates the presence of a channel and linear flow during long-term pumping test.

Figure 5.38: Realization 48 pressure head field at 32 m depth after 9.2 hours of pumping. Pumping interval between 29.75 m to 37.75 m depth.

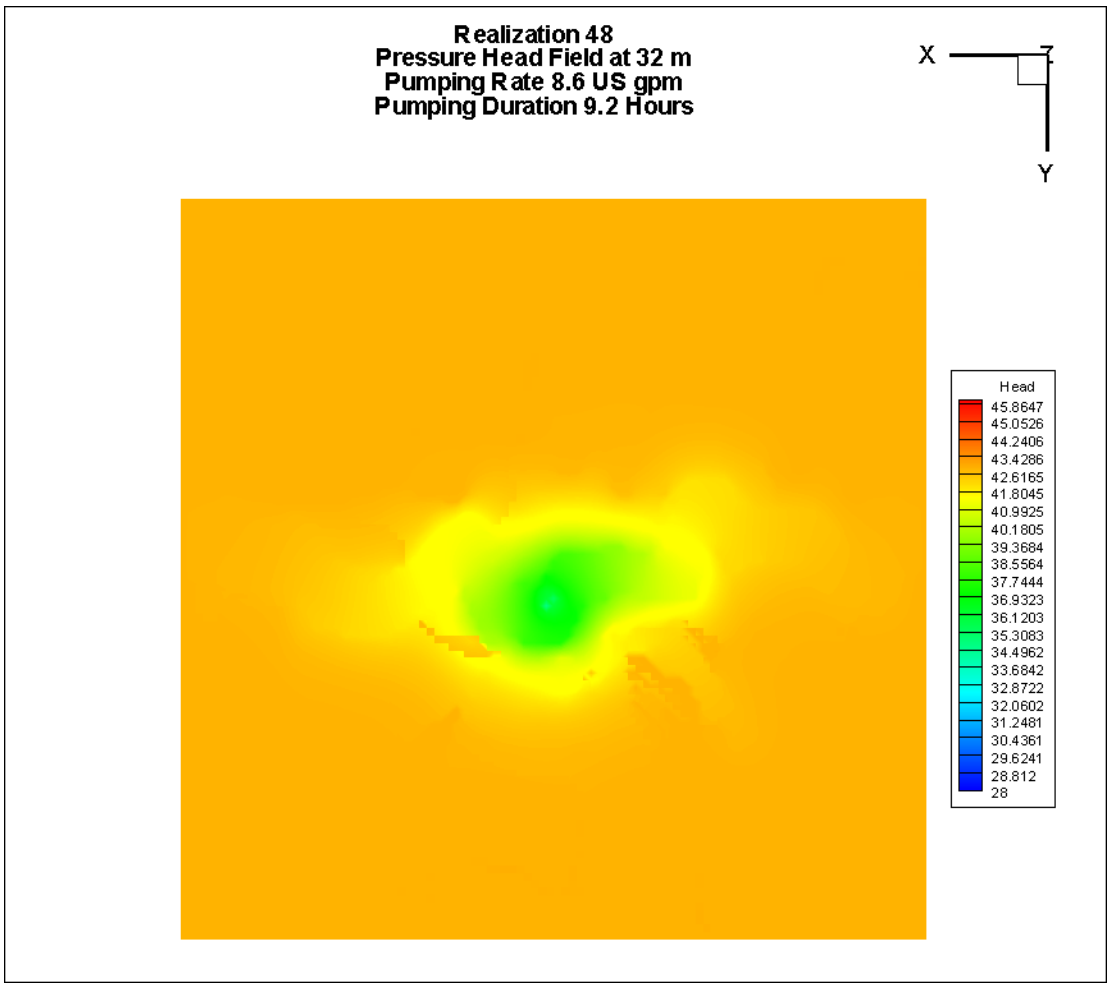

The figure illustrates what may have initially started as radial flow has now become an irregularly shape pressure wave where we see the edges of high permeability zones such as crevasses splays and channel sands.

Figure 5.39: Realization 48 pressure head field at 36 m depth after 9.2 hours of pumping. Pumping interval between 29.75 m to 37.75 m depth.

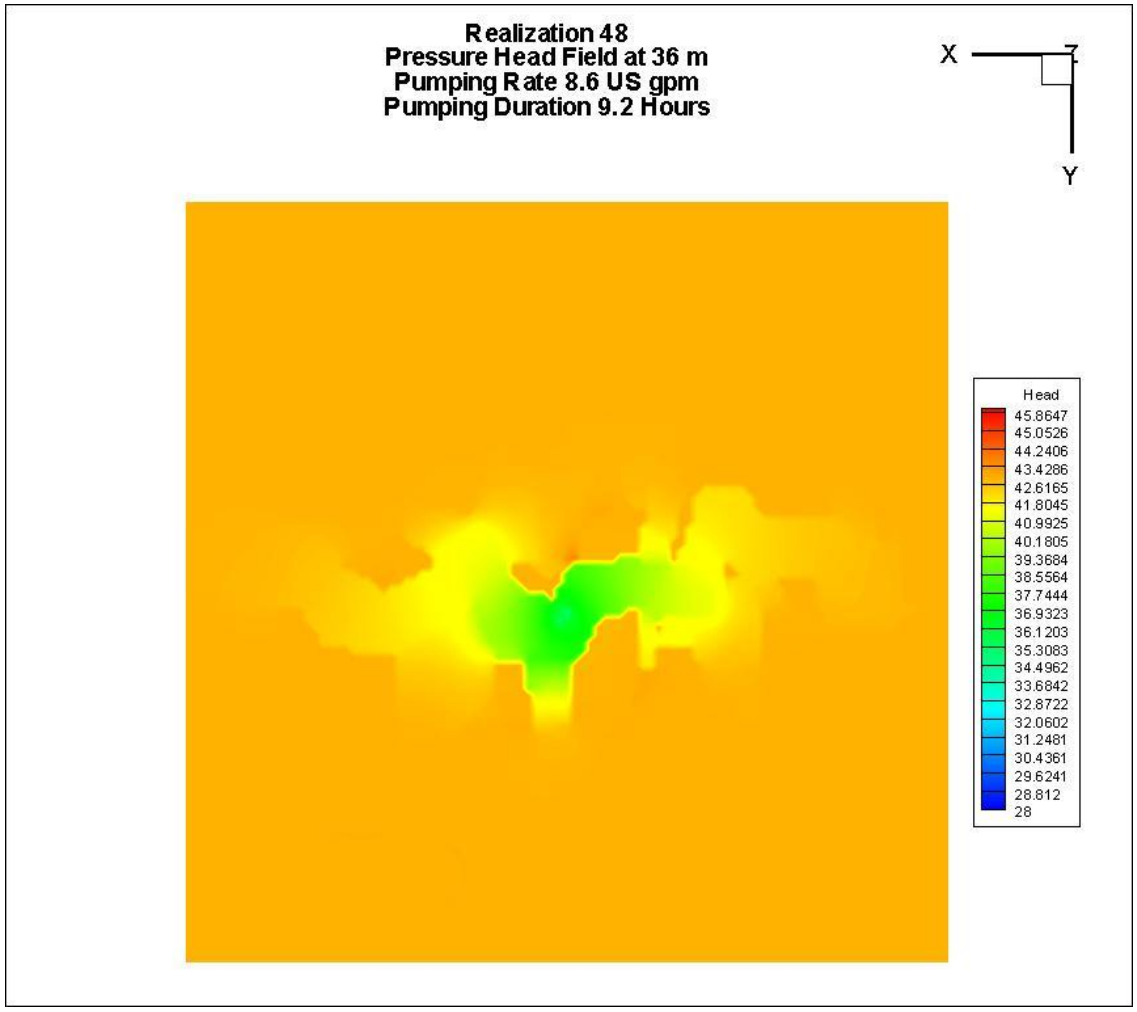

The figure illustrates linear flow in a channel sand. It can be seen that the flow regime has extended further through the channel than in the previous figure.

Figure 5.40: Realization 48 pressure head field cross section after 9.2 hours of pumping

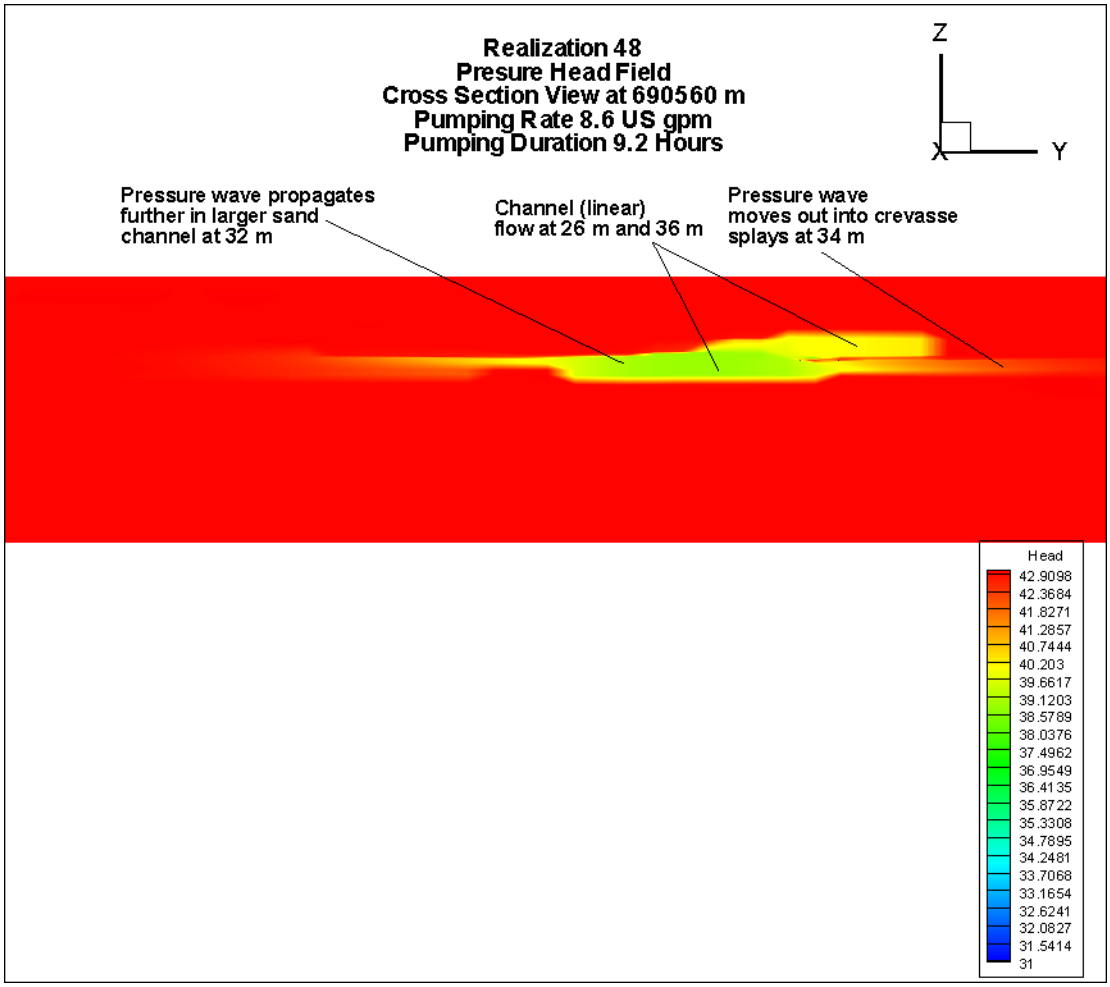

The figure illustrates a cross sectional view of the pressure head field illustrating the different flow regimes occurring at different stratigraphic levels.

Figure 5.41: Realization 48 hydraulic conductivity field cross section

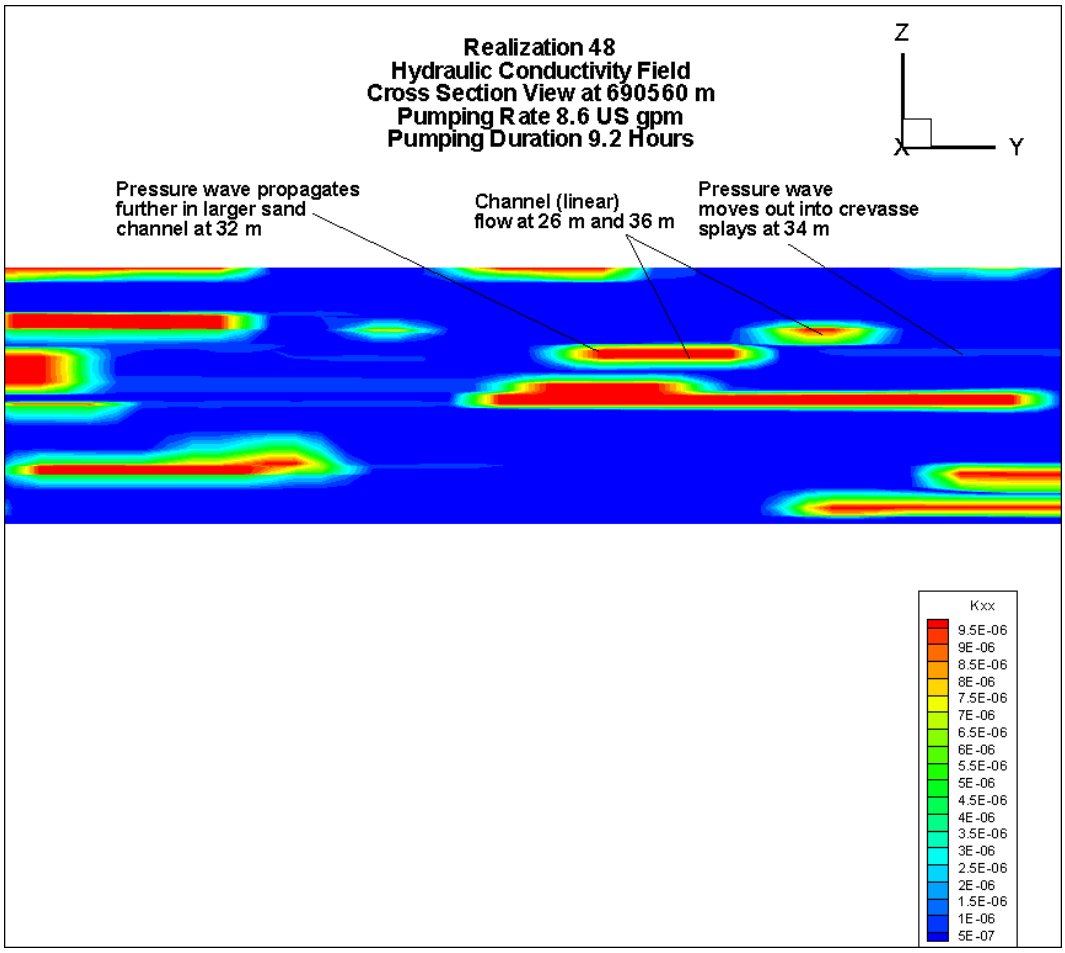

The figure illustrates the hydraulic conductivity field and the different geologic objects (sands, splays, and overbank deposits) in relation to the pressure wave illustrated in Figure 5.40.

Realization 48 (Rank: P90) Pressure Transient Analysis

Figure 5.42 illustrates the results of pressure transient analysis using Saphir. A standard model using a fracture with finite conductivity, homogeneous reservoir and one fault was used to fit the data and provide a solution. Review of the Saphir output illustrates a

proper fit to the data. The hydraulic conductivity for this solution was estimated at 9.80 x 10^{-07} m/s and a transmissivity of 7.84 x 10^{-06} m^2/s. The derivative curve in the figure illustrates a half slope indicative of linear flow. This flow regime is observed in Figures 5.35 at 36 m below the model surface layer after 4 hours of pumping, Figure 5.37 at 23 m below the model surface layer at 9.2 hours and in Figure 5.39 at 36 m after 9.2 hours. Figure 5.43 illustrates the results of the analysis by AQTESOLV using the Theis model.

Figure 5.42: Realization 48 pressure transient analysis test data after 9.2 hours of pumping

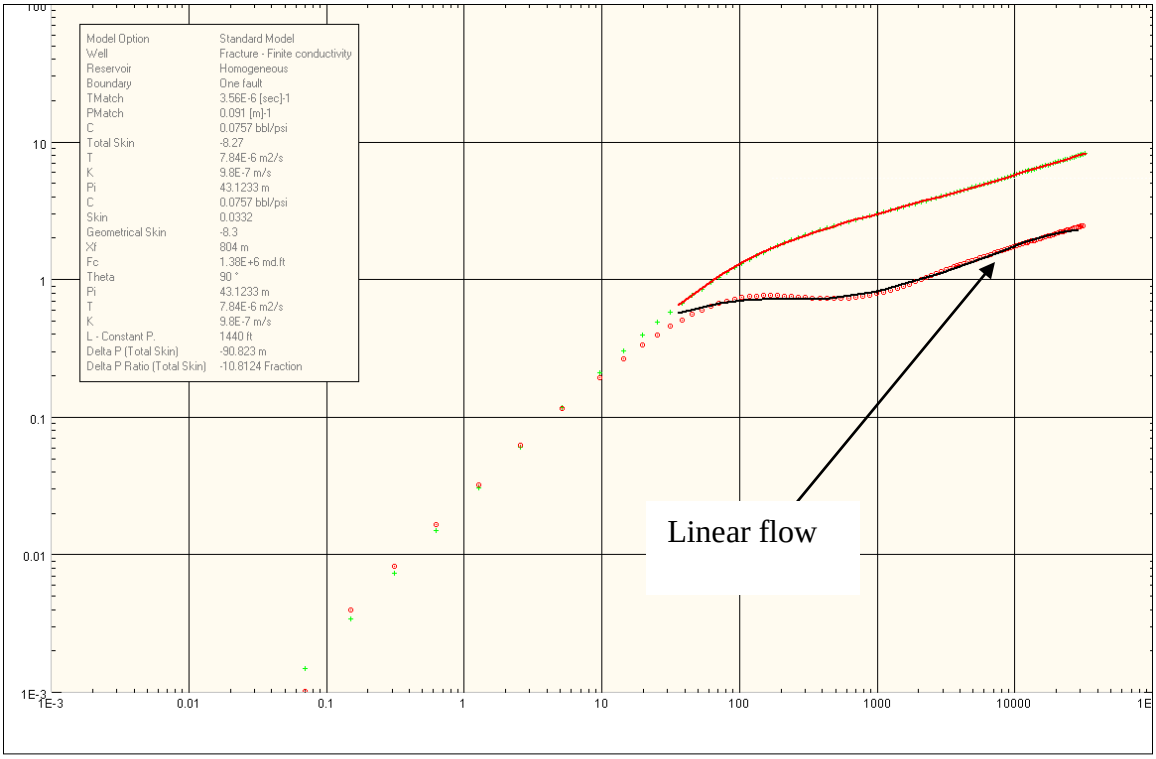

Log-Log plot: p-p@dt=0 and derivative [m] vs dt [sec]

Figure 5.43: Realization 48 AQTESOLV pressure transient analysis of test data after 9.2 hours of pumping

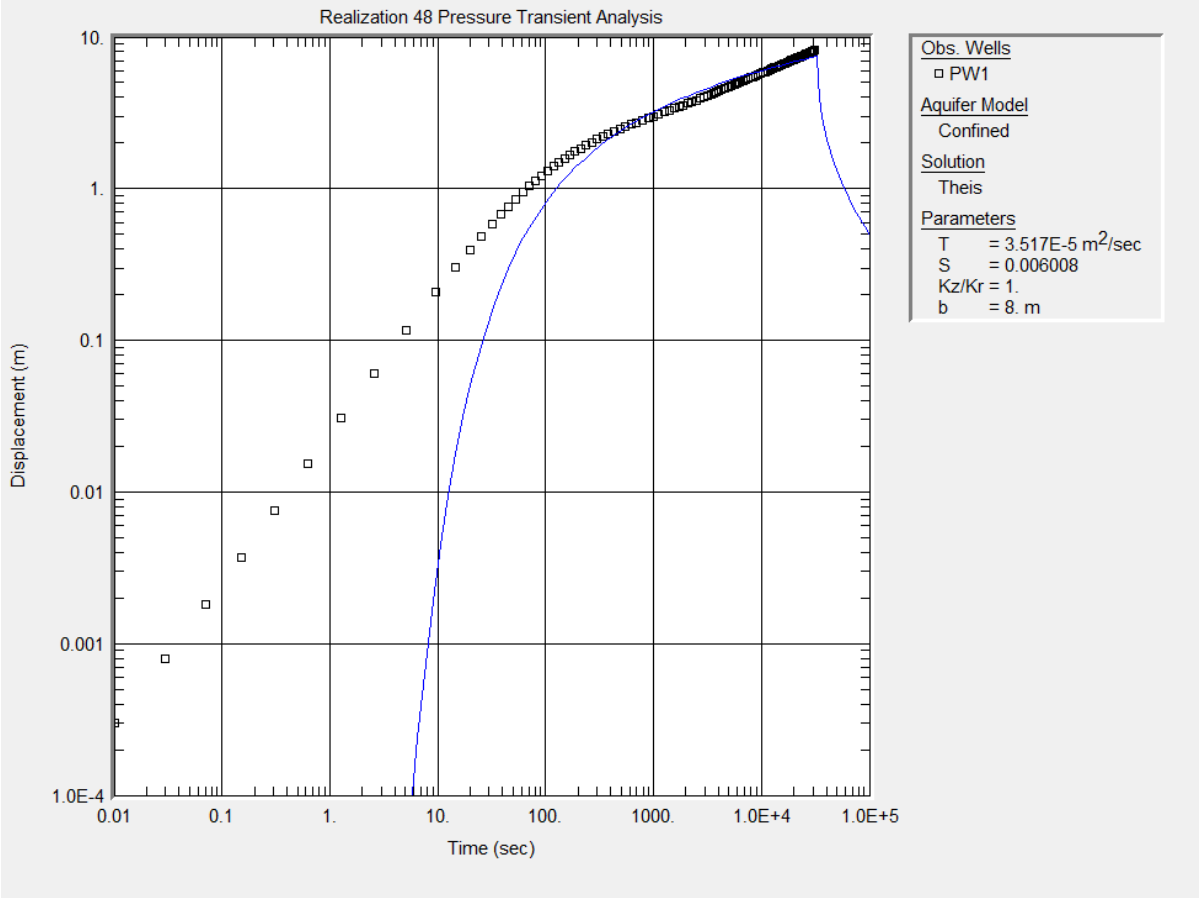

Figure 5.43 illustrates the results of the analysis using AQTESOLV and the Theis solution for a confined aquifer which yielded a transmissivity of 3.52 x 10^{-05} m^2/s (conductivity 4.40 x 10^{-06} m/s). Figure 5.43 indicates a poor fit to the data at less than 300 seconds as a result of the effect of wellbore storage on the early time pressure response.

The hydraulic conductivity determined by both Saphir (9.80 x 10^{-07} m/s) and AQTESOLV (4.40 x 10^{-06} m/s) are both less than the mean effective hydraulic

conductivity Kx (1.49 x 10^{-04} m/s) and Ky (4.61 x 10^{-05} m/s). The Saphir value for conductivity is less than the effective hydraulic conductivity eff_{Kx} evaluated for Realization 48 as 1.71 x 10^{-06} m/s; however, the AQTESOLV conductivity value was greater. Both fall within the minimum and maximum effective hydraulic conductivity in the y-direction (6.72 x 10^{-08} m/s to 1.50 x 10^{-04} m/s).

Realization 48 (Rank: P90) Theoretical Long Term Yield

The Theis solution, which does not include any influence from boundaries, yielded a transmissivity of 3.52 x 10^{-05} m^2/s with an available drawdown of 43 m. The calculated Q_{20} is 7.20 x 10^{-04} m^3/s. This resulted in a long-term safe yield of 22,701 m^3/year. The 20 year forward prediction using the Saphir model and associated parameters (K = 9.80 x 10^{-07} m/s) and the Q_{20} indicates a drawdown of 11.1 m and subsequently a sustainable 20 year yield.

Realization 61 (Rank: P31) Model Results

Realization 61 represents a model domain with an effective hydraulic conductivity at the thirty one percentile for all 100 realizations. The modeled system has a lateral and vertical connectivity near the minimum effective hydraulic conductivity. The lateral and vertical distribution of the facies can be seen in Figures 4.7 and 4.18.

After 4 hours the pressure wave has propagated radially from the pumping well. The sharp contrast between the sands and the overbank deposits can be seen on one side of the pumping well at the surface (Figure 5.44). At 14.2 hours the pressure wave has

propagated outward and the extent and width of the channel sands can be observed. The majority of the drawdown occurs on one side of the pumping well in the sands and crevasse splays (Figure 5.45). Figure 5.46 illustrates the hydraulic conductivity field of the model at a depth of 1 m. It can be seen how the pressure wave has moved through the hydraulically conductive facies (sand and splays).

Figure 5.47 shows the pressure wave distribution in cross section and how the wave has laterally moved out from the pumping well until it reached a lower channel sand located on the right hand side of the figure. At this point during the pumping test, the wave moves vertically downward into the lower channel sand and moves back toward the pumping well location. The distribution of the pressure wave can be matched to the locations of the channel sands as illustrated in Figure 5.48.

Figure 5.44: Realization 61 pressure head field early time (4 hours) results. Pumping interval between 0 to 6.25 m depth.

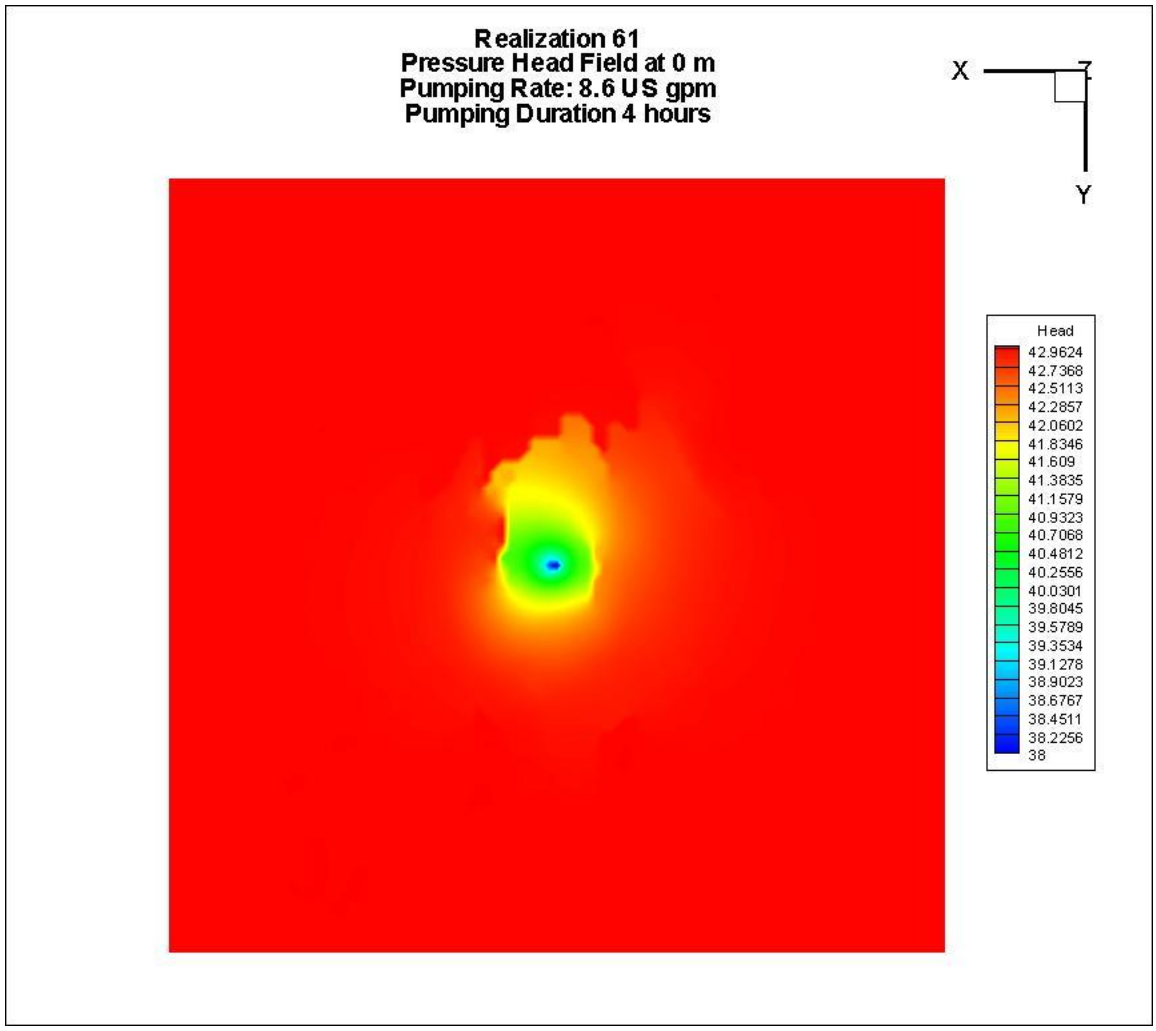

The figure illustrates the pressure wave at the surface. Here the pressure wave has initially radially propagated from the well until movement is primarily in one direction and intersects a sharp contrasting boundary on the opposite side of the pressure wave.

Figure 5.45: Realization 61 pressure head field after 14.2 hours of pumping. Pumping interval between 0 to 6.25 m depth.

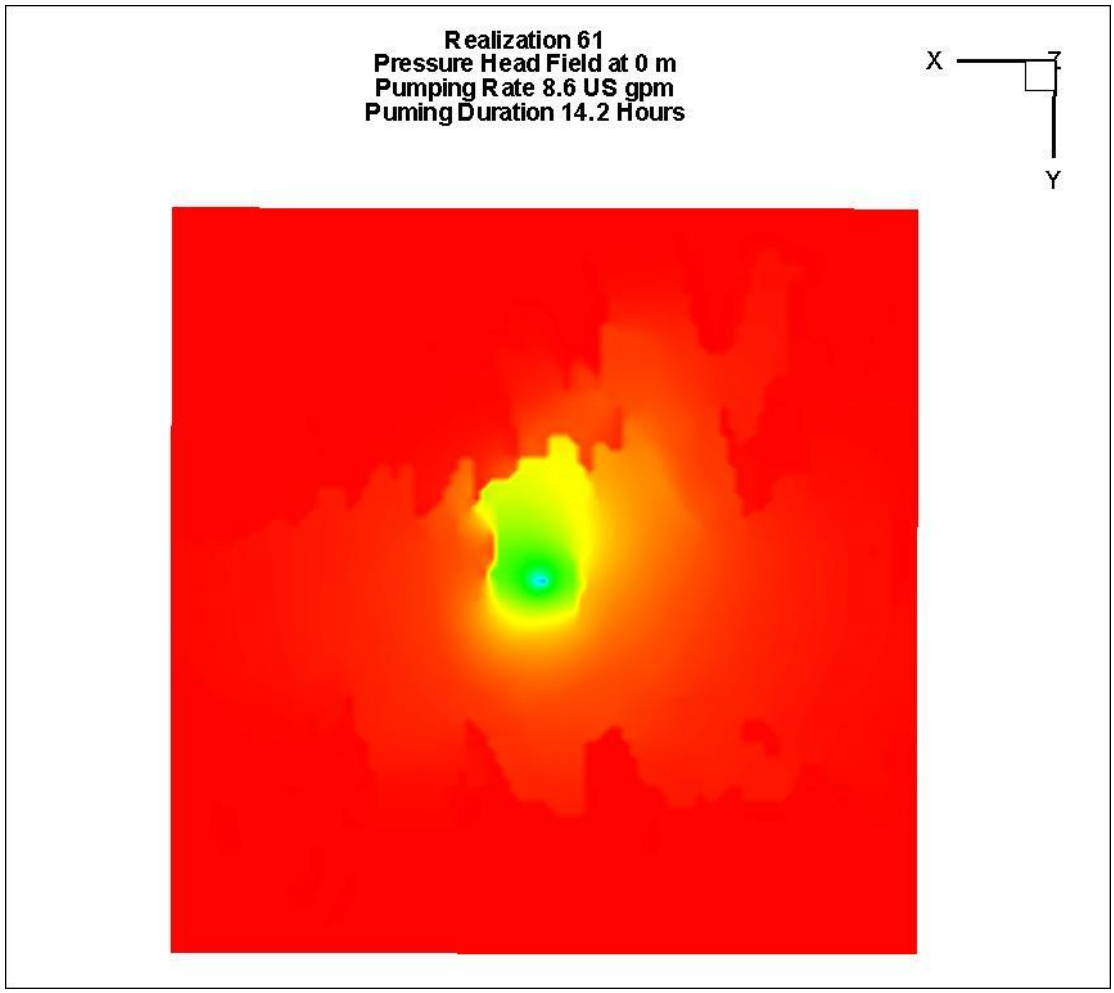

Here the pressure wave has propagated further intersecting the channel boundaries toward the top and lower portions of the model. The hydraulic conductivity field is presented in Figure 5.46. The outline of the sands and crevasse splays can be matched up with the pressure wave extent in Figure 5.47.

Figure 5.46: Realization 61 hydraulic conductivity field illustrating the distribution of the sands and crevasse splays. Pumping interval between 0 to 6.25 m depth.

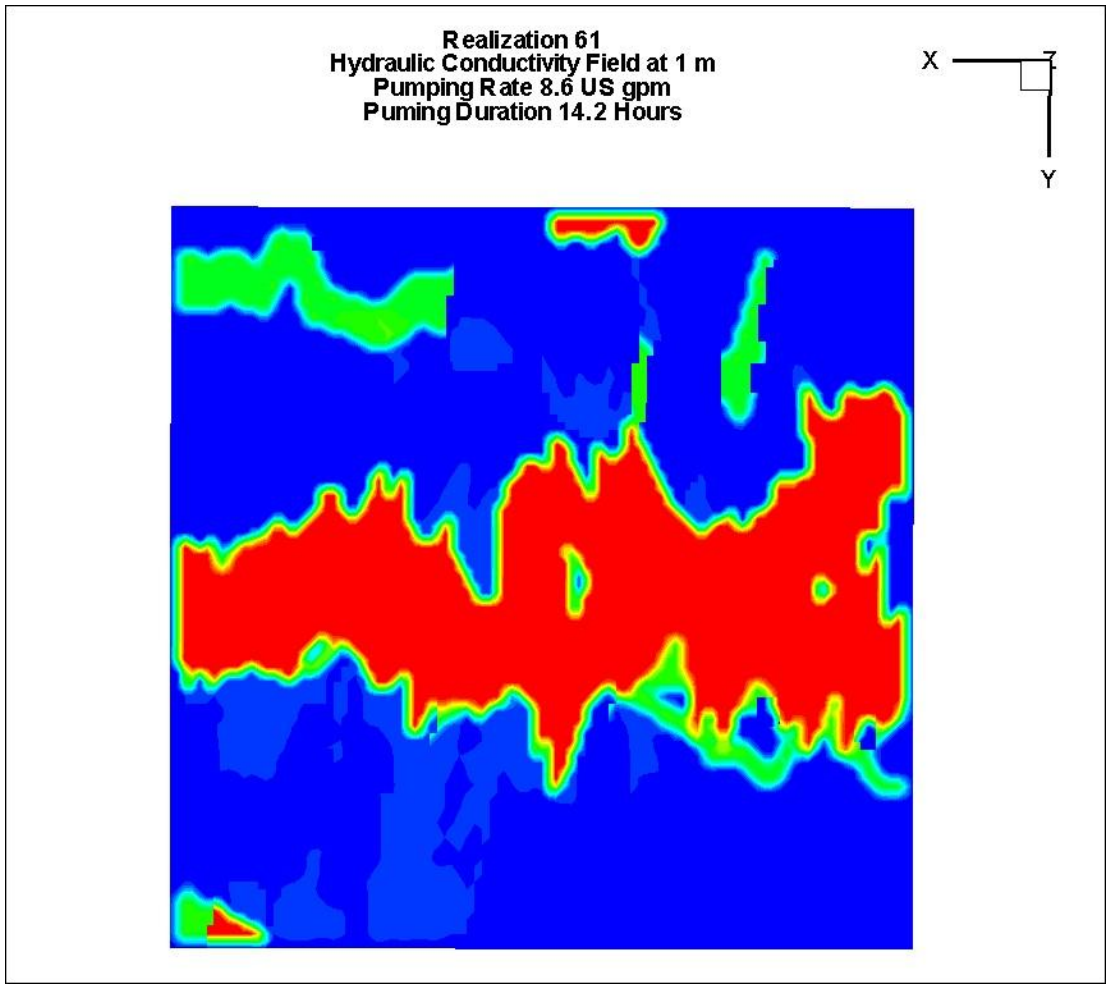

Figure 5.47 presents the pressure head field where the pressure wave propagated through the system. It can be seen that the wave moved out from the well until it reached another sand body and then moved vertically downward and then laterally back toward the direction of the well.

Figure 5.47: Realization 61 Pressure Head Field at 14.2 hours.

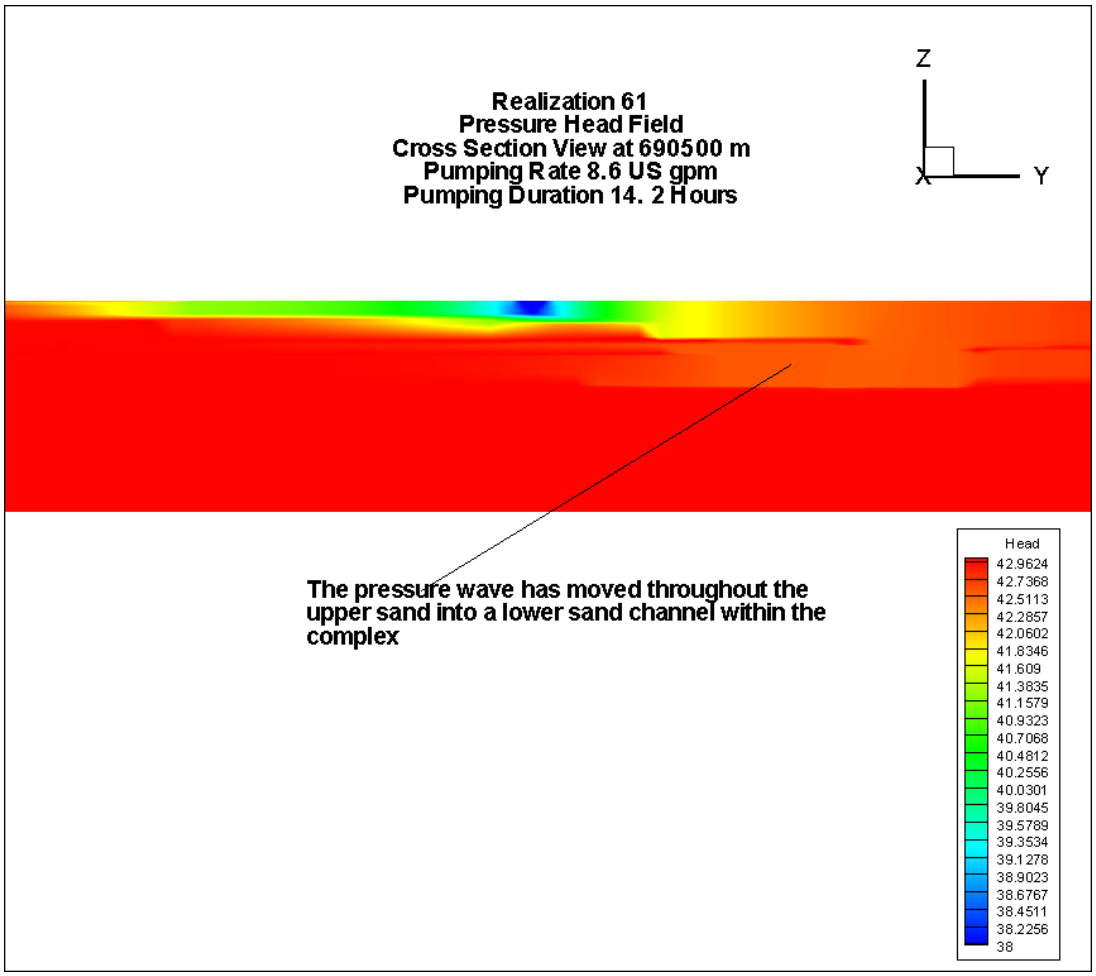

The cross section of the hydraulic conductivity field for Realization 61 is presented in Figure 5.48. The figure illustrates the relationship between the geologic objects of sands, crevasses, and overbank deposits.

Figure 5.48: Realization 61 Hydraulic Conductivity Field Cross Section.

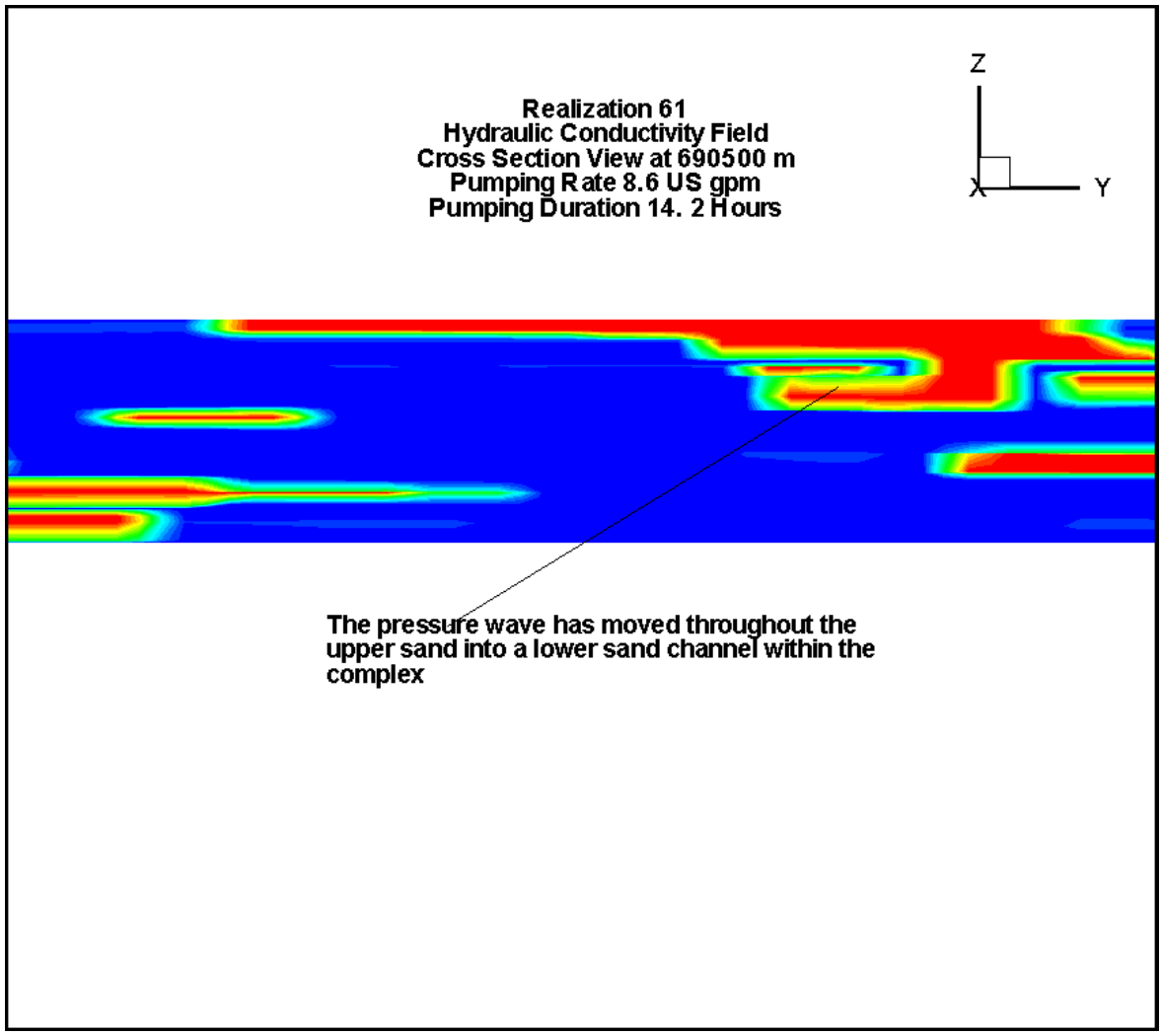

Realization 61 (Rank: P31) Pressure Transient Analysis

Figure 5.49 illustrates the results of pressure transient analysis using Saphir. A standard model with a fracture of infinite conductivity and a radial composite reservoir and a no flow circle boundary was used to fit the data and provide a solution. A second model was

selected and applied to the data which provided a similar solution. This solution used an infinite reservoir instead of a closed system. Both solutions yielded the same parameter values with a transmissivity of 6.23×10^{-05} m^2/s and a conductivity of 9.97×10^{-06} m/s.

This model has several elements which are relevant to how the pressure wave propagates through the system. The following is a discussion of this model. To fracture a formation it is imperative that fluid is pumped against a high resistance, at the bottom of the wellbore, so the bottom hole pressure rises above the fracture gradient of the formation. Once initiation of the fracture has been established, the bottom hole pressure must be maintained so that the fracture propagates away from the wellbore. During this operation a proppant is used so that the fracture faces will remain open. The model assumes that the fracture maintains a constant width and height or length. The infinite conductivity model assumes that the pressure drop along the inside of the fracture is negligible; therefore the final assumption is that there is no pressure drop along the fracture. Furthermore, unless the fracture length is too small, the behavior is dominated by a linear and uniform flow from the reservoir towards the fracture and orthogonally to the fracture plane (Houzé et al. 2008). The composite reservoir model allows for consideration of variation in the mobility in the lateral direction. Mobility (M) here is defined as the ratio of permeability (k) to viscosity (μ). Cases where observation of a change in mobility in the reservoir occurs where there is compartmentalization and actual changes in reservoir characteristics such as porosity and permeability (Houzé et al. 2008). The mobility between different compartments or changes between facies (i.e. facies 1 and facies 2) is defined in the following equation.

$$M = \frac{\left(\frac{\kappa}{\mu}\right)_1}{\left(\frac{\kappa}{\mu}\right)_2} \qquad [5.6]$$

Because we are modeling a single phase system this equation reduces to the ratio between the two permeability values. The analytical solutions which model these changes are referred to as composite models. Their geometry is straightforward and they are governed by two parameters. The most common is the radial composite. The radial composite model has two compartments, an inner compartment of radius r1 (compartment 1) where the well is at center and a second outer compartment. At the composite interface there is a change in the pressure gradient. The flux on both sides is the same however, since the mobility is different Darcy's law provides two different pressure gradients (Houzé et al. 2008). Early on in a pumping or injectivity test, the pressure will diffuse in compartment 1 resulting in a homogeneous behavior but when the composite limit is reached there is a change of apparent mobility and diffusivity (Houzé et al. 2008).

Figure 5.49: Realization 61 Saphir Pressure Transient Analysis of Pumping Test Data.

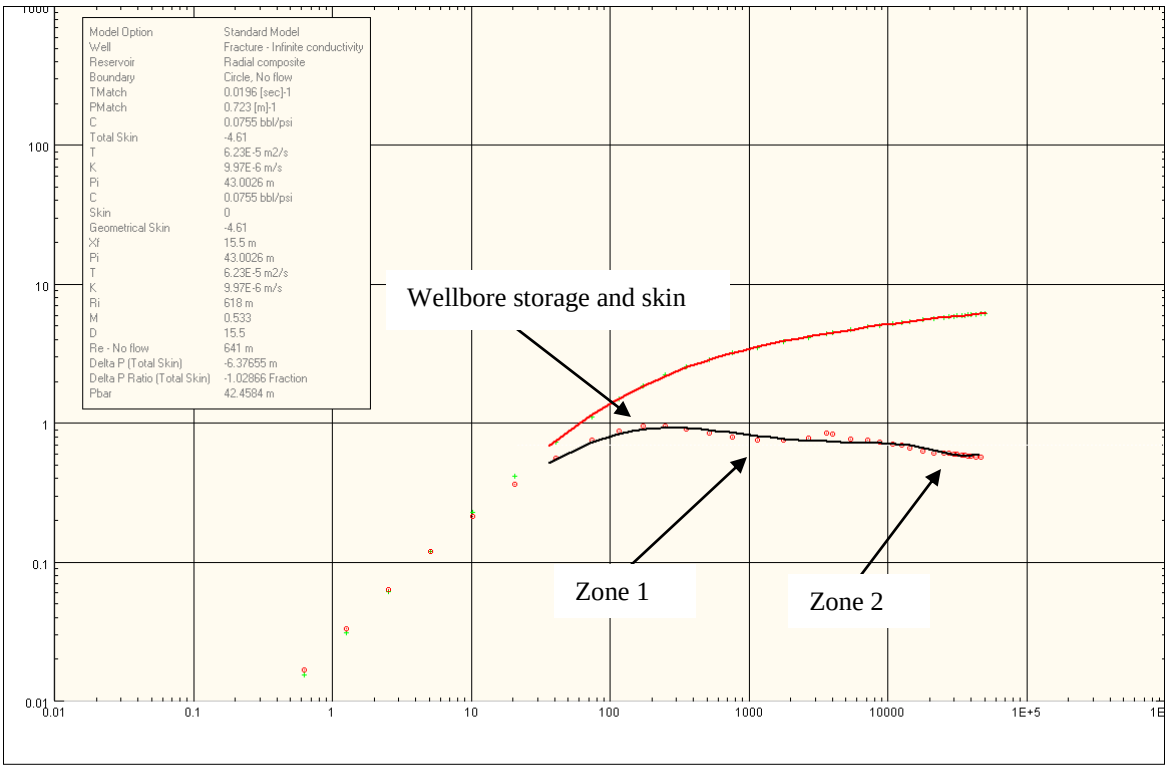

Log-Log plot: p-p@dt=0 and derivative [m] vs dt [sec]

Figure 5.50: Realization 61 AQTESOLV Pressure transient analysis of pumping test data

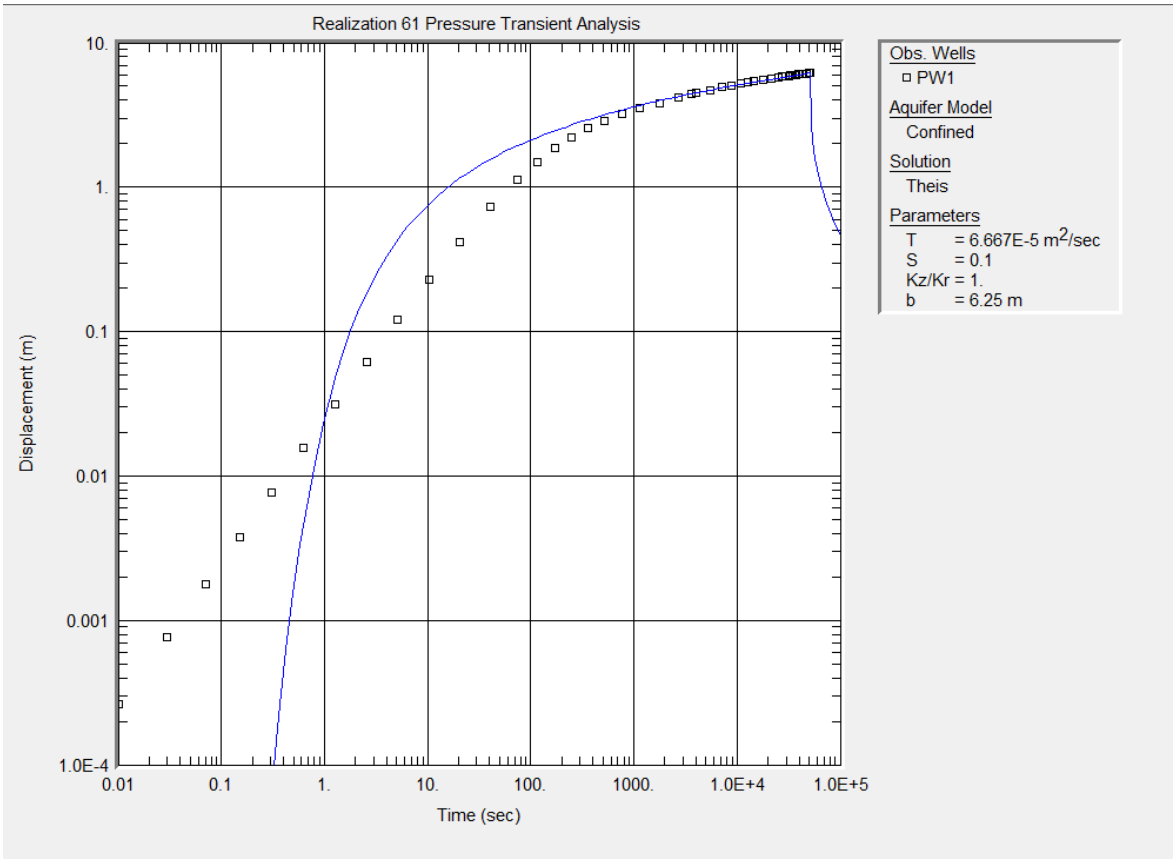

The Theis model for a confined aquifer was used and yielded a solution where the transmissivity is 6.67 x 10^{-05} m^2/s. The pressure wave intersects the model boundaries after 51,335 seconds (14.2 hours). The effects of wellbore storage are observed in the early time response within the initial 1,000 seconds.

The hydraulic conductivity determined by both Saphir (9.97 x 10^{-06} m/s) and AQTESOLV (1.07 x 10^{-05} m/s) are both are less than the mean effective hydraulic conductivity Kx (1.49 x 10^{-04} m/s) and Ky (4.61 x 10^{-05} m/s) but both are greater than the

effective hydraulic conductivity eff_{Kx} evaluated for Realization 61 at 1.38 x 10^{-06} m/s. Both fall within the minimum and maximum effective hydraulic conductivity in the y-direction (6.72 x 10^{-08} m/s to 4.50 x 10^{-04} m/s). The Saphir derived conductivity for this solution is less than the solutions for the previous realizations which are all close to the conductivity value (i.e., 1.0 x 10^{-05} m/s) which was assigned to the channel sands of the model.

Realization 61 (Rank: P31) Theoretical Long Term Yield

Using the Theis solution yielded a transmissivity of 6.67 x 10^{-05} m^2/s with an available drawdown of 43 m; the calculated Q_{20} is 1.34 x 10^{-03} m^3/s. This resulted in a long-term safe yield of 43,034 m^3/year. The 20 year forward prediction using the Saphir model (i.e., infinite boundary solution) and associated parameters and the Q_{20} indicates a drawdown of 37 m, approximately 6 m short of drawing down all of the available head. Use of the Saphir solution with a no flow circle boundary yielded a drawdown of approximately of over 2,000 m which suggests that it is important to evaluate the system and determine the proper reservoir type and boundary conditions when evaluating long-term safe yield as in this case the Q_{20} is unsustainable.

Discussion

The heterogeneous nature of these geologically complex aquifer systems poses a unique challenge to the characterization and evaluation of the system pertaining to water allocation and conservation. Deterministic methods for the description of these systems have limited utility. Once parameterization of the grid cells of the deterministic model

has been completed, the solution has already been fixed since deterministic models do not account for uncertainty. The object-based modeling approach of geomodeling can stochastically simulate channel complexes or belts and from this we can infer the behaviour of a statistically well defined aquifer (Deutsch 2002; Burns et al. 2010b).

The objective was to investigate an alternative method of evaluating the aquifer system behaviour for the purpose of determining the system performance and long-term yield and evaluate long-term (approximately 8 to 15 hours) pumping tests performed in non-ideal systems. The geomodel and parameter values used in the model were based on an analogue model of the Paskapoo Formation developed by Burns et al. (2010b) and parameter values for sands, silts, and shale published in the literature. The final model design used in the groundwater flow simulations assumed that the crevasse splays were hydraulically significant to flow and play an important role in the connectivity between channel sands allowing for the pressure wave induced by pumping to propagate laterally beyond a single channel. Based on the upscaled steady state simulations, the effective hydraulic conductivity was highest along the length of the channel systems (i.e., x-direction). This would suggest that we need an understanding of the primary valley directions and appropriate anisotropic conductivity values to be able to reproduce system behaviour at the regional scale.

Upscaling of the grid cells provides a means for modeling regional groundwater flow systems. Upscaling of reservoir parameters resulted in an anisotropic distribution of values where K_x (longitudinal to the sand channels) had the highest conductivity values

while K_z (transverse and vertical to the sand channels) had the lowest conductivity values. The implications of upscaling parameter values suggest that we must have an understanding of the primary direction of the subterranean river valley in order to model these systems. Furthermore, hydraulic conductivity is a tensor and numerical groundwater models are only capable of modeling the primary indices of the conductivity tensor K_x, K_y, and K_z. The tensor is a mathematical object that has nine indices as presented in matrix form below.

$$\begin{matrix} K_{xx} & K_{xy} & K_{xz} \\ K_{yx} & K_{yy} & K_{yz} \\ K_{zx} & K_{zy} & K_{zz} \end{matrix}$$

As stated numerical models do not incorporate the use of the conductivity offsets K_{xy}, K_{xz}, K_{yx}, K_{yz}, K_{zx}, and K_{zy}. When we align the numerical model's primary axis of anisotropy with the primary indices of the tensor the offsets of the tensor tend to zero and the tensor takes the form of

$$\begin{matrix} K_{xx} & 0 & 0 \\ 0 & K_{yy} & 0 \\ 0 & 0 & K_{zz} \end{matrix}$$

Due to the limitations associated with the numerical model we are only able to model reaches of the subterranean river valley that are straight where we can align the sand channels (Kx) with the primary model axis. Once the azimuth of the river valley changes we are not longer capable of modeling beyond this point. Because of this limitation current numerical models are incapable of modeling large scale systems beyond approximately 5 to 10 km^2.

Future modeling efforts of subterranean river valleys should include development of numerical models that are capable of modeling all indices of the hydraulic conductivity tensor. This will provide the capability of modeling large regional systems beyond current limitations. Here we will be able to model the abstraction of groundwater over a 20 year period and evaluate the distribution of the pressure wave within the system for a more accurate account of a long-term safe yield and reduction in the uncertainty surrounding long-term yield of an aquifer.

The late time or long-term (approximately 8 to 15 hours) pumping data, ranging from approximately 8 to 15 hours, provide more information about the groundwater system than only using early time data of 4 hours. This can be seen in the results from the 3-dimensional simulations. The longer duration of the pumping test yields information pertaining to model boundaries, identification of the sharp contrasting boundaries between sands and overbank deposits and also allows for multiple flow regimes to evolve. Ideally, simulating transient conditions over a 72-hour testing period or longer would have been preferable. However, the transient period was constrained by the model

domain size of 1,000 m by 1,000 m which limited the duration to between 8.8 to 15 hours. It is expected that the pressure wave will propagate further when the transmissivity value is large which results in a greater formation diffusivity of the system. This allows for the wave to move through the hydraulically conductive facies both laterally and vertically provided connectivity between these facies exists. Because time is measured on a log scale when evaluating pressure data, there is little difference between a short-term (4 hour) and long-term (approximately 8 to 15 hours) test. What is of importance is the identification of the flow regimes and proper reservoir model. Recall that the derivative response displays a characteristic shape during all flow geometries. This can be used to determine the appropriate reservoir model type. Furthermore, identification of these regimes is critical to understanding the reservoir parameters (Bourdet 2002, Horne 2005).

The response of the system to an imposed stress such as pumping is not fully dependent on the level of effective hydraulic conductivity but more importantly on the extensiveness of the permeable media. Laterally extensive sands and splays tend to allow for radial flow to develop. Although these systems consist of channel sands and complexes and crevasse splays, these systems can behave as a homogeneous infinite system if lateral connectivity between facies exists. Linear flow regimes tend to develop at stratigraphic levels in non-ideal systems where the sands channels and complexes are laterally isolated allowing for the pressure wave to propagate outward and intersect the sides of the channel and then propagate along the length of the channel. The linear flow in PTA is represented by the leaky faults used in the analysis.

In the PTA interpretations both wellbore storage flow regime and skin effect are observed in the pressure response of the production well and these responses have been accounted for in the PTA model. As previously discussed, both well and screen radiuses are input values for the HydroGeoSphere simulations which result in the presence of the wellbore storage flow regime in the pressure response of the well. The skin effect is observed in the early time (storage) response of the well. Skin does not change the position of the early time slope but affects the amplitude of the hump (Houzé et al 2008). The skin effect is a numerical artefact of how the pumping well is handled by the flow simulator. The pressure response at the well is averaged across the simulator grid block. This results in a pressure drop that is less than what would actually be seen in the well. Thus, for modeling a constant skin value, the well flowing pressure term is greater than the pressure at the well radius which results in a negative skin value. This can be explained by considering skin as an equivalent radius. For a negative skin, the equivalent wellbore radius (r_{wa}) will be larger than the wellbore with no skin (r_w). Figure 5.51 illustrates the concept of skin as an equivalent radius.

Figure 5.51: Equivalent Wellbore Radius for a Negative Skin (Houzé et al. 2008).

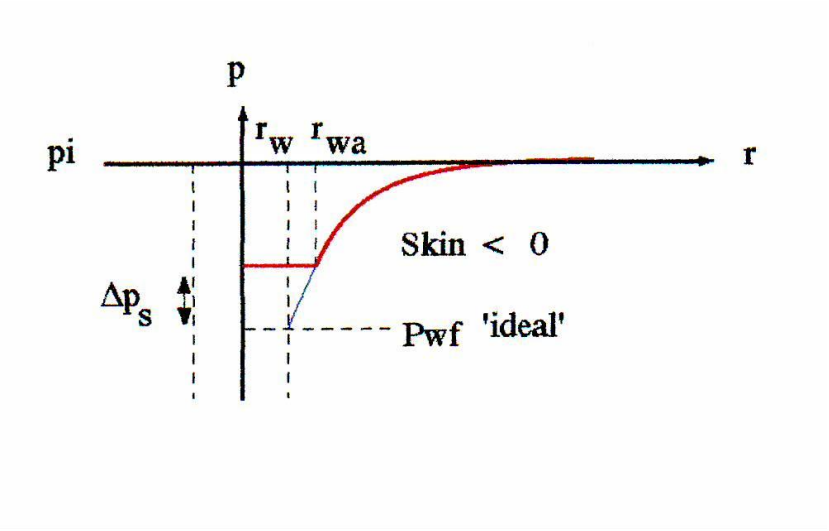

Where:

P = pressure

pi = initial pressure

Δps = change in between the well radius and the equivalent wellbore radius with skin

r_w = wellbore radius with no skin

r_{wa} = equivalent wellbore radius with skin

Pwf = well flowing pressure

From Figure 5.51, for a negative skin value, the pressure at the wellbore with no skin (rw) will be less than the pressure at the equivalent wellbore radius rwa resulting in a negative value. For the equivalent wellbore radius, the skin (S) is described by:

$$S = -\ln\left(\frac{r_{wa}}{r_w}\right) \quad [5.7]$$

Farvolden Q_{20}

The Q_{20}, which relies on the Theis equation for parameter estimation, is based on estimates of water level drawdown in a production well after 20 years of fluid withdrawal. The method is based on an overarching assumption that the aquifer is fully confined, laterally continuous of infinite extent, homogeneous and isotropic and does not receive pressure support from overlying or underlying aquifers through leaky aquitards. Furthermore, this method does not take into account well efficiency, heterogeneity, or boundaries (Parks and Bentley 1996). The assumptions limit the applicability of this methodology for establishing long-term yield.

It is suggested that employment of the Farvolden Q_{20} approach be abandoned in favour of a methodology which addresses the use of an appropriate reservoir model that matches the identified flow regimes observed in pressure transient analysis and which models the behaviour of the aquifer system. This will result in a more accurate estimation of aquifer parameters for determination of long-term yield and reduce or eliminate the inherent error in over or under prediction that have been observed in the use of the Farvolden Q_{20}. Case histories documenting problems associated with employment of the Farvolden Q_{20} in Alberta are summarized by Maathuis and van der Kamp (2006).

PTA results of pressure data from Realizations 6, 43, 46, 48, and 61 the production wells indicate that response of these non-ideal systems to the abstraction of water vary significantly as the permeability and connectivity of hydrofacies within these system vary in three-dimensional space. The long-term safe yield and Saphir forward predictions of drawdown over a 20-year period are presented in Table 5.3.

Table 5.3: Long-term 20 year safe yield, Saphir predicted drawdowns and Transmissivity estimates using both the Thesis and Saphir model methodology

Realization	Q_{20}		Saphir	Transmissivity	
				Theis/Q_{20}	Saphir
	m3/yr	Drawdown (m)	Drawdown (m)	m^2/s	m^2/s
R6	7,884	16.06	59.47	3.27×10^{-05}	4.79×10^{-05}
R43	54,220	42.99	21.76	8.40×10^{-05}	1.21×10^{-04}
R46	38,580	43.05	10.94	5.97×10^{-05}	9.01×10^{-05}
R48	22,701	43.08	11.10	3.51×10^{-05}	7.84×10^{-06}
R61	43,034	42.98	37.10	6.67×10^{-05}	6.23×10^{-05}

The drawdown predicted over a 20-year period using the Hydrogeology (i.e., Theis) and Reservoir Engineering methodologies are presented in Table 5.3. Drawdown using the Hydrogeology methodology varied between approximately 16 m to 43 m. Drawdown in four of the five transient simulations was approximately 43 m. Drawdown using the Reservoir Engineering methodology in the five simulations varied between approximately 11 m to approximately 60 m. For these explicit simulations, drawdown over a 20-year period was greater using the latter approach for R6. Drawdown was greater using the Hydrogeology approach in four of the five simulations (R43, R46, R,

48, and R61). This is likely a result of the slope of the drawdown curve is greater using and the assumption that drawdown over the 20 year period is at a consistent rate.

Based on the five PTA results, these systems can behave as a) homogeneous reservoir with a leaky fault (Realization 6; Rank:min),b) homogeneous reservoir (Realization 43; Rank:max); c) homogeneous reservoir with a leaky fault (Realization 46; Rank:P68); d) homogeneous reservoir, fracture with a finite conductivity (Realization 48; Rank:P90); and e) radially composite reservoir, fracture with infinite conductivity (Realization 61; Rank:P31). With the exception of Realization 43, which has the highest permeability and extensive lateral connectivity of channel sands (Figure 5.18), no other model behaved as a strictly homogeneous isotropic system. The models with permeability ≤ P90 all displayed either some behaviour of a linear flow component as described by a fracture or fault system in the reservoir model due to sand channels encased in floodplain deposits or behaviour indicative of a more complex reservoir. This flow behaviour is illustrated in Figures 5.6 and 5.7 (Realization 6); Figures 5.27 and 5.28 (Realization 46); Figures 5.35, 5.37, and 5.39 (Realization 48); and Figure 5.45 (Realization 61). This would suggest that only the non-ideal systems that have very high permeability and lateral connectivity (>P90) will behave as homogeneous systems and therefore the Theis equation and employment of standard industry practice for determining long-term yield (Q_{20}) will only be valid in a limited number of cases.

These non-ideal systems do not strictly behave in a manner that is consistent with the use of the Theis equation. Employment of this methodology on systems ≤P90 can result in

an erroneous over or under prediction of long-term well yield. Forward predictions using the Saphir reservoir, well, and boundary models indicate drawdown ranging from approximately 11 m to 60 m. However, there are limitations to using this approach. Although the methodology used for the Saphir generated forward predictions incorporate the model solution and estimated parameters of the long-term (i.e., approximately 8 to 15 hours) pumping tests the reliability of the forward predictions should be carefully scrutinized. This approach assumes that the system response does not deviate from that described by the PTA model for the period between the end of long-term test (i.e., 8 to 15 hours) and 20 years. This may be an unrealistic expectation as within this time period the pressure wave could propagate beyond the region where we have geological data and a conceptual understanding and into a region where a closed system, constant head (i.e., surface water body), or reduction in permeability could be encountered.

It must be kept in mind that determination of model applicability is determined using the derivative approach to PTA to identify the different flow regimes present and selection of an appropriate model that incorporates the observed flow regimes. It is the evaluation of flow regimes that identifies how these non-ideal systems behave and thus the flow regimes should be used to determine the safe long-term yield of the aquifer system.

The response of the system is a function of the hydrofacies intersected by the portion of the production well open to flow. Although a homogenous model fits the response of Realization 43, it is possible that a well completed in a different interval across less permeable hydrofacies could result in use of a more complex model. Because the

permeability and connectivity vary within these non-ideal systems, there will be variability in the reservoir models that are applicable and flow regimes that will evolve during a pumping test.

Alberta Research Council

In the mid to late 1970's, the Alberta Research Council (ARC) evaluated drawdown curves from 122 pumping tests which had been performed in heterogeneous clastic sediments of the Edmonton area (Figure 5.52). ARC observed that these curves had a high degree of variability and did not conform to theoretically expected curves (Bibby 1977). The short-term transmissivity of the tests was calculated by using the final unit slope of the curve and applying Jacob's straight line method. This approach assumes homogeneous conditions. ARC identified four basic shapes. However, these shapes could not be explained (Bibby 1977).

Figure 5.52: Diagrammatic type drawdown curves and examples from ARC (Bibby 1977).

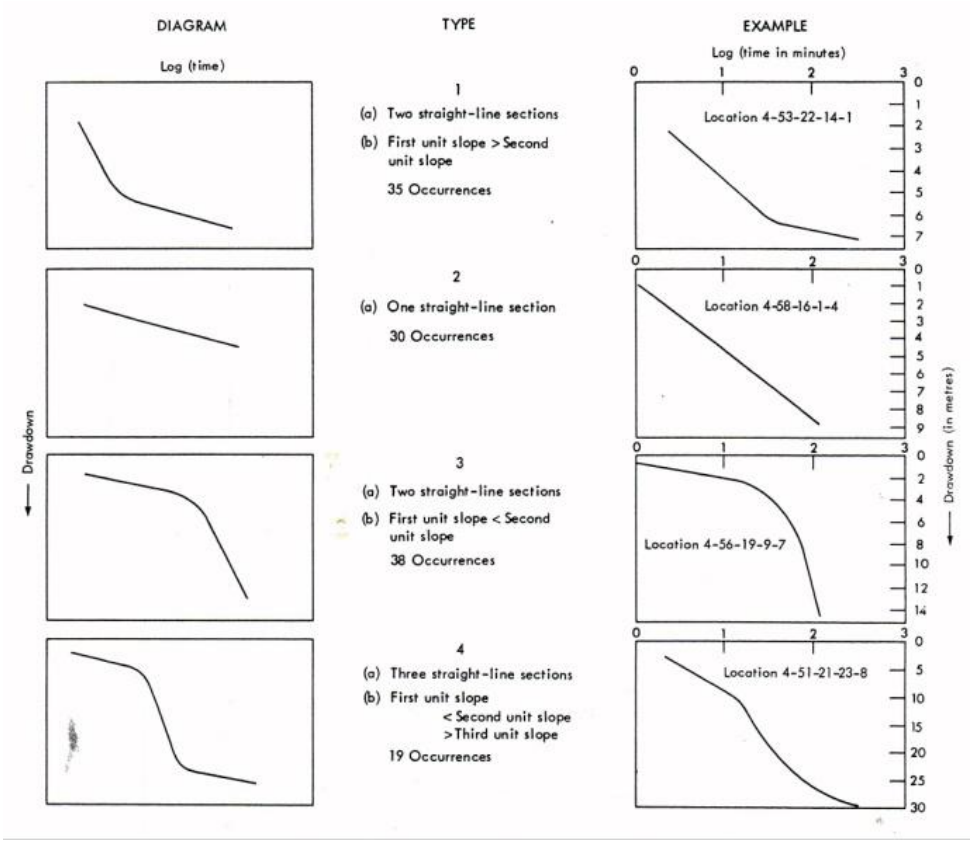

Burns et al. (2010a) surmised that wells completed in a good production zone results in the first slope of the drawdown curve representing flow in a fracture set or clean sandstone. The four curve types are presented in Figure 5.53. The Type 1 curves represent flow in channel sand connected to a more permeable zone such as a fracture set or more porous sandstone unit resulting in the break in slope. The Type 2 suggests response of a homogeneous system. The Type 3 curve suggested channel sand where the

break in slope represents a transition from radial flow to flow along a paleo-channel. Burns et al. (2010a) suggested that the Type 4 cures were the result of a response of channel sands or a fracture set which resulted in the break of slope.

Figure 5.53: Typical drawdown and recovery curves observed by ARC (Bibby 1977).

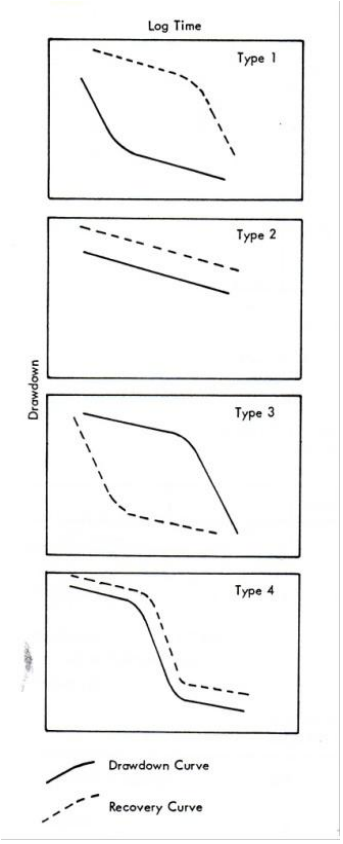

Figure 5.34 represents the drawdown observed in the pumping well PW-1 from Realization 48. This is a typical pressure response (i.e., drawdown vs. time) observed at the pumping well in each of the five simulations that were run for this research. The drawdown curve from the production wells in Realizations 6, 43, 46, 48, and 61 displayed either type 1 or type 3 curves presented in the work by Bibby. The type 1

curves (realizations R61 and R43) display a change in slope during the later portion of the testing period that indicates a movement of the pressure wave into permeable facies that results in a reduced drawdown rate. The type 3 curves (realizations R6, R46, and R48) have an increase in the slope of the drawdown curve during the later period of the test indicating movement into less permeable facies. It is possible that these responses could be observed under a variety different circumstances resulting from geology and test conditions. This may very well provide one such explanation for the variety of responses observed by the ARC. The curves evaluated by the ARC were from wells that were open to a variety of facies distributions and that the pressure response observed in each of these wells is a function of the flow regimes that developed during pumping which is a result of the extent of permeable facies, both laterally and vertically and the distribution of hydraulic conductivity within these facies.

The geometry of the geologic media and the lateral and vertical connectivity of the sands and splays control the pressure wave distribution and flow regimes that develop. It is likely that the four type curve classes observed by the ARC in the 122 pumping tests evaluated within the surrounding area of Edmonton were heavily influenced by shape and connectivity of the sand channels and complexes and the crevasses splays. Furthermore, it must be considered that the geomodel developed for this research using Burns et al.'s (2010b) hypothetical geomorphic analogue model might not capture the true heterogeneity inherent in these non-ideal systems since the analogue model does not incorporate the importation data (i.e., facies, core, wireline logs, log picks) gathered from drilled wells and does not take into consideration the cannibalization of channels and

splays by new developing channels, splays, and floodplain deposits and the underlying uncertainty in the geometry and thickness of the splays. As well, the geomodel also does not take into account diagenesis, fractures, and recharge that may play significant roles in the hydraulic response. Under actual conditions and with considerable data, a geologist might see evidence of a total reworking of the subsurface environment leading to possibly increased complexity in the geologic architecture than what has actually been modeled in this research. Therefore, it can be suggested that the results evaluated by ARC could represent greater geologic complexity and imposition of stress to a greater number of facies resulting in a non-ideal pressure response that could not be matched using this approach or analogue model.

CHAPTER 6: CONCLUSIONS

A 3-dimensional geomodel and stochastic approach was used to generate multiple realizations of hydrofacies consisting of geologically realistic shapes. This methodology was used to produce realistic sharp boundaries between the strongly contrasting hydraulic properties of the hydrofacies to describe the heterogeneity inherent in complex non-ideal systems representative of the Paskapoo Formation. These realizations were subsequently upscaled and simulations of steady-state and transient conditions were run using HydroGeoSphere. Property modeling was completed during the geomodeling process whereby the grid cells are populated with statistically relevant geologic and hydraulic values.

The effective conductivity of 100 coarse-grid and 100 upscaled-fine-grid realizations of the 3-dimensional geomodel were compared to evaluate the effective hydraulic conductivity in three principle directions Kx, Ky, and Kz and based on these results for the subsequent selection of an appropriate grid discretization for further study. Discretization of the coarse-grid model did not honour the statistics of the of the hypothetical geomorphic model's crevasse splays as appropriately as was honoured by the upscaled fine-grid discretization. As a result, the occurrence of the crevasse splay facies in the coarse-grid model was poorly represented as compared to the fine-grid model. Coarse-grid realizations yielded effective conductivities that were consistently higher than that of the upscaled fine-grid discretization. This suggested that the crevasses

splays are hydraulically significant facies and that the model discretization should account for these facies.

Upscaling of the final fine-grid 3-dimensional geomodel produced anisotropic responses whereby the effective conductivities were highest in the x-direction, parallel to the channel sands and complexes and lowest in the vertical direction. This suggests that we need to understand the primary valley direction and use of anisotropic values for the hydraulic parameters within our regional scale geomodel. Values for the upscaled fine-grid conductivities ranged from 1.33×10^{-04} to 1.72×10^{-04} m/s in the x-direction, from 6.72×10^{-08} to 1.50×10^{-04} m/s in the y-direction and 3.83×10^{-08} to 2.08×10^{-06} m/s in the z-direction. The values for the coarse-grid discretization ranged from 1.27×10^{-04} to 1.83×10^{-04} m/s in the x-direction, 2.91×10^{-06} to 7.60×10^{-05} m/s in the y-direction and 1.86×10^{-06} to 2.61×10^{-06} in the z-direction. Flow within these systems along the y-direction is dependent on the lateral distribution of crevasse splays and connectivity to channel sands and complexes. Response of the system is variable as the distribution and connectivity of the hydrofacies is variable. As such the upscaled fine-grid realizations were used for subsequent transient modeling.

Stochastic modeling of the Paskapoo formation has lead to the development of a series of realizations that range from displaying high connectivity to low connectivity with varying levels of horizontal and vertical connectivity between these two end members. A total of five realizations (Rankings: Pmin, P31, P68, P90, and Pmax), representing varying

degrees of connectivity were selected for transient modeling based on the effective conductivities and spatial variability of the hydrofacies.

Flow regimes observed during the first 4 hours of simulation as seen in the 3-dimensional model range from infinite acting radial flow in well connected and laterally continuous channels and crevasses to linear flow regimes at stratigraphic levels where channel sands are well defined. Where we see the pressure wave propagate along sharp contrasting physical boundaries of the channel. In some areas we see an evenly spreading wave. Consequently, it is possible under short-term (4 hours) pumping tests to have well developed linear flow occurring at some stratigraphic level within channel sands and yet use a reservoir model that is of a homogeneous reservoir but has characteristics of a leaky fault to accommodate the presence of linear flow even though linear flow is not well developed on the derivative plot. Short-term tests may have limited utility.

This could be because the pressure response of the system during a short duration test may be significantly different from that of a longer duration test or a test that more appropriately mirrors the production profile of the intended use of the water supply well. Therefore, long-term yields should be based on longer term testing that allows for a similar pressure response and development of flow regimes that would be seen once the water supply well has been placed on production and no further development of new flow regimes occur.

Evaluation of the five transient simulations indicates that the pressure wave from the pumping well reached the model boundaries within approximately an 8 to 15-hour period after which this could potentially influence the pressure wave response and thereby limiting the time interval that can be used in PTA of the simulated pumping test data.

Consequently, the interval used for analysis of pumping test data during PTA is limited to the period preceding intersection of the pressure wave with the model boundaries. Derivative analysis can be used to identify the presence of the boundaries (i.e., in this case the model boundaries) and the time it takes for the pressure wave to propagate to these boundaries (reservoir volume or extent).

Flow regimes observed at later time (8.8 to 15 hours) display a variety of characteristics from well developed infinite acting radial flow in hydraulically extensive and well connected channels and crevasse splays to linear flow in well developed channels juxtaposed with sharp contrasting physical boundaries of overbank deposits. Within the modeled system where intermediate levels of connectivity and distribution of hydraulically conductive hydrofacies exist we see a range of flow regimes at different stratigraphic levels corresponding to connectivity of the hydrofacies at that level. This suggests that the pressure response of the aquifer is variable and dependent on the connectivity of the hydrofacies at varying stratigraphic levels which influence the development of flow regime type.

Early time data can contain several different flow regimes including IRF and linear flow as seen in the 3-dimensional simulations. In some instances and at different stratigraphic levels, these flow regimes are not fully developed and sharp physical boundaries between the channel complexes and overbank deposits are observed in the 3-dimensional simulations. It is important to have access to PTA tools that allow for a custom fit of the data to accurately estimate aquifer parameters. However, these analyses should be carefully scrutinized. Since distinct flow regimes may not have fully developed, pressure transient analysis may not distinguish between infinite acting radial flow and other developing flow regimes or the contrasting physical boundaries between hydrofacies. This may result in misinterpreting pumping test data resulting in the application of an inappropriate model and adoption of the Theis equation, when in fact IARF is not the primary flow regime present in the system and long term yield should be based on a different flow regime or reservoir model such as the homogeneous reservoir with a leaky fault. The pressure response may be a combination of characteristics that are difficult to distinguish. Therefore, derivative plots and custom curve fitting techniques are essential to evaluating pressure data and estimation of aquifer performance when dealing with this style of heterogeneity.

Derivative analysis should be used to identify the flow regimes that describe the system response for determining the long-term safe yield of the aquifer. In many of the observed cases, it is apparent that another flow regime exists or is coincident with radial flow and that the system is not indicative nor behaves like a strictly homogeneous isotropic system. In these cases the Theis equation and use of the parameter estimation from this model for

use in the Q_{20} are might not be appropriate and use of other models for interpretation should be explored. Channel flow (linear flow) can be the dominant flow regime in well developed channels and channel complexes where there is little connectivity laterally throughout the system through crevasse splays and there are contrasting boundaries between hydrofacies. Where large laterally continuous sands are present and in cases connected by crevasse splays, IARF is observed. Under these conditions and prior to seeing any boundaries, Theis could be considered as an applicable model for estimating hydraulic parameters and determining long-term yield provided that no additional flow regimes develop and that it adequately reflects the final pressure behaviour of the non-ideal system. However, due to the complexity of the system response and pressure wave behaviour, evaluation of aquifer parameters using multiple viable models must be considered. Dual porosity systems are also possible under certain circumstances as an intermediate response between the two end members of linear flow and IARF. Based on this research the homogeneous reservoir with a leaky fault tends to accommodate the pressure response for many of the tests.

PTA results of pressure data from Realizations 6, 43, 46, 48, and 61 indicate the presence of a variety of model responses ranging from a homogenous reservoir to a more complex radially composite reservoir with fracturing. The majority of responses exhibited linear flow as a result of the presence of sand channels acting as a fairway for groundwater flow. Only the non-ideal systems that have very high hydraulic conductivity and lateral connectivity (>P90) behave as homogeneous systems and therefore the Theis equation and employment of standard industry practice for determining long-term yield (Q_{20})

might be valid in these cases. Non-ideal systems do not behave in a manner that is consistent with the use of the Theis equation. Employment of this methodology can result in an erroneous over or under prediction of yield capacity. The response of the system is a function of the distribution of hydrofacies. Because the hydraulic conductivity and connectivity vary within these non-ideal systems, there will be variability in the reservoir models that are applicable and flow regimes that will evolve during a pumping test. This variability must be tested.

Evaluation of the long-term safe aquifer yield in these non-ideal systems should be based on the primary flow regime and matching reservoir model observed in the pressure transient analysis. If we see boundaries during pressure transient analysis an appropriate long-term yield should be based on linear flow for long-term predictions of possibly the most dominate flow regime present in the pressure transient analysis.

The drawdown curve from the production wells in Realizations 6, 43, 46, 48, and 61 displayed either type 1 or type 3 Bibby curves. The type 1 curves are associated with the realizations R61 (Rank: P31) and R43 (Rank: max). The slope during the later portion of the testing period indicates movement of the pressure wave into more permeable facies resulting in a reduction in the drawdown rate. The type 3 curves are associated with Realizations R6 (Rank: min), R46 (Rank: P68) and R48 (Rank: P90). The slope of the drawdown curve in the later period of the test suggests movement into less permeable facies by an increase in the drawdown curve. These simulations have a component of linear flow associated with them. It might be possible that propagation of the pressure

wave through less permeable facies at different stratigraphic levels may be influencing the response of the curve. It is possible that these responses could be observed in other subsurface geologic settings but might indicate something different as the geology of the test formation must be considered.

It is unlikely that the analogue model developed for this research captures the true heterogeneity inherent in the actual system as it ignores recharge, fractures, diagenetic alteration, and cannibalization of the fluvial environment or total reworking of the depositional environment that would lead to artefacts or remnants of previously existing facies amongst younger complete facies. This would result in a very complex subsurface environment and complex geologic architecture. As well, the current work has not accounted for diagenesis, fracture systems and recharge which may play significant roles in the actual aquifers. This may account for the variability between the drawdown curves observed by ARC and of that observed in this research. Future research in this area should consider the simulation of more realizations with placement of the production wells yielding greater variability to facies distribution.

The Q_{20}, was established for the determination of a safe long-term yield based on production from a fully confined, infinitely continuous homogeneous and isotropic aquifer. When applying these assumptions to a system that is non-ideal, the assumptions are contravened voiding the validity of this method. Use of the Saphir model in forward simulations provides a more rigorous approach to a twenty year sustainable pumping rate.

When evaluating long term sustainable yield, flow regimes observed in pressure transient analysis must be honoured and taken into consideration. Furthermore, in instances where the system is not ideally homogeneous or consisting of laterally extensive permeable facies, a short term test will not yield the dominate flow regime prevalent in these systems once the water supply well goes on production. When planning a pumping test, where possible, the proposed production profile of the well must be considered to determine if a short-term (i.e., 4 to 6 hours) test will result in a pressure response that characterizes the groundwater system and subsequently can be used to determine a safe long-term yield.

The research performed was constrained by use of a simplified 3-dimensional geomodel and small domain size and not a groundwater basin. Future research toward a more comprehensive understanding of the Paskapoo system should include the development of a large scale geomodel for accommodation of longer tests. There should be an expansion of the types of geologic settings relevant to the Paskapoo which should also incorporate fracture sets in more complex geologic settings. Test results should be evaluated to understand the uncertainty in the drawdown as it relates to the heterogeneity in the system. This relationship and its implication to sustainable safe aquifer yield from a regulatory standpoint should be explored as current practice and licensing by the government does not address this problem.

References

Alberta Environment. (2003). *Groundwater Evaluation Guideline.* Water Section. Edmonton: Alberta Government.

Allan, J. A., & Sanderson, J. O. (1945). *Geology of Red Deer and Rosebud Sheets, Alberta.* Edmonton: Research Council of Alberta.

Anderson, M. P., & Woessner, W. W. (1992). *Applied Groundwater Modeling: Simulation of Flow and Advective Transport.* San Diego: Academic Press, Inc.

AQTESOLV. (1998-2009). *AQTESOLV - Aquifer Test Forum - Properties*. Retrieved January 1, 2008, from Aquifer Properties Hydraulic Conductivity (K): http://www.aqtesolv.com/forum/properties.htm

Australian Government. (n.d.). *Connected Water managing the linkages between surface water and ground water*. Retrieved January 15, 2007, from Hydraulic Conductivity Measurement: http://www.connectedwater.gov.au/framework/hydrometric_k.php

Bachu, S. (1999). *Bulletin of Canadian Petroleum Geology, Vol. 47 No. 4*, 455-474.

Bachu, S., & Michael, K. (2001). Fluids and Pressure Distributions in the Foreland-Basin Succession in the West-Central Part of the Alberta Basin, Canada: Evidence for Permeability Barriers and Hydrocarbon Generation and Migration. *American Association of Petroleum Geologists, Vol 85, No.7*, 1231-1252.

Bachu, S., & Michael, K. (2003). Possible controls of hydrogeological and stress regimes on the producibility of coalbed methane in Upper Cretaceous–Tertiary strata of the Alberta basin, Canada. *American Association Petroleum Geologists, Vol 87, No. 11*, 1729-1754.

Bibby, R. (1977). *Characteristics of Pumping Tests Conducted in Heterogeneous Clastic Sediments of the Edmonton Area, Alberta - Contributions to Hydrogeology.* Edmonton: Alberta Research Council.

Bourdet, D. (2002). *Well Test analysis: The Use of Advanced Interpretation Models.* (J. Cubitt, Ed.) Amsterdam: Elsevier.

Bridge, J. S., & Mackey, S. D. (1993). A theoretical study of fluvial sandstone body dimensions. (I. D. Bryant, & S. S. Flint, Eds.) *The Geological Modeling of Hydrocarbon Reservoirs and Outcrop Analogues: International Association of Sedimentologists Special Publication 15*, 213-236.

Burns, E. B., Bentley, L. R., Hayashi, M., Grasby, S. E., & Hamblin, A. R. (2010a). Hydrogeological Implications of Paleo-Fluvial Architecture of Complex Aquifer Systems: Numerical Modeling Results and Sensitivity Analysis for the Paskapoo Formation, SW Alberta Canada. *Hydrogeology Journal, 18* (No. 6), 1375-1390.

Burns, E. R., Bentley, L. R., Therrien, R., & Deutsch, C. V. (2010b). Upscaling facies models to preserve connectivity of designated facies. *Hydrogeology Journal, 18*, 1357-1373.

Burrows, W. A. (2004). *A 3-D Steady-state groundwater model for West Nose Creek watershed.* University of Calgary. Calgary: Faculty of Graduate Studies.

Carrigy, M. A. (1971). *Lithostratigraphy of the uppermost Cretaceous (Lance) and Paleocene strata of the Alberta Plains* (Vol. Bulletin 27). Alberta, Canada: Research Council of Alberta.

Chaudhry, A. U. (2004). *Oil Well Testing Handbook.* Oxford: Elsevier.

Chiles, J.-P., & Delfiner, P. (1999). *Geostatistics: Modeling Spatial Uncertainty.* New York: John Wiley & Sons, Inc.

Chow, R. (2009, October). Foundation Pressure Transient Analysis Training Course. (V. Matthews, Interviewer) Houston, Texas, U.S.A.

de Marsily, G., Delay, F., Goncalves, J., Renard, P., Teles, V., & Violette, S. (2005). Dealing with spatial heterogeneity. *Hydrogeology Journal, 13* (1), 161-183.

Demchuk, T. D., & Hills, L. V. (1991). A re-examination of the Paskapoo Formation in Central Alberta Plains: The designation of three new members. *Bulletin of Canadian Petroleum Geology, Vol. 39, no. 3*, 270-282.

Deutsch, C. V. (2002). *Geostatistical Reservoir Modeling.* (A. G. Journel, Ed.) New York: Oxford University Press, Inc.

EBA Engineering Consultants Ltd. (2003). *Spy Hill Provincial Aggregate Operation Hydrogeological Assessment 33-025-2W5M: Assessment Report for Alberta Transportation.* Calgary.

Eberth, D. A., & O'Connell, S. C. (1995). Changing Paleoenvironments across the Cretaceous-Tertiary boundary (Scollard formation) in the Red Deer river valley of southern Alberta. *Canadian Society of Petroleum Geologists, Vol 43, no. 1*, 44-53.

Fogg, G. E. (1986). Groundwater flow and sand body interconnectedness in a thick multiple-aquifer system. *Water Resources Research, Vol. 22*, 679-694.

Freeze, R. A., & Cherry, J. A. (1979). *Groundwater.* Englewood Cliffs: Prentice Hall.

Gabert, G. (1975). *Hydrogeology of Red Deer and Vicinity, Alberta* (Bulletin 31 ed.). Edmonton: Alberta Geological Society.

Gibling, M. R. (2006). Width and thickness of fluvial channel bodies and valley fills in the geological record: a literature compilation and classification. *Journal of Sedimentary Research, Vol. 76*, 731-770.

Goovaerts, P. (1997). *Geostatistics for Natural Resource Evaluation (Applied Geostatistics Series).* New York: Oxford University Press.

Government, A. (n.d.). *Hydraulic Conductivity Measurement*. Retrieved January 1, 2008, from Connect Water Managing the linkages between surface water and ground water: http://www.connectedwater.gov.au/framework/hydrometric_k.php

Grande, L. G.-Q. (2000). Amia cf. pettersoni from the Paleocene Paskapoo Formation of Alberta. *Canadian Journal of Earth Sciences* (37(1)), 31-37.

Hamblin, A. P. (2004). *Paskapoo-Porcupine Hills Formation in Western Alberta: Synthesis of Regional Geology and Resources Potential.* Calgary: Geological Survey of Canada.

Harrison, S.M., Gentzis, G., Labute, G., Seifert, S., and Payne, M. (2006). Preliminary hydrogeological assessment of Late Cretaceous - Tertiary Ardley coals in part of the Alberta Basin, Alberta, Canada. *International Journal of Coal Geology, 65* (1-2), 59-78.

Hatloy, A. S. (1995). Numerical Facies Modeling Combining Deterministic and Stochastic Methods. In A. A. Geologists, *Stochastic Modeling & Geostatistics: Principles, Methods, and Case Studies* (p. 379). American Association of Petroleum Geologists.

Horne, R. N. (2005). *Modern Well Test Analysis: A Computer-Aided Approach* (Second Edition.). Palo Alto, California, U.S.A.: Petroway, Inc.

Houze, O., Virurat, D., & Fjaere, O. S. (2008, October). Dynamic Flow Analysis. *Dynamic Flow Analysis - The Theory of Practice of Pressure Transient and Production Analysis & The Use of data from Permanent Downhole Gauges*. Kappa Engineering.

HydroSOLVE Inc. (1998-2009). *AQTESOLV - Aquifer Test Forum - Properties*. Retrieved January 15, 2007, from Aquifer Properties Hydraulic Conductivity: http://www.aqtesolv.com/forum/properties.htm

International Symposium on Groundwater Sustainability. (2006, 01 24-27). *International Symposium on Groundwater Sustainability (ISGWAS)*. Retrieved 09 15, 2009, from The Spanish Royal Academy of Sciences: http://www.interacademies.net/Object.File/Master/5/091/Alicante%20Brochure.pdf

Isaaks, E. H., & Srivastava, R. M. (1989). *Introduction to Applied Geostatistics.* New York: Oxford University Press, Inc.

Jerzykiewicz, T. (1997). *Stratigraphic Framework of the Uppermost Cretaceous to Paleocene Strata of the Alberta Basin* (Bulletin 510 ed.). Ottawa, Ontario, Canada: Geological Survey of Canada.

Jerzykiewicz, T., & LaBonte, M. (1991). *Representation and statistical analysis of directional sedimentary structures in the uppermost Cretaceous-Paleocene of the Alberta Foreland Basin.* Geological Survey of Canada.

Kansas Geological Survey. (1998, October). *Regional Dakota Aquifer Hydrostratigraphy*. Retrieved January 1, 2008, from Dakota Aquifer Program - Geohydrology Section, Kansas Geological Survey: http://www.kgs.ku.edu/Dakota/vol1/dkHome.htm

Koltermann, C. E., & Gorelick, S. M. (1996). Heterogeneity in sedimentary deposits: A review of structure-imitating, process0imitating, and descriptive approaches. *Water Resources Research, Vol. 32, No. 9*, 2617-2658.

Kresic, N. (1997). *Quantitative Solutions in Hydrogeology and Groundwater Modeling.* New York: Lewis Publishers.

Kupfersberger, H., & Deutsch, C. V. (1999). Ranking stochastic realizations for improved aquifer response uncertainty assessment. *Journal of Hydrology, Vol. 223* (1-2), 54-65.

Lerbekmo, J. F., Sweet, A. R., & Braman, D. (1995). Magnetobiostratigraphy of late Maastrichtian to early Paleocene strata of the Hand Hills, south central Alberta, Canada. *Bulletin of Canadian Petroleum Geology, Vol 43*, 35-43.

Lerbekmo, J., & Sweet, A. R. (2000). Magnetostratigraphy and biostratigraphy of the continental Paleocene in the Calgary area, southwestern Alberta. *Bulletin of Canadian Petroleum Geology, Vol 48 No. 4*, 285-306.

Maathuis, H., & van der Kamp, G. (2006). *The Q20 Concept: Sustainable Well Yield and Sustainable Aquifer Yield.* Saskatoon: Saskatchewan Research Council.

Mallet, J. L. (2002). *Geomodeling.* (A. G. Journel, Ed.) New York: Oxford University Press, Inc.

McKenna, S. A., & Smith, G. (2004). Sensitivity of Groundwater Flow Patterns to Parameterization of Object-Based Fluvial Aquifer Models. *SEPM Special Publication no. 80*, 29-40.

Meyboom, P. (1961). *Groundwater Resources of the City of Calgary and Vicinity* (Bulletin 8 ed.). Edmonton, Alberta, Canada: Research Council of Alberta.

Ozaray, G. F. (1972). *Hydrogeology of the Wabamun Lake area, Alberta.* Edmonton: Research Council of Alberta.

Ozoray, G. F., & Barnes, R. (1978). *Hydrogeology of the Calgary-Golden area, Alberta* (Report 77-2 ed.). Edmonton, Alberta, Canada: Alberta Research Council.

Parks, K. P., & Bentley, L. R. (1996). Derivative-assisted evaluation of well yields in a heterogeneous aquifer. *Canadian Geotechnical Journal, 33* (3), 458-469.

Parks, K. P., & Toth, J. (1995). Field evidence for erosion-induced under pressuring in Upper Cretaceous and Tertiary strata, west central Alberta, Canada. *Bulletin of Canadian Petroleum Geology, Vol 43, No. 3*, 281-292.

Parzen, E. (1962). *Stochastic Processes.* Holden Day.

Penguin Books. (2003). *The Penguin English Dictionary* (Second ed.). London: The Penguin Group.

Ravalec-Dupin, M. L. (2005). *Inverse Stochastic Modeling of Flow in Porous Media: Application to Reservoir Characterization.* Paris: IFP Publications t Editions TECHNIP.

Rubin, Y. (2003). *Applied Stochastic Hydrogeology.* New York: Oxford University Press.

Sen, Z. (1995). *Applied Hydrogeology for Scientists and Engineers.* Boca Raton: CRC Press Inc. Lewis Publishers.

Tokarsky, O. (1971). *Hydrogeology of the Rocky Mountain House Area, Alberta.* Edmonton: Research Council of Alberta, Government of Alberta.

Tokarsky, O. (1977). *Hydrogeology of the Whitecourt area, Alberta.* Edmonton: Alberta Research Council.

Toth, J. (1968). *A hydrogeological study of the Three Hills area, Alberta.* Edmonton: Research Council of Alberta.

Toth, J. (1966). *Groundwater Geology, Movement, Chemistry, and Resources near Olds, Alberta.* Edmonton: Research Council of Alberta.

U.S. Department of the Interior Bureau of Reclamation. (1995). *Ground Water Manual* (Second ed.). Highlands Ranch: Water Resources Publications, LLC.

Vogwill, R. J. (1983). *Hydrogeology of the Edson area, Alberta* (Earth Sciences Report 79-7 ed.). Edmonton, Alberta, Canada: Alberta Research Council.

Zhang, D. (2002). *Stochastic Methods for Flow in Porous Media: Coping with Uncertainties.* San Diego: Academic Press.

APPENDIX A: Hydraulic Conductivity and Mass Balance Error

Effective Hydraulic Conductivity Kx and Mass Balance

Realization No.	*Effective Kx (m/s)*	*Mass Balance Error (%)*
1	7.76599E-09	0.0000
2	1.29436E-06	0.0904
3	1.45028E-06	0.0000
4	1.32403E-06	0.0000
5	1.59247E-06	0.0000
6	1.25662E-09	0.1600
7	1.62748E-06	0.1100
8	1.46066E-06	0.0000
9	5.04290E-09	0.0000
10	1.33689E-06	0.0100
11	1.52943E-06	0.0000
12	1.40694E-06	0.0000
13	1.65527E-06	0.0000
14	1.40566E-06	0.0000
15	1.62122E-06	0.0000
16	1.60568E-06	0.0000
17	1.67040E-06	0.0000
18	1.35946E-06	0.0000
19	1.41739E-06	0.0000
20	1.46998E-06	0.0000
21	1.63795E-08	0.0001
22	1.82256E-06	0.0000
23	1.33697E-06	0.0000
24	1.64365E-06	0.0000
25	1.28533E-06	0.0000
26	1.74564E-06	0.0000
27	1.32800E-06	0.0000
28	1.49331E-06	0.0000
29	1.42942E-06	0.0000
30	1.39239E-06	0.0000
31	1.36371E-06	0.0000
32	1.68474E-06	0.0000
33	1.80788E-06	0.0000
34	1.53215E-06	0.0074
35	1.65062E-06	0.0061
36	1.30434E-06	0.0000
37	1.32397E-06	0.0000
38	1.69997E-06	0.0000
39	1.72536E-06	0.5505

40	1.39427E-06	0.0000
41	1.31816E-06	0.0000
42	1.22780E-06	0.0000
43	1.87452E-06	0.0003
44	1.46040E-06	0.0000
45	1.47474E-06	0.0000
46	1.55671E-06	0.0000
47	1.33093E-06	0.0000
48	1.71339E-06	0.0000
49	1.39167E-06	0.0000
50	1.42956E-06	0.0142
51	1.40676E-06	0.0000
52	1.32079E-06	0.0000
53	1.66091E-06	0.0000
54	1.33724E-06	0.0000
55	1.59367E-06	0.0007
56	1.36521E-06	0.0000
57	1.41972E-06	0.0000
58	1.27944E-06	0.8739
59	1.51538E-06	0.0009
60	1.52093E-06	0.0009
61	1.38007E-06	0.0000
62	1.58291E-06	0.0000
63	1.31051E-06	0.0000
64	1.54736E-06	0.0000
65	1.64170E-06	0.0000
66	1.38911E-06	0.0000
67	1.52921E-06	0.0000
68	1.34938E-06	0.0000
69	1.35241E-06	0.0000
70	1.72404E-06	0.0034
71	1.49677E-06	0.2333
72	1.73900E-06	0.0000
73	1.59448E-06	0.0000
74	1.86452E-06	0.0000
75	1.46055E-06	0.0003
76	1.51495E-06	0.0000
77	1.31680E-06	0.0000
78	1.42078E-06	0.0000
79	1.41462E-06	0.0000
80	1.48109E-06	0.0003

81	1.47387E-06	0.7105
82	1.63877E-06	0.0000
83	1.45653E-06	0.0009
84	1.52837E-06	0.0000
85	1.74663E-06	0.0000
86	1.58816E-06	0.0000
87	1.28571E-06	0.0000
88	1.31522E-06	0.0000
89	1.60624E-06	0.0026
90	1.85930E-06	0.0000
91	1.41755E-06	0.0164
92	1.65519E-06	0.0009
93	1.58060E-06	0.0000
94	1.59367E-06	0.0000
95	1.54683E-06	0.0000
96	1.49641E-06	0.0000
97	1.71729E-06	0.0000
98	1.38002E-06	0.0004
99	1.46851E-08	0.0004
100	1.24184E-06	0.0000

Effective Hydraulic Conductivity Ky and Mass Balance

Realization No.	*Effective Ky (m/s)*	*Mass Balance Error (%)*
1	2.76410E-07	0.0921
2	3.26633E-07	0.3375
3	2.11683E-07	0.0000
4	2.23301E-07	0.0000
5	3.90572E-07	0.0000
6	4.33889E-07	0.0000
7	4.10132E-07	0.0698
8	4.15066E-07	0.0214
9	1.95058E-07	0.0000
10	3.30367E-07	0.0069
11	4.38247E-07	0.0000
12	4.41826E-07	0.0288
13	4.60792E-07	0.0000
14	4.59018E-07	0.0000
15	1.76012E-07	0.0000
16	6.58585E-07	0.0027
17	3.66553E-07	0.0014
18	9.65029E-08	0.0352
19	2.78313E-07	0.0000
20	3.34045E-07	0.0000
21	3.20027E-09	0.0003
22	1.80647E-07	0.0000
23	3.47854E-09	0.0021
24	3.10076E-07	0.0000
25	1.24806E-09	0.0016
26	6.06754E-07	0.0012
27	4.28871E-07	0.0000
28	3.32052E-07	0.0000
29	1.61186E-07	0.0000
30	2.60970E-07	0.0000
31	4.18230E-07	0.0000
32	1.83799E-07	0.0000
33	3.28894E-07	0.0000
34	3.36981E-07	0.0000
35	3.76431E-07	0.1658
36	2.57648E-07	0.0000
37	5.89075E-08	0.0078
38	9.68159E-08	0.0000
39	6.24521E-07	0.1809

40	2.82091E-07	0.0000
41	1.77200E-07	0.0332
42	1.24780E-07	0.0446
43	8.02961E-07	0.0081
44	4.28976E-09	0.1019
45	1.37080E-07	0.0000
46	2.21919E-07	0.0205
47	2.02445E-07	0.0000
48	2.64439E-07	0.0000
49	1.96386E-07	0.0000
50	1.01874E-09	0.0013
51	2.67056E-07	0.0000
52	1.39903E-07	0.0009
53	3.70687E-07	0.0008
54	2.20965E-07	0.0000
55	3.24154E-09	0.0006
56	2.32540E-07	0.0032
57	3.85690E-07	0.0988
58	1.48484E-07	0.0355
59	6.45292E-08	0.0000
60	2.69947E-09	0.0328
61	3.33279E-07	0.0000
62	3.93953E-07	0.1821
63	1.33742E-07	0.0814
64	3.02297E-07	0.0000
65	5.24227E-09	0.0000
66	1.39553E-07	0.0000
67	1.85231E-07	0.0000
68	1.74528E-07	0.0000
69	3.32302E-07	0.0002
70	7.42333E-09	0.0004
71	2.46484E-07	0.0000
72	7.55957E-07	0.0006
73	2.04997E-09	0.2655
74	5.41617E-07	0.0000
75	9.49460E-08	0.0000
76	4.56203E-07	0.0023
77	2.41433E-07	0.2116
78	1.75700E-07	0.0000
79	2.39696E-07	0.0373
80	2.17671E-07	0.0006

81	1.54137E-07	0.0655
82	7.14552E-07	0.0000
83	3.29606E-09	0.0012
84	4.32380E-07	0.0000
85	2.78167E-07	0.0001
86	2.35923E-07	0.0000
87	2.19993E-07	0.0001
88	1.90592E-09	0.0000
89	5.47580E-07	0.0296
90	2.31311E-07	0.0000
91	1.56608E-07	0.0000
92	2.98289E-09	0.0007
93	5.65557E-07	0.0002
94	3.00418E-07	0.0000
95	1.30022E-07	0.0000
96	3.45018E-07	0.0000
97	2.22266E-07	0.0000
98	4.29310E-07	0.0000
99	3.33040E-09	0.0000
100	2.56722E-07	0.0000

Effective Hydraulic Conductivity Kz and Mass Balance

Realization No.	*Effective Kz (m/s)*	*Mass Balance Error (%)*
1	8.97404E-12	0.00000
2	5.43251E-12	0.07016
3	3.23560E-12	0.12304
4	5.97441E-12	0.00000
5	4.55439E-12	0.04254
6	1.25662E-11	0.66601
7	8.42849E-12	0.12165
8	7.46994E-12	0.00000
9	5.04290E-11	0.19719
10	2.80333E-10	0.43641
11	4.13355E-11	0.14253
12	6.01719E-10	0.00000
13	4.57991E-12	0.00000
14	3.98498E-12	0.00000
15	1.65042E-11	0.00000
16	8.67244E-12	0.11468
17	5.16664E-12	0.00000
18	6.08978E-12	0.00000
19	5.81384E-12	0.00000
20	3.45695E-10	0.33000
21	5.36282E-12	0.36832
22	1.28170E-11	0.07749
23	3.23560E-12	0.64573
24	1.48099E-10	0.00000
25	6.00690E-12	0.08261
26	9.05461E-11	0.76000
27	5.64182E-12	0.00000
28	5.23756E-11	0.34684
29	1.22585E-10	0.00000
30	3.40844E-10	0.00000
31	5.40820E-12	0.00000
32	1.23113E-10	0.00000
33	5.19565E-12	0.00000
34	1.09013E-11	0.00000
35	4.02172E-11	0.01456
36	1.79676E-11	0.32765
37	6.25791E-11	0.00000
38	1.03455E-11	0.00000
39	2.04751E-11	0.72401

40	4.31245E-12	0.13646
41	9.21740E-12	0.00000
42	4.64298E-12	0.00000
43	6.46128E-12	0.00000
44	1.63697E-10	0.88282
45	6.53035E-12	0.00000
46	3.43824E-12	0.34423
47	1.53036E-11	0.00000
48	5.76878E-12	0.00000
49	3.88730E-10	0.00000
50	1.14372E-11	0.00000
51	6.96831E-12	0.00000
52	5.48348E-12	0.03521
53	2.93486E-11	0.00000
54	6.61675E-12	0.00000
55	5.52862E-12	0.17873
56	1.94917E-11	0.00000
57	1.41162E-11	0.70258
58	7.05866E-12	0.00000
59	6.32808E-12	0.00000
60	2.94463E-10	0.00000
61	6.80841E-12	0.00000
62	1.00722E-11	0.00000
63	7.14671E-12	0.00000
64	1.84033E-11	0.41163
65	1.88025E-10	0.00000
66	7.79794E-12	0.62893
67	1.07047E-11	0.00000
68	6.90893E-12	0.00000
69	6.63980E-13	0.00000
70	8.60589E-12	0.00000
71	9.04777E-11	0.00000
72	4.39148E-12	0.00000
73	5.79228E-12	0.00000
74	4.04983E-12	0.00000
75	7.72680E-12	0.00000
76	5.48450E-12	0.00000
77	4.00412E-12	0.98401
78	4.15577E-12	0.00000
79	4.32743E-11	0.00000
80	5.59046E-12	0.00000

81	5.42385E-12	0.35939
82	7.81710E-12	0.00000
83	3.89887E-12	0.00000
84	6.48470E-11	0.30404
85	9.43690E-12	0.00000
86	5.21128E-12	0.00000
87	4.08644E-12	0.00000
88	3.67100E-11	0.00000
89	1.14444E-11	0.40556
90	1.28673E-11	0.00000
91	5.25891E-12	0.61237
92	4.54423E-11	0.12369
93	4.93474E-12	0.00000
94	6.23066E-12	0.00000
95	1.31623E-11	0.00000
96	7.89997E-11	0.00000
97	1.29131E-11	0.00000
98	2.92245E-11	0.00657
99	6.48060E-11	0.07711
100	1.87740E-11	0.16215

APPENDIX B: Observation Well Locations

Realization 6 Well Coordinates

Well Name	X-Coordinate (m)	Y-Coordinate (m)	Z-Coordinate (m)
PW-1	690505	5690505	1347.25
OBS1	690500	5690500	1347.25
OBS2	690495	5690415	1344.75
OBS3	690555	5690335	1344.75
OBS4	690365	5690405	1344.75
OBS5	690515	5690425	1344.75
OBS6	690655	5690345	1344.75
OBS7	690595	5690245	1344.75
OBS8	690805	5690555	1344.75
OBS9	690785	5690595	1344.75
OBS10	690905	5690575	1344.75
OBS11	690885	5690455	1344.75
OBS12	690985	5690545	1344.75
OBS13	690395	5690245	1344.75
OBS14	690425	5690045	1344.75
OBS15	690615	5690025	1344.75
OBS16	690845	5690025	1344.75
OBS17	690095	5690035	1344.75
OBS18	690035	5690315	1344.75
OBS19	690055	5690405	1344.75
OBS20	690115	5690415	1344.75
OBS21	690045	5690605	1344.75
OBS22	690135	5690755	1344.75
OBS23	690105	5690815	1344.75
OBS24	690135	5690975	1344.75
OBS25	690225	5690915	1344.75
OBS26	690565	5690955	1344.75
OBS27	690805	5690935	1344.75
OBS28	690855	5690845	1344.75
OBS29	690875	5690765	1344.75
OBS30	690905	5690635	1344.75
OBS31	690955	5690555	1344.75
OBS32	690835	5690465	1344.75
OBS33	690965	5690395	1344.75
OBS34	690975	5690315	1344.75
OBS35	690945	5690185	1344.75
OBS36	690945	5690045	1344.75
OBS37	690835	5690065	1344.75
OBS38	690645	5690035	1344.75
OBS39	690405	5690035	1344.75
OBS40	690595	5690185	1344.75
OBS41	690335	5690225	1344.75

OBS42	690225	5690235	1344.75
OBS43	690255	5690435	1344.75
OBS44	690195	5690125	1344.75
OBS45	690095	5690225	1344.75
OBS46	690365	5690005	1344.75
OBS47	690245	5690555	1344.75
OBS48	690295	5690655	1344.75
OBS49	690445	5690685	1344.75
OBS50	690675	5690515	1344.75
OBS51	690175	5690685	1344.75
OBS52	690805	5690495	1348.75
OBS53	690455	5690675	1348.75
OBS54	690295	5690615	1348.75
OBS55	690835	5690405	1348.75
OBS56	690265	5690375	1348.75
OBS57	690835	5690335	1348.75
OBS58	690225	5690495	1348.75
OBS59	690155	5690505	1348.75
OBS60	690805	5690875	1348.75
OBS61	690835	5690795	1348.75
OBS62	690485	5690815	1348.75
OBS63	690195	5690825	1348.75
OBS64	690425	5690105	1348.75
OBS65	690400	5690990	1348.75
OBS66	690050	5690050	1348.75
OBS67	690990	5690700	1348.75
OBS68	690990	5690800	1348.75
OBS69	690990	5690900	1348.75
OBS70	690995	5690480	1342.75
OBS71	690995	5690580	1342.75
OBS72	690995	5690400	1342.75
OBS73	690995	5690500	1342.75
OBS74	690995	5690650	1342.75

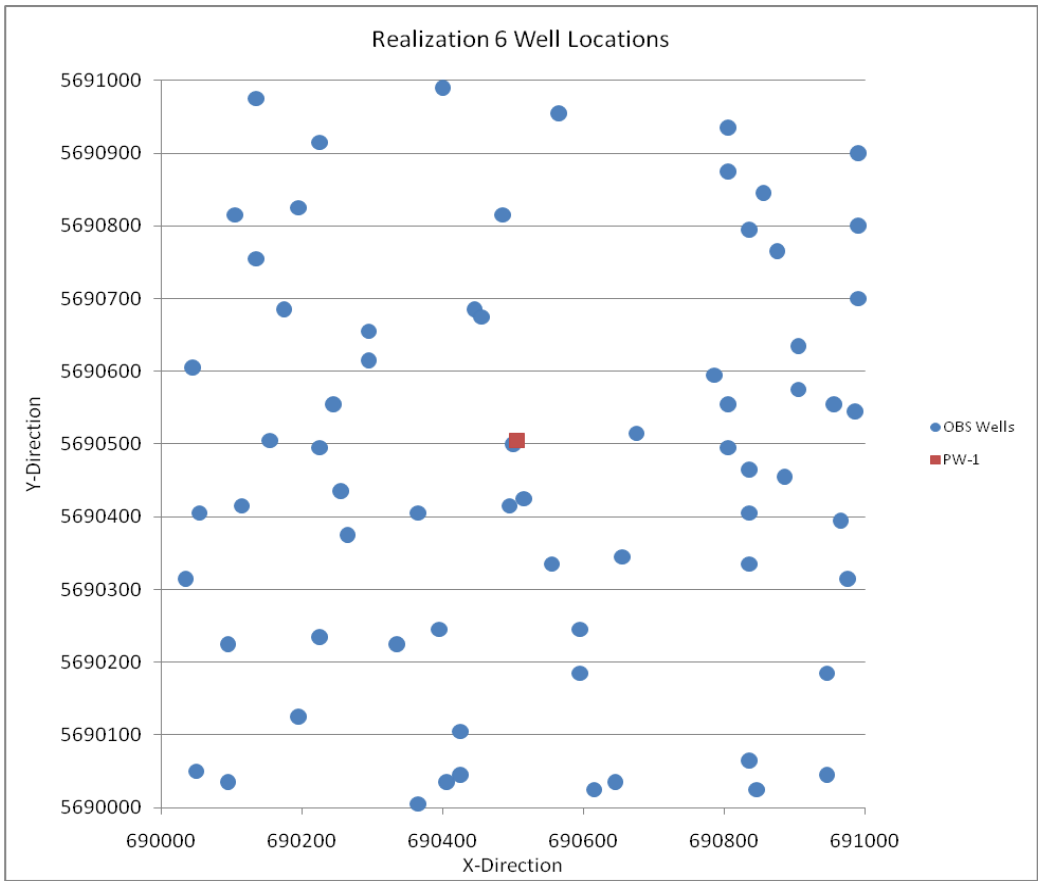
Realization 6 Well Locations
5691000
5690900
5690800
5690700
5690600
5690500
5690400
5690300
5690200
5690100
5690000
Y-Direction
690000
690200
690400
690600
690800
691000
X-Direction
OBS Wells
PW-1

Realization 43 Well Coordinates

Well Name	X-Coordinate (m)	Y-Coordinate (m)	Z-Coordinate (m)
PW-1	690495	5690505	1324.75
OBS1	690480	5690490	1324.75
OBS2	690055	5690935	1324.75
OBS3	690035	5690615	1324.75
OBS4	690055	5690415	1324.75
OBS5	690025	5690295	1324.75
OBS6	690025	5690225	1324.75
OBS7	690115	5690195	1324.75
OBS8	690045	5690165	1324.75
OBS9	690055	5690005	1324.75
OBS10	690205	5690045	1324.75
OBS11	690365	5690085	1324.75
OBS12	690275	5690165	1324.75
OBS13	690385	5690215	1324.75
OBS14	690435	5690225	1324.75
OBS15	690475	5690245	1324.75
OBS16	690525	5690295	1324.75
OBS17	690545	5690155	1324.75
OBS18	690535	5690075	1324.75
OBS19	690575	5690065	1324.75
OBS20	690715	5690235	1324.75
OBS21	690715	5690125	1324.75
OBS22	690735	5690015	1324.75
OBS23	690825	5690055	1324.75
OBS24	690985	5690135	1324.75
OBS25	690955	5690265	1324.75
OBS26	690975	5690405	1324.75
OBS27	690675	5690445	1324.75
OBS28	690925	5690635	1324.75
OBS29	690895	5690765	1324.75
OBS30	690955	5690905	1324.75
OBS31	690745	5690955	1324.75
OBS32	690715	5690795	1324.75
OBS33	690625	5690755	1324.75
OBS34	690375	5690585	1324.75
OBS35	690365	5690635	1324.75
OBS36	690255	5690985	1324.75
OBS37	690265	5690395	1324.75
OBS38	690705	5690285	1324.75
OBS39	690815	5690435	1324.75
OBS40	690565	5690385	1345.25
OBS41	690645	5690725	1345.25

OBS42	690645	5690525	1333.25
OBS43	690505	5690285	1333.25
OBS44	690565	5690215	1333.25
OBS45	690835	5690395	1333.25
OBS46	690265	5690145	1333.25
OBS47	690175	5690235	1333.25
OBS48	690425	5690695	1333.25
OBS49	690865	5690735	1329.25
OBS50	690275	5690485	1329.25
OBS51	690505	5690135	1329.25
OBS52	690445	5690555	1326.75
OBS53	690415	5690885	1326.75
OBS54	690305	5690655	1326.75
OBS55	690225	5690705	1326.75
OBS56	690462	5690990	1316.75
OBS57	690474	5690015	1316.75
OBS58	690992	5690710	1316.75
OBS59	690255	5690985	1316.75

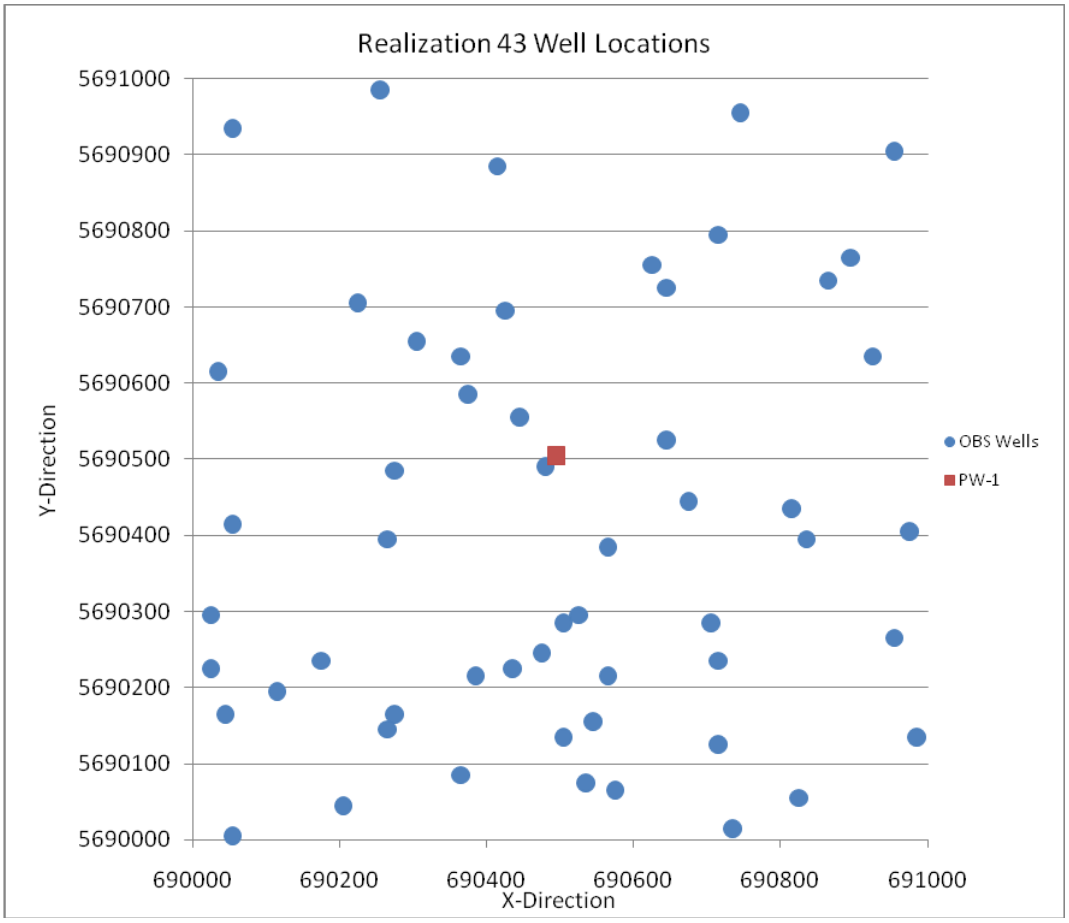

Realization 46 Well Locations

Well Name	X-Coordinate (m)	Y-Coordinate (m)	Z-Coordinate (m)
PW-1	690505	5690505	1393.75
OBS1	690505	5690510	1393.75
OBS2	690505	5690395	1385.75
OBS3	690645	5690435	1385.75
OBS4	690755	5690465	1385.75
OBS5	690885	5690515	1385.75
OBS6	690965	5690625	1385.75
OBS7	690895	5690395	1385.75
OBS8	690545	5690385	1385.75
OBS9	690615	5690305	1385.75
OBS10	690525	5690255	1385.75
OBS11	690315	5690415	1385.75
OBS12	690335	5690265	1385.75
OBS13	690215	5690385	1385.75
OBS14	690115	5690495	1385.75
OBS15	690575	5690395	1385.75
OBS16	690895	5690545	1385.75
OBS17	690445	5690015	1385.75
OBS18	690645	5690025	1385.75
OBS19	690825	5690015	1385.75
OBS20	690985	5690125	1385.75
OBS21	690975	5690235	1385.75
OBS22	690895	5690525	1385.75
OBS23	690045	5690635	1385.75
OBS24	690035	5690165	1385.75
OBS25	690135	5690325	1385.75
OBS26	690435	5690635	1385.75
OBS27	690775	5690555	1385.75
OBS28	690215	5690745	1385.75
OBS29	690325	5690575	1385.75
OBS30	690135	5690645	1387.75
OBS31	690145	5690155	1387.75
OBS32	690905	5690225	1387.75
OBS33	690975	5690145	1387.75
OBS34	690495	5690375	1387.75
OBS35	690145	5690895	1387.75
OBS36	690285	5690045	1387.75
OBS37	690045	5690505	1387.75
OBS38	690655	5690225	1387.75
OBS39	690055	5690425	1387.75
OBS40	690845	5690035	1387.75
OBS41	690035	5690275	1387.75

OBS42	690425	5690905	1387.75
OBS43	690805	5690875	1387.75
OBS44	690475	5690355	1390.75
OBS45	690095	5690505	1390.75
OBS46	690885	5690385	1390.75
OBS47	690275	5690795	1390.75
OBS48	690455	5690955	1390.75
OBS49	690995	5690875	1390.75
OBS50	690975	5690755	1390.75
OBS51	690795	5690125	1390.75
OBS52	690415	5690795	1390.75
OBS53	690995	5690335	1390.75
OBS54	690245	5690935	1390.75
OBS55	690045	5690945	1391.75
OBS56	690985	5690490	1391.75
OBS57	690065	5690045	1391.75
OBS58	690025	5690655	1391.75
OBS59	690525	5690395	1391.75
OBS60	690515	5690395	1392.75
OBS61	690225	5690565	1392.75
OBS62	690795	5690335	1392.75

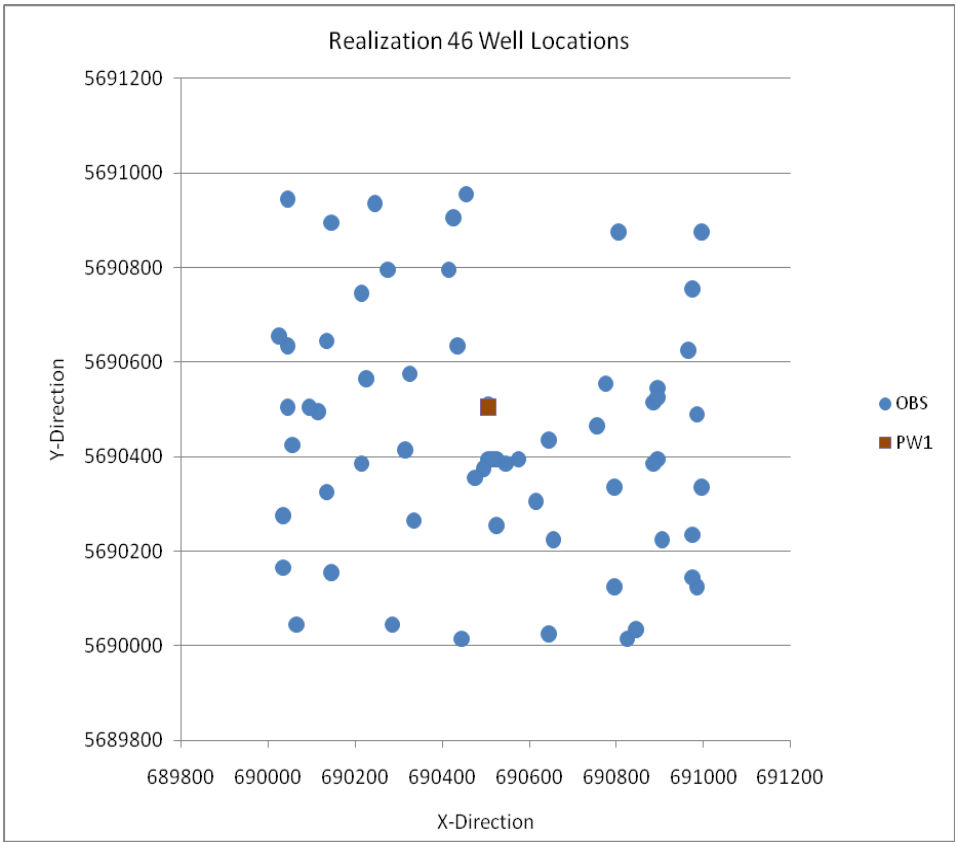

Realization 48 Well Locations

Well Name	X-Coordinate (m)	Y-Coordinate (m)	Z-Coordinate (m)
PW-1	690505	5690545	1362.25
OBS1	690015	5690195	1366.75
OBS2	690205	5690155	1366.75
OBS3	690345	5690175	1366.75
OBS4	690525	5690295	1366.75
OBS5	690715	5690325	1366.75
OBS6	690835	5690275	1366.75
OBS7	690685	5690235	1366.75
OBS8	690735	5690445	1366.75
OBS9	690935	5690395	1366.75
OBS10	690965	5690435	1366.75
OBS11	690885	5690175	1366.75
OBS12	690955	5690035	1366.75
OBS13	690405	5690555	1366.75
OBS14	690555	5690645	1366.75
OBS15	690245	5690455	1366.75
OBS16	690015	5690475	1366.75
OBS17	690095	5690720	1366.75
OBS18	690605	5690675	1366.75
OBS19	690935	5690735	1366.75
OBS20	690515	5690915	1366.75
OBS21	690155	5690835	1366.75
OBS22	690105	5690925	1366.75
OBS23	690685	5690965	1366.75
OBS24	690775	5690895	1366.75
OBS25	690625	5690904	1366.75
OBS26	690835	5690575	1370.25
OBS27	690975	5690535	1370.25
OBS28	690475	5690705	1370.25
OBS29	690435	5690325	1370.25
OBS30	690175	5690445	1370.25
OBS31	690305	5690285	1370.25
OBS32	690435	5690145	1370.25
OBS33	690545	5690065	1370.25
OBS34	690825	5690275	1370.25
OBS35	690945	5690365	1370.25
OBS36	690335	5690325	1370.25
OBS37	690725	5690445	1370.25
OBS38	690425	5690695	1370.25
OBS39	690875	5690835	1370.25
OBS40	690125	5690675	1370.25
OBS41	690505	5690915	1370.25

OBS42	690925	5690885	1370.25
OBS43	690715	5690035	1370.25
OBS44	690965	5690305	1370.25
OBS45	690215	5690955	1370.25
OBS46	690635	5690565	1370.25
OBS47	690845	5690545	1371.25
OBS48	690775	5690435	1371.25
OBS49	690345	5690505	1371.25
OBS50	690895	5690295	1371.25
OBS51	690405	5690545	1371.25
OBS52	690735	5690735	1371.25
OBS53	690685	5690515	1362.25
OBS54	690635	5690205	1362.25
OBS55	690845	5690745	1362.25
OBS56	690385	5690375	1362.25
OBS57	690745	5690305	1362.25
OBS58	690935	5690735	1362.25
OBS59	690155	5690825	1362.25
OBS60	690255	5690935	1362.25
OBS61	690355	5690585	1362.25
OBS62	690085	5690025	1390.00
OBS63	690345	5690025	1390.00
OBS64	690415	5690955	1390.00

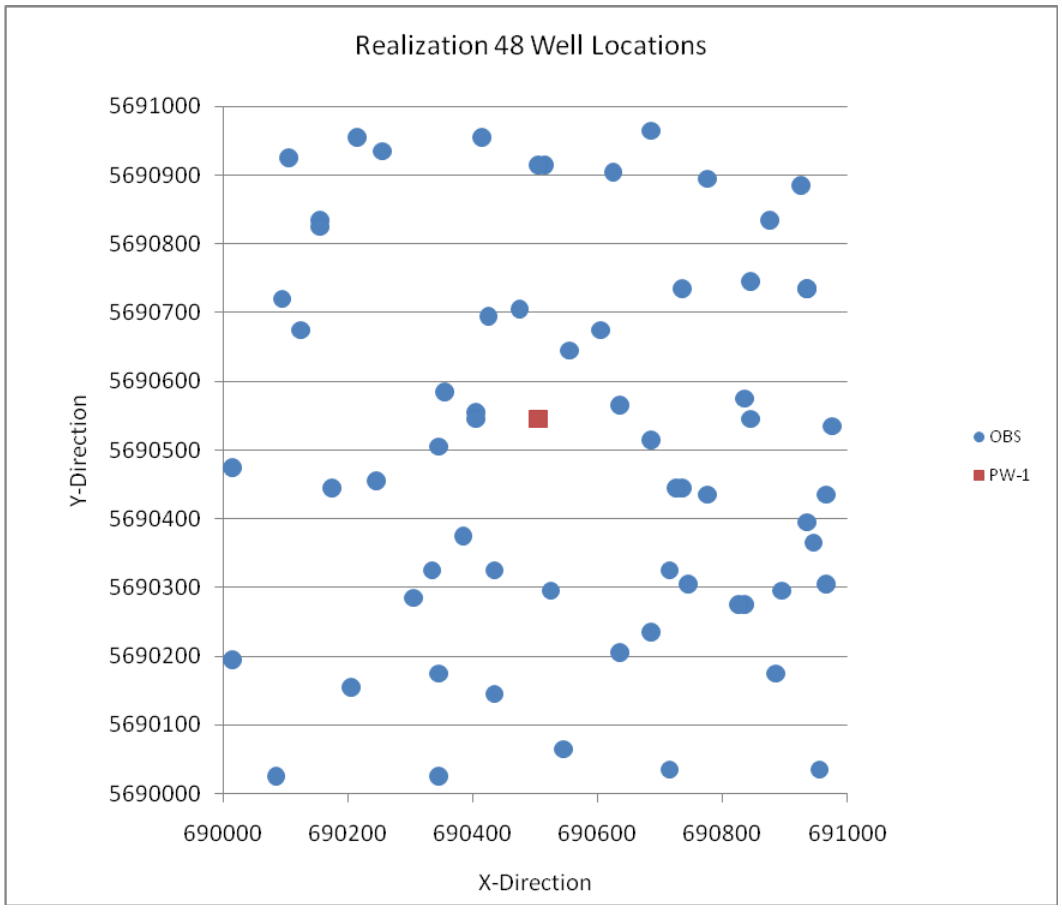

Realization 61 Well Coordinates

Well Name	X-Coordinate (m)	Y-Coordinate (m)	Z-Coordinate (m)
PW-1	690505	5690505	1400
OBS1	690500	5690500	1393.75
OBS2	690495	5690490	1393.75
OBS3	690555	5690475	1393.75
OBS4	690605	5690505	1393.75
OBS5	690715	5690425	1393.75
OBS6	690555	5690295	1393.75
OBS7	690435	5690415	1393.75
OBS8	690405	5690365	1393.75
OBS9	690315	5690365	1393.75
OBS10	690175	5690465	1393.75
OBS11	690535	5690755	1393.75
OBS12	690275	5690755	1393.75
OBS13	690095	5690655	1393.75
OBS14	690075	5690925	1393.75
OBS15	690005	5690445	1393.75
OBS16	690105	5690405	1393.75
OBS17	690285	5690385	1393.75
OBS18	690455	5690285	1393.75
OBS19	690475	5690175	1393.75
OBS20	690595	5690215	1393.75
OBS21	690675	5690285	1393.75
OBS22	690755	5690325	1393.75
OBS23	690885	5690385	1393.75
OBS24	690945	5690255	1393.75
OBS25	690925	5690165	1393.75
OBS26	690535	5690055	1393.75
OBS27	690445	5690145	1393.75
OBS28	690455	5690225	1393.75
OBS29	690545	5690155	1393.75
OBS30	690335	5690275	1393.75
OBS31	690265	5690295	1393.75
OBS32	690175	5690225	1393.75
OBS33	690125	5690195	1393.75
OBS34	690185	5690035	1393.75
OBS35	690025	5690125	1393.75
OBS36	690095	5690365	1393.75
OBS37	690545	5690955	1393.75
OBS38	690985	5690555	1393.75
OBS39	690335	5690565	1393.75
OBS40	690915	5690255	1396.25
OBS41	690125	5690425	1396.25

OBS42	690425	5690025	1396.25
OBS43	690985	5690955	1396.25
OBS44	690145	5690715	1396.25
OBS45	690775	5690775	1398.25
OBS46	690705	5690165	1398.25
OBS47	690095	5690455	1398.25
OBS48	690115	5690215	1398.25
OBS49	690235	5690235	1398.75
OBS50	690835	5690075	1398.75
OBS51	690985	5690095	1398.75
OBS52	690805	5690935	1398.75
OBS53	690915	5690965	1398.75
OBS54	690195	5690775	1398.75
OBS55	690375	5690255	1399.25
OBS56	690355	5690135	1399.25
OBS57	690665	5690145	1399.25
OBS58	690875	5690695	1399.25
OBS59	690005	5690135	1399.25
OBS60	690835	5690065	1399.25
OBS61	690625	5690415	1399.25
OBS62	690315	5690205	1399.25
OBS63	690365	5690205	1399.25
OBS64	690285	5690365	1399.75
OBS65	690715	5690915	1399.75
OBS66	690265	5690235	1399.75